Investigations of Water-Bearing Environments on the Moon and Mars

by

Julie Mitchell

A Dissertation Presented in Partial Fulfillment
of the Requirements for the Degree
Doctor of Philosophy

Approved November 2017 by the
Graduate Supervisory Committee:

Philip R. Christensen, Chair
James F. Bell III
Steven Desch
Hilairy E. Hartnett
Mark Robinson

ARIZONA STATE UNIVERSITY

December 2017

ABSTRACT

Water is a critical resource for future human missions, and is necessary for understanding the evolution of the Solar System. The Moon and Mars have water in various forms and are therefore high-priority targets in the search for accessible extraterrestrial water. Complementary remote sensing analyses coupled with laboratory and field studies are necessary to provide a scientific context for future lunar and Mars exploration. In this thesis, I use multiple techniques to investigate the presence of water-ice at the lunar poles and the properties of martian chloride minerals, whose evolution is intricately linked with liquid water.

Permanently shadowed regions (PSRs) at the lunar poles may contain substantial water ice, but radar signatures at PSRs could indicate water ice or large block populations. Mini-RF radar and Lunar Reconnaissance Orbiter Camera Narrow Angle Camera (LROC NAC) products were used to assess block abundances where radar signatures indicated potential ice deposits. While the majority of PSRs in this study indicated large block populations and a low likelihood of water ice, one crater – Rozhdestvenskiy N – showed indirect indications of water ice in its interior.

Chloride deposits indicate regions where the last substantial liquid water existed on Mars. Major ion abundances and expected precipitation sequences of terrestrial chloride brines could provide context for assessing the provenance of martian chloride deposits. Chloride minerals are most readily distinguished in the far-infrared (45+ μm), where their fundamental absorption features are strongest. Multiple chloride compositions and textures were characterized in far-infrared emission for the first time.

Systematic variations in the spectra were observed; these variations will allow chloride mineralogy to be determined and large variations in texture to be constrained.

In the present day, recurring slope lineae (RSL) may indicate water flow, but fresh water is not stable on Mars. However, dissolved chloride could allow liquid water to flow transiently. Using Thermal Emission Imaging System (THEMIS) data, I determined that RSL are most likely not fed by chloride-rich brines on Mars. Substantial amounts of salt would be consumed to produce a surface water flow; therefore, these features are therefore thought to instead be surface darkening due to capillary wicking.

DEDICATION

This dissertation is dedicated to my cats, who provided unwavering love and used litter throughout my years of graduate school. May their paw prints fly to Mars.

ACKNOWLEDGMENTS

This work was made possible by the support, encouragement, collaboration, and mentorship from the residents of the Mars Space Flight Facility (MSFF), including: Dr. Phil Christensen (graduate advisor and committee chair), the fellow MSFF graduate students (Chris Haberle, Jon Hill, Amber Keske, Chris Mount, Sean Peters, Allie Rutledge, Andy Ryan, Becky Smith, Mike Veto), Tara Fisher, Ashley Toland, the MSFF researchers (Briony Horgan, Jun Huang, Mike Kraft, Steve Ruff, Mark Salvatore), and the ever-patient JMARS and Davinci developers. I also thank Bill O'Donnell and the OTES team for taking the time to show me the ropes of instrument testing.

The LROC team was a source of both wisdom and positivity, including: Drs. Mark Robinson (dissertation and oral exam committee member), Sam Lawrence (oral exam committee member), Brett Denevi, and Ernest Cisneros, Kristen Paris and Emerson Speyerer. I also thank the rest of my dissertation committee – Drs. Jim Bell, Steve, Desch, and Hilairy Hartnett – for your honest and helpful feedback. At the department level, I thank Becca Dial and Becky Polley for both your kindness and competence.

This work would not have been completed if not for the incredible support – and patience – from my closest friends in SESE: Heather Meyer and Alli Severson, who made me better in every way; my roommates, Kim Ward-Duong, Prajkta Mane, Abhi Rajan, and Taisiya Kopytova; and the rest of the SESE graduate students. I also thank my family: Renae Mitchell (for showing me college is an option), Tracy Mitchell, Vitaliy Gyrya, and Nina Gyrya. And finally, I thank my team at Gracie Barra Brazilian Jiu-Jitsu (Arizona and Texas) for keeping me sane through this whole process.

TABLE OF CONTENTS

Page

LIST OF TABLES xi

LIST OF FIGURES xii

CHAPTER

1 INTRODUCTION 1

1.1 Motivation and Purpose 1

1.2 Background 4

1.2.1 The Moon 4

1.2.2 Mars 6

2 AN INVESTIGATION OF THE LIKELIHOOD OF WATER ICE AT THE LUNAR NORTH POLE USING RADAR AND VISIBLE IMAGES 13

2.1 Introduction 13

2.1.1 Preface 13

2.1.2 Permanently Shadowed Regions 14

2.1.3 Previous Results 15

2.1.4 Rationale for This Work 20

2.2 Data Sources and Methods 21

2.2.1 LROC Narrow Angle Cameras 21

2.2.2 Miniature Radio Frequency Experiment (Mini-RF) 23

2.2.3 M-chi Decomposition Maps 23

2.2.4 Quantifying the Abundance of Blocks 27

CHAPTER Page

2.2.5 Size-Frequency Distributions 27

2.2.6 Targets of Interest 28

2.3 Results 33

2.3.1 Polar CPR-Anomalous Craters.....33

2.3.2 Polar CPR-Normal Craters 44

2.3.3 CPR-Anomalous Equatorial Craters 44

2.3.4 Circular Polarization Ratio and Lunar Polar Craters 48

2.4 Discussion 49

2.4.1 Introduction 49

2.4.2 Resolution Limitations.....49

2.4.3 Implications of Crater Freshness and Age 50

2.4.4 The Presence of Water-Ice Deposits 52

2.4.5 Whipple Crater.....54

2.5 Outstanding Questions 55

2.6 Conclusions 57

2.7 Acknowledgments.....58

3 CHLORIDE-RICH BRINES: ANALOGS FOR WATER ON ANCIENT MARS 59

3.1 Introduction 59

3.1.1 Motivation for This Study 60

3.2 Background 62

CHAPTER Page

3.2.1 Brine Genesis 62

3.2.2 Brine Transport and Water-Rock Reactions 65

3.2.3 Chemical Evolution of Evaporating Waters 68

3.2.4 Cold Processes 73

3.2.5 Influences on Trace Metals 75

3.2.6 Seawater 76

3.2.7 Mars 77

3.3 Terrestrial Localities with Chloride-Rich Brines 79

3.3.1 Hydrothermal Continental Brines 79

3.3.2 Hydrothermal Oceanic and Mid-Ocean Ridge Brines 81

3.3.3 Temperate Endorheic Basinal Brines 83

3.3.4 Cold Endorheic Basinal Brines 85

3.3.5 Deep Basinal Brines 86

3.4 Methods 89

3.5 Data/Results 97

3.5.1 pH 97

3.5.2 Major Ions 97

3.5.3 Geochemical Modeling with PHREEQC 112

3.5.4 Trace Metals 117

3.6 Discussion 121

3.6.1 Major Ions 121

3.6.2 Trace Metals 127

CHAPTER Page

3.7 Conclusions 129

3.8 Acknowledgments 131

4 THE EFFECTS OF COMPOSITION AND TEXTURE ON THE INFRARED EMISSION SPECTRA OF CHLORIDE MINERALS 132

4.1 Introduction 132

4.1.1 Evaporite Minerals 132

4.1.2 Textural Variations 133

4.1.3 Purpose of This Study 134

4.2 Background 134

4.2.1 Chloride-Rich Environments 134

4.2.2 Precipitation Sequence 135

4.2.3 Physical Properties of Chlorides 136

4.2.4 Identification of Chlorides on Mars 139

4.2.5 Textural Variations with Environment 140

4.2.6 Quantifying Emissivity 144

4.2.7 Expected Variations in Spectral Properties 144

4.3 Methods 146

4.3.1 Field Sample Collection 146

4.3.2 Synthetic Sample Preparation 149

4.3.3 Infrared Emission Spectroscopy 151

4.3.4 Spectral Analysis 153

CHAPTER Page

4.4 Results 154
4.4.1 Salt Precipitation Process.....154
4.4.2 Synthetic Samples and Spectra.....158
4.4.3 Field Samples and Spectra.....177
4.5 Discussion 191
4.5.1 Constraining Chloride Mineralogy.....191
4.5.2 Constraining Chloride Texture and Grain Size.....192
4.5.3 Sensitivity to Contaminants.....195
4.5.4 Environmental Implications for Mars 196
4.5.5 Future Work 200
4.6 Conclusions 201
4.7 Acknowledgments.....202

5 RECURRING SLOPE LINEAE AND CHLORIDES ON THE SURFACE OF MARS 203
5.1 Introduction 203
5.2 Background 205
5.2.1 Evidence for Previous Water Activity on the Martian Surface 205
5.2.2 Temperature Constraints for RSL Formation 208
5.2.3 Water Reservoirs for RSL 209
5.2.4 Aqueous Chemistry of RSL.....211

CHAPTER Page

5.2.5 Detectability of RSL-Scale Chloride Deposits 213

5.3 Materials and Methods.....217

5.4 Results 223

5.4.1 Remote Sensing Observations.....223

5.4.2 Assessing the Abundance of Chlorides.....236

5.5 Discussion 241

5.6 Conclusions 243

5.7 Acknowledgments.....245

6 CONCLUSIONS 246

REFERENCES..... 255

APPENDIX

A IMAGE IDS FOR LRO DATA PRODUCTS USED 295

B PREVIOUS PUBLICATION/STATEMENT OF CO-AUTHORS 297

LIST OF TABLES

Table		Page
2.1	Summary of Craters of Study	30
2.2	Block Detection Limits, Block Counts, Densities, and B Values for Craters	35
2.3	Likelihood of Ice Deposits in PSRs Based on Study Results	54
3.1	Localities, Sample Names, and References for Major Ion Data	92
3.2	Sample Data for All Localities with Sample Names	93
3.3	Total Alkali Silica Contents for Major Units at Select Localities	95
3.4	Trace Metal Concentrations and Associated References	119
4.1.	Crystal Systems and Locations of Far-Infrared Absorptions for Chlorides	137
4.2.	Summary of Spectral Features for All Samples in this Study	189

LIST OF FIGURES

Figure		Page
1.1	The Chloride Cycle: Sources, Transport, and Alteration on Mars	10
2.1	LROC Wide Angle Camera Illumination Maps of the Lunar North Pole	16
2.2	Example of NAC Imagery Used for Block Counts in PSRs	23
2.3	M-chi Decomposition of CPR-Anomalous Crater Rozhdesvenskiy N	26
2.4	Example M-chi Maps of Craters in This Study	32
2.5	Long-Exposure NAC Images of PSRs in Lovelace E, Lovelace, And Whipple Craters	34
2.6	Block Densities for a) All Blocks, and b) Blocks >20-m Diameter	36
2.7	Crater Exterior Block Size Distributions in Percent of Total Blocks	38
2.8	Crater Interior Block Size Distributions in Percent of Total Blocks	39
2.9	Cumulative Block Size-Frequency Distributions for All Crater Exteriors	40
2.10	Cumulative Block Size-Frequency Distributions for All Crater Interiors	41
2.11	Comparison of Block Size-Frequencies for Different Crater Types	42
2.12	Comparison of Actual Versus Extrapolated Interior Block Abundances	43
2.13	Interior of Byrgius C Showing Numerous Blocks and a Large Down-Slope Bounced Block	45
2.14	M-chi Decomposition Map and LROC NAC of Gardner Crater	46
3.1	Chemical Divides Expected for Mars, from Tosca and McLennan (2006)	72
3.2	Terrestrial Chloride-Rich Brine Localities Included in This Study	79
3.3	Total Alkali Silica Plot Comparing Geologic Context of Study Sites	96

Figure Page

3.4 Ternary Ca-Cl-SO_4 Diagram Showing Dominant Anion for Each Brine in This Study 98

3.5 Major Cations Versus Chloride Concentration 101

3.6 Na/K Versus Chloride Concentration 102

3.7 Na/K Versus Ca/Mg For All Brines 103

3.8 Molar Ratios of Major Ions Relative to Na/Cl 106

3.9 Dissolved Chloride Minerals in Each Brine Type 107

3.10 Ternary Diagram of Cl-Ca-Na for All Brines, Classified By Brine Type 109

3.11 Ternary Diagram of Ca-Mg-Na+K for All Brines, Classified By Brine Type 110

3.12 Ternary Diagram of Ca-Mg-K for All Brines, Classified By Brine Type 111

3.13 Major Ion Concentrations Versus Ionic Strength 114

3.14 Mineral Precipitation Sequences Based on Saturation Indices 115

3.15 Chloride Divides Based on Geochemical Modeling 118

3.16 Log Bar Plot of Trace Metal Concentrations for Each Locality 120

3.17 Cartoons of Inclusions Showing the Precipitation Sequence of Chlorides 127

4.1 Halite Mushrooms as Observed at the Dead Sea, Israel 143

4.2 Surface and Aerial Views of Bristol Dry Lake, CA 148

4.3 Precipitation Tank for Producing Synthetic Chloride Textures 150

4.4 Textures Produced During Crystal Precipitation Process 157

4.5 Unusual Spire Textures in Precipitation Tank 158

4.6 Synthetic Halite Textures Used in Spectral Analysis 162

4.7 Mid-Infrared Through Far-Infrared Emission Spectra of Pressed Pellets 163

Figure Page

4.8 Far-Infrared Emission Spectra of Pressed Pellets 158

4.9 Mid-Infrared Through Far-Infrared Emission Spectra of Synthetic Textures 165

4.10 Far-Infrared Emission Spectra of Synthetic Textures 166

4.11 Band Depth Relative to Continuum Emissivity for Synthetic Textures 168

4.12 Locations of 180 cm^{-1} Band Center for Synthetic Samples 170

4.13 Band Centers Versus Band Depths at 180 cm^{-1} for Synthetic Samples 170

4.14 Band Depth Relative to Continuum Emissivity at 260 cm^{-1} 172

4.15 Locations of 260 cm^{-1} Band Center for Synthetic Samples 173

4.16 Christiansen Feature at First Emission Peak for Synthetic Samples 175

4.17 Band Ratio of Emissivities of 180 cm^{-1}/280 cm^{-1} Absorptions 176

4.18 Field Textures Corresponding to Synthetic Halite Samples 179

4.19 Field Samples Used for Spectral Analysis 180

4.20 Mid-Infrared and Far-Infrared Emission Spectra of Field Samples 183

4.21 Far-Infrared Emission Spectra of Field Samples 184

4.22 Band Depth and Band Center for Field Samples at 180 cm^{-1} Absorption 186

4.23 Band Ratios Between Fundamental Absorptions for Field Samples 186

4.24 Spectral Radiance of Halite, Sylvite Pressed Pellets Compared to Basalt 188

5.1 Recurring Slope Lineae Seen at Palikir Crater in HiRISE Falses Color Images .. 204

5.2 Distribution of Chlorides and RSL on the Surface of Mars 214

5.3 Area Covered by RSL Mapped on HiRISE Image of Horowitz Crater 218

5.4 Example Chloride Deposits in Miyamoto Crater 219

5.5 THEMIS DCS Map and RSL in Triolet Crater 224

Figure Page

5.6 Example of Steep Slope with Anisothermalities 225

5.7 Southeast of Huggins Crater, Showing Spectral Slopes Indicative of Anisothermal Steep Terrain 227

5.8 Outline of RSL Region of Study in Palikir Crater 228

5.9 THEMIS Emissivity Spectrum for Palikir Crater Indicative of Chlorides Compared to Reference Chloride Spectrum 230

5.10 Large RSL Site in Southeast Melas Chasma, Valles Marineris 232

5.11 Locations of Equatorial RSL Sites and Published Chloride Deposits in the Valles Marineris Region. 233

5.12 Indication of Chloride Deposits in Valles Marineris 235

5.13 THEMIS Emissivity Spectrum of RSL Indicative of Chlorides Compared with a Reference Chloride Spectrum from Osterloo et al. 2008 236

5.14 Representative RSL in Valles Marineris with dimensions shown in white dotted outline. 240

CHAPTER 1

INTRODUCTION

Water is a key resource both for human exploration and for developing a thorough understanding of Solar System evolution. On Earth, humans need water for drinking, personal hygiene, and as a component of many foods. In space, these needs also exist, in addition to many others that are unique to the space environment. For example, water is used as a coolant in internal thermal control systems on spacecraft, as a source of fuel for fuel cell and other energy-producing reactions, and it can be used for radiation protection on long-duration space missions. The drawback to these needs is the extreme mass constraint that water poses for human missions: the longer the mission, the more water is needed, resulting in a drastic increase in mass and cost with mission duration. Therefore, it is highly impractical – and unaffordable – to transport all the necessary water for long-duration planetary missions. A much smaller mass of water can be recycled, resulting in substantial mass savings for highly efficient water recycling systems. However, even the best water recycling system cannot compensate for water lost irretrievably due to extra-vehicular activities (EVAs), spacecraft leakage, or other unforeseen events. For long-term exploration, it is therefore critical to supplement spacecraft water with *in-situ* water, derived from the planetary region which the crew is investigating.

The scientific return in studying extraterrestrial water is substantial. Numerous gaps exist in our understanding of the beginnings of the Solar System and the role water played in its evolution. Comets and asteroids have been posed as possible sources of water in the Earth-Moon system, but so few analyses of extraterrestrial water exist that these hypotheses remain open for debate [*Arnold*, 1979; *Zhang and Paige*, 2009; *Svetsov*

and Shuvalov, 2015]. In a similar process, a recent cometary impact has been proposed as the source of water ice deposits at the poles of Mercury [*Paige et al.*, 1992; *Chabot et al.*, 2014].

The primary method linking differentiated meteoritic samples with their parent bodies is their oxygen isotope abundance, specifically the concentration of ^{18}O relative to the more common ^{16}O in extraterrestrial samples compared to the standard mean ocean water (SMOW) measured on Earth, known as $\delta^{18}O$. This measurement has been used to link meteoritic samples to the Moon, Mars, Vesta, and possibly Mercury [*Sautter et al.*, 2006; *Alexander et al.*, 2012; *Magna et al.*, 2014]. Similarly, the relative values of D (deuterium, or ^{2}H) relative to H (hydrogen, or ^{1}H) between extraterrestrial samples and SMOW (δD or $\delta^{2}H$) reveal the extent of degassing, fractionation, and thermal alteration in ancient Solar System materials [*Saal et al.*, 2008].

Comets condensed from the original solar nebula, and have remained at the edges of the solar system in the Oort Cloud where they preserve the δD values of proto-solar water; comets have high δD ratios relative to SMOW. The Late Veneer theory posits that comets brought water to Earth early in its history and were the source of its oceanic and mantle water; however, variations in δD between comets and SMOW call this theory into question. In contrast to cometary values, interstellar dust particles (IDPs) and interstellar matter have δD values lower than SMOW. Asteroids that formed in colder regions of the solar system may have brought ice to the inner solar system as part of the late veneer or have impacted the Moon or Mercury, acting as transportation for water from the outer solar system to the inner solar system. However, if the abundance of water in chondritic meteorites is the same as that of the ancient asteroid belt, then asteroids would not carry a

sufficient amount of water to account for the volume on Earth. [*Robert et al.*, 1999; *Morbidelli et al.*, 2000; *Marty and Yokochi*, 2006; *Albarede et al.*, 2013; *Yang, et al.*, 2013]

While other compounds in extraterrestrial samples can be a source of oxygen isotope measurements, the coupled measurements of $\delta^{18}O$, δD, and H_2O concentration can only be determined by direct measurement of water-bearing samples. The variability of δD values in comets, IDPs, asteroids, and meteorites is poorly constrained due to a lack of access to pristine water samples from those sources. Therefore, samples from these and planetary water-bearing environments provide a critical link between extraterrestrial samples, their parent bodies, and our understanding of Solar System evolution.

In order to collect these samples, a thorough reconnaissance of potential water-bearing environments must be carried out using remote sensing. Because the two closest and largest extraterrestrial reservoirs of water are the Moon and Mars, they have been explored most extensively by a suite of instruments and over a wide range of wavelengths. The purpose of this work is to build on previous investigations of the Moon and Mars to explore regions on both bodies where water resources and locations of scientific interest may exist. This work will set the stage for future, more focused remote sensing investigations, exploration by rovers and robotic instruments and, eventually, human exploration of the inner Solar System.

1.2 Background

1.2.1 The Moon

The Moon holds a unique record of the geologic history of the inner Solar System in the form of impact craters and crater basins, mare volcanics, and numerous tectonic features, which have been observed and studied from Earth for millennia. However, the thought that significant quantities of water ice may exist on the Moon has been hampered by a lack of visible evidence and low accessibility of potential ice deposits. While hypotheses for ice deposits on the Moon were published as early as the 1800s [*Birch,* 1866], only recent investigations have begun to test whether and to what extent water ice exists on the Moon. The Moon's low obliquity and orbital inclination can produce unique lighting conditions at a subset of lunar polar craters. Known as "permanently shadowed regions" or PSRs, the interiors of polar craters can therefore remain in darkness over the entirety of the lunar year and could harbor water ice deposits. As a result, the lunar poles became the focus of those prospecting for lunar ice as early as the 1960s. [*Watson et al.*, 1961a; *Arnold*, 1979; *Ingersoll et al.*, 1992; *Bussey et al.*, 1999, 2010; *Vasavada et al.*, 1999; *Mazarico et al.*, 2011; *Neumann et al.*, 2013; *Speyerer and Robinson*, 2013]

Because they receive little to no incident sunlight, PSRs have been hypothesized to reach and sustain extremely cold temperatures, serving as "cold traps" where water ice molecules can be frozen in place. [*Watson et al.*, 1961b; *Bussey*, 2003] Over time, these individual molecules can build up to produce potentially large water-ice deposits that could be detectable using remote sensing. Numerous modeling efforts have been undertaken to assess the stability of water ice at the poles in the context of micrometeoroid bombardment, solar wind influx, temperature fluctuations, and water-

rock reactions. While some have posed that large, crystalline ice deposits exist at the lunar poles [i.e., *Spudis et al.*, 2013], most models show that water-ice is metastable over much of the lunar surface and would need to be covered by tens of centimeters of regolith to protect it from micrometeoroids and from radiative heating [*Crider and Vondrak*, 2003; *Schorghofer*, 2007; *Paige et al.*, 2010; *Hayne et al.*, 2012, 2015; *McGovern et al.*, 2013; *Spudis et al.*, 2013; *Lucey et al.*, 2014; *Schorghofer and Aharonson*, 2014; *Stopar*, 2016]. Experimental efforts assessing the stability of water ice mixed with lunar simulant show that water ice is likely to be unstable at or above 100 K under vacuum (10^{-6} torr) over geologic timescales [*Piquette et al.*, 2017].

Several lunar missions have assessed the distribution and abundance of water-ice at the lunar poles, including Clementine and Lunar Prospector (1990s), SELENE (2007), Chandrayaan-1 (2008), LCROSS (2009) and the Lunar Reconnaissance Orbiter (LRO, 2009 - present) [*Nozette et al.*, 1996; *Feldman et al.*, 1998, 2000, 2001; *Pieters et al.*, 2009a; *Colaprete et al.*, 2010; *Vondrak et al.*, 2010; *Cheek et al.*, 2011]. Neutron spectroscopy, UV reflectance, visible images, infrared reflectance and emission, and radar have all been used to explore PSRs. A summary of the latest results using these techniques is given in Chapter 2 below. While none of these techniques has definitively proven that large water-ice deposits exist at the lunar poles, exploration using complementary techniques has provided new insights into the mysteries hidden within PSRs. Chapter 2 describes a unique effort to couple long-exposure visible images by the LRO Camera and the Mini-RF radar instrument onboard the LRO to explore the nature of PSRs at the lunar north pole.

1.2.2 Mars

The history of water on Mars is recorded in the morphology and chemical composition of its surface. A summary of the geologic, morphologic, and chemical evidence for extensive volumes of water in Mars' early history is provided in Chapters 3-5. While the martian poles are known to harbor large deposits of water ice, these environments are too cold to support initial human missions or any known forms of life. As a result, the exploration of water-bearing environments at lower latitudes has a high priority for the planning of human missions, the collection of water-bearing samples, and for astrobiological studies. The production of clays, carbonates, sulfates, and chloride minerals requires the presence of water, due to water-rock interactions and/or the evaporative concentration of a body of water. In particular, chloride minerals are found at equatorial to mid-latitudes on Mars and record the final stages of the period when liquid water was abundant on the martian surface (e.g., late-Noachian to early Hesperian). Chloride minerals therefore provide a unique opportunity for exploring martian and Solar System history and searching for signs of life, while also providing a possible water resource for future human crews.

A schematic of the origin, evolution, and alteration of chlorine and chloride ion on Mars is shown in Figure 1.1; this chlorine "life cycle" is briefly discussed here. Multiple mechanisms have been proposed as the source of chlorine on the martian surface. Chlorine could be provided by the acidic weathering of volcanic rocks (i.e., chloride ion-bearing basalt) and the resultant leaching of various ions into solution. Acidic weathering has been proposed as the cause of chemical alteration observed using remote sensing and *in-situ* measurements made by rovers of altered rocks [*Banin*, 1996;

Bullock, 2004; *Tosca et al.*, 2004, 2005; *Squyres and Knoll*, 2005; *Tosca and McLennan*, 2006; *Michalski et al.*, 2017]. Chloride could also be transported to the martian surface through volcanic outgassing of HCl where it could react with surface rocks by the acid-fog reaction [*Banin*, 1996; *Jakosky and Phillips*, 2001; *Tosca et al.*, 2004]. Direct precipitation of chlorides from volcanic gases as sublimates has been observed on Earth and demonstrated in laboratory experiments [*DiFrancesco*, 2016]. Finally, chloride could be transported to the surface via upwelling of hydrothermal or deep basinal brines, or neutral-pH water-rock reactions (i.e., ion exchange or freeze-concentration), which are all known to produce chloride-enriched brines on Earth [*Lowenstein and Risacher*, 2009; *Toner et al.*, 2013, 2017; *Michalski et al.*, 2017].

Chloride minerals can form on planetary surfaces by several mechanisms which are dependent on the sources listed above. Volcanic sublimates form thin crusts or microscopic particles on the surfaces on which they precipitate; sublimates generally form small-scale features and are localized to the volcanic vents they come from [*DiFrancesco*, 2016]. Large chloride deposits on Earth only form by the precipitation of chloride from highly concentrated brines. These brines can reach the surface through groundwater upwelling, where the surrounding geology and the water source (hydrothermal, deep basinal brine, neutral water-rock interactions) control the abundance of cations in solution [*Rosen*, 1994; *Squyres and Knoll*, 2005; *Lowenstein and Risacher*, 2009]. These cations dictate the specific forms of chloride mineral that eventually precipitate out of solution. In addition to groundwater upwelling, chlorides can precipitate from surface brines in channels/gullies or standing lacustrine bodies of water [*Hardie et al.*, 1978; *Catling*, 1999; *Jakosky and Phillips*, 2001; *Hynek et al.*, 2010;

Osterloo and Hynek, 2015]. Chlorides have been observed on Mars as both inverted channels [*Osterloo et al.*, 2008, 2010] and as precipitates in what may have been ancient crater lakes [*Cabrol and Grin*, 2010; *Osterloo and Hynek*, 2015].

After chlorides precipitate on the martian surface, they are altered by a suite of surface processes. Aeolian abrasion by dust, along with meteorite and micrometeorite impacts, can pulverize textures produced by the original precipitation event [*Osterloo et al.*, 2008, 2010; *Osterloo and Hynek*, 2015]. Aeolian and meteoritic processes can also destroy a chloride deposit altogether, causing the chloride to be incorporated as a component of the ubiquitous martian dust; this chloride component has been indicated by lander analyses of martian dust at Chryse Planitia by Viking and rover analyses at Meridiani Planum and Gusev Crater [*Clark et al.*, 1976; *Morris et al.*, 2006; *Berger et al.*, 2015; *Nield et al.*, 2016; *Ming and Morris*, 2017]. However, we know that the physical alteration of chlorides has not been complete, because polygonal cracks – diagnostic of the original desiccation/precipitation event – can still be resolved in orbital images [*El-Maarry et al.*, 2013, 2016]. The small-scale (cm or less) alteration of chloride deposits has not been explored; therefore, the full extent of the physical alteration of chloride deposits has not been constrained.

The chemical alteration of chlorides is a critical area of study for both Mars science and for human exploration efforts. Chemical alteration can convert chloride, which has a -1 oxidation state, to much higher oxidation states: +1 as hypochlorite, ClO^-; +3 as chlorite, ClO_2^-; +5 as chlorate, ClO_3^-; and the highest oxidation state, +7 as perchlorate, ClO_4^-. Perchlorate has a particular impact on human exploration, because it can be hazardous to humans [*Carrier and Kounaves*, 2015]. Atmospheric photo-oxidation

and/or interactions between chloride and oxidative species such as ozone (O_3) and peroxide (i.e., H_2O_2) are known to produce highly oxidized chlorine (or "oxychlorine") [*Dasgupta et al.*, 2005; *Catling et al.*, 2010; *Rao et al.*, 2010]. Some experimental studies have shown an enhancement of the production of oxychlorine species by photo-oxidation of halite (NaCl) in the presence of silica, which is thought to act as a catalyst in the oxidation process [*Carrier and Kounaves*, 2015].

Oxychlorine compounds are highly soluble, which is thought to be why they are only concentrated in dry, high-altitude environments on Earth [*Catling et al.*, 2010]. Oxychlorine compounds on Mars have been proposed to form by the same mechanisms as terrestrial oxychlorine species [*Catling et al.*, 2010; *Davila et al.*, 2013]. These mechanisms for the formation of oxychlorine compounds have been supported by *in-situ* measurements on Mars, that indicate the presence of chlorate and perchlorate on the martian surface. The Phoenix lander and measurements by the Sample Analysis on Mars (SAM) instrument on the Mars Science Laboratory (MSL) in Gale Crater both indicate perchlorate/chlorate salt concentrations up to ~1 wt % [*Hecht et al.*, 2009; *Leshin et al.*, 2013; *Ming et al.*, 2014].

The competing effect of the reduction of oxychlorine compounds to chlorite/chloride species is not well understood. In laboratory experiments, specific wavelengths of gamma radiation have been shown to reduce both chlorine species and O_2 in a carbon dioxide-rich environment. The radiolysis of oxychlorine compounds could account for the ambiguous chemical reaction observed by the Viking biological experiment after the addition of amino acids to martian soil [*Quinn et al.*, 2013] and for the persistence of reduced chloride deposits on Mars in spite of its highly oxidative

environment. This reduction reaction, if occurring, is would most likely be negated by Mars' highly oxidizing surface environment. However, the conversion of chloride to oxychlorine species must occur slowly, since large chloride deposits still exist on the martian surface today and oxychlorine species are only observed on a small (lander, rover) scale.

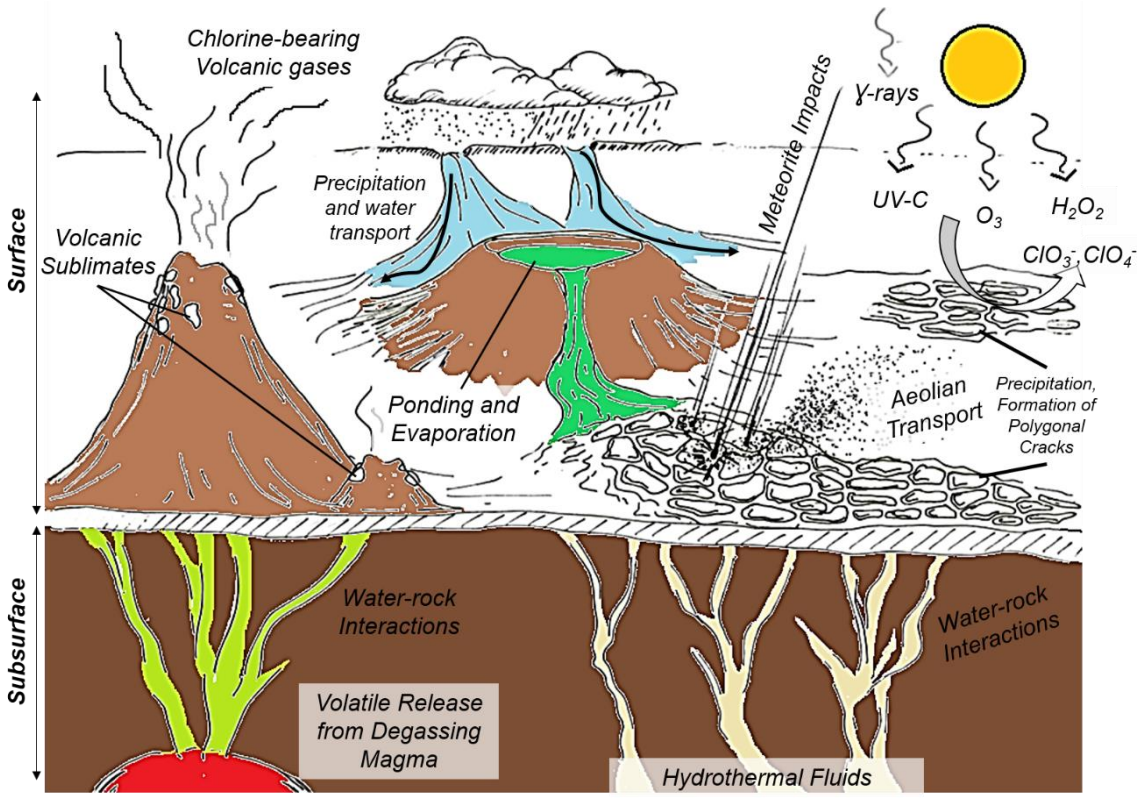

Figure 1.1. Schematic of the martian chlorine cycle: sources of chlorine/chloride, mechanisms of transport, and physical/chemical alteration processes.

Finally, perchlorate and chlorate species are known to significantly reduce the freezing point of water, and have been hypothesized as a mechanism by which brines could be metastable on present-day Mars [*Chevrier et al.*, 2009; *Chevrier and Rivera-Valentin*, 2012; *Hanley et al.*, 2012]. Recurring Slope Lineae (RSL) are possible metastable brine features and are observed as dark streaks that propagate downslope during warm periods across mid-to-equatorial latitudes on Mars. Hyperspectral observations of several RSL by the Compact Reconnaissance Imaging Spectrometer for Mars (CRISM) indicate the possible production of hydrated perchlorate species contemporaneous with RSL activity [*Ojha et al.*, 2015]. It is therefore possible that oxychlorine species continue to play a role in the present-day water cycle on Mars; however, hydrated perchlorates were only indicated at a small subset of RSL, leaving open the question of a global RSL formation mechanism.

Chapters 3-5 of this work attempt to shed light on the life cycle of martian chloride by systematically exploring the origins, evolution, and present-day activity of chloride on Mars. Chapter 3 uses terrestrial chloride-rich brines as analogs for ancient brines on Mars to determine the source of the brines that formed chloride mineral deposits (hydrothermal, deep basinal, or neutral/water-rock reaction). A new understanding of the precipitation sequences of major ions from chloride-rich brines now allows a systematic, targeted, *in-situ* study of martian chloride minerals. Chapter 4 explores the unique textures produced by the evaporation of chloride-rich brines and demonstrates how these textures can be discerned remotely using mid- and far-infrared emission spectroscopy. Additionally, the mid- and far-infrared emission spectra of several common chloride species are shown in Chapter 4, and will allow the composition

of martian chloride deposits to be constrained using future orbital instruments. Finally, Chapter 5 investigates whether Recurring Slope Lineae are caused by the flow of metastable chloride-rich brines, that are capable of depressing the freezing point of water to almost the same extent as perchlorate salts.

CHAPTER 2

AN INVESTIGATION OF THE LIKELIHOOD OF WATER ICE AT THE LUNAR NORTH POLE USING RADAR AND VISIBLE IMAGES

The following is reproduced from Planetary and Space Science, *where it was published in July 2017. Co-authors are S. J. Lawrence, M. S. Robinson, E. J. Speyerer, and B. W. Denevi.*

2.1 Introduction

Accurate knowledge of the distribution and concentrations of volatile species on the Moon has significance for both lunar science and human exploration. The distribution and abundance of water ice, in particular, is a record from which the history of volatiles in the Solar System can be better understood. Volatiles can be indigenous to the Moon itself [*Bogard and Hirsch*, 1975; *Arnold*, 1979] or sourced from asteroids or comets that passed through the inner solar system [*Wetherill*, 1976; *Arnold*, 1979; *Svetsov and Shuvalov*, 2015; *Barnes et al.*, 2016]. The presence of volatiles – or the lack thereof – may be indicative of lunar thermal and surface processes and their evolution over time. Lunar volatiles may refine our understanding of asteroids in the inner Solar System, the evolution and composition of comets, the geologic evolution of the Moon, the processes affecting transport and retention of volatiles at the lunar poles (i.e. meteorite bombardment), and the ancient solar wind environment [*Committee on the Scientific Context for Exploration of the Moon*, 2007].

The quantity and accessibility of volatiles such as water ice have important implications for human exploration. Water represents the single greatest potential source of mass savings for human missions beyond low-Earth orbit [*Spudis and Lavoie*, 2011]. A large *in-situ* reservoir of water ice could serve as a key resource in the establishment of a sustained settlement on the Moon and provide fuel for future missions. Water derived from the Moon would also offset the demand for efficiency on water recycling technologies [*Crawford et al.*, 2012]. It is therefore of critical importance that the locations and quantities of lunar polar water ice deposits be defined as accurately as possible to determine its grade and tonnage [*Anand et al.*, 2012; *Crawford et al.*, 2012; *Lemelin et al.*, 2014].

2.1.2 Permanently shadowed regions

Solar System bodies with low obliquities have regions (primarily craters) that are continually in shadow [*Watson et al.*, 1961a; *Margot et al.*, 1999]. Areas that never receive sunlight are called permanently shadowed regions (PSRs); PSRs have been mapped on both the Moon and Mercury [*Watson et al.*, 1961a; *Arnold*, 1979; *Ingersoll et al.*, 1992; *Bussey et al.*, 1999, 2010; *Vasavada et al.*, 1999; *Mazarico et al.*, 2011; *Neumann et al.*, 2013; *Speyerer and Robinson*, 2013; *Chabot et al.*, 2014]. The lack of direct sunlight prevents direct radiative heating of the surface; as a result, PSRs achieve some of the coldest temperatures in the Solar System. Water ice exposed to the vacuum of space sublimates at temperatures above ~104 K, and many lunar PSRs remain colder than 104 K throughout the lunar year [*Zhang and Paige*, 2009; *Paige et al.*, 2010a]. As a result, PSRs serve as “cold traps” where water molecules lack the thermal energy needed

to escape. Water ice could accumulate in these cold traps over time, forming potentially large deposits [*Watson et al.*, 1961b; *Bussey*, 2003]. PSRs therefore are likely reservoirs for ice sequestration.

2.1.3 Previous Results

The Lunar Reconnaissance Orbiter (LRO) is revolutionizing our understanding of the properties of the lunar polar regions [*Vondrak et al.*, 2010]. The Lunar Reconnaissance Orbiter Camera (LROC) Wide Angle Camera (WAC) has repeatedly imaged the polar regions with pixel scales of 100 m, accurately defining the location and extent of regions of permanent shadow at high resolution (Figure 2.1) [*Robinson et al.*, 2010; *Speyerer and Robinson*, 2013]. Additionally, the LROC Narrow Angle Camera (NAC) provides meter-scale images of illuminated terrain around the PSRs and has acquired long-exposure images of PSRs, where diffuse sunlight reflected off of nearby Sun-facing topographic facets illuminates surfaces that are too dark to view using nominal imaging techniques and exposure times [*Speyerer and Robinson*, 2013]. No albedo variations indicative of ice deposits have been observed in LROC images of PSRs to date [*Koeber et al.*, 2014]. Other LRO instruments have been used to determine other polar environmental properties, including illumination conditions [*Mazarico et al.*, 2011; *Gläser et al.*, 2014], albedo [*Lucey et al.*, 2014], and average annual bolometric brightness [*Paige et al.*, 2010a].

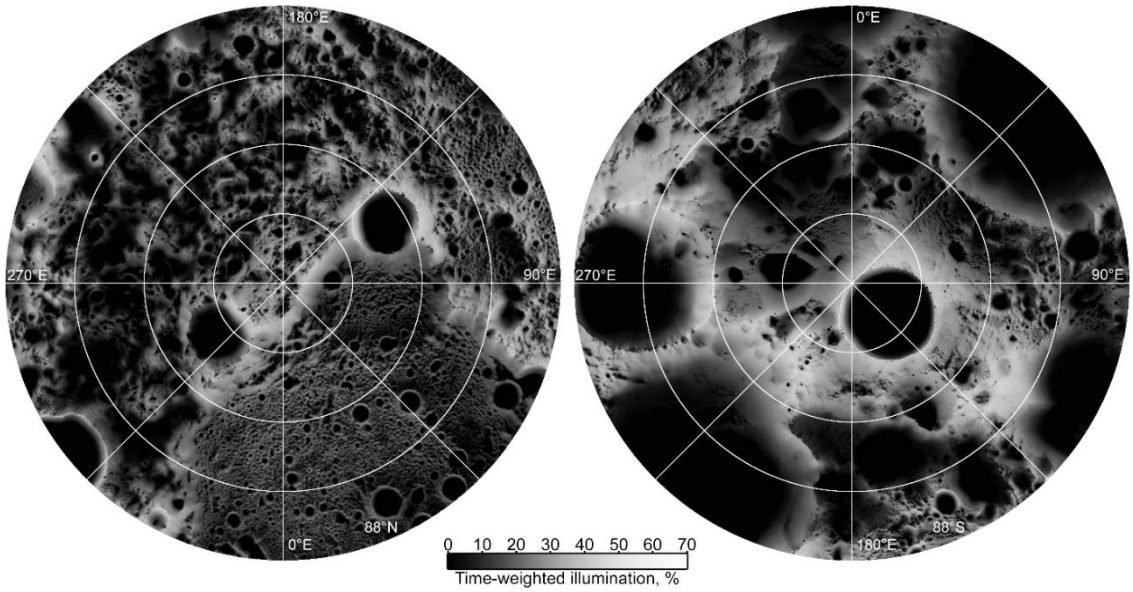

Figure 2.1. LROC Wide Angle Camera (WAC) illumination maps of the lunar North Pole (left) and South Pole (right). Both mosaics 88° - 90° latitude [*Speyerer and Robinson*, 2013].[1]

Indications of hydrogen and water ice in PSRs are reported from analyses of neutron, ultraviolet (UV), and near-infrared measurements. In 1998, the Lunar Prospector spacecraft measured the absorption of epithermal neutrons, where decreases in measured epithermal neutrons were interpreted to indicate the presence of hydrogen. While the >40-km full-width half maximum (FWHM, at 30-km altitude) of the Lunar Prospector neutron detector was too coarse to pinpoint the locations of the putative volatiles in terms of PSRs smaller than that scale, there was a general decrease in epithermal neutrons at the lunar polar regions, consistent with the presence of water ice [*Feldman et al.*, 1998, 2000,

[1] *Reprinted from Icarus, Vol 222, Speyerer, E. and Robinson, M., Persistently illuminated regions at the lunar poles: Ideal sites for future exploration, 122-136, Copyright (2013), with permission from Elsevier.*

2001]. The Lunar Exploration Neutron Detector (LEND) [*Mitrofanov et al.*, 2010b] on LRO also detected a decrease in epithermal neutrons at certain PSRs, but the locations of some neutron suppressions do not fully align with areas of permanent shadow; these were hypothesized by Siegler et al. (2016) to be a result of ancient (3+ Gy) water ice deposits that are no longer at the poles due to true polar wander [*Siegler et al.*, 2016]. Conversely, LEND detected an increase in epithermal neutrons at some PSRs relative to adjacent unshadowed regions, which could be more recently emplaced water ice deposits [*Sanin et al.*, 2012].

Spectral observations of PSRs have returned mixed results. The LRO Lyman-Alpha Mapping Project (LAMP) [*Gladstone et al.*, 2010] spectrometer measures UV reflectance in PSRs illuminated only by starlight and Lyman-Alpha emission. LAMP detected a decreased reflectance in its entire far-UV range (119-190 nm) within some PSRs, which could be the result of increased porosity relative to non-PSR regions. However, it also detected spectral reddening (increased reflectance at longer far-UV wavelengths, 155-190 nm) within PSRs, which could be due to the presence of 1-2% water ice [*Gladstone et al.*, 2012]. The Chandrayaan-1 mission carried a near-infrared spectrometer called the Moon Mineralogy Mapper (M^3) [*Pieters et al.*, 2009b], which had the ability to search for absorption features indicative of water at wavelengths of 2.8 and 3.0 μm. M^3 observed enhanced absorption features in these bands at high (>65°) latitudes, providing further evidence for the presence of water at/near the lunar poles, though the abundance and source has yet to be determined [*Pieters et al.*, 2009a; *Cheek et al.*, 2011]. The Lunar Orbiter Laser Altimeter (LOLA) measured the backscattered light from five nadir-pointing lasers (1064 nm), characterizing the topography at the poles and mapping

the relative reflectivity of the surface under photometrically uniform conditions (0° phase angle) [*Smith et al.*, 2010; *Mazarico et al.*, 2011]. Simulations using topographic data along with LROC WAC images allowed the distribution of areas in permanent shadow to be quantified. LOLA also measured an increase in reflectivity within some PSRs, which could be due to surface water ice. The reflectivity anomaly could also be the result of reduced space weathering in PSRs; therefore, no definitive conclusion concerning water abundance was reached based on LOLA data alone [*Mazarico et al.*, 2011; *Lucey et al.*, 2014].

The Lunar CRater Observation and Sensing Satellite (LCROSS) launched in 2009 along with LRO on an Atlas V vehicle. LCROSS was designed to analyze PSR material vaporized by the impact of the Centaur stage of its Atlas V launch vehicle. The Centaur impacted a large PSR within Cabeus crater, which had previously been measured to have high neutron suppression interpreted as high hydrogen abundance and some of the coldest temperatures on the Moon [*Noda et al.*, 2008; *McClanahan et al.*, 2009; *Mitrofanov et al.*, 2010a; *Paige et al.*, 2010a]. Both LCROSS and LRO instruments observed the plume and detected volatiles, including OH, H_2, and H_2O [*Colaprete et al.*, 2010].

Radar observations have also provided a means to search for water ice on the Moon by allowing the ratio of opposite-sense to same-sense polarized radar signatures, known as circular polarization ratio (CPR) to be quantified. CPR can be used to distinguish between dry, fine-grained, or smooth regolith (low CPR) and ice-rich or blocky (high CPR) materials [*Raney et al.*, 2011; *Thomson et al.*, 2012a]. Water ice deposits with thickness at or greater than the wavelength result in enhanced radar backscatter due to the Coherent Opposition Backscatter Effect (COBE) [*Gorodnichev et*

al., 1990; *Mishchenko*, 1992; *Peters*, 1992; *Ostro*, 1993; *Nozette et al.*, 1996; *Raney et al.*, 2012]. Blocks at the wavelength scale can also enhance radar backscatter, but their exposure to the surface will affect their size – and therefore radar properties – over time. The constant in-fall of micrometeoroids results in a continual degradation and overturn of material on the lunar surface; this process is one part of the continuum of surface-space interactions frequently referred to as space weathering [*Hapke*, 1973; *Arnold*, 1979; *Pieters et al.*, 2000; *Lucey et al.*, 2006]. Younger craters have had less exposure to this environment, and will therefore retain a higher proportion of blocks and large clasts relative to older craters, making younger craters a more likely location for high CPR radar signatures in both their interiors and exteriors. Craters where high CPR values are only observed in the interior, with no appreciable CPR enhancements associated with the crater exterior, were labeled as "CPR-anomalous" because this signature was not thought to fit with crater degradation paradigm described by Spudis et al. (2013). At the lunar poles, this type of anomalous CPR signature is a possible indicator of water ice. "CPR-normal" craters are those with no measurable variation between the CPR of the crater interior and exterior.

The first radar measurements indicative of possible polar ice deposits were acquired by the Clementine bistatic radar experiment in 1994; Clementine observed enhanced same-sense polarization at the lunar poles, which is indicative of COBE [*Nozette et al.*, 1996]. In 2009, the Miniature Synthetic Aperture Radar (Mini-SAR) instrument onboard the Chandrayaan-1 mission [*Spudis et al.*, 2009] observed anomalous CPR signatures at the poles [*Spudis et al.*, 2010]. The LRO Miniature Radio-Frequency (Mini-RF) was the next generation of radar instrument after Mini-SAR and was designed

to transmit circularly-polarized radar signals at both X-band (4.2 cm, partial coverage) and S-band (12.6 cm, complete coverage) wavelengths [*Nozette et al.*, 2010]. Mini-RF observations used in this analysis are in the form of Stokes parameter values, which quantify the polarization (i.e. CPR) and phase of the backscattered signal [*Raney et al.*, 2011]. The Stokes parameters are also used to derive other useful parameters, discussed in Section 2.0, that complement CPR measurements.

2.1.4 Rationale for this Work

Since ice deposits can cause high CPR returns, CPR-anomalous craters are considered to be possible reservoirs of water ice. Mini-RF measurements to date have shown a correlation between anomalous CPR craters and those with PSRs, in line with observations made by Mini-SAR [*Fa and Cai*, 2013; *Spudis et al.*, 2013].

Any ice deposits emplaced on the Moon have likely been modified by the same space weathering process that reduces the overall grain size in and around lunar craters [*Crider and Vondrak*, 2003; *Zimmerman et al.*, 2011]. The Mini-RF experiment is only sensitive to decimeter-scale (in S-band) pure ice deposits within the top meter of the lunar surface; smaller ice deposits mixed with regolith by space weathering are not detectable using radar [*Hurley et al.*, 2012]. Other deposits that are not detectable by Mini-RF include adsorbed water, hydrated minerals, implanted solar wind hydrogen altered to OH^- or H_2O, or buried patches of formerly clean ice [*Cocks et al.*, 2002; *Crider and Vondrak*, 2002; *Hurley et al.*, 2012].

Individual remote sensing datasets have not provided a definitive answer as to the nature, abundance and distribution of water ice in lunar PSRs. While results from several

investigations using LRO instruments are consistent with ice at the poles, there are discrepancies in these observations that make the interpretations ambiguous (i.e. increased or neutral epithermal neutron detection in some PSRs as observed by LEND) [*Crawford et al.*, 2012; *Sanin et al.*, 2012; *Lucey et al.*, 2014]. However, these datasets can be used to assess the likelihood of water ice versus other candidate scenarios, such as reduced space weathering in PSR regions or porous regions.

The radar anomalous locations of high CPR in some craters could also be explained by the presence of a blocky interior and smooth exterior (at radar scales). There is a statistically significant correlation between surface roughness measured by LOLA, LROC, and S- and X-band CPR [*Jawin et al.*, 2014]. Because S-band CPR has been proven to positively correlate with surface roughness at low latitudes, it can be used to assess block abundance and surface roughness in high-latitude, PSR-bearing craters. In this study, we use new LROC NAC observations to investigate the distribution and abundance of blocks in and around PSR-bearing craters at the north pole to evaluate whether block abundance is responsible for the observed radar properties.

2.2 Data Sources and Methods

2.2.1 LROC Narrow Angle Cameras

The LROC instrument consists of the WAC and two NACs; details on LROC's capability and performance can be found in *Robinson et al.*, 2010, *Humm et al.*, 2016, *Mahanti et al.*, 2016, and *Speyerer et al.*, 2016. The LROC NAC is capable of collecting 0.5 meters per pixel (m/px) images of illuminated terrain from an altitude of 50 km. The NAC is able to image within PSRs illuminated by diffuse sunlight reflected off of nearby

Sun-facing topographic facets. The increased integration time required of the low light levels within PSRs results in significant along-track smear and thus a decrease in spatial resolution (typically 10-20 m pixel scales). From these NAC observations, 20-40 m diameter blocks can be detected (using a minimum of two pixels). Because the exteriors of PSR-bearing craters are relatively well lit, they can be imaged by nominal-exposure NACs and mapped at the typical pixel scales (~1-2 m at the poles) thus revealing blocks down to the meter scale.

Long-exposure NAC images of PSRs were processed using the standard LROC NAC calibration and correction methods [*Humm et al.*, 2016]. The increased exposure times (11.8-24.2 ms versus 0.7-2.0 ms nominal exposure) resulted in down-track to cross-track aspect ratios typically between 20 to 40 [*Koeber et al.*, 2014]. Due to the down-track smear caused by extended exposure, the pixel size of the map-projected image was selected to be intermediate between the down-track and cross-track values; resampling used an averaging scheme, which increased the signal-to-noise ratio of the final product. An example of nominal exposure (optimized for illuminated terrain) versus long-exposure images used for PSR block counts in the crater Main L is shown in Figure 2.2, and a list of image products used in this study is provided in Table S1.

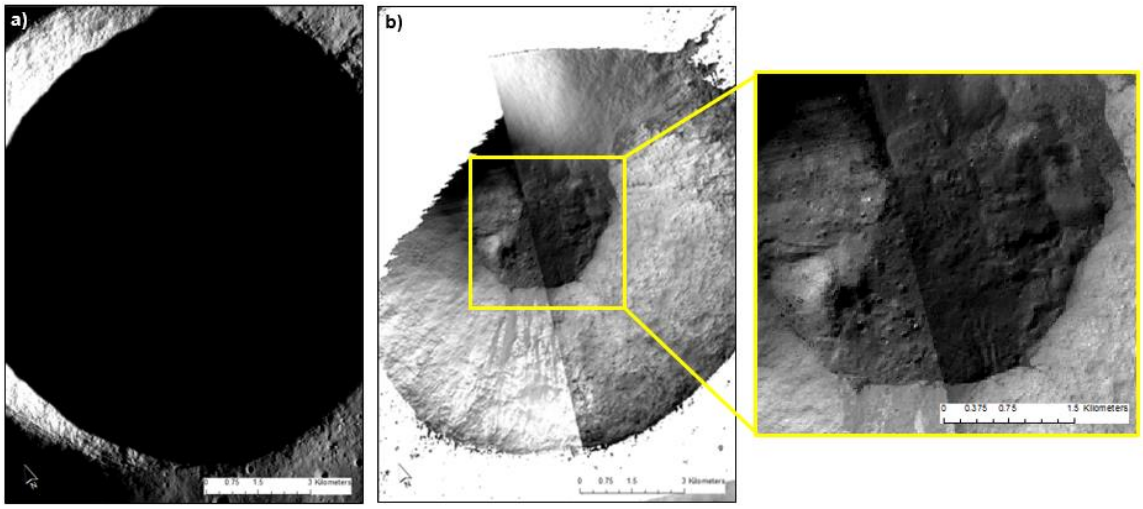

Figure 2.2. Example of NAC imagery used for block counts. a) Nominal-exposure (~1.2 ms) NAC of Main L. b) Long-exposure (~10.0 ms) NAC of Main L PSR, with crater interior in inset. Image center at 81.4°N, 22.7°E. Image IDs are listed in Table S1.

2.2.2 Miniature Radio Frequency Experiment (Mini-RF)

As described in Nozette et al. (2010), the LRO Miniature Radio Frequency Experiment (Mini-RF) uses a hybrid polarimetric architecture to measure the backscatter characteristics of the regolith. Mini-RF transmits a left circular polarized signal, but receives coherently horizontal (H) and vertical (V) linear polarizations. The resulting data are sufficient for deriving the Stokes parameters for the images as well as daughter products such as Circular Polarization Ratio (CPR). Mini-RF can acquire data in one of two radar bands, S (~12 cm) and X (~4 cm) and has two resolution modes: Baseline (150 m) and Zoom (15 m) [*Nozette et al.*, 2010].

2.2.3 M-chi Decomposition Maps

As described above, Mini RF observations have been used to delimit candidate ice-rich regions based on the CPR enhancement [*Thomson et al.*, 2012b; *Spudis et al.*,

2013]. An additional metric to assess the presence of ice is the *m-chi* (m-χ) parameter. This parameter uses the degree of polarization (*m*) and the Poincaré ellipticity parameter (χ) to assess the radar backscatter characteristics: volume (randomly polarized), single-bounce, or double-bounce scattering. Volume scattering measured by Mini-RF S-band is indicative of materials that cause random scattering in multiple directions, such lunar regolith, which can have embedded blocks that eliminate the polarization of the signal. Single bounce scattering includes specular reflection off of a surface or scattering from materials spaced at half-multiples of the wavelength (Bragg scattering). Double-bounce backscatter is caused by multiple reflections due to the presence of blocks or a dihedral geometry (i.e. a crater). The dielectric constant and crystal structure of water is such that wavelength-scale water ice deposits would also produce a double-bounce backscatter signal due to COBE [*Hapke*, 1990; *Peters*, 1992]. The *m-chi* decomposition results in a parameter map which is often colorized based on the type of backscatter, with volume scattering displayed as green, single-bounce scattering displayed as blue, and double-bounce backscatter displayed as red [*Raney et al.*, 2012]. Therefore, both block- and ice-rich regions would be red in *m-chi* decomposition maps; these double-bounce backscatter regions were the focus of this study.

To generate *m-chi* decomposition maps of the regions of interest, Stokes parameter maps for those regions were obtained from the PDS. The level 2 Stokes parameter maps were previously calibrated and georeferenced by the Mini-RF team [*Raney et al.*, 2011]; a list of the Mini-RF products used in this study is shown in Table S1. The degree of polarization, m, was calculated using equation (3) in Raney et al. (2012), where S_1-S_4 represent the individual Stokes parameter values provided in the

Mini-RF products. The quantity $\sin(2\chi)$ was calculated using equation (4) of Raney et al. (2012) where χ is the angle of ellipticity and $\sin(2\chi)$ is the degree of circularity. Finally, the color-coded map was generated using equations (5) of Raney et al. (2012) for red, green, and blue. An example of a complete *m-chi* map for a CPR anomalous crater at the north pole is shown in Figure 2.3. Raney et al. (2012) produced an *m-chi* map of Goldschmidt, in the north polar region, to assess whether it had coherent water ice deposits; its single-bounce scattering signature indicated that adsorbed H_2O/OH or water frost were more likely to be present.

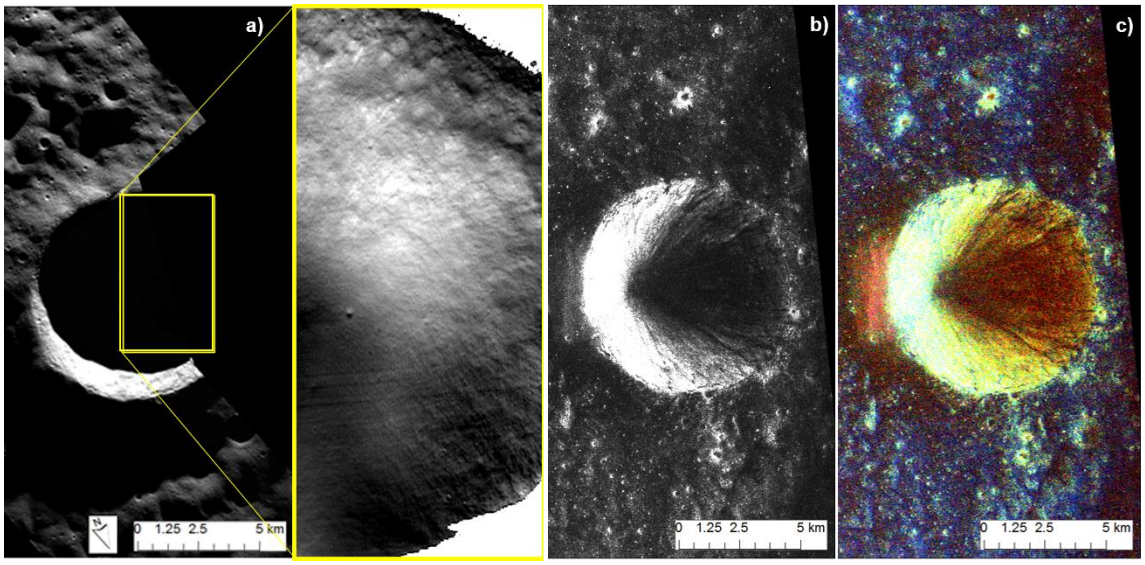

Figure 2.3. *M-chi* deconvolution of CPR-anomalous, potential ice-bearing crater Rozhdestvenskiy N at the lunar North Pole. a) NAC images of Rozhdestvenskiy N, with long-exposure NAC of crater interior in yellow box; b) S1 Stokes parameter map of the same region showing total radar reflected power; c) *m-chi* deconvolution. In c), the large double-bounce region exterior to the crater is due to the crater geometry, where the incident radar wave bounced across the crater and the opposite wall; this produced a time-delay in the signal return that is projected on the external rim of the crater. Image center at 84.0°N, 204.3°E. Image IDs are provided in Table S1.

Blocks imaged by NAC were counted and compared to *m-chi* maps (Figure 2.4) to assess the correlation between blocks and double-bounce backscatter at PSRs. Block size distributions were used to estimate the number of blocks below the resolving limit of long-exposure NACs (10 – 20 m) and at the size needed to affect Mini-RF signatures (decimeter scale or greater) [*Bandfield et al.*, 2011; *Jawin et al.*, 2014]. Blocks outside of PSRs were counted and compared to block distributions in PSRs to predict the population of small blocks in PSRs.

2.2.4 Quantifying the abundance of blocks

CraterTools was used to measure the size-frequency distribution of surface block populations in map-projected NAC images [*Kneissl et al.*, 2011]. Block diameters were determined by selecting three points around their circumference, with the centroid coordinates and diameters recorded for each. Blocks below two pixels in diameter were excluded. Regions with the strongest *m-chi* double-bounce backscatter were used to define the area where blocks were counted. A control region no further than one crater radius exterior to each crater was used for non-PSR, exterior block counts. Many regions exterior to craters contained patches of shadowed areas that were not used for block counts, and as a result many block count areas were irregularly shaped. Misidentification of blocks, lighting conditions, and obscuration of boulders by burial or viewing angle are sources of block count uncertainty; block size uncertainty is defined as one pixel in each direction (± 1 pixel along the block diameter) for a block at or greater than two pixels in size.

2.2.5 Size-frequency distributions

Hartmann (1969) investigated the degree to which block populations can be linked to surface features such as impact craters. The block populations in each region of study were characterized using their size-frequency distributions. The slope of the size-frequency distributions of lunar blocks on a log-log plot, known as B, varies as a function of composition and the energy of a geologic process [*Hartmann*, 1969; *Lawrence et al.*, 2013; *Jawin et al.*, 2014]. The B value for each region was calculated using only the

linear portion of the size-frequency distribution, avoiding regions of roll-off at small block diameters (due to resolution limitations) and large block sizes (limited by to the size/energy of the impact that produced it and/or regolith thickness) [*Cintala and McBride*, 1994].

While the B value itself cannot be used to definitively assess the presence or absence of water ice, it may indicate if ice dominates in CPR-anomalous versus CPR-normal craters over wavelength-scale blocks. Additionally, comparisons between the B values of CPR-anomalous craters at the poles and those at the equator inform the likelihood of water ice being present within polar PSRs; if B values of polar and equatorial CPR-anomalous craters are similar, it is unlikely that CPR anomalies in polar craters are attributable to significant ice deposits.

2.2.6 Targets of interest

Craters within 10° of the north pole with CPR-anomalous radar signatures, fresh north polar craters with CPR-normal radar signatures, and two equatorial CPR-anomalous craters were included in this study (Table 2.1) [*Vasavada et al.*, 1999]. Fresh craters have well-defined, sharp rims, resolvable ejecta, and the presence of blocks. Craters with subdued rims, gradual rim-to-wall transitions, and an absence of blocks are considered degraded [*Wilcox et al.*, 2005; *Stopar et al.*, 2014]. While CPR-anomalous craters are considered candidates for hosting water ice, CPR-normal fresh craters could also contain ice deposits. Fresh craters have an abundance of blocks in their ejecta deposits, and could have water ice and/or blocks in their interiors; this non-distinction is a limitation of the technique used in this study. Block abundance can be correlated with

age, where large blocks are found around younger craters, and small blocks around older craters [*Thompson et al.*, 1974].

The depth-to-diameter ratio (d/D) decreases as a result of decreasing depth over time due to an influx of debris to the crater floor and erosion at the uplifted rim [*Pike*, 1974; *Eke et al.*, 2014]. Additionally, d/D has an impact on the thermal stability of crater interiors. Craters with low d/D (< ~0.2) have shallow wall slopes, where energy reflected from warm, sunlit crater walls onto crater floors is minimal. In this case, the high angle between the crater floor and wall allows the crater interior to remain cooler than craters with higher d/D (> ~0.2) and steeper walls [*Siegler et al.*, 2011]. Most craters in this study have shallow wall slopes and should therefore have cooler interiors than craters with steeper slopes. The specific craters of study include (Table 2.1): Rozhdestvenskiy N, Lovelace E, Lovelace, Whipple (polar CPR-anomalous); Main L and Plaskett U (CPR-normal); and Byrgius C and Gardner (equatorial CPR-anomalous).

Table 2.1. Summary of Craters of Study.

Crater	Center Lat (°N)	Center Long (°E)	Diam. (km)	Depth/Diam Ratio (d/D)	Type	Age
Rozhdestvenskiy N	84.04	203.73	9.0	0.190	CPR Anomalous	Copernican[1]
Lovelace E	82.04	263.22	21.6	0.131	CPR Anomalous	Imbrian[2]
Lovelace	82.08	250.49	57.0	0.065	CPR Anomalous	Imbrian[2]
Whipple	89.14	120.05	14.2	0.201	CPR Anomalous	Imbrian
Main L	81.44	22.73	14.3	0.219	CPR Normal	Copernican[3]
Plaskett U	82.41	162.29	15.5	0.204	CPR Normal	Eratosthenian[2]
Byrgius C	-21.17	295.49	5.0	0.253	CPR Anomalous	Copernican[1]
Gardner	17.73	33.80	18.8	0.160	CPR Anomalous	Imbrian[1,3]

[1]Spudis et al. (2013). [2]Lucchitta et al. (1978). [3]Spudis et al. (2010).

The Copernican crater Rozhdestvenskiy N (9-km-diameter, Figure 2.3) has an anomalous CPR signature and sits inside the larger Rozhdestvenskiy crater, one of the largest craters near the north pole [*Spudis et al.*, 2013]. Lovelace E is a 22-km diameter Imbrian [*Lucchitta*, 1978] crater with a PSR in its interior and an anomalous CPR signature [*Bussey*, 2003]. Lovelace is a 57-km diameter Imbrian crater [*Lucchitta*, 1978], only a portion of which was included in this study. Lovelace has multiple PSRs in its interior and is a high-priority target because its 1064-nm albedo is one of the highest of any PSR at the north pole [*Lucey et al.*, 2014]. Whipple, a 14-km-diameter crater, is the highest-latitude CPR-anomalous crater included in this study (89.1°N, 120.1°E) [*Spudis et al.*, 2013]. Whipple was identified as pre-Nectarian by Lucchitta (1978); however, we propose that it is of Imbrian age based on LROC WAC and NAC images of its well-defined rim and lack of discernable ejecta or rays. While much of Whipple's interior is permanently shadowed, portions of its rim experience near-permanent illumination [*Speyerer and Robinson*, 2013]. The Copernican crater Main L (14-km-diameter) has

high CPR both in its interior and exterior and discernable ejecta [*Spudis et al.*, 2010]. Plaskett U is an Eratosthenian, CPR-normal polar crater with a diameter of 14 km [*Lucchitta*, 1978; *Gladstone et al.*, 2012; *Spudis et al.*, 2013]. Byrgius C (5.0-km diameter) and Gardner (18-km diameter) are Copernican and Imbrian, respectively, equatorial craters that have CPR-anomalous signatures but whose thermal environments cannot support water ice [*Spudis et al.*, 2010, 2013].

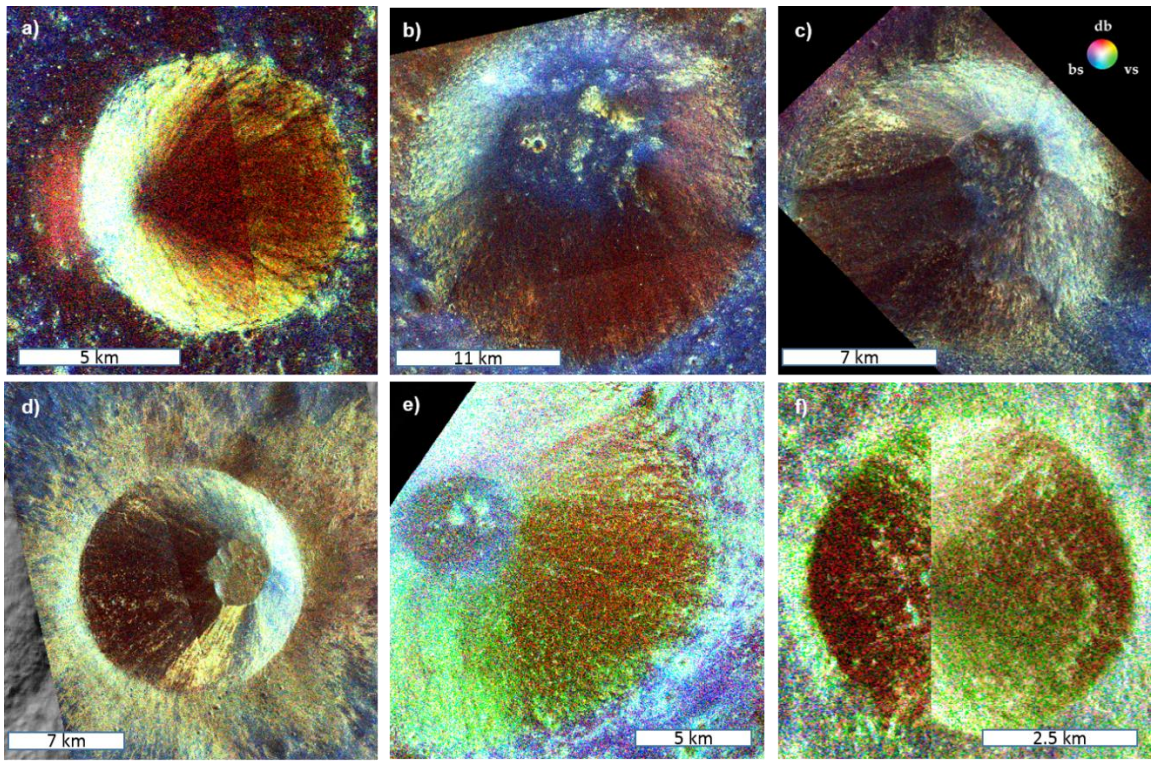

Figure 2.4. Example *m-chi* maps of craters in this study. a) Rozhdestvenskiy N (CPR anomalous,), b) Lovelace E (CPR anomalous), c) Whipple crater (CPR anomalous), d) Main L (CPR normal), e) Plaskett U (CPR normal), and f) Byrgius C (CPR anomalous images from two different look angles). Image IDs are in Table S1.

2.3 Results

2.3.1 Polar CPR-anomalous craters

Consistent with its anomalous CPR signature, Rozhdestvenskiy N (Figure 2.4a) shows a single-bounce scattering signature (blue in *m-chi* decomposition) immediately beyond the crater rim, and double-bounce/volume-scattering (red and green, respectively; yellow in combination) within the crater. The red region exterior to the crater (left of the crater rim in Figure 2.4a) is an artifact of the crater geometry and is not indicative of blocks or ice. Lovelace E (Figure 2.4b) shows single-bounce scattering exterior to the crater, double-bounce backscatter on crater walls, and single-bounce scattering with patches of double-bounce backscatter in its interior. The large PSR within Lovelace shows single-bounce scattering, with single and double-bounce scattering isolated to craters internal to the PSR. Whipple (Figure 2.4c) shows a mixture of all three types of scattering throughout its interior and exterior, and no ejecta blanket or distinct morphologies (rampart, bench, etc.) are detectable in NAC images.

Long-exposure NACs used for identifying blocks in PSRs are shown in Figure 2.3a (inset, Rozhdestvenskiy N) and Figure 2.5 (Lovelace E, Lovelace, and Whipple). A summary of block counts is shown in Table 2.2 and a graph comparing block densities at areas interior and exterior to each PSR is shown in Figure 2.6. Rozhdestvenskiy N has no detectable blocks interior or exterior to the crater, while Lovelace E and Lovelace have detectable blocks in their exteriors only. These craters lack an interior (PSR) block population that is within the detection limits of LROC long-exposure NACs (blocks >20-40 m diameter), though double-bounce backscatter on crater walls indicates the presence

of a block population at Lovelace E. Whipple was the only polar CPR-anomalous crater with a non-zero block count in its interior (11 blocks total). The number of blocks at Whipple is higher in the crater interior than the exterior for all block sizes (Figure 2.11). No blocks were observed at Rozhdestvenskiy N, in contrast to the measurements of Fa and Cai (2013); this discrepancy is most likely due to differences in the size of count areas between the two studies (~5 km^2 - Fa and Cai; ~20 km^2 - this work).

The characterization of block populations within PSRs is a function of pixel scale. The two craters with the highest block densities – Gardner and Byrgius C – have no blocks that would be detectable in LROC long-exposure NACs in their exteriors, and in the case of Byrgius C, none in the interior. If Byrgius C, the most block-rich crater in this study, were placed at the lunar north pole and imaged using LROC long-exposure NACs, one would not be able to resolve the numerous blocks in and around the crater. Empirical measurements of large blocks (> 20-m diameter), and their resulting B values, are therefore critical to estimating the abundances of smaller blocks outside the detection limits of LROC long-exposure NACs.

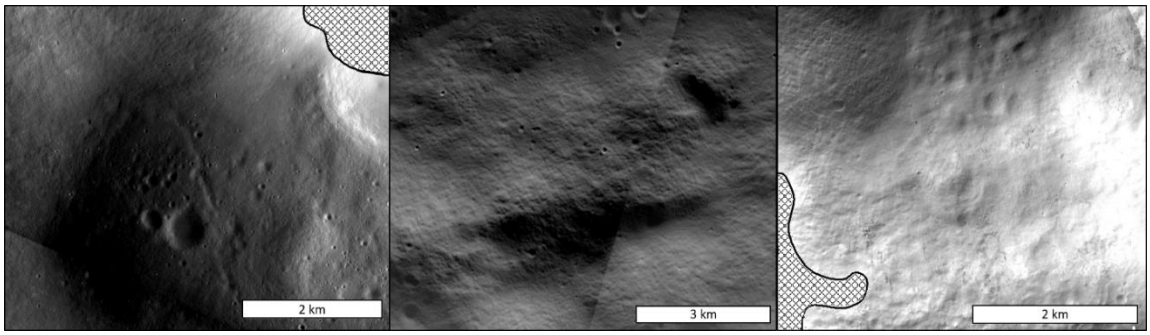

Figure 2.5. Long-exposure NAC images of PSRs in Lovelace E (left), Lovelace (center), and Whipple (right). Edges of permanently shadowed regions are outlined in black and non-PSR exteriors are crosshatched.

Table 2.2. Block detection limits, total block counts, block densities, and B values for study craters. The diameters of the smallest resolvable block for each crater are based on a line pair of pixels from the highest-resolution product used for each block count (LROC NACs, Lunar Orbiter for Surveyor sites); pixel scales are reported for each image product in Table S1. Grey boxes indicate that no B value could be determined due to a lack of detectable blocks.

	Diameter of Smallest Resolvable Block (m)		**Total Visible Blocks**		**Blocks Densities (blocks per km^2)**		**B Values**	
Crater	**Interior**	**Exterior**	**Interior**	**Exterior**	**Interior**	**Exterior**	**Interior**	**Exterior**
Rozhdestvenskiy N	18.61	4.57	0	0	0	0		
Lovelace E	17.68	5.75	0	47	0	0.59		-4.88
Lovelace	38.11	5.72	0	41	0	0.84		-4.64
Whipple	20.67	7.35	11	5	0.16	0.1	-2.42	-0.93
Main L	17.75	4.51	12	633	0.91	11.3	-3.43	-3.14
Plaskett U	38.03	7.41	0	0	0	0		
Byrgius C	1.64	1.64	8127	132	399.27	36.24	-6.45	-5.44
Gardner	2.04	2.04	141	141	68.49	26.93	-2.56	-3.17
Surveyor I*	2.50*	2.50*	--	--	--	--	-3.29*	-3.93*
Surveyor III*	2.40*	2.40*	--	--	--	--	-4.93*	-6.16*
Surveyor VI*	2.31*	2.31*	--	--	--	--	-4.23*	-3.52*
Surveyor VII*	--	10.91*	--	--	--	--	--	-4.03*

**Values from Cintala and McBride (1994).*

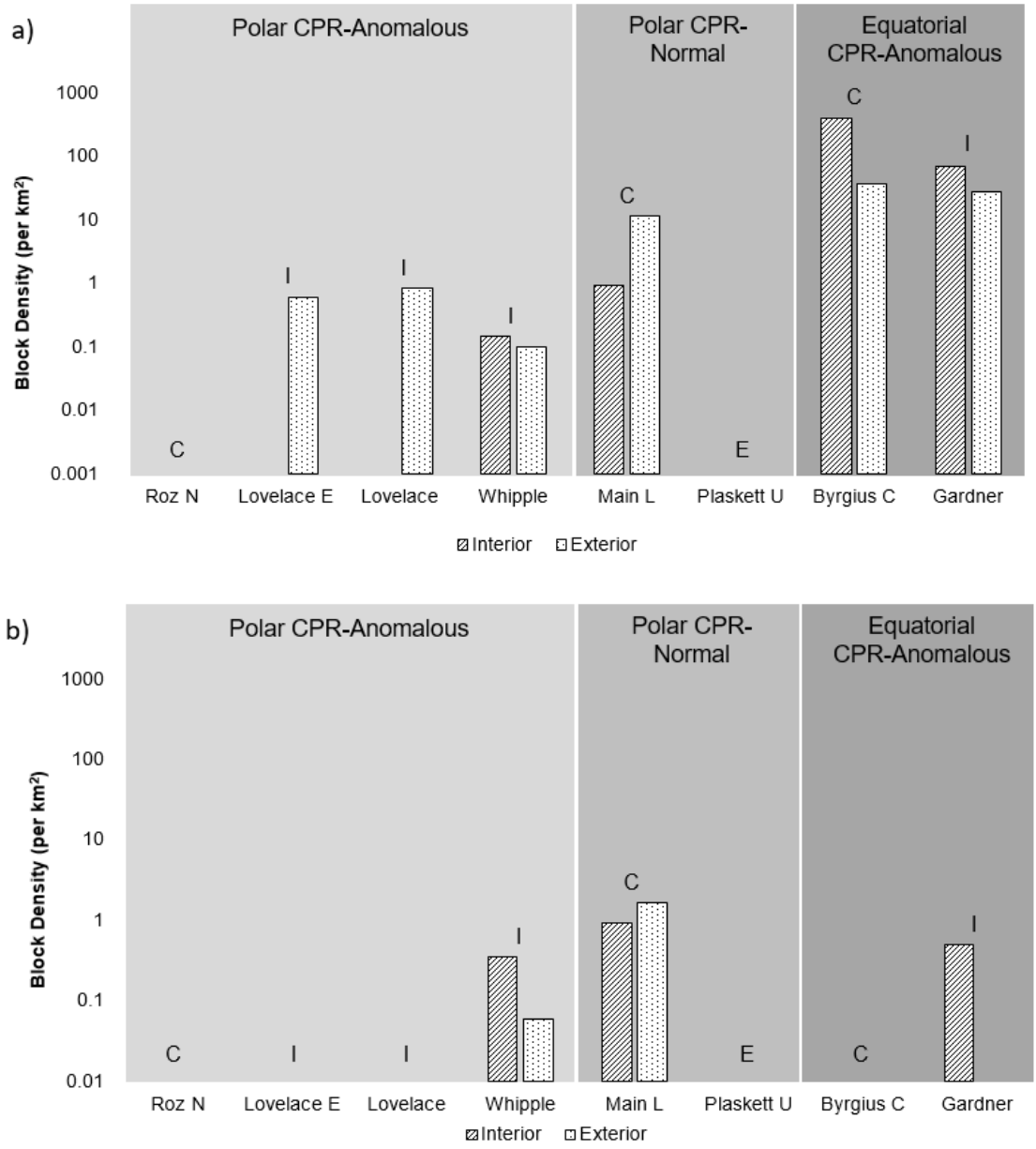

Figure 2.6. a) Block density in number of total blocks of all sizes (2+ m, including nominal and long-exposure NACs) per square kilometer for crater interiors (hashmarked bars) and exteriors (speckled bars). b) Density of blocks greater than 20 m diameter (long-exposure NACs only) to illustrate the effects of image resolution limitations; all other labels same as a). Crater ages are denoted by letters over each block count, where I = Imbrian, E = Eratosthenian, and C = Copernican. Craters with no bars indicate a detectable block density of zero.

A summary of B values for each PSR is shown in Table 2.2. Whipple was the only polar CPR-anomalous crater for which blocks were identified in the PSR and an interior B value was determined (B = -2.42). B values for the exteriors of polar CPR-anomalous craters Lovelace E, Lovelace, and Whipple were -4.88, -4.64, and -0.93 respectively. Relative and cumulative block size-frequency distributions for all craters are shown in Figure 2.7 (exteriors, relative), Figure 2.8 (interiors, relative), Figure 2.9 (exterior, cumulative), and Figure 2.10 (interior, cumulative). The B value for each crater was determined using the curves in Figures 2.9 and 2.10. Interior and exterior block counts were also compared to assess whether block size frequency distributions are consistent between interiors and exteriors of the same crater (Figure 2.11). The exterior block abundances for Lovelace E, Lovelace, and Whipple were used to extrapolate the abundances of blocks below the resolving limit of LROC long-exposure NACs using a power law relationship [*Hartmann*, 1969; *Cintala and McBride*, 1994; *Bandfield et al.*, 2011]. These extrapolated abundances are compared to measured interior block abundances for Byrgius C and Gardner in Figure 2.12.

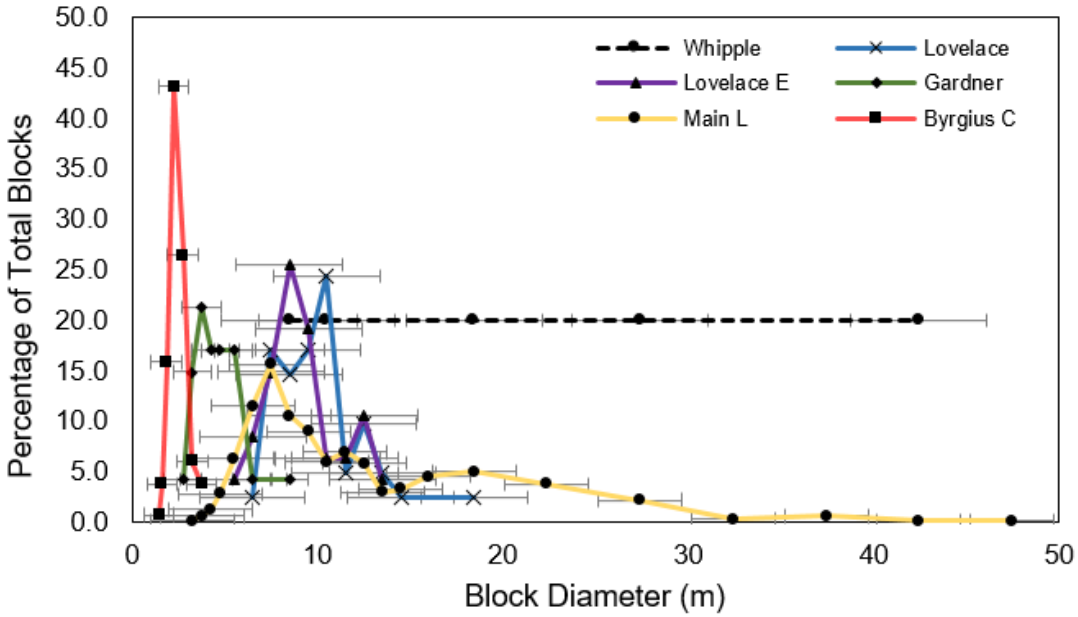

Figure 2.7. Crater exterior block size distributions. Block quantities as a percent of total are plotted versus block diameter for each crater with resolvable blocks. Block diameter uncertainty is one pixel in each direction.

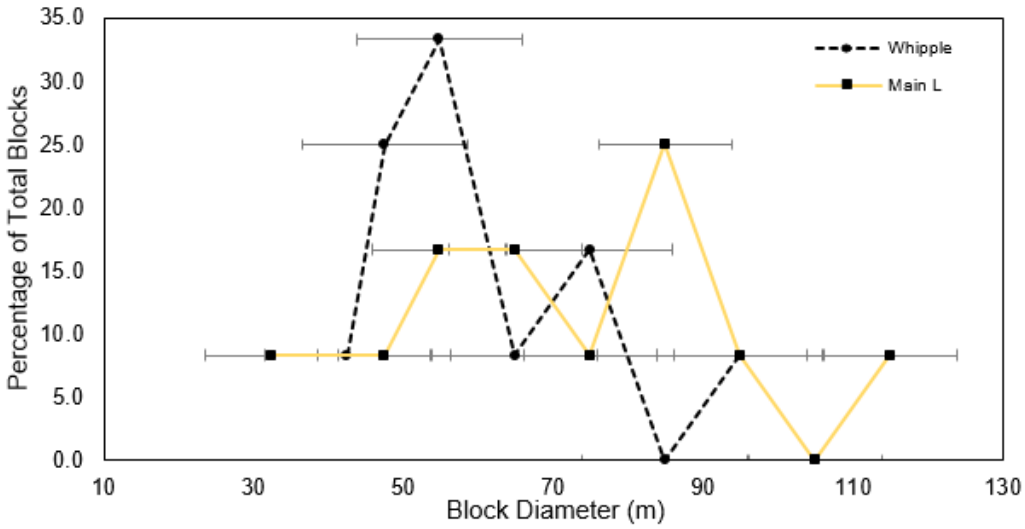

a)

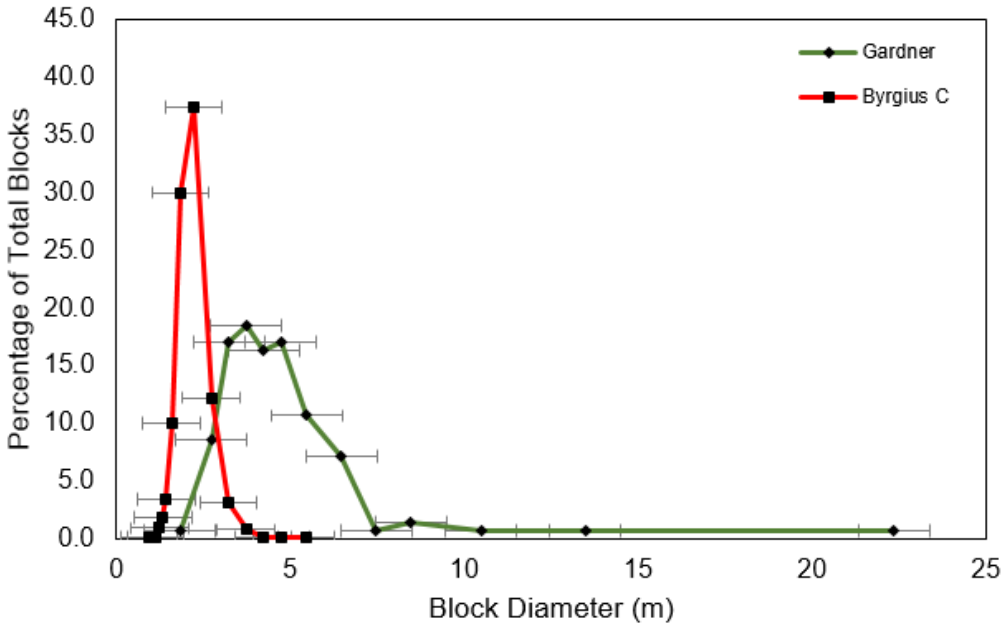

b)

Figure 2.8. Crater interior block size distributions. Block quantities as a percent of total are plotted versus block diameter for each crater where blocks were resolvable. a) Polar craters where blocks were resolvable in their interiors. Because these data were drawn from long-exposure imagery, image resolution is lower than for other block counts. Pixel scales were ~10 m/px at Main L and ~20 m/px at Whipple. b) Equatorial craters. Uncertainties are defined as in Figure 2.7.

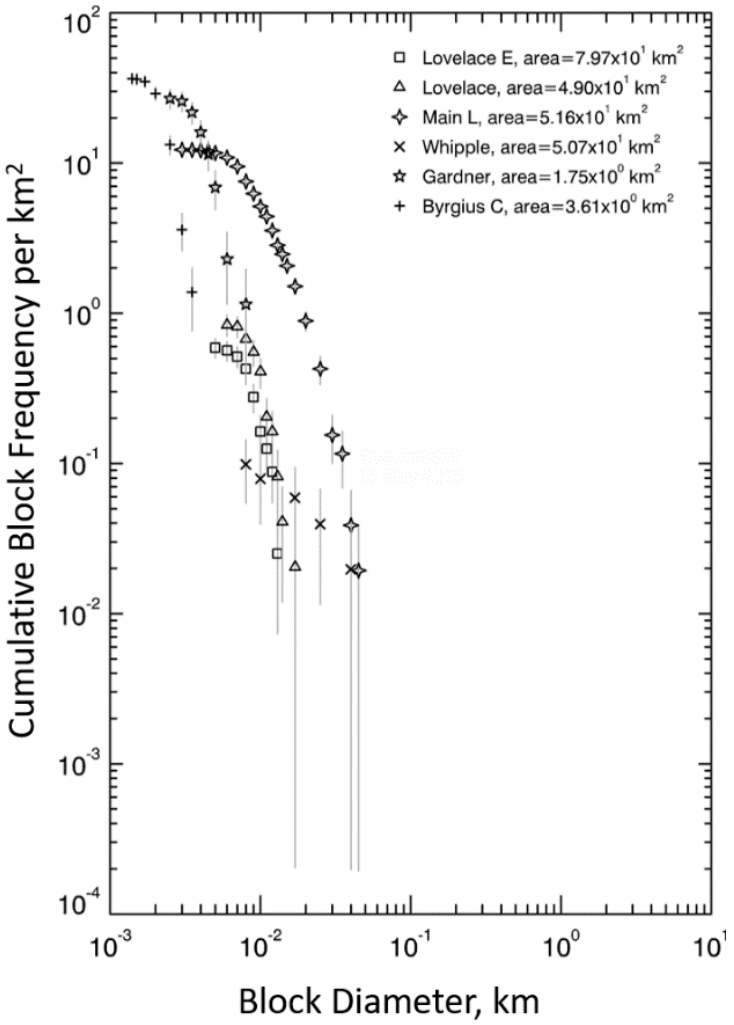

Figure 2.9. Block cumulative size-frequency distributions for crater exteriors where blocks were resolvable. B values for each crater were as follows: Lovelace E: -4.88, Lovelace: -4.64, Main L: -3.14, Whipple: -1.0, Gardner: -3.17, Byrgius C: -5.44. Values listed next to each crater in the legend are the areas used for block count measurements. Standard pseudo-log binning and errors from CraterStats [*Michael*, 2013].

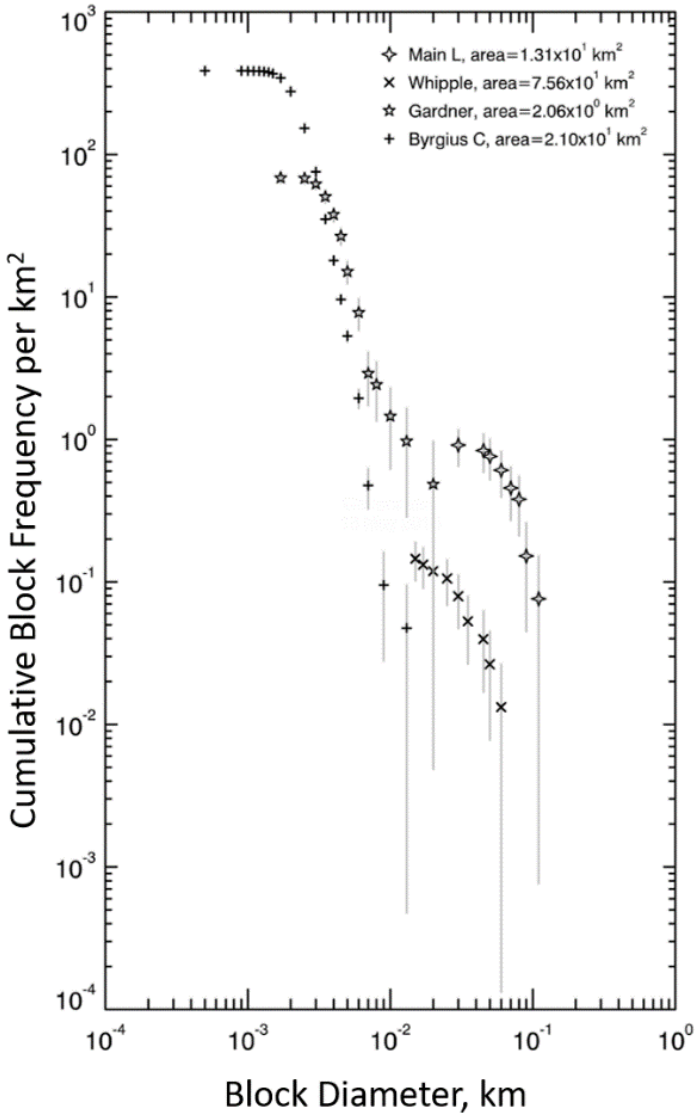

Figure 2.10. Block cumulative size-frequency distributions for crater interiors where blocks were resolvable. B values for each crater were as follows: Main L: -3.43, Whipple: -2.42, Gardner: -2.56, Byrgius C: -6.45. Values listed next to each crater in the legend are the areas used for block count measurements. Standard pseudo-log binning and errors from CraterStats [*Michael*, 2013].

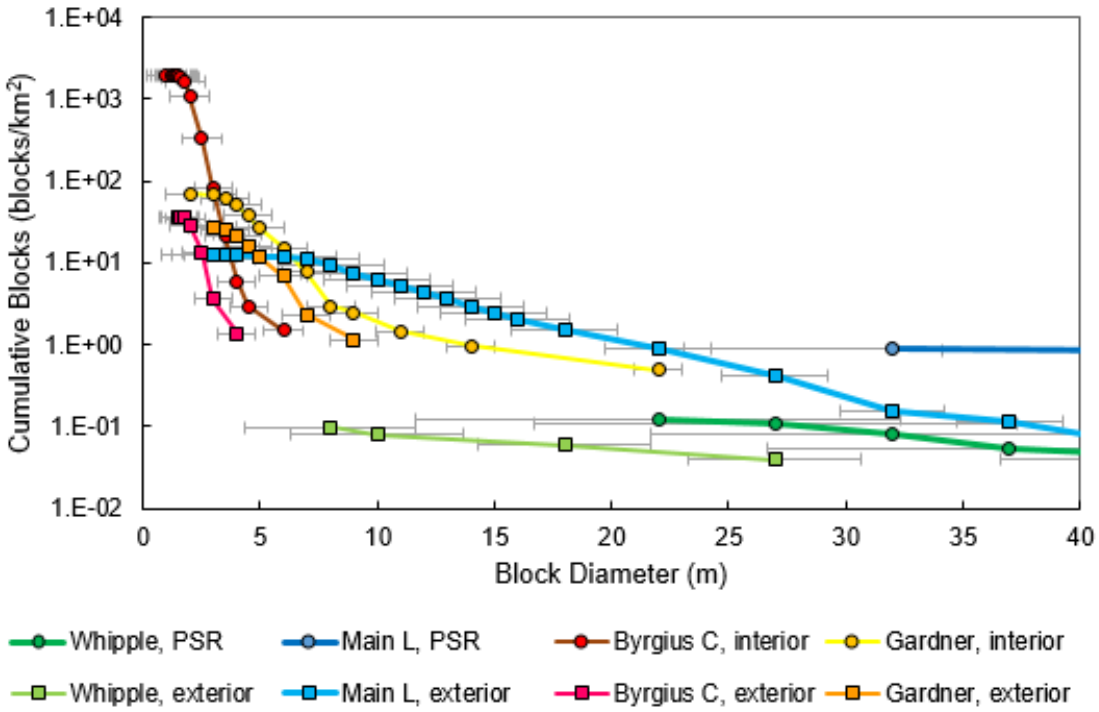

Figure 2.11. Measured cumulative block size-frequency distributions for CPR-anomalous polar (Whipple) and equatorial craters (Byrgius C and Gardner) and a CPR-normal polar crater (Main L). Circles show block distributions for crater interiors/PSRs and squares show block distributions for crater exteriors. Error bars are ± one pixel.

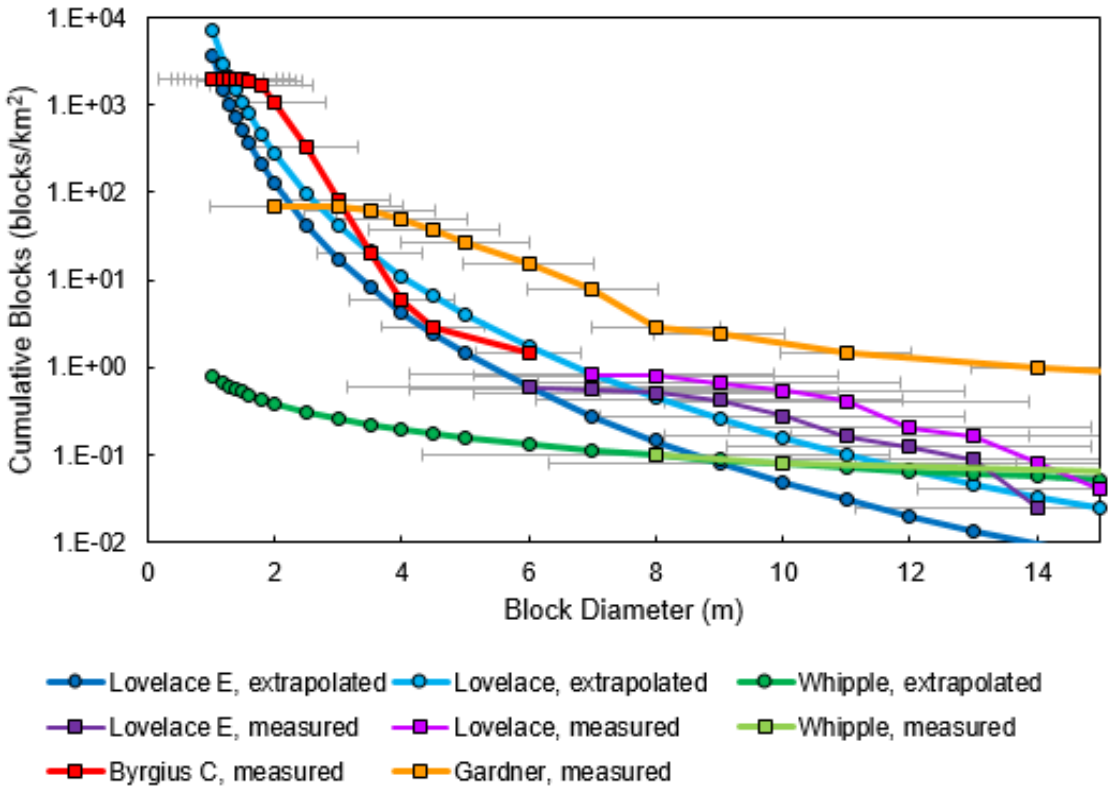

Figure 2.12. Comparison of measured interior blocks at CPR-anomalous equatorial craters (Byrgius C and Gardner) with extrapolated exterior block distributions at CPR-anomalous polar craters (Lovelace E, Lovelace, and Whipple). PSR block counts were estimated by extrapolating a power law fit of the exterior visible block population down to block sizes below the resolving limit of long-exposure NACs ("extrapolated"). Exterior ("measured") block distributions are directly from empirical block counts. Error bars are ± one pixel for measured values.

2.3.2 Polar CPR-normal craters

Main L (Figure 2.4d) shows a combination of double-bounce and volume-scattering in both its interior and exterior. Complementary to the *m-chi* decomposition, LROC NAC observations show a distinct ejecta blanket and visible blocks both interior and exterior to the crater. Plaskett U shows dominant single-bounce scattering at the crater floor and exterior (Figure 2.4e), double-bounce backscatter on the crater walls, and a lack of visible blocks in LROC images. Patches of bright material around the crater could be indicative of an ejecta blanket that has since been eroded. Main L had <1 20-m or greater blocks per km^2 in its interior, and Plaskett U had no detectable blocks. The B value for Main L's interior is -3.43 and its exterior B value is -3.14. The average number of blocks at all sizes is higher in the interior than the exterior of Main L (Figure 2.11).

2.3.3 CPR-anomalous equatorial craters

Byrgius C has a combination of double-bounce and volume scattering in its interior, and a patchy single-bounce scattering signature exterior to the crater (Figure 2.4f). LROC NAC images show a discontinuous ejecta blanket and distinct debris flows on the crater walls. The density of blocks (Figure 2.13) on the walls and floor of Byrgius C is consistent with the double-bounce backscatter observed in Mini-RF *m-chi* maps. Byrgius C has a high block density relative to other craters in this study: 399 blocks greater than 2-m diameter per km^2; this block density was less than the 978 blocks per km^2 measured by Fa and Cai (2013), likely a result of the count area used in this study, which was four times larger than that used by Fa and Cai (2013). The exterior block density was an order of magnitude lower than the interior block density: ~36 blocks per

km^2. Byrgius C has an exterior B value of -5.44; while high relative to other B values derived in this study, this value is similar to the interior B value of -6.45.

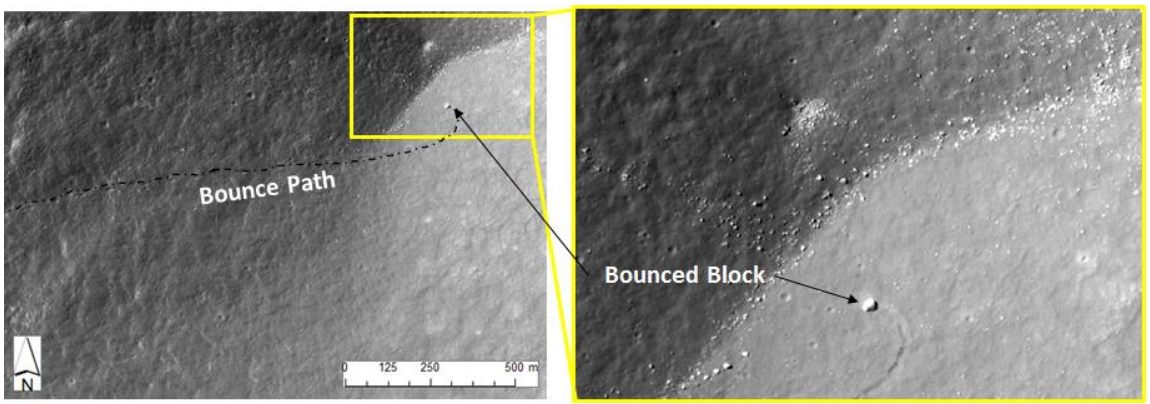

Figure 2.13. Interior of Byrgius C, including a block with evidence of bouncing down-slope (center-left to upper right); image center at -21.2°N, 295.5°E. Inset: central peak of Byrgius C with numerous blocks. Image IDs are shown in Table S1.

At Gardner, debris flows are ubiquitous on the crater walls, as previously described by Spudis et al. (2013) and seen in Figure 14; debris flows were not observed in PSR-bearing, CPR-anomalous polar craters. Double-bounce and volume scattering in *m-chi* decompositions are commensurate with these regions of high erosion, though a sharp boundary is present in the interior of the crater where these debris flows reach the crater floor. The transition to single-bounce scattering is abrupt both at the floor of the crater and at its rim. Gardner's block density (69 blocks per km^2) was lower than Byrgius C and lower than Main L for blocks greater than 10 m diameter (1.42 blocks per km^2). The exterior B value for Gardner was -3.17 and its interior B value was -2.56.

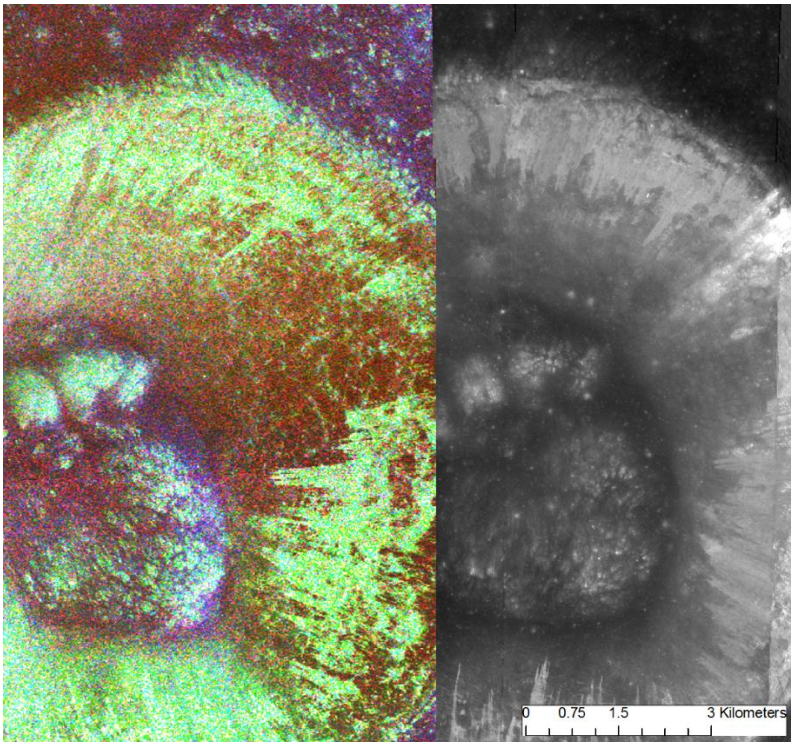

Figure 14. *M-chi* map (left) and LROC NAC (right) of the interior of Gardner crater. Bright, block-rich regions show double-bounce backscatter signals (orange-red in *m-chi* decomposition). Image IDs are shown in Table S1 and image center is located at 17.7°N, 33.8°E.

The cumulative block size-frequency distributions in Figure 2.11 and Figure 2.12 illustrate two important relations between interior and exterior block populations. First, all craters have a higher average number of blocks of a given size in their interiors than their exteriors. Error estimates (± one pixel) indicate little to no variation in block abundance between crater exteriors and interiors for blocks greater than 5 m diameter. However, for blocks below 5 m, the block abundances diverge. This variation is most likely due to the fact that crater interiors accumulate blocks as crater walls degrade, whereas crater exteriors do not. Crater walls therefore preferentially produce blocks at or less than 5 m, resulting in an enhancement of blocks of this size at the crater floor. Since the majority of detectable blocks are less than 5 m diameter (Figures 2.7 and 2.8b),

exterior block size-frequency distributions cannot be used to accurately estimate the number of smaller, unresolvable blocks in crater interiors. Such an extrapolation would underestimate the number of blocks in crater interiors. Second, it is unclear whether the power law relationships derived from large blocks in PSRs provide a correct estimate of smaller blocks that may be present in PSRs. Whipple interior block counts overlap between the interior and exterior; however, the pixel scale for the PSR block counts results in larger error bars when looking at small block sizes. Therefore, due to the uncertainty in those measurements, we cannot make definite conclusions regarding the block abundances in Whipple's interior relative to its exterior. High-resolution visible images of the interiors of a subset of polar craters will be needed to assess whether such an extrapolation would prove accurate for all PSRs.

B values measured at the Surveyor landing sites provide a useful comparison between CPR-anomalous equatorial craters and the CPR-normal craters found to dominate the surface of the Moon. Cintala and McBride (1994) measured block abundances at the sites of Surveyors I, III, VI, and VII from Lunar Orbiter images, which have a pixel scale of ~1-5 m/px. B values ranged from -3.3 to -4.9 for crater interiors, and -3.5 to -6.2 for intercrater regions [*Cintala and McBride*, 1994]. The Surveyor sites were on basaltic terrains (Surveyor I – Flamsteed Crater, Surveyor III – eastern Oceanus Procellarum, and Surveyor VI – northwest Sinus Medii), except for the one highlands site (Surveyor VII – ejecta north of Tycho). All of the Surveyor sites ranged in age from 2.5 – 3.5 Gy, except for Surveyor VII, which was on a highlands ejecta blanket as young as 100 My. The highlands Surveyor VII site had a B value intermediate to the mare basalt sites, indicating that age and composition may not be significant factors when comparing

block size distributions. Equatorial CPR-anomalous craters had B values higher than those of polar craters, but all fell within the range of values reported by Cintala and McBride (1994). Therefore, the B value did not provide a metric for distinguishing between potential ice-bearing craters and those with blocky surfaces.

2.3.4 Circular Polarization Ratio and Lunar Polar Craters

Previously published CPR values for Rozhdestvenskiy N, Main L, and Byrgius C are used as representative of CPR-anomalous polar, CPR-normal polar, and CPR-anomalous equatorial craters, respectively. Using the CPR values obtained by Fa and Cai (2013), the average interior CPR was 0.93 ± 0.50 for Rozhdestvenskiy N, 0.92 ± 0.48 for Main L, and 1.12 ± 0.59. The average exterior CPR values were 0.60 ± 0.33 for Rozhdestvenskiy N, 0.88 ± 0.45 for Main L, and 0.77 ± 0.43 for Byrgius C [*Fa and Cai,* 2013]. The interior CPR values are virtually indistinguishable between Rozhdestvenskiy N and Main L, whereas Rozhdestvenskiy N has a distinctly lower exterior CPR than Main L. Therefore, Rozhdestvenskiy N's anomalous CPR is not due to CPR enhancement within the crater, but an abnormally low CPR exterior to the crater. Byrgius C has a higher interior CPR than either polar crater and an exterior CPR that is intermediate between the two. The presence of large deposits of water ice should result in a CPR enhancement (CPR >1) within a crater. In fact, Byrgius C was the only crater of the three to show a measureable CPR enhancement. Therefore, anomalous CPR is not a necessary characteristic of craters likely to contain water ice.

2.4 Discussion

Radar backscatter and CPR, block densities, and block size-frequency distributions were used to investigate the nature of CPR-anomalous craters at the lunar north pole. Water ice was hypothesized as a possible cause of enhanced *m-chi* double-bounce backscatter at S-band wavelengths in CPR-anomalous polar craters [*Raney et al.*, 2012]. Because the double-bounce backscatter could be the result of blocks instead of ice, the source areas of the radar signatures were investigated using visible images of both crater exteriors (via nominal-exposure NACs) and permanently shadowed interiors (via long-exposure NACs). We systematically assess different causes for the observations described above, including crater freshness and the presence of water ice. Possible causes of the unique observations at Whipple crater are also explored.

2.4.2 Resolution Limitations

For CPR-anomalous craters, a lack of blocks coupled with *m-chi* double-bounce backscatter in their PSRs is consistent with the presence of water ice deposits. An example of such a crater is Rozhdestvenskiy N, where we observed no blocks (>20-m diameter) in its PSR. The interiors of Lovelace E, Lovelace, and Plaskett U also have no detectable blocks ≥20-m diameter. Their PSRs also exhibit single-bounce scattering in *m-chi* maps, which is indicative of specular reflection, with only patches of double-bounce backscatter. While the dominance of single-bounce scattering in Lovelace and Lovelace E PSRs indicate that there are no coherent ice deposits within the top meter, it is possible that water ice could be finely distributed within the regolith possibly due to vapor diffusion [*Salvail and Fanale*, 1994; *Vasavada et al.*, 1999]. In this scenario, the source

of the CPR-anomalous radar signatures could be due to the presence of blocks exposed due to eroding slopes, which are not resolved in LROC long-exposure images (i.e. Figure 2.5 center). Patches of double-bounce backscatter in *m-chi* maps that align with those slopes are consistent with the presence of erosively exposed blocks (unresolved in PSR images), while single-bounce backscatter is indicative of smooth surfaces at the wavelength scale.

Multiple remote sensing techniques were used in this study because no single existing measurement allows conclusive determination of the presence or abundance of water ice at the poles. However, the results of this study indicate that even two instruments cannot definitively confirm the presence of water ice. Several improvements in the next generation of instruments in lunar orbit are therefore required. Higher spatial resolution measurements will be needed to constrain the distribution of water ice deposits, and higher spectral resolution will be needed to fully characterize PSR compositions. High-resolution, high signal-to-noise imaging of PSRs with pixel scales less than 2 m is necessary to allow definitive testing of blockiness versus ice deposits as the cause of the observed CPR anomalies. Direct imaging of PSRs at the same scale and high signal-to-noise may also reveal albedo variations that are not resolvable in the existing PSR images, in addition to characterizing the populations of small (<20 m) blocks.

2.4.3 Implications of Crater Freshness and Age

Fresh craters with block-rich ejecta blankets can be distinguished from older craters lacking blocks in their ejecta using the *m-chi* decomposition [*Raney et al.*, 2012].

However, a fresh crater with ice deposits cannot be definitively distinguished from a fresh crater without ice deposits using the techniques in this study. Main L is the best example of a fresh crater showing *m-chi* signatures that are consistent with its high CPR values, block-rich surface, and Copernican age. Block-rich slopes are indicated in *m-chi* maps at Plaskett U, an Eratosthenian crater [*Lucchitta*, 1978], but its ejecta blanket is less bright than that of Main L as a result of its older age. The two *m-chi* maps of Byrgius C (Copernican-aged) and Gardner (Imbrian-aged) show evidence of erosion, including significant debris flows on crater walls (Figure 2.4). The B-values at Byrgius C are higher than those at Gardner, indicating that higher-energy block-forming processes have occurred in both the interior and exterior of Byrgius C.

CPR-anomalous craters may simply be one stage in the natural crater aging process. The interiors and ejecta blankets of fresh craters have not been subjected to substantial space weathering [*Hapke*, 1973; *Arnold*, 1979]. Therefore, a diagnostic feature of fresh craters is that they have a higher density of blocks relative to older craters [i.e. *Soderblom*, 1970]; these blocks decrease in size as the crater is subjected to space weathering. While the interior of the crater is also subjected to space weathering and erosion, active gradation of the crater walls may replenish the population of interior blocks. Over time, the interior block population may persist relative to the exterior; eventually, the walls of the crater become shallower as the production of interior blocks ceases. In middle-age, the contrasting block distributions would result in a high CPR signature interior to the crater and a low CPR signature exterior to the crater, that is, CPR-anomalous. Older craters have low CPR signatures in both their interiors and exteriors – they are CPR normal. Previous studies investigating PSRs using rectified

Mini-SAR and Mini-RF CPR maps show that high-CPR regions within craters do not show spatial correlation to PSR areas [*Eke et al.*, 2014], consistent with the hypothesis for intermediate-age block distributions in polar CPR-anomalous craters.

2.4.4 The Presence of Water-Ice Deposits

Of the four polar CPR-anomalous craters that were included in this study, we consider Rozhdestvenskiy N to be the best candidate for harboring significant water ice deposits. First, it is CPR-anomalous with a double-bounce backscatter signature in its permanently shadowed interior. Second, it has no detectable blocks in LROC long-exposure images (20-m pixel scale) that would indicate blockiness rather than ice. The other CPR-anomalous craters that were studied show single-bounce scattering in their PSRs, indicating that, if ice is present, it is likely diffused throughout the regolith and therefore unlikely to interact with S-band radar waves. LROC observations show that three of the four polar CPR-anomalous craters - Rozhdestvenskiy N, Lovelace E, and Lovelace - had no detectable blocks in their interiors. While the lack of blocks is consistent with the presence of ice deposits in PSRs, it could also be a result of resolution limitations in long-exposure PSR imaging instead of water ice.

If polar and equatorial CPR-anomalous craters show similar *m-chi* signatures, block densities, and block size-frequency distributions, it could be inferred that their CPR trends are a result of similar processes. If polar to equatorial variations were found, the CPR anomaly could be attributed to a different process. Polar CPR-anomalous craters showed double-bounce backscatter in their interiors, though in some cases (i.e. Lovelace) only in patches. They also had low numbers of exterior blocks, with the exception of

Whipple. Equatorial CPR-anomalous craters were dominated by double-bounce backscatter in *m-chi* maps and had the highest block densities of any of the craters included in this study. However, the majority of their blocks was below 20-m diameter, and would therefore remain unresolved in long-exposure NACs. Therefore, the lack of visible blocks in PSRs may simply be a function of lower image resolution, and not water ice deposits.

Previous studies have described the poor overlap between regions with high CPR and regions of permanent shadow [*Eke et al.*, 2014]. These observations were corroborated upon examination of published CPR values for several craters included in this study. The interior CPR values for polar craters were less than 1, indicating no signal enhancement indicative of a large water-ice deposit due to COBE. Because the CPR value for Byrgius C - an equatorial, block-rich crater – was greater than 1, CPR enhancement can be empirically linked to block abundance for non-polar craters. Using S-band radar, no distinction can be made between fresh craters with ice deposits and fresh craters without ice; therefore, the likelihood of ice deposits in Plaskett U and Main L remains undetermined.

Observations of PSRs on Mercury reveal two classes of albedo anomalies: high and low. The high-albedo areas are consistent with water ice on the surface, and the low-albedo areas are consistent with an organic-rich, thermally insulating layer [*Neumann et al.*, 2013; *Chabot et al.*, 2014]. LROC NAC images of lunar PSRs included in this study (i.e. Figure 2.5) showed no such albedo relations, indicating that lunar PSRs are deficient in surface deposits of water ice relative to PSRs on Mercury.

Table 3. Likelihood of ice deposits in PSRs based on the observations in this study. A positive ("Y") rating in the CPR Anomalous? column indicates that a crater was CPR anomalous. A positive ("Y") Double-Bounce? rating indicates that double-bounce backscatter was observed interior but not exterior to the crater. A positive ("Y") in the PSR Blocks? column indicates that blocks were detected in the PSRs using long-exposure LROC NACs. B Value ratings would be used to assess the energy of weathering processes interior and exterior to PSRs; since no blocks were observed in these PSRs, no definite conclusions could be drawn using that analysis.

PSR Target	CPR Anomalous?	Double-Bounce?	PSR Blocks?	B Value
Rozhdestvenskiy N	Y	Y	N	Inconclusive
Lovelace E	Y	Patches	N	Inconclusive
Lovelace	Y	Patches	N	Inconclusive
Whipple	Y	Admixture	Y	Inconclusive

2.4.5 Whipple Crater

Whipple was found to be an outlier among all the craters included in this study. Its *m-chi* decomposition indicates a wide range of particle sizes occurring in patches and as admixtures (equal proportions of fine, wavelength-scale, and large blocks), which appear white in *m-chi* maps (Figure 2.4c). It has few blocks in its interior and exterior relative to other crater with blocks in this study, and the lowest exterior B value. Previous work reported high CPR values in Whipple's interior, interpreted as blocky material or ice [*Spudis et al.*, 2010; *Mohan et al.*, 2013]. Because a substantial portion of Whipple is in permanent shadow due to its high latitude (89.1°), it is possible that some amount of water ice could be the cause of the high CPR in the PSR. This possibility is consistent with LEND observations, which show depressed epithermal neutron signatures for Whipple and the surrounding region [*Sanin et al.*, 2012]. However, Diviner measurements indicate that portions of Whipple's interior may exceed the stability range of water ice, though not by a substantial amount [*Paige et al.*, 2010b]; it is therefore

possible that a combination of materials (blocks and subsurface ice) could be present. Whipple's high latitude, and therefore high incidence angle, also produce unique exposure and lighting conditions which could manifest in reduced space weathering relative to craters at lower latitudes [*Lucey et al.*, 2014; *Hemingway et al.*, 2015]. This reduction in space weathering would mitigate the degradation of large block populations into small block populations, causing an enhanced radar backscatter signal that would persist longer than craters of the same age at lower latitudes.

2.5 Outstanding Questions

There are a variety of hypotheses as to how water can be delivered to the lunar poles, including discrete events such as comet impacts or longer-scale build-up (i.e. from solar wind hydrogen implantation) [*Watson et al.*, 1961a; *Arnold*, 1979; *Crider and Vondrak*, 2003 and others]. If substantial quantities of near-surface water ice require long timescales to accumulate, then older (1+ Gy) craters are more likely to have ice in their interiors, assuming they have not been altered by younger impact events. If near-surface water ice has a short residence time at the lunar poles, then a recent asteroid or comet impact would be required to emplace such a deposit. A survey assessing the likelihood of water ice at a series of polar craters as a function of age could shed light on the timing of water ice deposition at the lunar poles.

Characterizing the threshold block population at which double-bounce backscatter signatures are produced would allow for estimates of PSR block populations where direct observations of block populations do not exist. However, numerous other factors, including regional topography, observation angle, rock composition, and subsurface

variations in block size make such a threshold extremely difficult to assess [*Fa et al.*, 2011]. Further studies of equatorial CPR-anomalous craters should be conducted to determine the cause of their radar properties. Additional comparisons between equatorial and polar CPR-anomalous craters could also shed light on the likelihood of water ice at the lunar poles, in addition to furthering our understanding of crater morphologic evolution through time.

New observations using active remote sensing – where light of multiple wavelengths is transmitted into PSRs – will offset the lack of passively emitted/reflected energy from within PSRs. Radar with improved spatial resolution will be needed to assess block abundances in the subsurface, complementing higher-spatial-resolution epithermal neutron studies which can assess hydrogen abundance to similar depths as radar. Thermal infrared will be required to constrain areas where patches of water ice are thermally stable and to provide contextual mineralogy for those areas. Visible, near-infrared, and ultraviolet observations will be needed to constrain the nature of the deposits (H_2O, OH, etc.) and to characterize small-scale albedo variations as seen in PSRs on Mercury. However, sample collection from within PSRs will ultimately be required to verify the interpretations made using orbital instruments. Cryogenic returned samples will allow a full characterization of the volatiles trapped in PSRs and any geologic material (regolith, micrometeorites, etc.) embedded within them.

2.6 Conclusions

Four PSR-bearing, CPR-anomalous craters at the lunar north pole were studied to assess the presence of blocks relative to the likelihood of water-ice deposits. Based on analyses of LROC NAC and Mini-RF radar data, Rozhdestvenskiy N is considered the most likely of the four craters to contain water ice. Its CPR-anomalous radar signature and temperature are consistent with the presence of a substantial ice deposit. It also displays a double-bounce backscatter signal in *m-chi* decomposition maps, which is indicative of wavelength-scale water ice. Additionally, it has no blocks greater than 20 m in its interior, though this could be due to resolution limitations rather than a lack of blocks. Two other polar CPR-anomalous craters, Lovelace and Lovelace E, show single-bounce scattering in their interiors, indicative of specular reflection from subsurface rock. If ice is present in either of these craters, it is not in a coherent layer and more likely diffused through the regolith. Whipple also shows a mixture of different types of scattering in its interior, preventing a definitive assessment of its potential for containing water ice. Block counts between CPR-anomalous and CPR-normal craters showed that polar craters could have large block populations that cannot be resolved in long-exposure NAC images. Block size-frequency distributions provided limited insight into erosional processes, and B values fell within the range measured by previous workers studying CPR-normal equatorial sites. More block counts, B values, and associated visible images of consistent spatial resolution must be acquired to assess whether there are large-scale trends between CPR-normal and CPR-anomalous craters. While the data in this study indicates a lack of large (meter-thick or greater) ice deposits at the lunar poles, it does not preclude smaller or more diffuse deposits in lunar PSRs. Alternative techniques (near-

infrared, high-spatial-resolution neutron spectroscopy, surface sampling) should be used at these sites to assess the absolute abundance of water ice. High-resolution (<2-m pixel scale) optical observations in PSRs are required to characterize block populations within PSRs. Additional follow-on work should study PSRs near the south pole to assess the consistency of these observations on a global scale.

2.7 Acknowledgments

This work was supported by the LRO project. The authors also acknowledge Kristen Paris, Ernest Bowman-Cisneros, Heather Meyer, and the LROC team for their guidance and support throughout this work. The authors would also like to acknowledge the helpful input of two anonymous reviewers, which significantly improved the final version of this manuscript.

CHAPTER 3

CHLORIDE-RICH BRINES: ANALOGS FOR WATER ON ANCIENT MARS

3.1 Introduction

The surface of Mars records a complex history of geologic, fluvial, and atmospheric processes. The late Noachian and early Hesperian periods (~3.5-4.2 Ga) were a time of significant aqueous activity on Mars. Valley networks, outflow channels, deltas, small channels, possible paleolakes, and other geomorphic features from this period of Mars' history are clear evidence for large volumes of water flowing across the surface [*Carr*, 1979; *Forsythe and Zimbelman*, 1995; *Cabrol and Grin*, 1999; *Fassett and Iii*, 2008; *Harrison and Chapman*, 2008; *DiAchille and Hynek*, 2010; *Hynek et al.*, 2010; *Hoke et al.*, 2011; *Osterloo and Hynek*, 2015]. In addition, minerals unique to aqueous environments, including evaporites, clays, hydrated minerals, and minerals that require the presence of water to form provide key information for interpreting the history of liquid water on the martian surface [*Bibring et al.*, 2006; *Ehlmann et al.*, 2009, 2011; *Murchie et al.*, 2009; *Carter et al.*, 2011; *Mustard et al.*, 2011].

Remote visible/near-infrared (VNIR) and thermal infrared (TIR) spectrometers/imagers, have also provided evidence for the sustained presence of liquid water on the martian surface. Water-bearing clay minerals formed by the aqueous alteration of basalt, are found in increasingly greater abundance as more hyperspectral data are collected [*Mustard et al.*, 2008; *Ehlmann et al.*, 2011; *Carter et al.*, 2013]. Sulfates, including gypsum and other, more highly-hydrated sulfates, dominate the mineralogy of much of Mars as indicated by remote sensing and rover surface analyses

[*Clark et al.*, 2005; *Gendrin et al.*, 2005; *McLennan et al.*, 2005; *Wang and Ling*, 2011]. Chloride minerals have also been identified on Mars. Because they are highly soluble, chlorides are the last species to precipitate out of most natural solutions [*Hardie and Eugster*, 1970; *Hardie et al.*, 1978; *Warren*, 2006]. Therefore, chloride deposits could pinpoint the locations where the last vestiges of significant liquid water existed on the martian surface [*Osterloo and Hynek*, 2015].

Over 630 discreet chloride mineral deposits have been identified on Mars; the largest is ~25 km^2 in areal extent (in Terra Sirenum), though the majority are less than half that size. Chlorides on Mars are typically found in topographic lows and, in many cases, are marked by polygonal cracks. Concentrated in the southern mid-latitudes on Mars, chloride deposits are typically found on late-Noachian/early-Hesperian terrains (3.5 – 4.2 Ga) and hence are thought to date from that period of martian history [*Baldridge et al.*, 2004; *Osterloo et al.*, 2008, 2010; *El-Maarry et al.*, 2016]. In fact, chloride deposits such as those in Miyamoto Crater tend to form in the centers of paleolakes and are often co-located with clays [*Osterloo and Hynek*, 2015]. Chlorides are considered prime targets for astrobiological studies because they mark regions where liquid water, warm (>~225K) temperatures, and possible radiation protection may have persisted over geologic timescales [*Schubert et al.*, 2009; *Parro et al.*, 2011; *Fischer et al.*, 2016].

3.1.1 Motivation for this Study

The chlorides deposits found on Mars could have been produced by a number of natural processes for which we can describe terrestrial analogs [*Osterloo et al.*, 2010].

Detailed investigations need to be undertaken to determine the source of the martian chlorides and the processes that produced the brines they likely came from. Endorheic (closed) basins in both cold and temperate environments, hydrothermal fluids circulated through continental and oceanic crust, and deep basinal brines are all well-known environments on Earth that produce chloride-dominated brines [*Hardie and Eugster*, 1970; *Hardie et al.*, 1978; *Li et al.*, 1997; *Warren*, 2006; *Lowenstein and Risacher*, 2009; *Bąbel and Schreiber*, 2013; *Deocampo and Jones*, 2013; *Toner et al.*, 2013; *Weis et al.*, 2014; *Iskandar et al.*, 2016; *Torii et al.*, 2017]. One or several of these types of chloride brines could produce the chloride mineral deposits that have been observed from Mars orbit. This study is the first global investigation of the major and trace metal compositions of terrestrial chloride-dominated brines conducted for the purpose of guiding future surface studies of martian chlorides.

Systematic variations in major ions and trace metals are compared for several natural brine environments, providing insight into the future study of the provenance of chloride brines on Mars. The precipitation sequence of chloride minerals is determined for each environment, providing a context upon which future small-scale studies of martian chlorides can be based. Additionally, water activities and ionic strengths of the various brines are compared, allowing the habitability potential of each brine to be compared. Finally, a summary of the major distinctions between all environment types is provided, and we make suggestions for additional specific small-scale measurements that should be made in future investigations.

3.2 Background

3.2.1 Brine Genesis

Chloride. Chlorine is highly mobile and coordinates poorly in most geologic materials because of its large ionic radius (1.81 Å). As a result, chlorine (and its ionic form, chloride) become concentrated in the residuals during magma crystallization and are thus enriched in hydrothermal solutions, gases, and unique rock types such as pegmatites and volcanic glasses [*Johns and Huang*, 1967]. In the subsurface, chloride can initially be derived from the degassing of HCl from magma [*Caron et al.*, 2008; *DiFrancesco et al.*, 2016]. In this case, the chloride migrates to the surface with water, CO_2, and other volatiles [*Bucher and Stober*, 2011]. Direct deposition of HCl gas can produce chloride-bearing volcanic sublimates, that can then be mobilized by reaction with liquid water [*Tosca et al.*, 2004; *Osterloo et al.*, 2008; *DiFrancesco et al.*, 2016; *Zolotov and Mironenko*, 2016]. Chlorides have also been found in extraterrestrial materials (H-chondrites like Zag and Monahans) [*Rubin et al.*, 2002; *Zolensky*, 2007]. Therefore, it is possible that some quantity of chloride on Earth and/or Mars is from an interplanetary source.

Chlorine abundance is enhanced in more evolved rocks and is generally positively correlated with SiO_2, though this trend is damped by the replacement of chloride ion for hydroxyl in micas and amphiboles [*Teiber et al.*, 2014]. Chloride is also more concentrated in extrusive than intrusive rocks. In basalts and gabbros, chloride is most often found in the mineral apatite for the same reason it is found in micas (i.e., replacement of OH^-), and chloride is enhanced in hydrothermally altered oceanic basalts due to the presence of amphibole in those rocks and chloride ion in the brine [*Barnes and*

Cisneros, 2012]. Chloride is preferentially found in apatite over micas or amphiboles in granitic rocks due lower incompatibility with that mineral resulting from a greater accommodation of the large chloride ion [*Teiber et al.*, 2014]. Subsequent chemical reactions between water and chlorine-bearing rocks can result in leaching of chloride from the rock [*Hardie and Eugster*, 1970; *Warren*, 2006].

The origin of chlorides on Earth's surface has been investigated by the study of various chloride-dominated brines [*Bucher and Stober*, 2011; *Kharaka and Hanor*, 2013]. On Earth, chloride enrichment in brines can be produced by hydrothermal activity, evaporative concentration in endorheic (closed) basins, environments where cold ion exchange and freeze concentration take place, and by deep basinal water-rock interactions at high temperature [*Hardie and Eugster*, 1970; *Rosen et al.*, 1990; *Lowenstein and Risacher*, 2009; *Toner et al.*, 2013; *Weis et al.*, 2014]. While chloride itself may be sourced from the environments listed above, it becomes concentrated in solution and eventually precipitates in a predictable way [*Hardie and Eugster*, 1970]. Chloride-rich brines can also be produced by the dissolution and transport of chloride-bearing salts from pre-existing salt deposits, but these do not represent the original genesis of the chloride-enriched fluids [*Kharaka and Hanor*, 2013; *Möller et al.*, 2017]. In this case, the brines formed from the dissolution of previously generated chloride-bearing evaporite are a secondary product and not directly indicative of the process that initially produced the chloride minerals [*Warren*, 2006; *Kharaka and Hanor*, 2013; *Möller et al.*, 2017].

Chloride abundances in martian meteorites have provided a link between terrestrial processes and martian geology. Bulk chlorine contents of martian basalts from

meteorite samples can be as high as 140 ppm, similar to those of tholeiitic basalts found at mid-ocean ridges and most terrestrial oceanic crust. Based on analyses of the martian meteorite Nakhla, martian basalts have 2-3 times more chloride relative to La and K than terrestrial oceanic basalts [*Dreibus and Wanke*, 1985]. Cl-scapolite and chlorapatite have been identified in Nakhla, indicating an origin from a water-poor, high-temperature (700°C) late-stage magma or a Cl-rich hydrothermal brine [*Filiberto et al.*, 2014]. The presence of halite in interstitial areas of Nakhla has been interpreted as alteration by a Cl-CO_2-S dominated fluid at temperatures up to 200°C [*Gooding et al.*, 1991]. Chlorine-rich amphibole has also been found in the nakhlite MIL 03346 [*Sautter et al.*, 2006]. Chlorine has been found in shergottites as well, though they indicate chlorine fugacities in martian magmas equal to or less than those of terrestrial mid-ocean ridge mantle sources [*Gross et al.*, 2013]. Mars landers have all found elevated chlorine in martian soils; Viking measured chlorine at levels up to 1.5 wt % [*Clark and Van Hart*, 1981], the Spirit rover measured up to 1 wt % at Gusev Crater [*Haskin et al.*, 2005], the Opportunity rover measured ~0.7 wt % at Meridiani Planum, and the Curiosity rover also measured ~0.7 wt % chlorine at Rocknest in Gale Crater [*Blake et al.*, 2013].

pH and pCO_2. pH is generally controlled by equilibrium between Na-K-Ca minerals and pCO_2; therefore, pH can be a useful link between mineralogy and dissolved gases at the time of brine formation [*Lower*, 1999; *Christov and Moller*, 2004; *Ding et al.*, 2005; *Smith et al.*, 2017]. pH can roughly indicate the depth of circulation of subsurface waters, where pH < 7 implies a shallow depth, and pH > 7 implies a deep circulation. Near-neutral pH (pH = 6-8) can indicate buffering by carbonate or weathering of feldspars to clays, both of which are acid-consuming reactions. The

availability of calcium in terrestrial waters is indirectly sensitive to pH; this sensitivity is due to the retrograde solubility of Ca-bearing minerals such as calcite that can enhance aqueous Ca concentrations when they are dissolved. pH does not generally correlate with dissolved trace metal abundance. [*Cortecci et al.*, 2005; *Caron et al.*, 2008]

B and Li. Similar Cl:B ratios generally indicate a common feeding body of hot water and an ascending path along one supply fissure or through very chemically homogenous rocks [*Risacher and Fritz*, 1991; *Rudnick et al.*, 2004; *Ingle and Banerjee*, 2008; *Witherow and Lyons*, 2011]. Due to the limited availability of B and Li data in the literature, these ions were not used in this study. As more global data sets are acquired, these components should be revisited.

3.2.2 Brine Transport and Water-Rock Reactions

Na and K. Highly evolved, silicic rocks (granite/granodiorite, rhyolite/dacite) are rich in Na and K. Leaching and other high-temperature water-rock reactions can add these species to natural waters. Hot, hydrothermal waters leach K more efficiently from silicic/felsic host rocks than Na; therefore, hydrothermal fluids generally show an inverse relationship between Na/K and water temperature [*Cortecci et al.*, 2005]. Na-rich waters can also be associated with large faults near plutons. They are considered to have a "granitic" influence on their composition. The weathering of feldspar and ion-exchange reactions with Na and K-bearing clays can affect the abundances of these species in natural waters [*Carroll*, 1959; *Caron et al.*, 2008; *Toner et al.*, 2013; *Hussien and Faiyad*, 2016].

Ca and Mg. Water-rock reactions with mafic rocks (gabbro/diorite, basalt/andesite) are the primary controls on Ca and Mg concentrations. The formation of clays from plagioclase, pyroxene, and/or olivine have major controls on the concentration of Mg in solution [*White and Buss*, 2013; *Hussien and Faiyad*, 2016; *Möller et al.*, 2017]. In hydrothermal fluids, the quantitative removal of Mg occurs rapidly during high-temperature seawater–rock interaction and during the formation of saponite and chlorite [*Hardie and Sea*, 1983].

Here we include a brief summary of the primary water-rock reactions that can effect brine composition during and after transport to the surface. Chloritization, reaction 1 shown below, removes Mg from solution and exchanges it with Ca in the production of chlorite, a Mg-phyllosilicate [*Kirsimae et al.*, 2002; *Beaufort et al.*, 2015].

$$CaAl_2Si_2O_8 + 5Mg^{2+} + SiO_2 + 8H_2O \leftrightarrow Mg_5Al_2Si_3O_{10}(OH)_8 + Ca^{2+} + 8H^+ \quad (1)$$

Anorthite Chlorite

Kaolinization is the formation of kaolinite clay from any of several forms of feldspar. The conversion of anorthite to kaolinite (reaction 2) adds Ca to solution without the removal of any major cations. The conversion of alkali feldspar to kaolinite (reaction 3) adds K to solution without the removal of any major cations [*Keller*, 1961; *Möller et al.*, 2017].

$$CaAl_2Si_2O_8 + 2H^+ + H_2O \leftrightarrow 0.5Al_4Si_4O_{10}(OH)_8 + Ca^{2+} \quad (2)$$

Anorthite Kaolinite

$$2KAlSi_3O_8 + 2H^+ + 9H_2O \leftrightarrow Al_2Si_2O_5(OH)_4 + 4H_4SiO_4 + 2K^+ \quad (3)$$

K-Feldspar Kaolinite

After clay minerals are formed, they can undergo ion exchange reactions with ions in solution, altering the composition of the brine and producing varied assemblages of clays. All the major cations (Na, Ca, K, Mg) can be exchanged with numerous clay minerals, including kaolinite and saponite, illite, montmorillonite, and others. Therefore, the presence of clay minerals in proximity to evaporite deposits should be considered when investigating the composition of the evaporite source brine. Terrestrial chloride-rich brines typically lose K and Mg to clays in nearby sediments, resulting in higher Na and Ca concentrations in the brine [*Jones et al.*, 2009; *Toner et al.*, 2013]. Investigations of clays in proximity to chloride deposits may provide insight into the reactions that took place between brines and the rocks they were in contact with on ancient Mars.

Serpentinization reactions can take place with pyroxene, plagioclase, or olivine minerals, and involve the removal of Mg from solution and integration of Mg into the mineral structure to produce one of several kinds of serpentine minerals. The reaction of Mg-bearing water with diopside, a pyroxene, is shown below; this reaction adds Ca to solution as Mg is removed [*Müntener*, 2010; *Baumberger et al.*, 2016; *Möller et al.*, 2017].

$$CaMgSi_2O_6 + 3Mg^{2+} + 4H_2O \leftrightarrow Mg_3Si_2O_6(OH)_4 + Ca^{2+} + 4H^+ \quad (4)$$

Diopside Serpentine

Albitization occurs when Na is removed from solution and exchanged with Ca, converting anorthite to albite. This reaction results in an increase in Ca in solution.

$$CaAl_2Si_2O_8 + 2Na^+ + 4SiO_2 \leftrightarrow 2NaAlSi_2O_8 + Ca^{2+} \quad (5)$$

Anorthite Albite

Albitization and serpentinization result in a similar behaviors between Ca/Mg and Na/K by weight (that is, waters with high Ca/Mg generally have high Na/K and vice-versa). Therefore, a correlation between these ions in natural waters of an unknown origin can provide insight into the chemical reactions that resulted in the observed water chemistry [*Deocampo and Jones*, 2013]. For example, waters with high Ca/Mg and high Na/K likely experienced albitization and/or serpentinization processes, waters with high Ca/Mg and low Na/K likely experienced kaolinization or chloritization. Waters with low Ca/Mg likely indicate minimal water-rock reactions.

3.2.3 Chemical Evolution of Evaporating Waters

Natural terrestrial waters are generally dominated by the ions HCO_3^-, SO_4^{2-}, and Cl^- (major anions) and Ca^{2+}, Mg^{2+}, Na^+, and K^+ (major cations). The chemical evolution of standing bodies of water has been extensively studied and well characterized. Regardless of the source of the natural waters, the major ions behave in a predictable way as a result of: 1) the relative solubilities of the precipitating minerals, and 2) water-rock

interactions. Therefore, any investigation into the source of a brine or evaporite salt must take into account the evaporite sequence.

To form a chloride deposit such as that observed on Mars, a natural body of water must undergo evaporative concentration, where the rate of meteoric or groundwater inflow is significantly less than the rate of water loss to evaporation [*Sears and Chittenden*, 2005]. The concept of chemical divides describes this mineral precipitation sequence. As water is removed from the closed system due to evaporation, carbonate minerals with alkaline earth counter ions (Ca and Mg) will precipitate first due to their low solubilities (relative to sulfates and chlorides). Calcite ($CaCO_3$) is the first to precipitate, causing a removal of Ca in molar proportion to CO_3. If waters are particularly high in Mg, dolomite or magnesite can be precipitated as well. After complete removal of carbonate from solution, sulfate precipitation begins. Gypsum ($CaSO_4 \bullet 2H_2O$) and anhydrite ($CaSO_4$) are precipitated first, resulting in an additional commensurate removal of calcium from the brine solution. Mg-sulfates can be produced as well, in molar proportion to their original abundances relative to Ca and the species of minerals that have precipitated [*Hardie and Eugster*, 1970; *Hardie et al.*, 1978; *Warren*, 2006].

Up to this point in the evaporative concentration of the body of water, chloride has remained conserved in solution. The persistence of chloride is a direct result of the high solubilities of chloride minerals relative to sulfates and carbonates. The original abundances of cations determine the final chloride species that will precipitate. If $(Ca^{2+} + Mg^{2+}) > (HCO_3 + SO_4^{2-})$, there will be a non-zero amount of Ca and Mg in solution after the precipitation of carbonate and sulfate species. If $(Ca^{2+} + Mg^{2+}) < (HCO_3 + SO_4^{2-})$, Na and K will be the only remaining major cations. As the chloride-dominated brine

continues to concentrate, the threshold solubility of halite will be crossed, and that species will begin to precipitate out of solution [*Hardie and Eugster*, 1970; *Hardie et al.*, 1978; *Rosen*, 1994; *Warren*, 2006].

In contrast to carbonates and sulfates, alkali chlorides (i.e., halite and sylvite) have lower solubilities than alkaline earth chlorides (i.e., antarcticite and bischofite). Therefore, most natural solutions will precipitate halite and sylvite before precipitating the calcium/magnesium chlorides [*Hardie and Eugster*, 1970; *Bąbel and Schreiber*, 2013; *Toner et al.*, 2017]. Calcium and magnesium chlorides are so soluble, they will adsorb water from the surrounding atmosphere; they are also able to significantly depress the freezing point of any brines in which they are concentrated, allowing brines to remain liquid well below the typical freezing point (i.e., Don Juan Pond, Antarctica with a mean annual temperature of -20°C) [*Toner et al.*, 2013, 2017; *Gough et al.*, 2017]. While the precipitation sequence of chlorides generally follows the above description, geochemical modeling of natural solutions demonstrates that this sequence (halite → sylvite → antarcticite/bischofite) is not always followed (see Data/Results section below).

On Mars, the abundance of iron might have an effect on the precipitation sequence; the presence of iron was not included in the geochemical modeling performed in this study. However, previous work by Tosca and McLennan (2006) showed that the general sequence of precipitation remains the same in the presence of iron (Figure 3.1), where carbonates precipitate out of solution first and chlorides last. In fact, Tosca and McLennan (2006) predicted the precipitation of chlorides on Mars in their modeling of evaporatively concentrated brines produced by weathering of basalt. They grouped late-stage brines into five types, where they define brine "type" as a specific proportion of

cations relative to anions in solution. Type I brines are bicarbonate-rich and Types II-V are chloride-rich. Types II – IV are all poor in HCO_3 and SO_4 and rich in Na, Mg, Ca, K, and/or K. Type V is poor in HCO_3 and rich in SO_4 and Cl. Types II-IV result in the precipitation of halite, sylvite, bischofite, and antarcticite, and Type V brines result in sulfate assemblages. While Tosca and McLennan (2006) laid the groundwork for understanding the chemical evolution of martian brines, further resolution of the sequence of chloride precipitates is needed to fully constrain which branch of the chemical divides framework martian chloride minerals came from. [*Tosca and McLennan*, 2006]

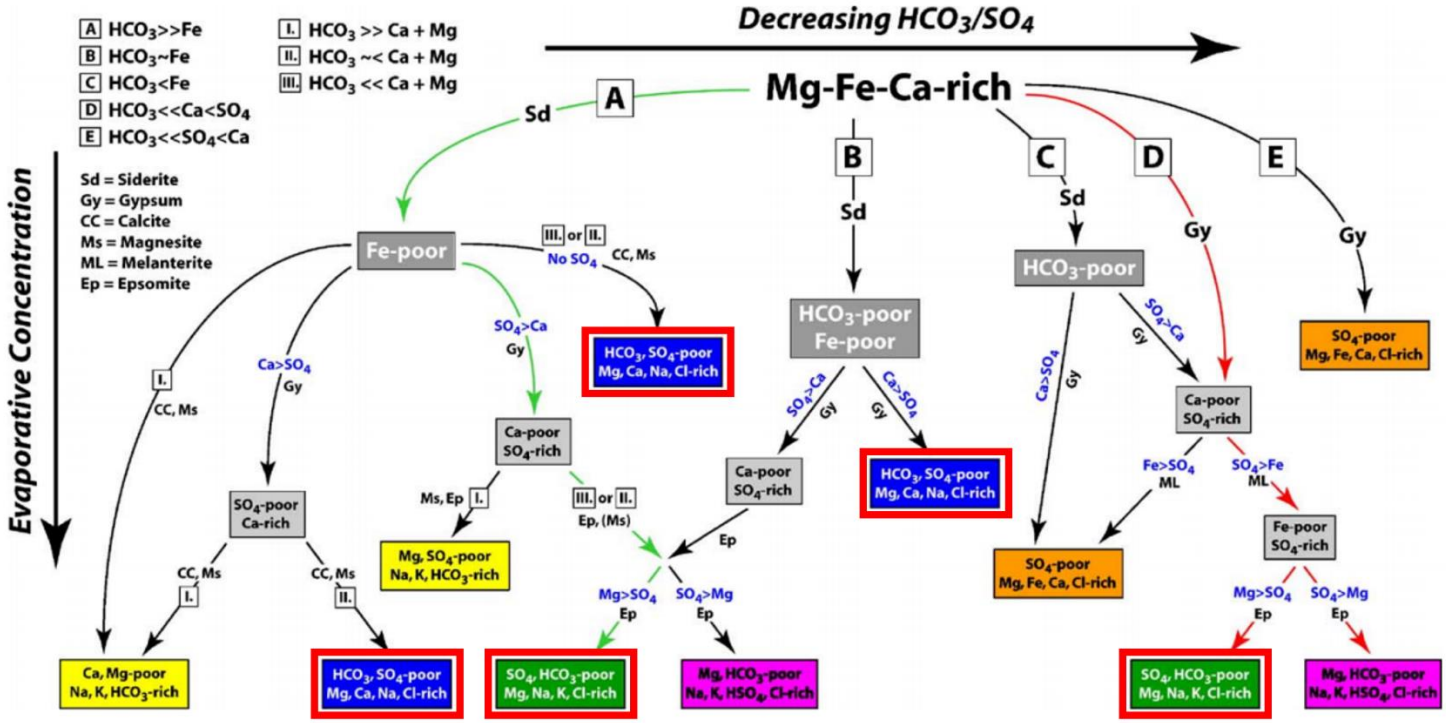

Figure 3.1. Chemical divides for Mars showing the modeled precipitation sequence of minerals. The sequence of mineral precipitation proceeds from less- to more-concentrated (top to bottom), with divisions in precipitation sequence based on the original abundance of ions shown in the top left (A-E). The red boxes show the eventual appearance of chloride-dominated brines in virtually every scenario. Orange-filled boxes also show chloride-dominated brines, but these have a significant iron component in contrast to terrestrial brines. Adapted from [*Tosca and McLennan*, 2006].

3.2.4 Cold Processes

Freezing or below-freezing temperatures can produce unique chemistries and mineralogies that must be taken into account when assessing the evolution of a brine and its precipitates. Hydrohalite ($NaCl \cdot 2H_2O$) begins to form at -5°C and can remain stable up to 0.1°C, above which it converts to a saturated brine and halite [*Light et al.*, 2009; *Drebushchak et al.*, 2017]. Freeze concentration, ion exchange, and the influence of snow and glacial melt are all unique processes that affect the composition of cold brines and the minerals that precipitate from them.

Freeze concentration is driven by the relative solubilities of minerals at low temperatures, and their abilities to depress the freezing point of liquid water. Because the freezing point of water is higher than that of any chloride brine, water ice will precipitate (freeze) out of solution prior to salts [*Light et al.*, 2009; *Lu and Xu*, 2010]. As the temperature decreases and water ice freezes out, the residual brine becomes concentrated until it reaches its eutectic point; the eutectic temperature of a brine is the point beyond which it cannot remain liquid, regardless of its concentration [*Knauth*, 2002; *Drebushchak et al.*, 2017]. For mixed-solute chloride brines, the freezing points of the various chloride species will dictate the sequence of precipitation of salt minerals. The chloride with the lowest eutectic temperature is calcium chloride (eutectic temperature = -51°C); it is therefore usually the last mineral to freeze out of a chloride-rich brine [*Brass*, 1980; *Sinke and Mossner*, 1985; *Altheide et al.*, 2009].

Ion exchange processes between solutions and soils also manifest differently under freezing temperatures. Instead of being taken up by clays exposed to brines, exchangeable ions such as Ca and Mg are added to solution and replaced by Na within

the clay structure; this is the direct result of freeze concentration driving divalent cations into the aqueous phase while monovalent cations are taken up by clays/soils. Below-freezing ion exchange therefore results in the conversion of a Na-Cl brine to a Ca-Mg-Cl brine, consistent with the observed composition of subsurface brines in the McMurdo Dry Valleys, Antarctica. However, some brines – such as those at Don Juan Pond in Antarctica, an endorheic cold pond – are deficient in Mg, which cannot be explained by ion exchange alone. Therefore, ion exchange plays a role in dictating the compositions of brines in cold environments, but is not the only factor determining brine composition and thus evaporite mineral sequence. The specific causes of the unique chemical composition of the Don Juan Pond brine are poorly constrained and are a topic of ongoing study. [*Toner et al.*, 2013, 2017]

Cold climates must also contend with the influence of snow and glacial melt. In Antarctica, snow and glacial melt tend to impart a dilute seawater-like component to surface and groundwater brines; this is due to the deposition of seawater aerosols into relatively pure water ice. However, most terrestrial cold-temperature chloride brines are concentrated enough that snow and glacial melt tend to have a minimal dilution effect; the impact on major ion composition in concentrated brines is negligible [*Witherow and Lyons*, 2011; *Toner et al.*, 2013; *Takamatsu et al.*, 2017]. On Mars, however, the introduction of snow and glacial melt to stagnant brines may have altered the brine chemistry in different ways than their terrestrial analogs; for example, the unique composition of martian dust intermixed with ice-melt could result in a unique proportion of dissolved solids that is not seen in cold brines on Earth.

3.2.5 Influences on Trace Metals

Hydrothermal waters can be hot (up to 300+ °C), form under high pressure (100+ MPa), and can have extremes in pH (either highly acidic or basic); as a result, hydrothermal fluids are highly reactive [*Hellman and Ramsey*, 2004; *Butterfield*, 2009; *Baumberger et al.*, 2016]. Hydrothermal waters are capable of dissolving trace metals that might otherwise be insoluble at lower temperatures. Elevated (> 20 μg/L) trace metals are often considered indicative of hydrothermal fluids. Virtually the entire periodic table of elements can be detected in terrestrial and marine hydrothermal fluids, but typical dissolved trace elements with high concentrations in hydrothermal fluids are Fe, Mn, Cu, Pb, Zn, and Ba [*Metz and Trefry*, 2000; *Cortecci et al.*, 2005; *Caron et al.*, 2008; *Baumberger et al.*, 2016; *Guo et al.*, 2017]. In a closed basin where a hydrothermal fluid component has been allowed to concentrate, elevated trace metals can be found in some evaporatively concentrated brines. Often, mineralization in bedrock fractures or in sediments within and marginal to a closed basin offer evidence for circulation of hydrothermal fluids at or near the surface [*Risacher et al.*, 2003; *Lowenstein and Risacher*, 2009]. Carbonates (calcite, dolomite), sulfates (gypsum/anhydrite), and chlorides (halite, sylvite/KCl, or carnallite/$KMgCl_3 \bullet 6H_2O$) may have relatively high concentrations of trace elements incorporated within crystals and in fluid inclusions [*Caron et al.*, 2008]. For the purposes of this study, we assume elevated trace metal compositions are expected for hydrothermal fluids or for those brines bearing a hydrothermal component.

3.2.6 Seawater

Seawater represents the largest chloride-dominated natural water reservoir on Earth. There are numerous sources and sinks for the major ions and trace metals found in seawater. The source of seawater chloride is thought to primarily be due to volcanic activity and the magmatic degassing of HCl. The weathering of crustal rocks and the transport of soluble species (including chloride ion) to the sea has a direct impact on seawater salinity [*Knauth*, 1998]. Additionally, hydrothermal brines that are the result of seawater circulation through oceanic crust contribute to the oceanic budget of both chloride and magnesium. Chloride is removed from seawater primarily due to the sequestration of seawater by: 1) localized isolation on the surfaces of continents, 2) evaporative concentration and precipitation of chloride salts, or 3) incorporation into continental groundwater reservoirs [*Knauth*, 1998]. A very small component of seawater salinity loss is the landward movement of aerosols [*Witherow and Lyons*, 2011].

Seawater is also lost during tectonic plate subduction when it is carried through the lower crust/mantle in the forearc of the subducting slab. This chloride, however, can be reintroduced to the surface through back-arc volcanic activity and transport to the ocean [*Kawamoto et al.*, 2013]. The influence of seawater on a number of terrestrial chloride brines is critical to putting their compositions in proper context. In order to understand the influence of seawater on various brines, it is included separately as a point of comparison in this study.

3.2.7 Mars

Detection of Chlorides. Chloride minerals are unique in that they have no spectral features in the thermal infrared and, due to their graybody behavior, impart a slope to their thermal infrared spectra; these properties have allowed chlorides to be detected using remote sensing [*Eastes*, 1989; *Baldridge*, 2008; *Osterloo et al.*, 2008; *Bandfield*, 2009]. Over 630 chloride deposits have been identified on Mars by the Thermal Emission Imaging System (THEMIS) [*Christensen et al.*, 2004; *Osterloo et al.*, 2010]. These deposits are generally associated with topographic lows, are sometimes found as inverted channels, and in many cases are co-located with clay minerals. To date, no chloride deposit has been observed in proximity to sulfate minerals [*Osterloo et al.*, 2010]. Martian chlorides show no evidence of mineral hydration features in the visible and near-infrared, and have inconsistent evidence of adsorbed water [*Jensen and Glotch*, 2011]. Estimates of chloride abundance are 10-25% based on Hapke modeling of their thermal and near-infrared spectral features [*Glotch et al.*, 2016].

The Environment of Ancient Mars. There are numerous environmental differences between the climate on Earth and that of ancient Mars. These variations must be taken into account when assessing the context and provenance of martian chloride deposits and their relation to terrestrial analogs. One of the primary controls on the pH of surface waters on Earth is the partial pressure of atmospheric CO_2. On ancient Mars, this would have been a key control on the acidity of brines, where acidic brines are more reactive with rocks and therefore more likely to be rich in dissolved solids [*Catling*, 1999; *Tosca et al.*, 2004]. The contextual geology is also largely different between Earth and Mars. Basalt, which dominates the martian surface, would act as a significant source of Ca, Mg,

and Fe for brines; therefore, it is likely that Ca-Cl dominated terrestrial brines are the best analogs to brines on ancient Mars [*Brass*, 1980; *Bandfield*, 2000; *Christensen et al.*, 2000; *Burt and Knauth*, 2003]. The surface temperature on ancient Mars is not well constrained, and the scientific community continues to debate the surface conditions that would have existed at the time the martian chlorides formed [*Sagan et al.*, 1973; *Howard et al.*, 2005; *Chamberlain and Boynton*, 2007; *Carr and Head*, 2010; *Osterloo and Hynek*, 2015]. A cold environment would have been dominated by freeze concentration and cold ion exchange, whereas a warmer environment (though by no means hot) would have been dominated by more familiar behaviors such as those described in sections 3.2.2 and 3.2.3.

3.3 Terrestrial Localities of Chloride-rich Brines

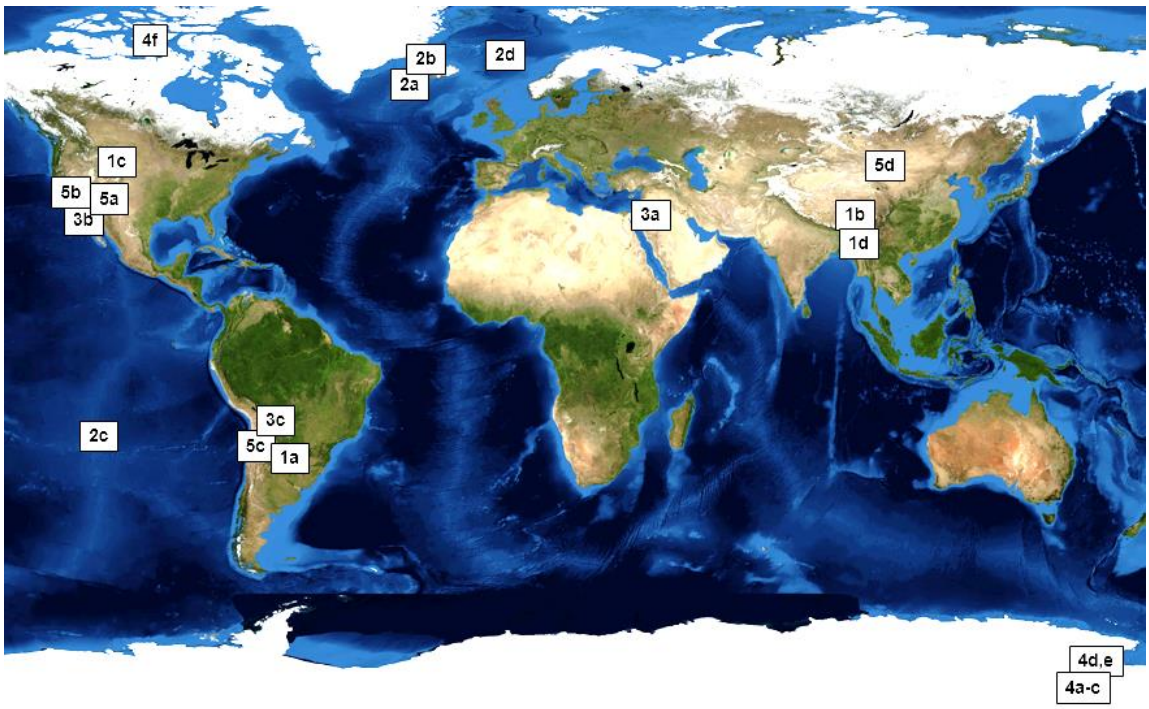

Figure 3.2. Locations of chloride-dominated brines included in this study. (1) Hydrothermal continental brines: a) El Tatio, Chile; b) Yangbajing, Tibet; c) Heart Lake, Yellowstone; d) Tengchong, China. (2) Hydrothermal oceanic brines: a) Reykjanes, Iceland; b) Svartsengi, Iceland; c) East Pacific Rise; d) Loki's Castle. (3) Temperate endorheic basins: a) Dead Sea, Israel; b) Salton Sea California; c) Salar de Uyuni, Bolivia. (4) Cold endorheic basins: a-c) Lakes Bonney, Fryxell, and Hoare, Taylor Valley, Antarctica; d-e) Lake Vanda and Don Juan Pond, Wright Valley, Antarctica; f) Lost Hammer Spring, Axel Heiberg Island, Canada. (5) Deep basinal brines: a) Bristol Dry Lake, California; b) Death Valley, California; c) Salar de Atacama, Chile; d) Da Qaidam, China. (Earth Image Credit: Blue Marble, NASA)

3.3.1 Hydrothermal Continental Brines

The composition of continental hydrothermal fluids is largely driven by geologic context. If hydrothermal fluids are sourced by intruding granitic plutons, the brine will be enriched in Na and K. This enrichment can also occur if a brine heated in the subsurface passes through silicic/felsic rocks on its way to the surface [*Fritz*, 2009; *Bucher and*

Stober, 2011]. Hydrothermal fluids from both continental and oceanic crust typically have higher trace metals than meteoric or unheated groundwater fluids [*Caron et al.*, 2008; *Iskandar et al.*, 2016].

El Tatio, Chile. El Tatio, Chile, is one of the highest-altitude geyser fields in the world. Situated at high altitude on the Andes cordillera, El Tatio is driven by subsurface heating due to the subduction of oceanic crust under the South American continental plate. While El Tatio contains both chloride and sulfate-dominated waters, only the chloride-rich waters are included in this study. The source of chloride at El Tatio is generally from volcanic degassing and water-rock interactions. El Tatio thermal spring waters are extensively heated, with chloride-rich brines that originated at up to 300°C, although they are below boiling (100°C) when they reach the surface. (Table 1) [*Cusicanqui et al.*, 1975; *Giggenbach*, 1978; *Cortecci et al.*, 2005; *Boschetti et al.*, 2007]

Yangbajing, Tibet. The Yangbajing Geothermal Field in Tibet is part of the Himalayan Geothermal Belt and is the highest-altitude geothermal fieled in the world. The Yangbajing Basin, where the geothermal field is located, is heated by a near-surface magma chamber, which was allowed to rise due to large-scale slip faulting. Most of the surrounding geology is Quaternary alluvium underlain by Himalayan granite and tuff. The sodium-chloride-dominated water in this region reaches up to 330°C and is generally considered to be a mixture of cold groundwater and deep hydrothermal water. [*Bingqiu and Hui*, 1995; *Ji and Ping*, 2000]

Heart Lake, Yellowstone. Yellowstone Caldera is the largest volcanic feature in North America, and is well-known for extensive geothermal activity. The generally accepted mechanism for this feature is the movement of North America along a deep

mantle plume, forming a continental hot spot. The Yellowstone Caldera is dominated by rhyolitic and basaltic deposits, including tuffs and lavas. Heart Lake Geyser Basin is at the intersection of the Yellowstone Caldera and is a site of active faulting along the east side of the Red Mountains; it contains both acidic and neutral Cl-dominated waters; previous studies have shown that it has significant inputs of magmatic gases such as CO_2, H_2, and HS [*Lowenstern et al.*, 2012].

Tengchong, China. The Tengchong region is one of the largest geothermal regions in China, and located near the border between China and Myanmar. The Rehai geothermal field is the largest geothermal field in the Tengchong region, and consists of Precambrian gneiss, Cretaceous granites, and Quaternary sandstones and conglomerates. Young (~5-50ka) andesitic and basaltic volcanism in the region is indicative of a subsurface magma chamber that could be the source of geothermal heating. However, the volcanism may be relict and the heating due to orogenic activity or associated with tectonic activity. The Rehai field has boiling springs, steam, and fumaroles. [*Zhijie and Guoying*, 1986]

3.3.2 Hydrothermal Oceanic and Mid-Ocean Ridge Brines

Most oceanic hydrothermal brines, sourced from mid-ocean ridge vents, are thought to be products of exolved water from deep crustal magmas; oceanic hydrothermal brines are rich in major ions and trace metals. Oceanic hydrothermal brines are typically reduced, with sulfur in the form of H_2S, until the brine exits the vent, at which point it is oxidized. The sulfide minerals either precipitate out of solution (producing “black smokers”) or are oxidized and then precipitated (producing sulfate “white smokers”);

either way, sulfur is quickly removed from solution. K, if present, is also leached from basalt into seawater [*Von Damm et al.*, 1995; *Ding et al.*, 2005; *Baumberger et al.*, 2016]. If the brine contains Mg, it can react with basalt through serpentinization (section 3.2.2) and produce Mg-clays (i.e., chlorite and saponite), resulting in the near-quantitative removal of Mg from marine hydrothermal systems and a loss of Mg from solution.

Iceland - Reykjanes and Svartsengi. Iceland is a unique geologic region where the Atlantic mid-ocean ridge intersects a deep-mantle hot-spot. Iceland is composed almost entirely of Tertiary and Quaternary basalts. There are numerous geothermal sites on the island that are used for the production of geothermal power; Iceland is also volcanically active, with multiple volcanic eruptions occurring within the last century. The Reykjanes and Svartsengi high-temperature geothermal fields are located on the Reykjanes peninsula in southwestern Iceland. The geothermal brine in this region is believed to have originated as seawater. While the water samples included in this study are dominantly geothermal brines, they also include a variable (up to 1/3) seawater component. [*Uz-Zaman*, 2013]

East Pacific Rise. The East Pacific Rise is a divergent oceanic crust boundary located south of Mexico; it is an extension of the spreading zone in the Gulf of California. The East Pacific Rise is one of the fastest spreading centers on Earth and an active zone of basaltic lava eruption [*Kelley et al.*, 2002]. Black smoker hydrothermal vents were first discovered here, and the region is covered in significant sulfide deposits [*Von Damm et al.*, 1995].

Loki's Castle. Loki's Castle is a hydrothermal vent field at one of the slowest spreading ridge segments on Earth. Loki's Castle sits on the Mohns Ridge, part of the

Arctic mid-ocean ridge system between Greenland, Norway, and Iceland. The fluid from Loki's Castle produces black smokers. Camel Vent, on the western sulfide mound of Loki's Castle, was the source of chemical data used for this study. [*Baumberger et al.*, 2016]

3.3.3 Temperate Endorheic Basinal Brines

Closed, or endorheic, basins commonly contain waters with high Cl concentrations due to the convergence of surface runoff and subsequent evaporative concentration. Endorheic basins in dry regions are where evaporative concentration takes place, and the production of a chloride-enriched brine becomes possible. Dry regions include hot deserts, where evaporation is accelerated by brine heating, and cold deserts, where freeze concentration and ion exchange play a major role. Multiple examples of each basin type were included in this study.

Dead Sea, Israel. The Dead Sea was formed during the Neogene when seawater flowed into the Dead Sea rift. Since its original infilling by seawater, the Dead Sea has been dominated by evaporative concentration and the subsequent precipitation of numerous evaporite minerals such as gypsum, anhydrite, and halite. Inflows from surface water have maintained some level of water in the Dead Sea, but recent diversions of this surface water for irrigation and domestic uses has resulted in the precipitous decline in the Dead Sea water level [*Stiller et al.*, 2007, 2016]. An increase in concentration of the Dead Sea brine is commensurate with the decline in water level; for the purposes of this study, the Dead Sea represents a seawater-derived temperate endorheic basin. Water compositions from Ganor and Katz (1989) at depths of 0-400 m were used for major ions

analysis and Nissembaum (1976) for trace metals [*Nissenbaum*, 1977; *Ganor and Katz*, 1989].

Salton Sea, CA. The Salton Sea is located in the Salton Trough, a northward extension of the crustal spreading zone in the Gulf of California. The Salton Trough contains various rhyolitic domes and basaltic rocks as xenoliths on the surface, and hydrothermally altered basalts in the subsurface. While the Salton Sea was periodically dry due to variations in the level and flow of the Colorado River, the most recent water infill was produced as a result of human activity. The Colorado River overflowed a riverbank cut made to facilitate irrigation in 1905, and the outflow produced the Salton Sea as it is known today. Inflows to the Salton Sea are low and largely agricultural; the evaporation rate of water is higher than the inflow rate, resulting in a decreasing water level with time and an increase in salinity. Seawater from the Gulf of California, previously deposited evaporites, and possible hydrothermal influences from the nearby Salton Sea Geothermal Field are contributors to the dissolved solids in the Salton Sea. [*Elders*, 1976]

Salar de Uyuni, Bolivia. With an area of 10,000+ km^2, the Salar de Uyuni is the largest salt flat in the world. Situated on the Bolivian Altiplano (3653 m altitude), the Salar de Uyuni was formed as the result of evaporative concentration of a giant prehistoric lake (~40 ky), that covers the tops of multiple andesitic volcanoes in the Andes Mountain range. The Salar de Uyuni is covered by a cm-to-m-thick crust of evaporatively produced halite deposits that is underlain by a concentrated chloride brine. [*Retting et al.*, 1980]

3.3.4 Cold Endorheic Basinal Brines

Antarctic lakes. In the McMurdo Dry Valleys, average annual temperatures are very low (-16 to -21°C) and <10 cm of snow falls each year. Lakes Bonney, Fryxell, and Hoare are meromictic (contain layers of water that don't intermix) lakes in Taylor Valley, with surface layers that are fed by glacial melt enriched in marine aerosols that are permanently covered with ice. The Taylor Valley Lakes have sodium as the dominant cation. Lake Vanda in Wright Valley is also meromictic and ice-covered, but it is replenished by a freshwater melt stream, and has increasing salinity with depth. Lake Vanda's major cation is calcium. The only inflow to any of the lakes is from ephemeral summer streams. All of the lakes are saline and chloride-dominated; the source of the chloride is hypothesized to be aeolian marine salts. [*Witherow and Lyons*, 2011; *Takamatsu et al.*, 2017]

Don Juan Pond, Antarctica. Don Juan Pond is the most saline body of water on Earth (40% dissolved salts by weight). Situated in the McMurdo Dry Valleys, in Wright Valley close to Lake Vanda, Don Juan Pond's dominant cation is calcium and its dominant anion is chloride. Don Juan Pond is surrounded by precipitates of gypsum, halite, and antarcticite, and the bottom of the pond is covered in antarcticite precipitates. Don Juan Pond is considered a Mars-analog site due to the local cold, dry environment and the presence of nearby water tracks similar to recurring slope lineae (RSL) on Mars [*Levy et al.*, 2011; *Levy*, 2012]. The extreme concentration of $CaCl_2$ (95% of dissolved solids) results in a significantly decreased freezing point of the brine, allowing Don Juan Pond to stay liquid throughout the year. [*Witherow and Lyons*, 2011; *Toner et al.*, 2013]

Lost Hammer Spring, Canada. Lost Hammer Spring, also called Wolf Spring, is a saline cold spring on Axel Heiberg Island, Nunavut, Canada. Water at Lost Hammer

Spring is sourced form a “salt tufa,”, with a vent-like morphology [*Niederberger et al.*, 2010]. The vent is higher in the winter due to outflow blockage. Methane, N_2, CO_2, and other gases percolate through the nearby sediment and pore water. A thin (mm-cm thick) salt pan of sulfates (thenardite and mirabilite) and halite surrounds the vent. The annual average water temperature is -4.7 to -5.9 degrees C, likely due to freezing point depression from the dissolved salts. [*Battler et al.*, 2013]

3.3.5 Deep Basinal Brines

Deep basinal brines are produced by the circulation of groundwater into the deep crust, where the water is heated and its composition altered by water-rock reactions. Tectonic faulting provides a conduit upward, where the brines can surface with little change in their deep-basinal composition. Such brines are therefore often found isolated from large bodies of water and in proximity to known tectonic faulting. Previous studies have shown that the composition of deep basinal brines is dominantly controlled by albitization at depth, where Na is removed from solution to produce albite, and Ca is added to solution from anorthite (section 3.2.2) [*Möller et al.*, 2017]. In fact, the Ca-Cl rich composition of deep basinal brines is often considered diagnostic of their origin [*Lowenstein and Risacher*, 2009].

Bristol Dry Lake, CA. Bristol Dry Lake is a dried lake bed (playa) in the Mojave Desert [*Burt et al.*, 2003] north of Joshua Tree National Park. It is near several felsic igneous geologic units, including the Calumet, Bristol, and Sheep Hole Mountains. Northwest of Bristol is Amboy Crater, a 80-ka basaltic cinder cone volcano, and associated lava flows [*Phillips*, 2003; *Kienenberger and Greeley*, 2012]. Bristol Dry Lake

is located in the Bristol Trough, the deepest of several structural troughs in the Sheep Hole Mountains/Amboy area. The playa is characterized by a central halite salt pan covered in meter-scale polygonal cracks, surrounded by gypsum/celestite, which is in turn surrounded by debris from nearby alluvial fans. Several mining operations at Bristol Dry Lake collect and evaporate the groundwater to produce antarcticite ($CaCl_2 \cdot 6H_2O$) in the center of the salt pan. It is possible that the magma chamber below Amboy Crater heats the subsurface waters and enhances water-rock reactions between the brine and the nearby basalt [*Duning and Cooper*, 1969; *Rosen*, 1991; *Lowenstein and Risacher*, 2009; *Dolginko*, 2014].

Death Valley, CA. Death Valley is a narrow basin in southern California, at the southern edge of the Great Basin. Death Valley is surrounded by multiple mountain ranges (Panamint, Black, and Funeral Mountains) and is dominated by sedimentary and metamorphic rock rypes. Badwater Basin in southern Death Valley is the lowest point in the Western Hemisphere and covered by evaporite salts, primarily sulfates (gypsum and anhydrite) and halite. Ca-Cl-dominated spring water flows into Badwater Basin from Mormon Point Spring and several well sites; numerous strike-slip and normal faults in the region may serve as conduits by which spring waters reach the surface. The presence of a young cinder cone (Split Cone, 300 ka) indicates the presence of a mid-crustal magma chamber. The co-location of numerous steep faults with the spring indicates that the Ca-Cl-rich waters are likely deep basinal brines that were heated and traveled to the surface through faults. [*Li et al.*, 1997; *Lowenstein and Risacher*, 2009]

Salar de Atacama, Chile. The Salar de Atacama is a closed salt pan basin in northern Chile, and is the third largest salt flat in the world (the second largest is the

Salinas Grandes in Argentina). Located in the Andes Mountains, the Salar de Atacama is surrounded by active andesite-dominated volcanoes produced by the subduction of the Nazca Plate under the South American Plate. While numerous meteoric and groundwater inflows to the Salar de Atacama are SO_4- or HCO_3-dominated, Ca-Cl-dominated seeps are found in the southern portion of the subaerial halite nucleus, just north of the Cordon Lila. These seeps are co-located with numerous N-S-trending reverse faults, and were likely heated by subsurface magmas, where they returned to the surface along faultlines. [*Risacher et al.*, 2003; *Lowenstein and Risacher*, 2009; *Ogawa et al.*, 2014]

Da Qaidam, China. The Qaidam Basin in Tibet is underlain by Precambrian basement, granites, and various sedimentary units. The hot springs of Da Qaidam are thought to be non-magmatic due to an absence of volcanic activity and seismicity typically associated with near-surface magma chambers. Da Qaidam's hot spring fluids thought to be sourced from deep-circulating water that is heated at depth and driven upward by pressure gradients. These fluids are allowed to reach the surface through crustal fracturing through steep faults. The spring fluids are subject to water-rock interactions at depth and rapidly ascend to the surface. [*Lowenstein and Risacher*, 2009; *Stober et al.*, 2016; *Fan and Wei*, 2017; *Guo et al.*, 2017]

3.4 Methods

Field Samples. Brine samples from the Salton Sea and in proximity to Bristol Dry Lake were collected during a field campaign to California, USA, in October 2016. Samples were collected with sterile pipettes and filtered using (large to small) 0.2, 0.8, and 1.2-μm sterile polyethersulfone (PES, Supor™) filters for all sites. Major ions samples were diluted with DI water upon collection to prevent precipitation, and stored in polypropylene snap-cap vials. Samples for trace metals analysis were diluted and acidified with 2% HNO_3 in the field. pH was measured in the field using an Oakton 150 pH Meter, and conductivity measured using an Orion Star A122 Conductivity Meter. Because the native brines were off-scale for the pH and conductivity meters, pH and conductivity measurements were made on diluted major ion samples. The values reported in Table 3.2 have been adjusted for this dilution.

Major ions (Na, K, Ca, Mg, SO_4, Cl) were measured using a DX600 (Dionex) Ion Chromatography (IC) system in the Group Exploring Organic Processes in Geochemistry (GEOPIG) laboratory at Arizona State University. Trace metals were measured using the Thermo X Series quadrupole inductively coupled mass spectrometry (ICP-MS) system in the W. M. Keck Foundation Laboratory at Arizona State University.

Published Sample Data. Major ion and trace metal concentrations for all other sites were obtained from previously published work. In most cases, major ion and trace metal concentrations for a single site came from different published works. Some studies did not measure the full suite of major ions (K^+ and Mg^{2+} were excluded in several studies); these exceptions are noted in the data analysis section and associated figures/tables. The sources and values for the data for each site are listed in Table 3.1. All

derived values and ratios are based on the concentrations of major ions and trace metals in Table 3.2.

Geochemical Modeling. The pH-REdox-EQuilibrium in C ("PHREEQC") geochemical modeling software suite published by the US Geological Survey (USGS) was used to calculate ionic strength and water activity for each brine sample [*Parkhurst and Appelo*, 1999, 2013]. Additionally, PHREEQC was used to model the Saturation Index (SI) of chloride minerals for each brine, allowing the precipitation sequence of chloride minerals to be determined. The SI is defined as the log of the ratio between the ion activity product and the equilibrium product for a specific compound (mineral), where high (positive) SI indicates saturation with respect to a mineral and low (negative) SI indicates under-saturation with respect to a mineral. All PHREEQC geochemical modeling in this study used the Pitzer equations due to the high ionic strength of the water samples [*Parkhurst and Appelo*, 2013].

Contextual geology. The interaction of brines and surface waters (i.e., meteoric or river waters) is heavily influenced by water-rock reactions. Therefore, the geologic context of each site was compared to assess the influence of water-rock reactions on the brine after its genesis (Figure 3.33). Geologic maps and previously published works were used to catalog the rock type(s) in each region. In some cases, geologic context was varied (i.e., a combination of disparate rock types) or not previously studied; sites with these constraints are noted as necessary. A total-alkali-silica (TAS) plot is used to assess the rock types in each region [*Le Bas et al.*, 1986]. TAS plots have been made for the Mars surface using remote sensing, rover-based, and meteorite sample analyses, allowing

direct first-order comparisons between the Mars surface and corresponding terrestrial analogs [*McSween et al.,* 2009].

Table 3.1. Localities, sample names, and references for brine major ion analyses included in this study. Localities are grouped according to the process that produced their respective brines.

Locality	Sample Name	Reference
Hydrothermal Continental Brines		
Yangbajing Field, Tibet	20-40 deg.	Bingqiu 1995
El Tatio, Chile	El Tatio, Well	Giggenbach 1978
	El Tatio, Spring	Ellis 1969
	El Tatio, Brine	Cusicanqui 1975
	El Tatio, Pool	Cortecci 2005
	El Tatio, Gey. (Geyser)	Cusicanqui 1975
Yellowstone Spring	Heart Lake	Lowenstern 2012
DaQaidam, China	DaQaidam	Stober 2016
Tengchong Springs, China	Rehai - Dgg	Hartnett (personal comm.)
Hydrothermal Oceanic Brines		
Icelandic Brines	Reykjanes, Svartsengi	Zaman 2013
Mid-Ocean Ridge: East Pacific Rise	E. Pacific Rise	Von Damm 1994
Mid Ocean Ridge: Loki's Castle	Camel 2010 (Loki)	Baumberger 2016
Endorheic Temperate Basins		
Salton Sea, CA	Salton Sea	This Work
Dead Sea, Israel	DS (0m, 200m, 400m)	Ganor & Katz 1989
Salar de Uyuni, Bolivia	SdU	Retting, Jones & Risacher 1980
Seawater	SW	Witherow & Lyons 2011
Endorheic Cold Basins, Cold Springs		
McMurdo Dry Valleys, Antarctica:		Witherow & Lyons 2011
Lake Hoare	LH (4, 14, 30m)	"
Lake Fryxell	LF (6, 12, 18m)	"
Lake Bonney	E. LB (6m), W. LB (5m)	"
Lake Vanda	LV (10, 70 m)	"
Don Juan Pond	DJP	"
Lost Hammer Spring, Canada	Wolf, Pore Water	Battler 2013
Deep Basinal Brines		
Bristol Dry Lake, CA	BDL 3, 8	This Work
	BDL 1, 2, 13, 14	Rosen 1991
	BDL In (219m, 359m, 450m)	Dolginko 2014 (Inclusions)
Badwater Basin, Death Valley, CA	DV40	Li 1997
Salar de Atacama, Chile	CaCl Brines (A,C)	Lowenstein and Risacher 2012

Locality	Sample Name	T (°C)	Density	A, H_2O	IS	pH	Ca++	Mg++	K+	Na+	SO4--	Cl-
Bristol Dry Lake	BDL 3	22.1	1.244	*0.688*	*9.31E+00*	6.45	1.72E+00	7.16E-02	2.54E-01	2.53E+00	3.97E-03	6.37E+00
	BDL 8	28.4	1.323	*0.582*	*1.29E+01*	6.12	3.30E+00	1.55E-01	3.05E-01	6.17E-01	8.55E-04	7.88E+00
	BDL 1						8.58E-01	6.91E-02	3.80E-02	2.00E+00	1.47E-02	2.95E+00
	BDL 2						2.16E+00	1.24E-01	8.50E-02	2.50E+00	2.93E-03	4.88E+00
	BDL 13	*25*	1.2805	*0.616*	*9.98E+00*	*7.00*	7.49E-01	1.40E-01	9.70E-02	3.74E+00	3.33E-04	5.92E+00
	BDL 14						2.59E+00	2.67E-01	5.90E-02	2.83E+00	6.67E-04	5.92E+00
	BDL In (219m)						2.84E+00	3.88E-01	*1.00E-04*	2.50E+00	1.37E-01	8.34E+00
	BDL In (359m)						4.11E+00	1.08E-01	*1.00E-04*	1.58E+00	*1.00E-04*	9.96E+00
	BDL In (450m)						4.02E+00	2.80E-01	*1.00E-04*	1.64E+00	*1.00E-04*	1.00E+01
Death Valley	DV40	*25*	1.14621	*0.843*	*4.34E+00*	*7.00*	2.06E-02	1.00E-02	2.58E-02	3.32E+00	4.27E-02	3.30E+00
Salar de Atacama	CaCl Brines (A,C)	*25*	*1.2982*	*0.6180*	*1.04E+01*	7.28	3.42E-01	8.16E-01	6.16E-01	2.59E+00	5.05E-03	6.05E+00
Salton Sea	Salton Sea	22.1	1.029	*0.982*	*8.72E-01*	7.46	2.34E-02	8.26E-02	8.25E-03	7.24E-01	1.49E-01	6.73E-01
Dead Sea	DS (0m)	28.8	1.285	*0.596*	*1.20E+01*		6.38E-01	2.70E+00	2.81E-01	6.20E-01	2.61E-03	7.40E+00
	DS (200m)	30.1	1.287				6.54E-01	2.77E+00	3.00E-01	5.02E-01	1.39E-03	7.65E+00
	DS (400m)	34.0	1.29				6.61E-01	2.87E+00	3.11E-01	4.32E-01	9.77E-04	7.76E+00
Salar de Uyuni	Salar de Uyuni	*25*	1.23159	*0.704*	*7.76E+00*	7.25	1.40E-02	3.24E-01	2.23E-01	4.60E+00	1.07E-01	5.37E+00
Seawater	SW	*20*	1.026	*0.983*	*6.70E-01*	8.14	1.05E-02	5.41E-02	1.05E-02	4.81E-01	2.89E-02	5.59E-01
Lake Hoare	LH (4m)					9.05	3.24E-04	1.50E-04	9.21E-05	8.83E-04	1.41E-04	9.51E-04
	LH (14m)					7.85	1.45E-03	1.03E-03	5.83E-04	5.96E-03	9.40E-04	4.96E-03
	LH (30m)		0.987			7.28	1.80E-03	1.25E-03	7.01E-04	7.18E-03	1.08E-03	5.81E-03
Lake Fryxell	LF (6m)					7.95	1.47E-03	1.43E-03	7.52E-04	1.29E-02	6.46E-04	1.17E-02
	LF (12m)					7.53	2.50E-03	6.50E-03	2.66E-03	5.79E-02	1.58E-03	5.22E-02
	LF (18m)					7.46	3.24E-03	1.31E-02	4.76E-03	1.17E-01	1.09E-03	1.04E-01
Lake Bonney	E. LB (6m)					8.71	1.80E-03	2.11E-03	3.35E-04	1.54E-02	1.64E-03	1.92E-02
	W. LB (5m)					8.75	1.47E-03	1.60E-03	2.37E-04	1.24E-02	1.29E-03	1.55E-02
Lake Vanda	LV (10m)					8.35	2.02E-03	8.02E-04	3.12E-04	2.29E-03	1.76E-04	7.08E-03
	LV (70m)	*0*	1.08315	*0.946*	*2.79E+00*	5.91	5.24E-01	2.66E-01	1.15E-02	2.17E-01	5.47E-03	1.66E+00

Table 3.2a. Sample data. Density is in g/cm^3. Ionic strength (IS) is in mol/L. Major ion concentrations are in mol/L and derived from references in Table 1. Values in italics were modeled using PHREEQC geochemical modeling software.

Locality	Sample Name	T (°C)	Density	A, H_2O	IS	pH	Ca++	Mg++	K+	Na+	SO4--	Cl-
Don Juan Pond	DJP	*0*	1.28676	*0.623*	*1.16E+01*	6.15	3.49E+00	8.23E-02	3.84E-03	5.31E-01	1.48E-03	7.98E+00
Lost Hammer Spr.	Wolf, Pore Water	-5.3	1.16266	*0.84*	*4.61E+00*	6.67	4.24E-02			2.91E+00	5.41E-02	3.95E+00
Yangbajing Field	20-40 deg	30	1.01461			6.86	3.34E-04	4.40E-05	9.48E-04	1.27E-02	2.08E-04	4.20E-03
El Tatio	El Tatio, Well					6.72	4.88E-03		7.85E-03	1.44E-01	4.23E-04	1.62E-01
	El Tatio, Spring					6.95	4.48E-03		6.26E-03	1.14E-01	4.79E-04	1.30E-01
	El Tatio, Brine	*25*	1.212	*0.738*	*6.66E+00*	2.00	1.56E-01		1.20E-01	4.65E+00	0.00E+00	5.22E+00
	El Tatio, Pool					6.63	5.95E-03	3.65E-05	1.18E-02	1.81E-01	4.65E-04	2.07E-01
	El Tatio, Gey					7.14	5.01E-03	7.58E-05	8.69E-03	1.45E-01	6.94E-04	1.65E-01
Yellowstone	Heart Lake			*0.999*	*1.85E-02*	9.71	2.37E-05	2.06E-07	7.49E-04	1.86E-02	1.87E-03	9.87E-03
DaQaidam, China	DaQaidam	*25*	0.99763	*1*	*1.53E-02*	7.91	7.46E-04	8.39E-06	3.35E-04	1.37E-02	1.91E-03	9.02E-03
Tengchong Springs	Rehai - Dgg						0.00E+00	4.11E-06	3.94E-03	3.75E-02	1.37E-04	2.33E-02
Icelandic Brines	Reykjanes	22	*1.02131*	*0.985*	*6.18E-01*	7.76	1.31E-02	3.55E-02	1.18E-02	3.76E-01	4.27E-02	4.46E-01
	Svartsengi	22.3	*1.01461*	*0.993*	*2.71E-01*	6.75	1.54E-02	9.46E-06	1.48E-02	1.71E-01	1.86E-02	2.12E-01
Mid-Ocean Ridge	E. Pacific Rise	351	*1.9999*	*0.985*	*8.38E-01*	2.60	0.00E+00		4.15E-02	6.83E-01		8.46E-01
Loki's Castle	Camel 2010 (Loki)	305	*1.9999*	*0.985*	*1.83E+00*	5.62	5.89E-01	1.94E-02	3.21E-02	3.95E-01	3.00E-04	5.89E-01

Table 3.2b. Sample data, continued. Density is in g/cm^3. Ionic strength (IS) is in mol/L. Major ion concentrations are in mol/L and derived from references in Table 1. Values in italics were modeled using PHREEQC geochemical modeling software.

Locality	Unit	SiO_2	TiO_2	Al_2O_3	FeO+ Fe_2O_3	MnO	MgO	CaO	Na_2O	K_2O	P_2O_5	Reference
BDL: Bristol/Calmumet Mtns	Gran./Granod.	*65.30*		*16.10*	*4.40*		*1.70*	*3.90*	*3.80*	*2.70*		1, 2
BDL: Amboy Crater	Basalt (MD99-5AC)	49.81	2.46	16.01	11.63	0.17	5.53	8.99	3.76	1.60	0.54	1, 2, 3
Badwater Basin, CA	Diorite, Gab., Bas.	*48.60*		*16.80*	*10.80*		*5.10*	*8.90*	*3.70*	*1.90*		4
Salar de Atacama	Andesite	57.83	1.01	16.73	6.75	0.12	4.27	7.02	3.62	0.00	1.48	1,
Salton Sea - Basalt	Basalt (W832-J)	53.66	2.19	14.54	10.83	0.06	6.10	6.09	4.37	3.12	0.06	6
Salton Sea - Rhyolite	Rhyolite (W772)	73.68	0.21	13.14	2.43	0.05	0.22	0.90	4.60	4.10	0.02	6
Dead Sea	Qtz Sands., Carb.	*80.00*					*5.00*	*15.00*				7
Salar de Uyuni	Andesite	57.83	1.01	16.73	6.75	0.12	4.27	7.02	3.62	0.00	1.48	8
Yangbajing Field	Granite	*71.50*		*14.00*	*2.90*		*0.60*	*1.60*	*3.40*	*4.30*		9
El Tatio	Andesite, Dacite	*58.20*		*17.00*	*6.90*		*3.50*	*6.30*	*3.50*	*2.10*		10
Yellowstone Fissure Spring	Rhyolite - DCV14	77.06	0.16	12.04	1.49	0.04	0.05	0.48	3.43	5.37	0.01	11, 12
DaQaidam, China	Sandstones											1, 13,
Iceland	Basalt, Reykjanes	48.29	3.59	14.66	12.71	0.28	4.39	8.87	3.80	1.55	0.93	14, 15
Mid-Ocean Ridge	Basalt, Ultramafics	50.47	1.68	14.70	10.43	0.18	7.58	11.39	2.79	0.16	0.18	16, 17, 18

Table 3.3. Total Alkali Silica contents for major units at select localities in wt. %. References: [1] USGS Geologic Map, [2] Lowenstein and Risacher (2009), [3] Philips (2003), [4] Machette, M., et al. (1999), [5] Deruelle (1982), [6] Robinson et al. (1976), [7] The Niemi et al. 1997, [8] Risacher (2003), [9] Bingqiu (1995), [10] Cortecci et al. (2005), [11] Lowenstern (2012), [12] Vasquez et al. (2001), [13] Lai et al. (2017), [14] Uz-Saman (2013), [15] Heier (1966), [16] Baumberger et al. (2016), [17] Kelley et al. (2002), [18] Gale et al. (2013)

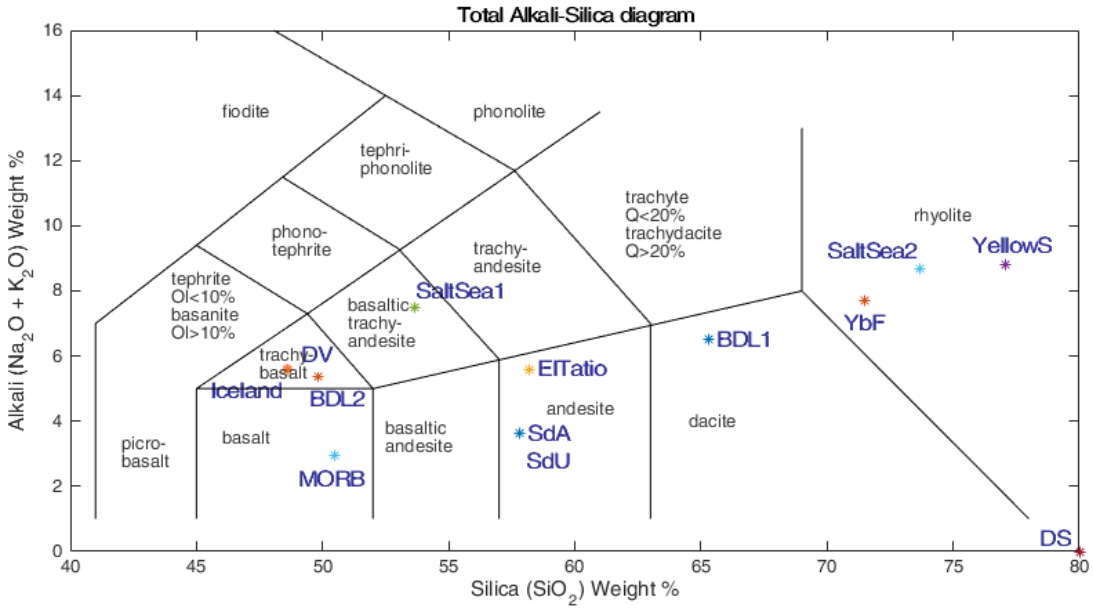

Figure 3.3. Total Alkali Silica (TAS) plot comparing the geologic context of study sites. For comparison, the majority of the martian surface falls into the basalt/basaltic-andesite range [*McSween*, 2009]. For those sites that are listed twice, there are two geologic units of significantly varying composition. DV = Death Valley, BDL = Bristol Dry Lake, MORB = Mid-Ocean Ridge Basalt, SaltSea = Salton Sea, SdA = Salar de Atacama, SdU = Salar de Uyuni, YellowS = Yellowstone, YbF = Yangbajing Field.

3.5 Data/Results

This section describes the pH, major ion, trace metal, and modeling results for each brine of study and each general process type. In some cases, the majority of the brines for a specific process group together with a small number of outliers. Only data and observations are described here; interpretations of the various processes and causes of outlying values are addressed in the Discussion section.

3.5.1 pH

The geochemical and compositional data for all sites are shown in Table 2. The pH for each type of site fell into distinct pH ranges, with a few exceptions. Deep basinal brines had pH values of 7.0 ± 0.5. Temperate endorheic basins had pH values of 7.25±0.25; cold endorheic basins had pH values of 8.10±0.6 for the Antarctic lakes, and 6.24±0.32 for Don Juan Pond, Lost Hammer Spring, and the 70-m highly saline Lake Vanda sample. Hydrothermal continental brines ranged from 6.73±1.91, with two brines as extreme outliers: El Tatio pH =2.0, and Yellowstone Heart Lake pH = 9.71. Hydrothermal oceanic brine pH was 5.68±1.93, though the East Pacific Rise was an outlier with pH = 2.60.

3.5.2 Major ions

Molar concentrations for major ions are shown in Table 2. To demonstrate that all the brines in this study are Cl-dominated, a ternary diagram is shown with Ca and SO_4; all brines plot at the 50% molar concentration or greater for chloride (Fig. 3.4). Major

cations (Na^+, K^+, Ca^{2+}, Mg^{2+}) were first assessed relative to chloride to look for general patterns associated with each brine type (Figure 3.5).

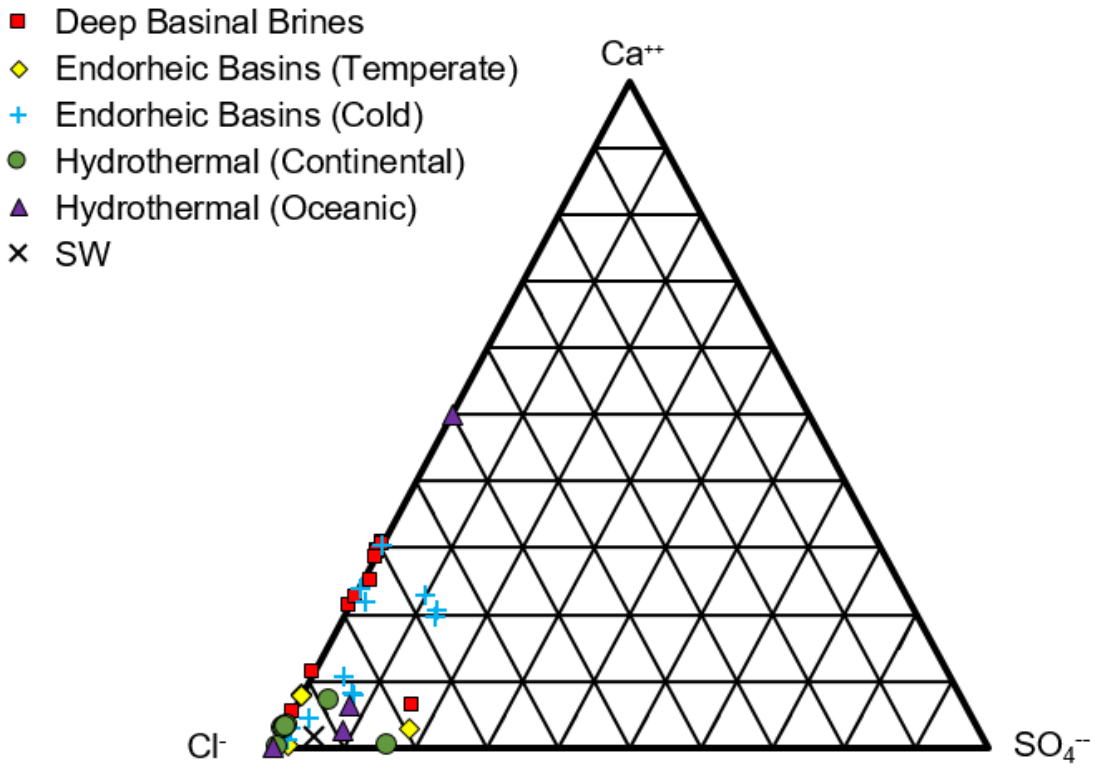

Figure 3.4. Ternary Ca-Cl-SO_4 diagram showing the dominant anion (Cl-) for each brine included in this study.

Na^+. Na^+ as a function of Cl^- is shown in Figure 3.5, bottom left. Hydrothermal continental brines (shown as "x" in Figure 3.5) had low Na^+ concentration (<1 M Na); it also follows a 1:1 Na:Cl trend, suggesting equilibration with halite. Don Juan Pond, Dead Sea, and BDL-8 (Bristol Dry Lake) all had high Cl- (>1 M) with relatively low Na; likely due to some other cation (Ca, Mg) balancing charge instead of Na. BDL-8 is likely an

evaporatively concentrated version of the other BDL data points. El Tatio also lies near the 1:1 Na:Cl line, but has much higher Cl- than the other hydrothermal fluids. The El Tatio brine is likely representative of a concentrated hydrothermal fluid – but not concentrated enough for NaCl to precipitate out of solution. Death Valley may also represent an evaporatively concentrated brine that is in balance with halite, since it too is on the Na:Cl line.

Ca^{2+}. Ca^{2+} as a function of chloride is shown in Figure 3.5 (top left). Deep Basinal Brines show an increase in Ca^{2+} relative to Cl^-, along with Don Juan Pond and Lake Vanda (70 m). El Tatio has higher Ca^{2+} than any other hydrothermal brine. Dead Sea brines have very high Cl^- (7.7+ M) but also fall well below the [Ca]=[Cl] line. All other sites have almost no Ca^{2+} and <1 M Cl^-.

Mg^{2+}. All brines plot well below the $[Mg^{2+}]=[Cl^-]$ line in Figure 3.5 (top right). Most brines were at or less than <0.5M Mg^{2+}, except for the Dead Sea, which was 2.7M Mg^{2+}. The Salar de Atacama deep basinal brine had the second highest Mg^{2+} after the Dead Sea (0.82 M).

K^+. There are no clear trends in terms of brine type, but all sites lie well below the 1:1 K:Cl line. The Salar de Atacama deep basinal brine has by far the highest K^+ concentration (Figure 3.5, bottom right), which suggests the possible influence of contextual geology. Evaporatively concentrated brines, including deep basinal brines at Bristol Dry Lake, along with the Dead Sea and Salar de Uyuni, have high K^+ as well; all of these sites are known to have significant NaCl precipitation, so the removal of Na^+ from the brine likely facilitates an increase in K^+ concentration. K^+ is highest for all brine

types at around 6.0M Cl^-, but then drops to very low concentrations at >8.0M Cl^- – possibly due to saturation with respect to sylvite.

Na/K vs. Cl-. A linear increase in Na/K with respect to Cl^- is observed for cold basins, hydrothermal systems, and some deep basinal brines. At Cl^- ~3.3M, the Na/K drops precipitously. The Dead Sea (400m) had the lowest Na/K (0.74) at a Cl concentration of 7.76M (Figure 3.6). Halite precipitation causes Cl^- to be concentrated regardless of the type of brine, until eventually it reaches saturation and comes out of solution. When it precipitates, Na^+ is removed from the brine, and Na/K decreases. Don Juan Pond has an unusually high Na/K but that is because its K^+ is so low compared to other localities. This has been explored in recent investigations into Don Juan Pond's unique chemistry [*Toner et al.*, 2017].

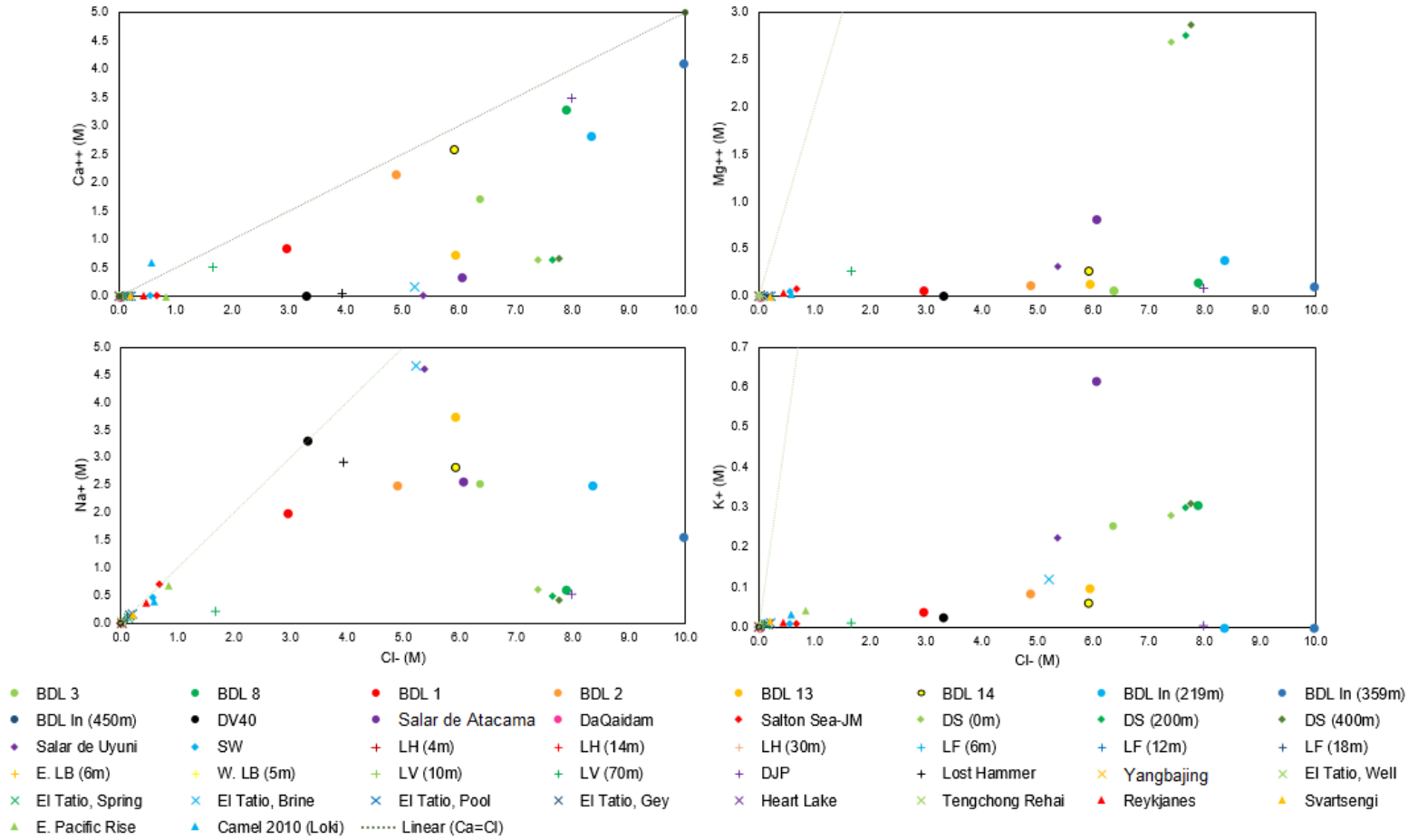

Figure 3.5. Major cations as a function of Cl concentration. Top left: Ca; top right: Na; bottom left: Mg; bottom right: K. Symbols for each brine type are the same shape: X=hydrothermal continental brines, Δ=hydrothermal oceanic brines, ◊=desert endorheic basins, +=cold endorheic basins, ○=deep basinal brines. Lines are 1:1 mole for reference.

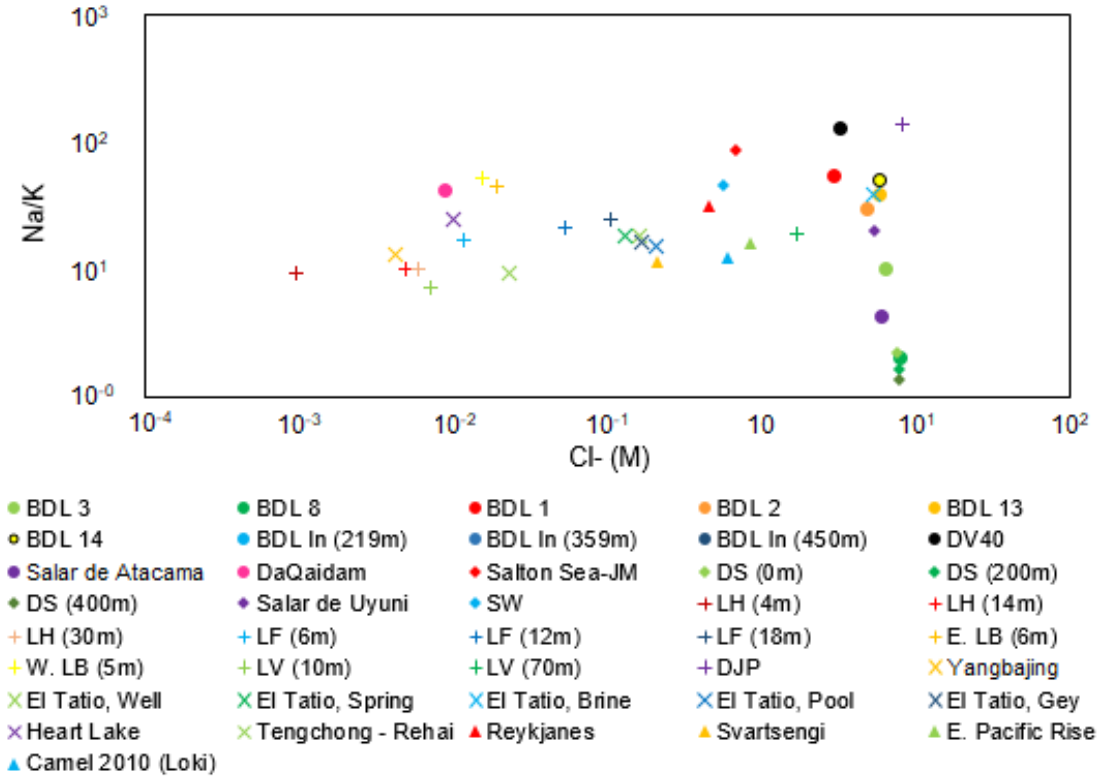

Figure 3.6. Na/K versus Cl (M) for all brines.

Na/K vs. Ca/Mg. No consistent trends can be observed across brine types (Figure 3.7). However, within specific brine types some trends can be observed. Continental hydrothermal fluids show increasing Na/K with increasing Ca/Mg, while hydrothermal oceanic fluids have a relatively constant Na/K ratio, but have a wide range of Ca/Mg values. Temperate endorheic basins generally fall into a similar Ca/Mg ratio with seawater (with varying Na/K), except for Salar de Uyuni, which has a lower Ca/Mg than any other brine in this study. Cold endorheic basins generally show decreasing Na/K with increasing Ca/Mg, with the exception of Don Juan Pond, which has both high Na/K and

high Ca/Mg. Deep basinal brines show a range of Ca/Mg and Na/K values, with no discernable trends.

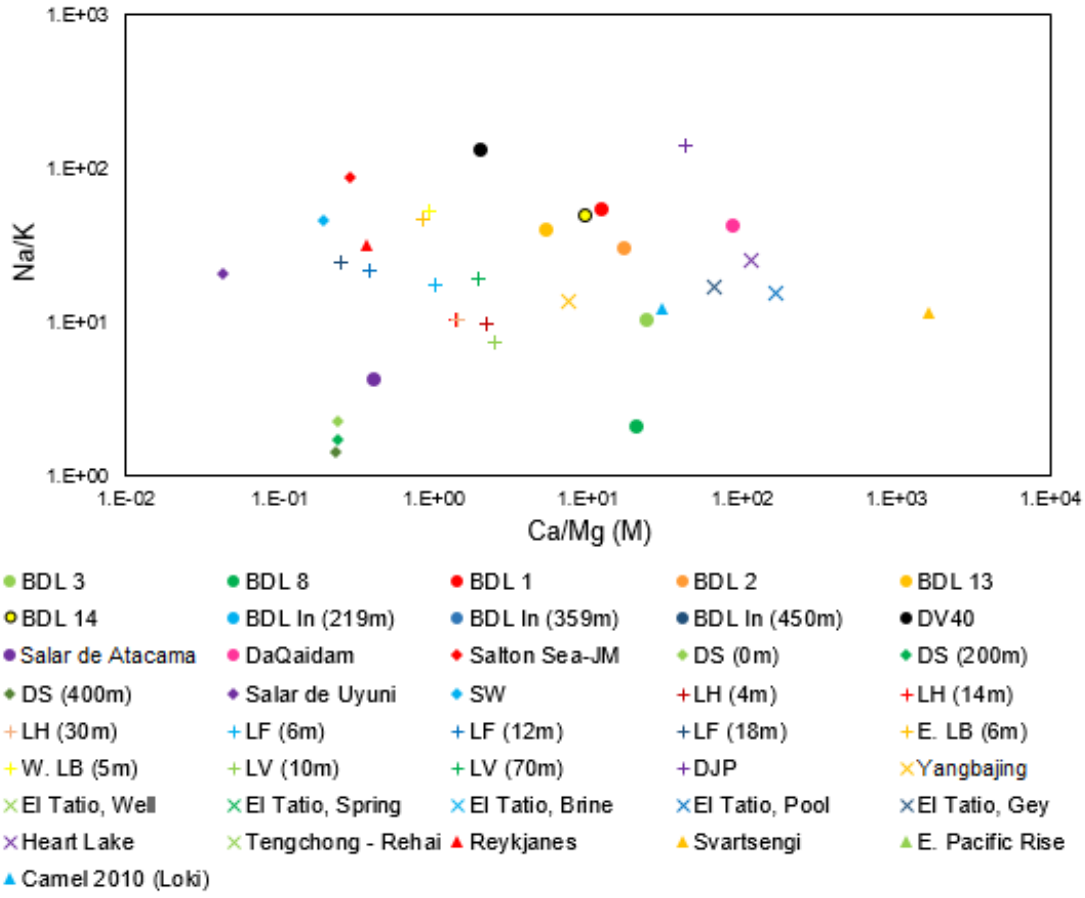

Figure 3.7. Na/K versus Ca/Mg for all brines; all ratios are molar.

Ca/Mg vs. Na/Cl. Hydrothermal continental fluids (X) show little variation in Ca/Mg with an increase in Na/Cl (Figure 3.8, top left). Hydrothermal oceanic brines (Δ) have constant Na/Cl and varying Ca/Mg. Deep basinal brines (O) behave similarly to hydrothermal continental fluids, with Ca/Mg proportional to Na/Cl, but with much lower values of both. Temperate endorheic basins (◊) have constant Ca/Mg with varying Na/Cl, and cold endorheic basins (+) behave similarly to hydrothermal fluids and overlap significantly with deep basinal brines; they have high Ca/Mg with high Na/Cl and low Ca/Mg-low Na/Cl trends.

Ca/Cl vs. Na/Cl. Almost all brines fall into a wedge-shaped cluster, with high-ionic strength brines having low Na/Cl and high Ca/Cl (0.1-1), and other brines having decreasing Ca/Cl with increasing Na/Cl or constant Ca/Cl with increasing Ca/Cl (Figure 3.8, top right). Outliers are, again, hydrothermal continental brines, which have generally increasing Ca/Cl with increasing Na/Cl, but their ionic strengths are very low.

Mg/Cl vs. Na/Cl. Almost all brines fall into a cluster at low Na/Cl and Mg/Cl = 0.01-1 (Figure 3.8, bottom right). The lowest Na/Cl brines were the highest ionic strength. Brines outside of this cluster are distributed radially away from it, with all of them but Death Valley being hydrothermal brines. Most are continental hydrothermal brines, though Svartsengi is also in proximity to Death Valley and El Tatio pool/geyser brines.

K/Cl vs. Na/Cl. All processes behave along a large-scale trend (Figure 3.8, bottom left). KCl increases steeply at Na/Cl~0.3, until K/Cl reaches ~0.1, at which point K/Cl increases shallowly with increasing Na/Cl. The highest Na/Cl and K/Cl values are for the hydrothermal continental brines.

$CaCl_2$ vs NaCl saturation. Dissolved minerals are calculated by determining the product of the molar concentrations of their ions raised to the power (exponent) of their stoichiometric ratios. All brines follow a linear trend until they approach the saturation limits of $CaCl_2$ and NaCl, at which point they form a cluster (Figure 3.9, top). A few brines are in excess of the saturation limits for those minerals. This trend is the same as that seen by a recent study of Ca-Cl brines in Germany – it turns out the trends holds for Na-Cl brines too [*Moller et al.*, 2017]. The slope of the line in my plot was 0.175, and the slope for the German Ca-Cl brine was 0.18; they are essentially identical.

$MgCl_2$ vs. KCl saturation. Linear increase in both for all brines, except for the BDL inclusions which have a high $MgCl_2$ concentration, likely due to the precipitation of sylvite in the inclusion (Figure 3.9, bottom). The slope of the line is 7.99.

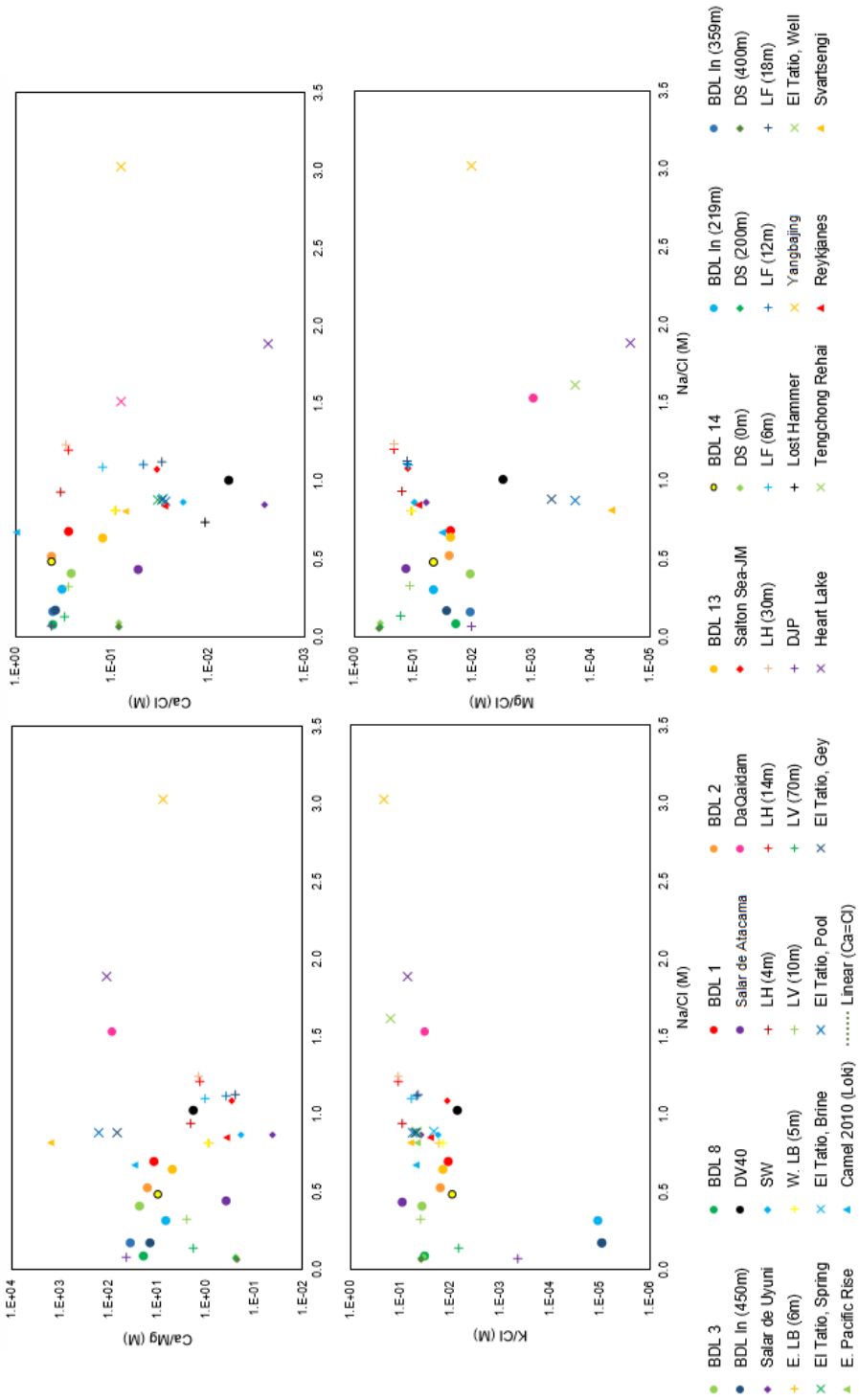

Figure 3.8. Molar ratios relative to Na/Cl. Top left: Ca/Mg; top right: Ca/Cl; bottom left: K/Cl; bottom right: Mg/Cl.

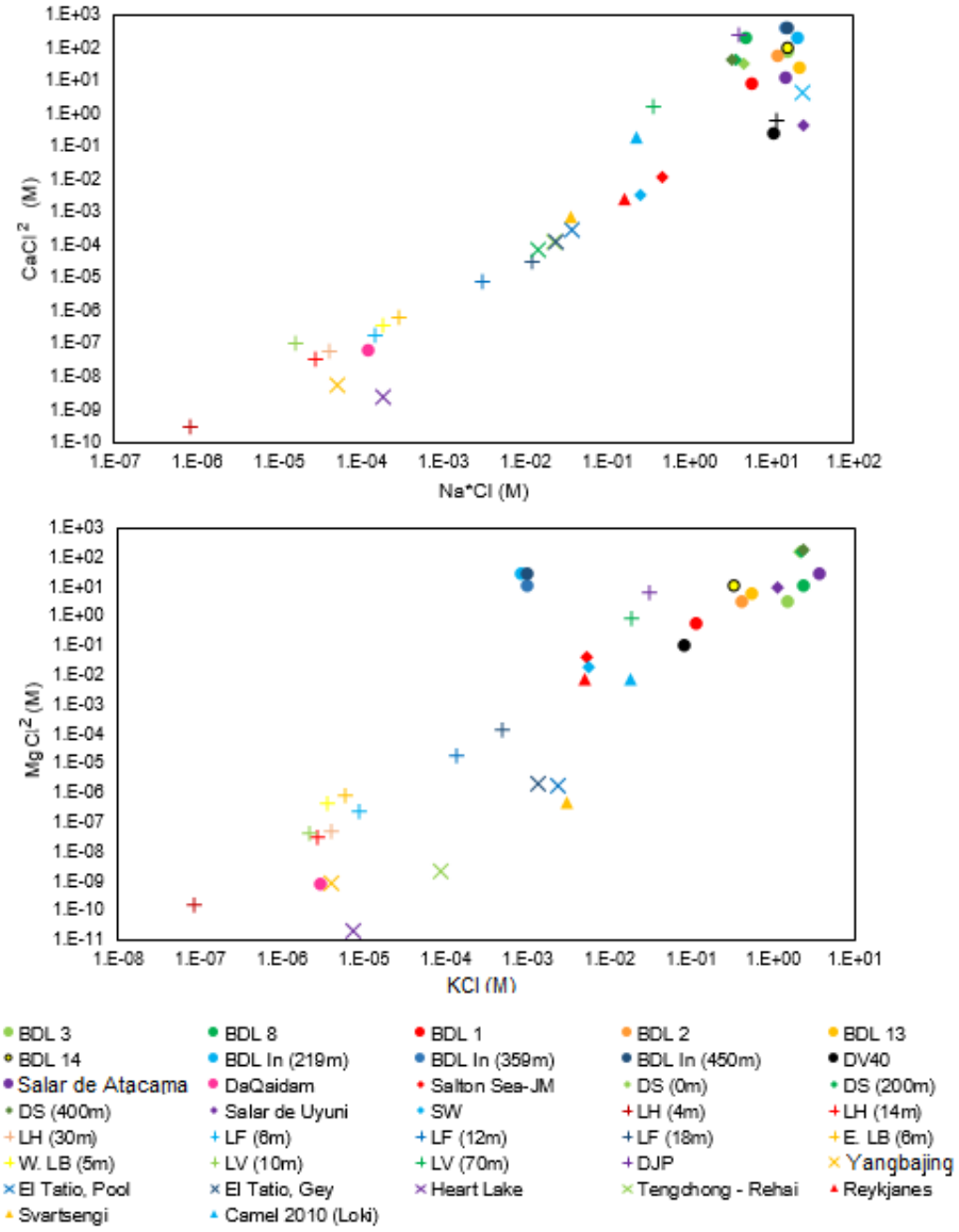

Figure 3.9. Dissolved chloride minerals in each brine type. Left: Calcium chloride (CaCl2) versus halite (NaCl). Right: Magnesium chloride (MgCl2) versus sylvite (KCl).

Ca-Cl-SO_4. All brines in this study are Cl- dominated (see Figure 3.4). Hydrothermal continental fluids tend to be the least Cl-dominated and have a $CaSO_4$ component.

Cl-Ca-Na. Endorheic temperate brines were deficient in Ca relative to other brine types; they clusters as either highly Cl-rich (90%) or intermediate Na and Cl (Figure 3.10). Endorheic cold brines had extremely low Cl^- relative to cations: 10 ± 10% Cl^-. Continental hydrothermal brines were consistently 60 ± 10% Na, while oceanic hydrothermal brines were very close to seawater in composition, with one exception. Several distinct clusters based on brine-producing process were observed. Deep basinal brines were consistently 60±10% Cl^-, with cations distributed between equivalent ratios of Ca^{2+} and Na^+.

Ca-Mg-(Na+K). Endorheic temperate basins are consistently Ca-poor, likely due to evaporative concentration/precipitation and Ca removal by gypsum (Figure 3.11). Endorheic cold basins also become Ca-rich, likely due to freeze concentration. Continental hydrothermal brines are consistently Mg-poor and Ca-poor, but Na+K rich; this is consistent with water-rock interactions with highly evolved materials in the continental crust. Oceanic hydrothermal brines are similar to continental hydrothermal brines, but with one exception (Camel Vent, Loki's Castle). Deep basinal brines have consistently very low Mg, which is consistent with water-rock interactions at depth (dolomitization and serpentinization processes).

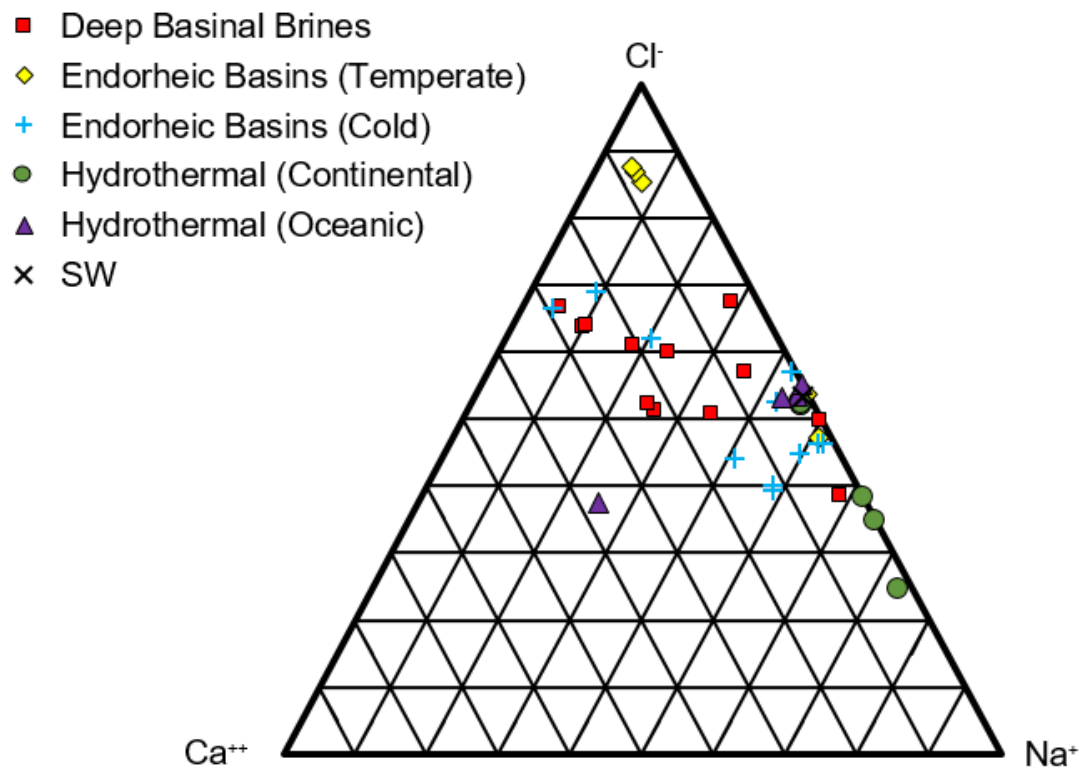

Figure 3.10. Ternary diagram of Cl-Ca-Na for all brines, classified by process/brine type. Units are mole percent.

Ca-Mg-K. All endorheic basins (temperate and cold) are relatively K-poor, likely due to precipitation of monovalent chloride minerals, ion exchange processes, and the possible recirculation of subsurface brines after upwelling (Figure 3.12) [*Toner et al.*, 2017]. Hydrothermal continental brines are all Mg-poor, consistent with water-rock interactions. Hydrothermal oceanic brines are generally Mg-poor, with one exception (Reykjanes). These brines could have a seawater component causing enhanced Mg relative to hydrothermal continental brines. Deep basinal brines are very Ca-rich, due to water-rock interactions at depth, and Mg/K-poor for the same reason.

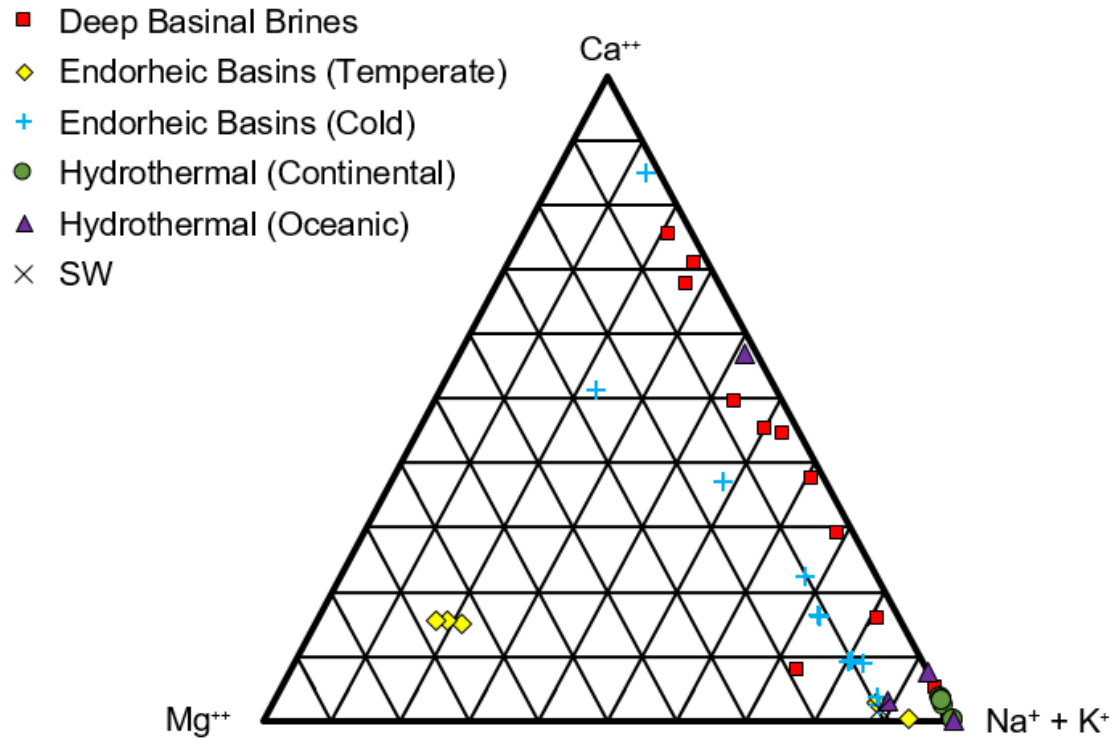

Figure 3.11. Ternary diagram of Ca-Mg-Na+K for all brines, classified by process/brine type. Units are mole percent.

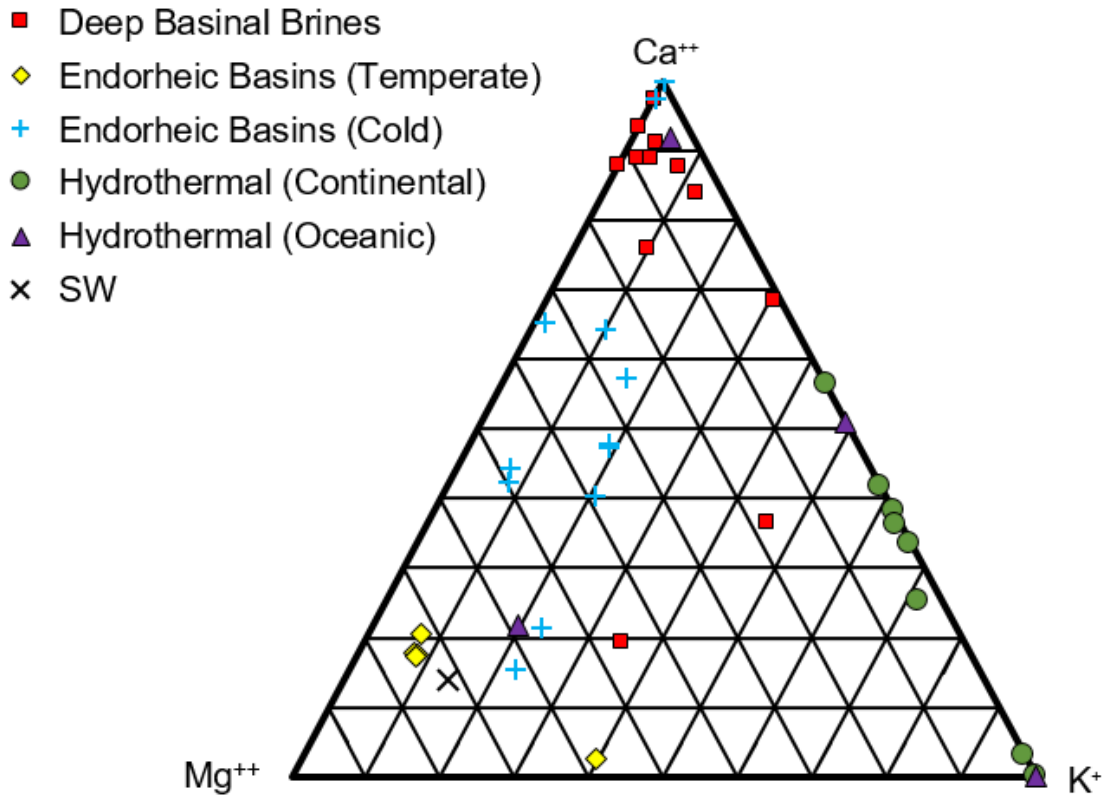

Figure 3.12. Ternary diagram of Ca-Mg-K for all brines, classified by process/brine type. Units are mole percent.

3.5.3 Geochemical Modeling with PHREEQC

Major Ions vs. Ionic Strength. The ionic strength of each brine was determined using the geochemical modeling software PHREEQC. Precipitation sequences can begin to be resolved when assessing trends in major ion concentration as a function of ionic strength. Dissolved Na decreases when halite precipitation begins, and peaks at ~7 M ionic strength (Figure 3.13). Dissolved Ca has a local decrease at the same ionic strength, while K and Mg continue to increase with increasing ionic strength. Cl also increases with ionic strength, approaching an asymptote at ~10M Cl.

Water Activities. Endorheic temperate basins have an average water activity of 0.76 ± 0.16. Endorheic cold basins have an average water activity of 0.80 ± 0.13, which includes Don Juan Pond, Lost Hammer, and Lake Vanda (70m). Hydrothermal continental brines have a large range of water activities: 0.74 (El Tatio brine) to ~1 (Heart Lake, Yellowstone). Hydrothermal oceanic brines have an average water activity of 0.987 ± 0.01. Deep basinal brines have an average water activity of 0.67 ± 0.09.

Saturation indices. PHREEQC geochemical modeling software, incorporating the Pitzer database, was used to determine the precipitation sequence of chloride minerals for brines representative of each type (Figure 3.14). Minerals included in the modeling were gypsum ($CaSO_4 \cdot 2H_2O$), halite (NaCl), sylvite (KCl), antarcticite ($CaCl_2 \cdot 6H_2O$), bischofite ($MgCl_2 \cdot 6H_2O$), and carnallite ($KMgCl_3 \cdot 6H_2O$); gypsum, a sulfate, was used to link the sequence of chloride precipitation to other common mineral species with lower solubilities. The precipitation sequence is determined by the relative saturation indices for a single brine. A saturation index of zero indicates that a mineral is in equilibrium with a solution, positive saturation indices indicate saturation of a mineral, and negative

saturation indices indicate that the mineral is not saturated and remains dissolved. While specific saturation index values were calculated for each mineral, the values themselves are dependent on the degree to which the brine is concentrated; therefore, only the sequence of mineral precipitation is considered here. The precipitation sequence begins with the minerals closest to (or in excess of) saturation, followed by minerals with lower saturation indices. The "last" mineral to precipitate out of solution is the mineral with the lowest (most negative) saturation index.

Gypsum, in most cases, is at or close to saturation, followed by halite. Some brines are saturated with respect to gypsum/gypsum + halite, resulting in positive saturation indices for those minerals. However, the Salar de Uyuni was saturated with halite to a greater degree than gypsum, and was the only brine to show that behavior.

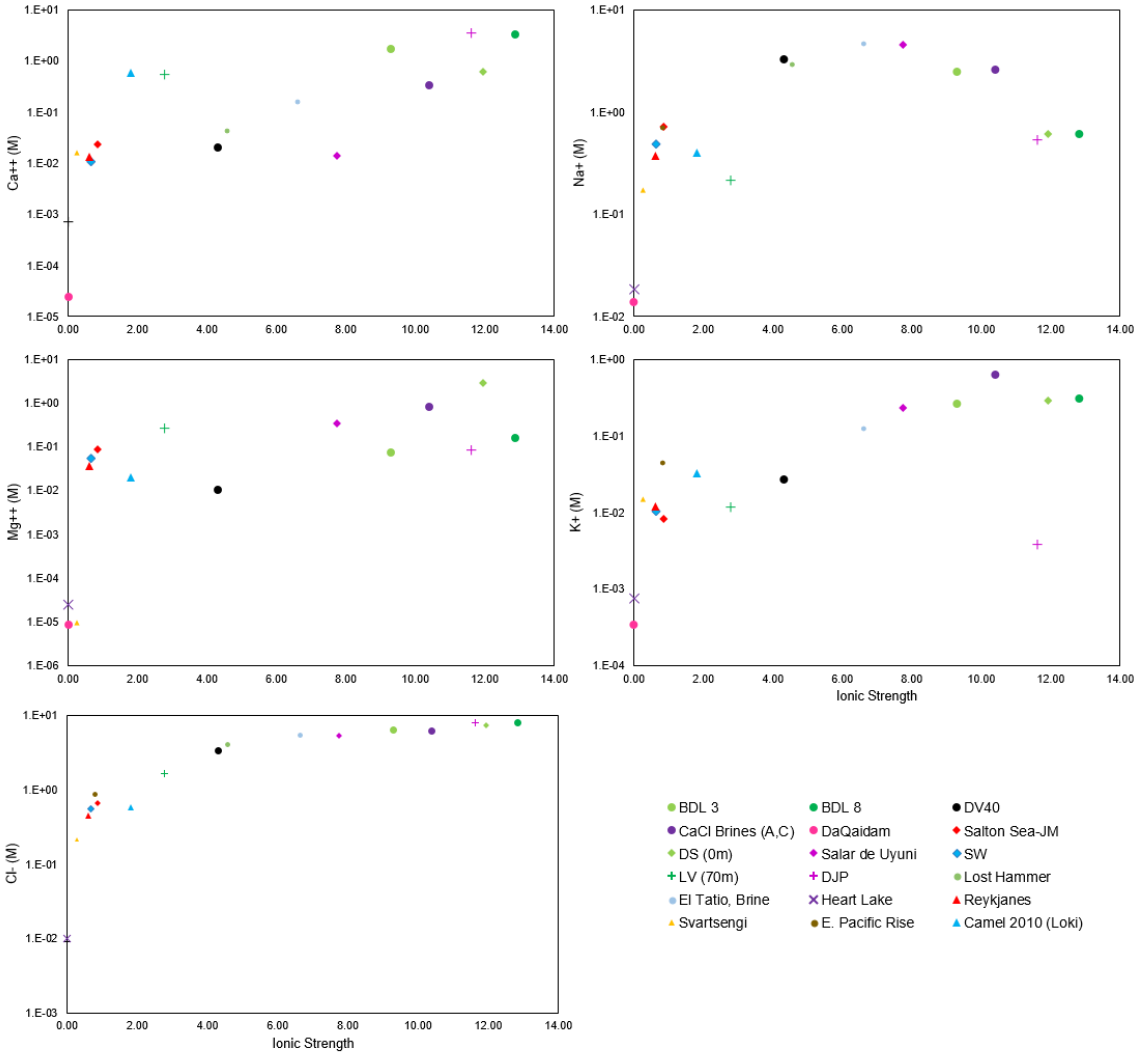

Figure 3.13. Major ion concentrations versus ionic strength for a subset of each brine type. Ionic strengths were calculated using the PHREEQC geochemical modeling software. All values are in mol/L.

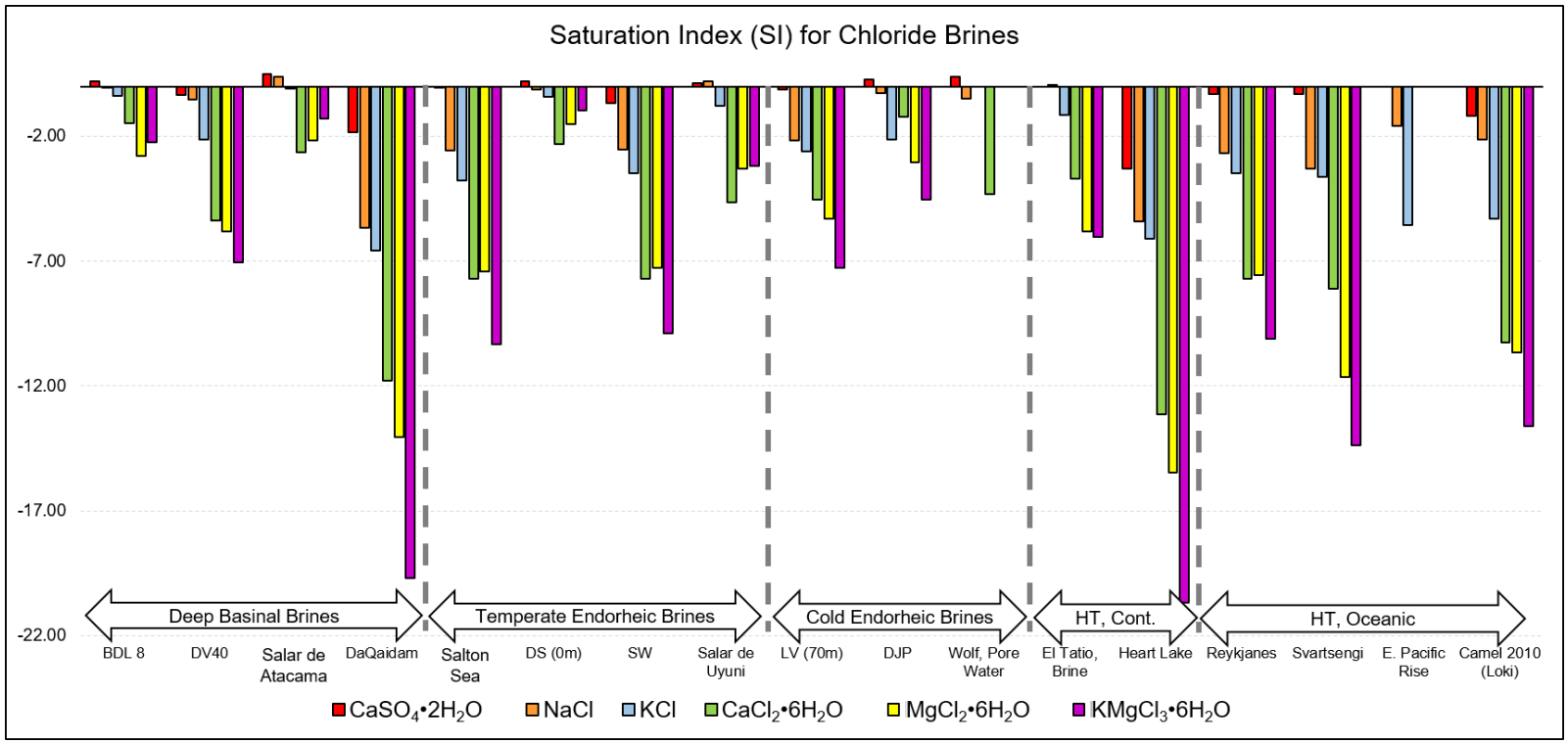

Figure 3.14. Saturation indices for a suite of minerals: gypsum ($CaSO_4 \cdot 2H_2O$), halite (NaCl), sylvite (KCl), antarcticite ($CaCl_2 \cdot 6H_2O$), bischofite ($MgCl_2 \cdot 6H_2O$), and carnallite ($KMgCl_3 \cdot 6H_2O$). Saturation indices were calculated using PHREEQC geochemical modeling software. The precipitation sequence is the order of solubility of minerals from highest to lowest saturation index. (HT = hydrothermal)

The most common precipitation sequence was as follows:

$Ca(SO_4)•2(H_2O) \rightarrow NaCl \rightarrow KCl \rightarrow CaCl_2•6(H_2O) \rightarrow MgCl_2•6(H_2O) \rightarrow KMgCl_3•6(H_2O)$

Gypsum → Halite → Sylvite → Antarcticite → Bischofite → Carnallite

This sequence was followed by Death Valley, Da Qaidam, Lake Vanda (70 m), and all of the hydrothermal brines (both continental and oceanic). The deep basinal brines at Bristol Dry Lake showed a similar sequence, but Bischofite precipitated after Carnallite. The deep basinal brine at the Salar de Atacama, along with the Dead Sea and Salar de Uyuni, showed the following precipitation sequence:

Gypsum → Halite → Sylvite → Carnallite → Bischofite → Antarcticite

Seawater and the Salton Sea showed the same precipitation from gypsum through sylvite, but then showed bischofite precipitation after sylvite, then antarcticite, and finally carnallite.

The most unique precipitation sequence was that of Don Juan Pond, which showed a marked variation in the sequence of antarcticite, sylvite, and bischofite precipitation due to its unusual concentrations of K and Mg:

Gypsum → Halite → Antarcticite → Sylvite → Bischofite → Carnallite

The saturation index chart (Figure 3.14) can be implemented as an extension of the classic chemical divides diagram by showing the sequence of chloride mineral precipitates for each terrestrial brine. This sequence of empirical "chloride divides" is shown in Figure 3.15 below.

3.5.4 Trace Metals

Trace metal abundances that are common indicators of a hydrothermal component are shown in Table 3.5 and Figure 3.16 below. The three hydrothermal localities with trace metal data – Reykjanes, Iceland, the Juan de Fuca mid-ocean ridge (oceanic), and El Tatio (continental) showing varying trace metal trends. Juan de Fuca and El Tatio were comparable (within and order of magnitude of each other) in terms of Cu, Fe, and Zn. However, Reykjanes was lower than the other hydrothermal brines by more than an order of magnitude for all trace metals except for Ba and Mn, for which it was indistinguishable from El Tatio. In some cases (Cu, Fe, Pb, Zn), a hydrothermal fluid had the lowest concentration of trace metals. Highly concentrated brines such as Bristol Dry Lake, Dead Sea, and Don Juan Pond were among the highest of all samples for most trace metals (Ba, Fe, Mn, and Zn).

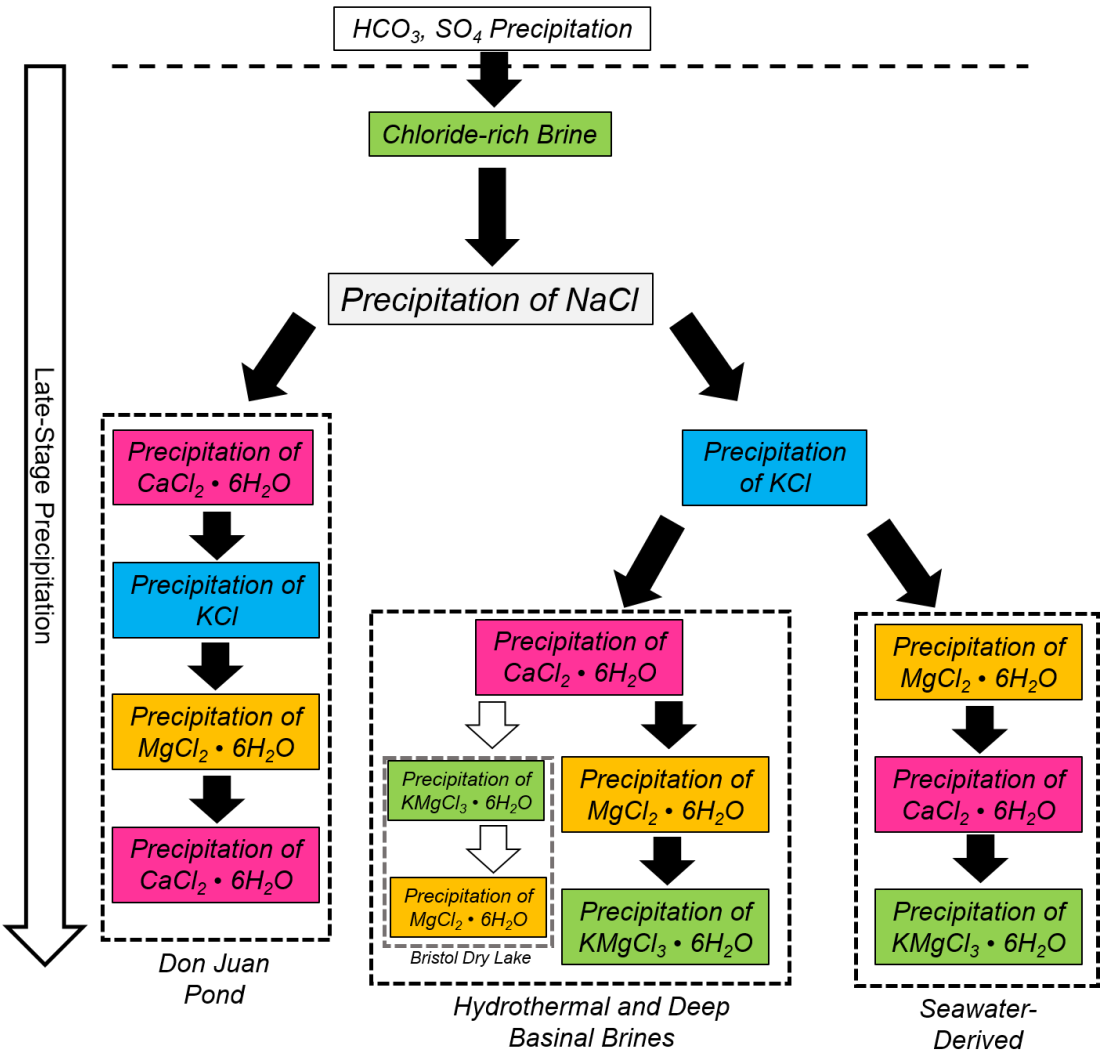

Figure 3.15. Sequence of chloride mineral precipitates (chloride divides) based on geochemical modeling of saturation index using empirical data from various terrestrial environments. Three endorheic basins fell outside of these broad classifications and were not included on this chart.

Table 3.4. Trace metal concentrations in μg/L and associated references.

Locality	Ba	Cu	Fe	Mn	Pb	Zn	Reference
Hydrothermal Continental Brines							
El Tatio, Chile	152.60	21.26	1.80	206.40	--	168.60	Cortecci 2005
Hydrothermal Oceanic Brines							
Reykjanes, Iceland	561.00	1.29	24.70	341.00	0.31	4.37	Uz-Zaman 2013
Mid-Ocean Ridge: Juan de Fuca	--	15.00	8.50	--	626.67	354.67	Metz and Trefry 2003
Endorheic Temperate Basins							
Salton Sea, CA	86.47	0.00	123.79	0.00	0.00	0.00	This Work
Dead Sea, Isreal	--	--	12.00	3100.00	189.00	510.00	Ganor & Katz 1989
Seawater	10.00	0.00	0.00	--	0.06	0.01	Witherow & Lyons 2011, Metz & Trefry, 2003
Endorheic Cold Basins							
Don Juan Pond, Antarctica	1920.72	2.80	68.69	1462.80	1462.80	165.36	Webster 1982
Deep Basinal Brines							
Bristol Dry Lake, CA	3985.31	0.00	2499.94	4987.82	70.19	3663.53	This Work

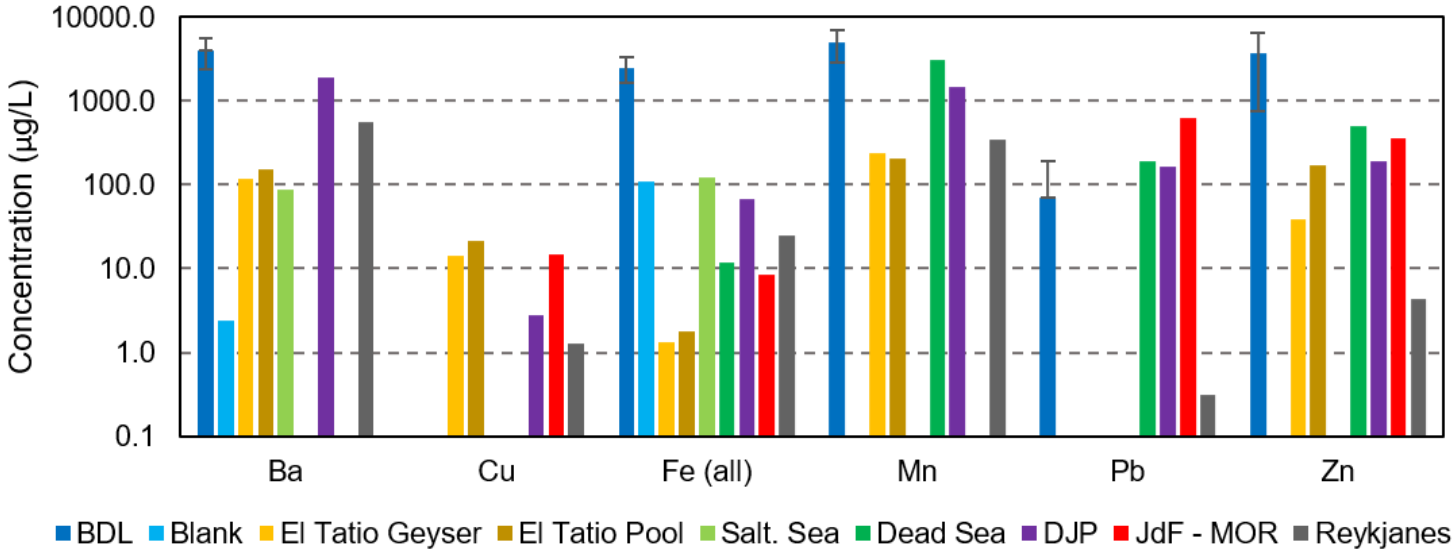

Figure 3.16. Log bar plot of trace metal concentrations in ug/L for each locality and for field blanks used for samples collected in this study. Error bars show range in laboratory values for multiple samples collected at Bristol Dry Lake.

3.6 Discussion

3.6.1 Major ions

Hydrothermal brines have unique major ion compositions, allowing them to be distinguished from other types of brines. Hydrothermal brines have reduced Mg relative to Ca, likely due to water-rock reactions such as serpentinization, which act to remove Mg from solution. Continental hydrothermal brines are enriched in Na relative to other brines as a result of water-rock reactions with silicic and felsic rocks. Oceanic hydrothermal fluids vary in terms of their major ion proportions; most are Na-dominated like continental hydrothermal brines, though some are dominated by Ca. They are also deficient in Mg (<10%).

The wide range of compositions of oceanic hydrothermal brines show that they are affected by water-rock reactions to varying degrees; homogenous water-rock reactions with basalt should make them Mg-deficient due to serpentinization, and Ca- and K-enriched due to leaching from basalt. However, the large overlap between many of the oceanic hydrothermal fluids reveals the possibility of brine mixing with surrounding seawater; this seawater component might account for the higher concentration of Na and the amount of Mg in the samples included in this study. Additionally, the degree to which volatiles such as HCl and CO_2 are intermixed with the brines will have a significant effect on their chemical reactivities as they travel to the surface. Therefore, this study demonstrates the need to better understand the sources of compositional heterogeneity in oceanic hydrothermal fluids independent of ambient seawater; this understanding will allow a more accurate constraint on what could be expected for martian hydrothermal fluids and the evaporite deposits produced from them.

Endorheic basins represent complex environments where meteoric, surface, and groundwaters are mixed and concentrated. Temperate endorheic basins are often in dry, salt pan/playa settings, and therefore strongly affected by the precipitation of evaporite minerals such as gypsum, anhydrite, and halite. As such, brines from temperate endorheic basins can be low in Na relative to other cations if they have reached halite saturation (Figure 3.11, Figure 3.13, and Figure 3.14) and all contain very little SO_4. Other minerals that are known to precipitate at such basins have a further effect on the solution chemistry; for example, the Dead Sea is a known locality of halite, sylvite, and carnallite precipitates. The precipitation of halite removes Na, while sylvite precipitation removes K, and carnallite precipitation removes both K and Mg. Therefore, in the Dead Sea, Na and K are disproportionately removed from solution, while Mg and Ca become further concentrated. This is in agreement with the precipitation sequence determined from geochemical modeling (see below). While not the highest ionic-strength solution, brine from Salar de Uyuni has one of the highest Na concentrations of any brine in this study (second only to El Tatio brine). Salar de Uyuni also has the highest Mg and K of any endorheic basin in this study and is known to precipitate both halite and sylvite. Even though it is classified as an endorheic basin, the Salton Sea is exposed to the runoff from nearby farming irrigation and anthropogenic contamination; in spite of this influx of solutes, the Salton Sea is not distinct from other brines and in fact behaves similarly to seawater, with carnallite as the final species precipitating likely due to the low proportion of Mg in both the Salton Sea and seawater.

Endorheic cold basins show a range of cation distributions, which appear to be influenced by the effects of seawater aerosols (Lakes Bonney, Fryxell, and Hoare) or

groundwater (Lake Vanda and Don Juan Pond) [*Takamatsu et al.*, 2017; *Toner et al.*, 2017]. Water composition indicates that Taylor Valley, where Lakes Bonney, Fryxell, and Hoare are located, has a greater input of marine aerosols than Wright Valley, where Lake Vanda and Don Juan Pond are located, though this has not been confirmed by previous studies. Taylor Valley Lakes show the same proportions of cations as seawater (Figure 3.11 and Figure 3.13) with increasing concentrations of Ca with increasing ionic strength. While Lake Vanda waters have a similar proportion of Mg as the Taylor Valley lakes, they are much more concentrated and enriched in Ca (Figure 3.5 and Figure 3.11). Previous studies have explored the composition of the groundwaters in Wright Valley, and found them enriched in Ca and Cl relative to other natural waters in that region. These studies determined that Don Juan Pond's unique composition is likely a combination of cold ion exchange and the recirculation of a deep groundwater that is heavily influenced by water-rock reactions. These water-rock reactions are thought to include albitization, chloritization, and/or dolomitization [*Toner et al.*, 2013, 2017]. We have shown that, among chloride-rich brines, Don Juan Pond has a globally unique composition. Its expected precipitation sequence is unique among any other brine in this study, and its proportion of Ca is higher than any other brine. The subsurface of Wright Valley includes many Ca-dominated rocks, which may play a part in the compositional uniqueness of Don Juan Pond as a result of water-rock interactions.

Similar to hydrothermal brines, deep basinal brines are deficient in Mg, which is expected for brines from depth that have the opportunity to form clays and participate in varying degrees of serpentinization. Deep basinal brines are unique in that they have the highest proportions of dissolved Ca, on average, than any other type of brine. Other

studies have determined that this is due to extensive albitization of crustal basement rocks, which produce a substantial amount of dissolved Ca with a molar-equivalent removal of Na. Deep basinal brines also tend to be highly concentrated in both dissolved $CaCl_2$ and dissolved NaCl, though Ca is largely the dominant cation; they have an inverse relationship between dissolved Na and Ca and have a range of Na:Ca ratios. Their high Na concentrations are likely due to the influence of silicic/felsic crustal rocks, which leach large quantities of Na into solution without removing Ca. While the concentrations of Mg and K are always lower than Ca and Na (respectively), deep basinal brines have higher dissolved $MgCl_2$ and KCl than any other type of brine. Relative to Cl- concentration, however, they are not outliers in terms of dissolved Mg or K. This indicates that their high absolute Mg and K concentrations are a result of the high ionic strength of the solution.

Most deep basinal brine samples evaluated here were collected from regions with extensive halite and other evaporite precipitation (i.e., Bristol Dry Lake, Death Valley, Salar de Atacama); therefore, the high ionic strengths of these solutions are likely a direct result of evaporative concentration in dry regions with little surface water input. The Salar de Atacama sample was collected from a region in the south portion of the Salar where there is known river input that is thought to be the cause of the higher proportion of Mg and K for that particular sample. Da Qaidam, China, is a unique deep basinal brine in that it is believed to be sourced from a granitic pluton that imparts a strong Na and K signature to brines from that location. Additionally, these waters are quite warm (72°C) and therefore have stronger indicators (Mg, K) of water-rock interactions than the other deep basinal brines in this study [*Stober et al.*, 2016]. We conclude that the Mg and K

concentrations of deep basinal brines can be used to surmise the temperature of the solution at the time water-rock reactions took place.

In spite of the variations in the composition of brines at their genesis, the heavy influence of water-rock interactions, and the alteration of brines after they reach the surface, there are a number of global trends that can be observed. First, the concentrations of the various cations in solution move along notable trends as a function of ionic strength because ionic strength is largely affected by evaporative concentration and the solubility limits of various species. The concentration of sodium, for example, peaks at ionic strengths of ~7 (Figure 3.13), and tapers off with increasing ionic strength due to the precipitation of halite. Conversely, the Ca concentration reaches a local minimum at the point where sodium concentration is greatest. As halite precipitation progresses, the residual Ca in solution holds an increasing proportion of the remaining ions and becomes a major contributor to ionic strength. Similarly, Mg and K (Figure 3.13) both show increases in concentration with increasing ionic strength, but their increases are muted relative to Na and Ca. The shallow increase of Mg and K with ionic strength is likely due to the competing effects of water-rock interactions with evaporative concentration, where water-rock interactions have a more pronounced effect at low ionic strength.

Because chloride brines on Mars likely underwent complete evaporative concentration to produce the chloride deposits seen from orbit, the full evaporation sequence of terrestrial analog brines must be considered to place the martian precipitates in proper context. Saturation indices were used to predict the precipitation sequence of minerals from each of the brines included in this study. The vast majority of brines of all types precipitate halite first, followed by sylvite. Late-stage mineral precipitates varied,

with loose correlations between the type of brine and the precipitation sequence. Hydrothermal brines behaved similarly regardless of whether they were associated with continental or oceanic crust, and even then they would be indistinguishable from some deep basinal brines and Antarctic lakes. Only small differences in saturation index distinguish some brines from each other (i.e., Death Valley deep basinal brine and Reykjanes oceanic hydrothermal brine), and these differences could easily be the result of variations in sample collection or analytical technique between studies. Therefore, the large majority of brines could only be distinguished by the precipitation of minor, late-stage phases such as antarcticite, bischofite, and/or carnallite. In this case, inclusions incasing the remnants of these final precipitates likely hold the key for understanding the final precipitation sequence (Figure 3.17). If such inclusions were found and analyzed on Mars, the formation process that produced their source brines could be better associated to analogous brines on Earth.

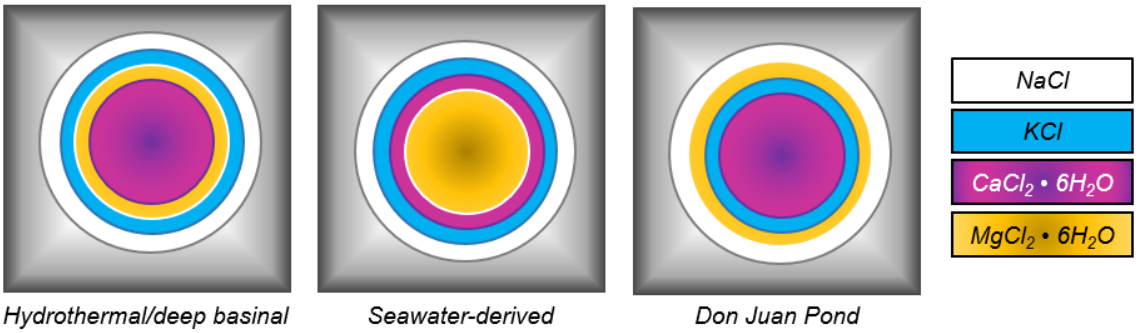

Figure 3.17. Cartoons of idealized inclusions showing the precipitation sequence of final-stage chloride minerals. The precipitation sequences are distinct for hydrothermal systems, seawater-derived systems (not expected for Mars), and Don Juan Pond-like systems.

The Don Juan Pond brine had a substantially different precipitation sequence from all the other brines. It was the only brine where sylvite precipitated later in the sequence than antarcticite. This site is also a well-known Mars analog; therefore, it is possible that Don Juan Pond represents what may be a common brine on Mars in spite of its terrestrial uniqueness. If that is the case, then this site holds a particular value for understanding the formation of chloride brines and precipitates on ancient Mars.

3.6.2 Trace Metals

Trace metals are generally insoluble, and as a result should come out of solution rapidly as ionic strength increases due to evaporative concentration. Therefore, trace metals are expected to be low for high ionic-strength solutions (endorheic temperate basins, other concentrated brines). Hydrothermal fluids generally carry a high proportion of trace metals due to the contributions of magmas. We therefore conclude that variations

in both the behavior of individual trace metals and the environments in which hydrothermal brines form prevents trace metals from being an accurate measure of a hydrothermal provenance. We also observe that ionic strength does not necessarily preclude a high trace metal abundance, as observed for Bristol Dry Lake, Don Juan Pond, and the Dead Sea; these localities consistently had the highest abundance of trace metals for all brines included in this study.

3.7 Conclusions

In this study, chloride-rich brines from a suite of terrestrial localities were compared to assess whether brine composition correlates to its provenance. By classifying the process that produced brines, this study lays the groundwork for classifying the provenance of brines on ancient Mars. Because chloride deposits on Mars are fully desiccated, the precipitation sequences of each brine type were determined; these sequences can be used as a framework for future Mars exploration. Major ion composition, trace metal abundance, and precipitation sequence based on geochemical modeling were all used in this study.

Hydrothermal brines can be distinguished from other brine types based on their major ion composition (reduced Mg relative to Ca). The degree to which brines have been concentrated plays a major role in interpreting their origins. Endorheic basins that have reached halite saturation tend to become enriched in Ca as ionic strength increases. For all brine types, major ions follow specific trends as a function of ionic strength. Na and Ca are inversely proportional to each other as ionic strength increases, likely due to the concentration and then precipitation of halite. Mg and K are much more sensitive to water-rock interactions and show less pronounced increases with ionic strength relative to Ca. Trace metals did not correlate to brine type in any way.

The majority of terrestrial brines precipitate halite first, and then sylvite. Distinct precipitation sequences were observed for hydrothermal fluids and deep basinal brines, seawater/surface runoff brines, and Don Juan Pond. Hydrothermal fluids, deep basinal brines, and seawater-derived brines reach halite saturation first, followed by sylvite. Hydrothermal and deep basinal brines precipitate antarcticite after sylvite, while

seawater-derived brines precipitate bischofite after sylvite. Don Juan Pond was unique among all the brines in this study because it reaches antarcticite saturation before reaching sylvite saturation.

This study has demonstrated that several types of terrestrial brines can be distinguished by their chloride mineral precipitation sequences. In some cases, brine types can only be distinguished at the very end of the precipitation sequence, where the precipitation of antarcticite, bischofite, and carnallite vary relative to each other. Therefore, the relative abundances and precipitation sequences of these minor minerals should be considered a priority for future Mars exploration. For Mars, the full precipitation sequence must be explored to understand the provenance of the chloride deposits seen from orbit. Minor chloride minerals such as antarcticite and bischofite would most likely to be observed only on a small scale as precipitates in halite inclusions. This study demonstrates the need for in-situ investigations by landers, rovers, or human crews so these small-scale studies can be undertaken.

Don Juan Pond, Antarctica, is thought to be similar to Mars due to its high salinity and its dry, cold environment. Don Juan Pond was unique in this study due to its abnormally low K concentration that resulted in the precipitation of sylvite after antarcticite. If this unique precipitation sequence is observed on Mars, it lends credence to the hypotheses that ancient Mars was a cold, dry environment, and Don Juan Pond can be used to assess the behavior of rocks – and perhaps microorganisms – that existed at that time.

3.8 Acknowledgments

Many thanks go to Dr. Hilairy Hartnett for teaching the Field Geochemistry course that gave me the original idea for this project and the technical know-how to execute it successfully. I also thank Dr. Stephen Romaniello for his helpful feedback on field sample collection techniques and for providing the necessary containers/chemicals for clean and sterile collection of trace metal samples. Finally, thanks to Kris Fecteau of the GeoPIG laboratory at Arizona State University, whose patience and help with ion chromatography helped me obtain my major ion data.

CHAPTER 4

THE EFFECTS OF TEXTURE AND COMPOSITION ON THE THERMAL INFRARED SPECTRA OF CHLORIDE MINERALS

4.1 Introduction

4.1.1 Evaporite Minerals

Liquid water has played an important role in determining the morphology, composition, and evolution of the martian surface. The presence of valley networks, outflow channels, deltas, and other fluvial features indicate a period in Mars' history where significant volumes of liquid water existed on its surface. In addition to these geomorphologic features, specific minerals including clays, hematite, sulfates, salts, and carbonates are present that can only form in the presence of water [*McLennan et al.*, 2005; *Ehlmann et al.*, 2008, 2013; *McKeown et al.*, 2009; *Michalski and Fergason*, 2009; *Michalski et al.*, 2010; *Roach et al.*, 2010; *Wang and Ling*, 2011; *Kaplan et al.*, 2016]. Evaporite deposits are formed when soluble salts precipitate out of a natural solution undergoing evaporation. The minerals in this precipitation sequence are determined by the relative concentrations of specific ions in solution and the solubilities of the resulting mineral precipitates. The most soluble of the major evaporite mineral sequence are the chloride minerals [*Hardie and Eugster*, 1970; *Hardie et al.*, 1978; *Lowenstein and Hardie*, 1985].

As a result of their high solubilities, chloride minerals remain in solution after other species – such as sulfates, carbonates, and phosphates (among others) – have precipitated out. The significant chloride deposits on Mars that are large enough to be

resolved from orbit provide evidence for the last period during which liquid water was present on a planetary surface [*Osterloo et al.*, 2008, 2010]. The detection of chlorides on Mars, therefore, allows this final stage of substantial aqueous activity to be investigated. Understanding the environmental conditions under which chloride deposits formed provide insight into a period of time of great geologic and astrobiological significance on Mars.

4.1.2 Textural Variations

The precipitation of chlorides from solution, their rates of crystallization, and the resulting surface texture may be sensitive to environmental conditions. Ambient temperature, atmospheric composition, rate of evaporation, and geologic context all influence the spatial extent and morphology (texture) of the resulting chloride deposit [*Warren*, 2006b]. Surface textures are particularly important because they represent the youngest portion of the evaporation sequence. The orientations and sizes of chloride crystals are directly linked to specific environmental conditions, as observed in many terrestrial playa such as Death Valley, the Atacama Desert, and Bristol Dry Lake, CA, all of which have a range of textures and morphologies on their surfaces [*Lowenstein and Hardie*, 1985; *Ganor and Katz*, 1989; *Rosen*, 1991, 1994; *Crowley and Hook*, 1996; *Baldridge et al.*, 2004]. Therefore, characterization of chloride textures can be used to assess the surface conditions at the time that the chlorides were deposited.

4.1.3 The Purpose of This Study

In this study, we used infrared emission spectroscopy to characterize a suite of chloride textures from both field and laboratory samples. Specific variations in spectral contrast and the shapes and locations of absorption features were characterized for each texture. Variations in infrared emissivity can be linked to a specific number of reflections due to the geometry of the surface and the number of pore spaces within the mineral. If these variations are large enough to be detectable by a rover or from orbit using current or future thermal infrared instruments, then the surface textures of chlorides on Mars can be better characterized. These textures, produced by unique environmental processes, will allow the environmental conditions at the time of last mineral precipitation – the critical time period during which Mars lost its reservoirs of surface/near-surface liquid water – to be better understood.

4.2 Background

4.2.1 Chloride-Rich Environments

Chloride minerals can be deposited as a result of several processes. Volcanic outgassing, surface ponding, and groundwater upwelling provide a source of chloride to planetary surfaces. Volcanic gases can cause direct precipitation of chloride sublimate crusts, where the chloride mineral is deposited in proximity to volcanic vents; however this process typically happens on a small scale and is unlikely to account for the large deposits seen on Mars [*DiFrancesco et al.*, 2016]. Surface ponding results from the accumulation of water in topographic lows. In most terrestrial settings, the water flows through slopes and channels and progresses downslope during and after episodes of

atmospheric precipitation, eventually ponding in closed basins [*Hardie and Eugster*, 1970; *Warren*, 2006b]. Groundwater upwelling can result from atmospheric precipitation as well, where the water table exists near, but beneath, the surface. Groundwater can also be sourced from subsurface hydrothermal activity, where hot, ion-rich fluid is driven buoyantly upward along thermal and chemical gradients or along steep faults [*Lowenstein and Risacher*, 2009; *Bucher and Stober*, 2011; *Deocampo and Jones*, 2013; *Kharaka and Hanor*, 2013]. The relative abundances of evaporite mineral species can be used to constrain the source of water from each of these processes [*Hardie and Eugster*, 1970; *Catling*, 1999].

4.2.2 Precipitation Sequence

Because they are highly soluble, chlorides are typically the last minerals to precipitate from a standing body of evaporating water. The characteristic dissolved solids in terrestrial waters include carbonate, sulfate, and chloride as major ions, where the major cations are determined by water-rock interactions and/or previous evaporation/erosion events. Low pH can produce unique minerals that can serve as indicators of water composition at the time of mineral precipitation [*Benison and Laclair*, 2003; *Tosca et al.*, 2004; *McLennan et al.*, 2005; *Kaplan et al.*, 2016]. Additionally, the presence of reduced versus oxidized species can indicate the oxidation state of the environment at and after the time of deposition [*Catling*, 1999]. Because carbonates are the least soluble of these species, they precipitate out of solution first. Sulfates are more soluble than carbonates, but less soluble than chlorides, and therefore precipitate out as an intermediate unit, stratigraphically younger than the carbonates. Chlorides, typified by

halite (NaCl) are the last minerals to precipitate out, and are stratigraphically the youngest (atop of) the other minerals discussed here [*Hardie and Eugster,* 1970; *Catling*, 1999]. This characteristic evaporation sequence in an open, contracting basin can be seen as a "bullseye" pattern in remote sensing of many terrestrial playa and reflects the shrinkage of the body of water due to evaporation and vertical stratification of mineral species in the subsurface due to the above-mentioned precipitation sequence [*Baldridge et al.*, 2004]. On Mars, this precipitation sequence is also predicted, though the cations in each mineral species may be different due to the relative abundance of Fe, Mg, and Ca compared to Earth [*Catling*, 1999].

4.2.3 Physical Properties of Chlorides

The physical properties of anhydrous chloride salts are unique among most planetary materials and account for their distinct signatures in the thermal infrared. Halite (NaCl) is an isotropic mineral with a face-centered cubic structure. Each chloride ion is coordinated with four sodium ions, and vice-versa, resulting in a lack of the single ion-ion interactions that are responsible for most diagnostic absorption features used for mineral identification in the mid-infrared (4000-400 cm^{-1} or 2.5-25 μm). Because the crystal vibrates as a unit rather than at a single discreet chemical bond, its fundamental vibration frequency is much lower than those of common silicate minerals and falls in the far-infrared (25+ μm) and outside the range of any instrument that has been to Mars [*V. C. Farmer*, 1974; *Ferraro*, 1995; *Baldridge*, 2008].

Halite and other chlorides (KCl/sylvite, $CaCl_2$, $MgCl_2$, and others) have fundamental absorptions at 30+ μm and peak emissivities less than unity through the mid-infrared [*Ferraro and Walker*, 1966; *Nyquist and Kagel*, 1971; *V. C. Farmer*, 1974; *Ferraro*, 1995]. A summary of the crystal systems and spectral properties of the most common chlorides is shown in Table 4.1.

Table 4.1. Crystal systems and locations of far-infrared absorption features for common chloride minerals. Absorptions are in wavenumber (cm^{-1}). T=transverse mode, L=longitudinal mode.

	Crystal System	Cation-Cl Stretch (cm^{-1})	Cation-O Stretch (cm^{-1})	H-bond Stretch (cm^{-1})
NaCl	Cubic	164(T)[1], 264(L)[2]	-	-
KCl	Cubic	146(T)[1], 214(L)[2]	-	-
$CaCl_2$	Orthorhombic	250, 230, 139[1,3]	-	-
$CaCl_2 \cdot 6H_2O$	Trigonal	136, 100, 80[1]	380[1]	240, 192[1]
$MgCl_2$	Hexagonal (rhom.)	230[1,3]	-	-
$MgCl_2 \cdot 6H_2O$	Monoclinic	112[1]	384[1]	200, 162[1]

[1]Ferraro 1971, [2]Farmer 1974, [3]Baldridge 2008.

Numerous studies have characterized the unique spectral properties of chlorides that are a manifestation of the chemical properties described above. Previous investigators observed that anhydrous chlorides minerals (hereafter referred to simply as chlorides) are largely transparent in the mid-wavelength portion of the infrared (5-20 μm) [*Eastes*, 1989; *Lane and Christensen*, 1998; *Baldridge*, 2008; *Osterloo et al.*, 2008]. This transparency prevents an accurate application of Kirchoff's Law for determining reflectance from emissivity (and vice-versa), because a substantial portion of the energy is transmitted through the sample or scattered, and not reflected or absorbed/emitted.

Thermal gradients in a chloride mineral can cause a misidentification in temperature due to the window chlorides provide to deep portions of a natural deposit. Additionally, contaminants (i.e., sulfates or adsorbed water) appear as transmission features due to the low emission of chlorides in the mid-infrared [*Eastes*, 1989; *Lane and Christensen*, 1998; *Baldridge*, 2008].

In planetary remote sensing, infrared emissivity spectra are derived by dividing the radiance spectrum by a Planck function fit to the peak emissivity, assumed to be 1 at some point in the mid-infrared [*Ruff et al.*, 1997; *Lane and Christensen*, 1998; *Feely and Christensen*, 1999; *Christensen et al.*, 2000]. Chlorides do not have peak emissivities of 1 in the mid-infrared; therefore, the assumption that the emissivity equals 1 results in division by the incorrect Planck function, which in turn produces a sloped emissivity spectrum [*Lane and Christensen*, 1998; *Baldridge*, 2008; *Osterloo et al.*, 2008]. Additionally, chlorides are featureless (have no absorptions) and largely transparent in the mid-infrared [*Nyquist and Kagel*, 1971; *Eastes*, 1989]. However, because no other common geologic mineral produces a sloped, low-emissivity, featureless spectrum, these characteristics have been used to indirectly identify chlorides on Mars [*Osterloo et al.*, 2008].

To date, far-infrared spectra of chloride minerals have been measured in either transmission or reflection [*Farmer*, 1974; *Baldridge*, 2008]. However, the practical application of mineral identification on planetary surfaces requires a thorough knowledge of mineral behavior in emission. This work seeks to fill this gap in understanding of chlorides in preparation for future far-infrared emission studies of potential salt-bearing planetary bodies. In emission, energy has been absorbed by and passed through the

sample, providing a more accurate characterization of the whole volume of a mineral rather than only its surface. Quantifying the locations of the Christiansen feature (emissivity peak) and fundamental absorptions, and how these features change in a variety of natural settings, will allow planetary chloride deposits to be better characterized in preparation for high-risk and costly sample return missions.

4.2.4 Identification of Chlorides on Mars

The sloped, low-emission, featureless spectrum is considered the first identification of chlorides on Mars. The Thermal Emission Imaging System (THEMIS) has nine bands for mineral identification that have been used for this detection [*Christensen et al.*, 2004]. Osterloo et al. (2008) used a decorrelation stretch (DCS) product to identify regions on Mars with a featureless, sloped spectrum. A DCS using THEMIS bands 8, 7, and 5 shows regions with a spectral slope as bright cerulean blue. This slope persists in DCS products of bands 9, 6, and 4, where chlorides appear green-blue, and disappears in DCS products of bands 6, 4, and 2, where chlorides appear yellow-orange. Further investigation of these chloride deposits by Osterloo et al. (2010) using other instruments ruled out other minerals using data from other Mars-orbiting instruments. Bandfield (2009) used THEMIS and a thermodynamic model to rule out topographic slope-induced anisothermalities as the cause of the spectral slope [*Bandfield*, 2009].

Recent efforts have refined estimates of both the species of chloride present and its physical state [*Jensen and Glotch*, 2011; *Berger et al.*, 2015; *Glotch et al.*, 2016]. These studies have determined that the most likely material comprising martian chloride

deposits is a mixture of chloride particles, comprising 10-25% by weight, and flood basalt-type rock [*Glotch et al.*, 2016]. The thickness of the deposits varies based on which estimates of particle size are used, but observations by THEMIS indicate that it is optically thick; with the above range of compositions, an optically thick chloride deposit is 150-180 μm in the thermal infrared [*Mitchell and Christensen*, 2016]. This minimum thickness can be used as the lower bound of an estimate of chloride abundance using Equation 1 of Mitchell and Christensen (2016). Osterloo and Hynek (2015) used an impact crater to estimate the thickness of the chloride deposit in Miyamoto Crater, providing a more empirical estimate of chloride deposit thicknesses; this estimate bounded the thickness of chloride deposits in Miyamoto Crater to several meters [*Osterloo and Hynek*, 2015].

4.2.5 Textural Variations with Environment

Field observations of chloride deposits on Earth have revealed a suite of surface textures that potentially complicate the characterization of such deposits on other planets. Fundamental works by Lowenstein and Hardie (1985) and others have described these textures at a number of field sites in the American southwest as well as other playa (salt flat) settings such as the Atacama Desert, Chile; the Salar de Uyuni, Bolivia; and many sites in the Middle East (i.e., the Dead Sea, Israel) [*Gornitz and Schreiber*, 1981; *Handford*, 1982; *Lowenstein and Hardie*, 1985; *Ganor and Katz*, 1989; *Rosen*, 1991; *Warren*, 2006a].

Textures vary based on the age of the deposit, the cyclical nature of water influx and desiccation, environmental conditions (wind, temperature, rain), geologic context,

and geographic location. For example, Hardie and Lowenstein (1985) describe chevron and cornet features that are only produced from the crystallization of halite cubes in a standing brine. The cubes continue to grow at the water surface due to high evaporation rates at the air-water interface; eventually, the weight of the cube overcomes buoyancy forces and the cube sinks. If the cube lands pointed-edge-up, it produces a chevron pattern, and if it lands on its side, it produces a cornet [*Lowenstein and Hardie*, 1985]. Observations of these patterns are a direct indication of a halite-saturated standing body of water.

Other surface textures have been observed at numerous playas across the globe and serve as diagnostic features of the processes that formed them [*Gornitz and Schreiber*, 1981; *Talbot et al.*, 1996; *Warren*, 2006b; *Taj and Aref*, 2015]. "Mushroom" structures form when a halite crystals grow over the top of a standing body of water; the classical large-scale example of these is the Dead Sea, Israel (Figure 4.1). Rafts form when many small nucleated crystals aggregate together [*Talbot et al.*, 1996; *Taj and Aref*, 2015]. "Needle" structures form when a series of chevrons or cornets grow as primary features in a standing brine. Large halite cubes, known as hoppers (up to centimeters on a side), are produced as displacive features in a salt-saturated fine-grained mud. Efflorescence occurs when a small volume of brine evaporates on a surface, resulting in direct precipitation of chloride into a thin crust. Efflorescence produces a disorganized agglomeration of fine-grained halite crystals, which in most cases is not optically thick. Pyramid-shaped crystals (referred to as "rafts" by Warren) begin to form at the air-water interface, and remain suspended due to surface tension [*Warren*, 2006a]. These crystals grow disproportionally at their edges due to evaporative concentration at their edges until

they become too heavy to remain suspended and fall to the bottom of the water column [*Gornitz and Schreiber*, 1981; *Warren*, 2006a]. Aggregates of chloride crystals can form after the initial precipitation/deposition of cubes or crusts. These aggregates are loosely bound and friable as primary structures; however, in environments of repeated saturation and precipitation, these aggregates can become well-cemented and eventually form large polygonal crack structures [*Warren*, 2006a; *El-Maarry et al.*, 2015].

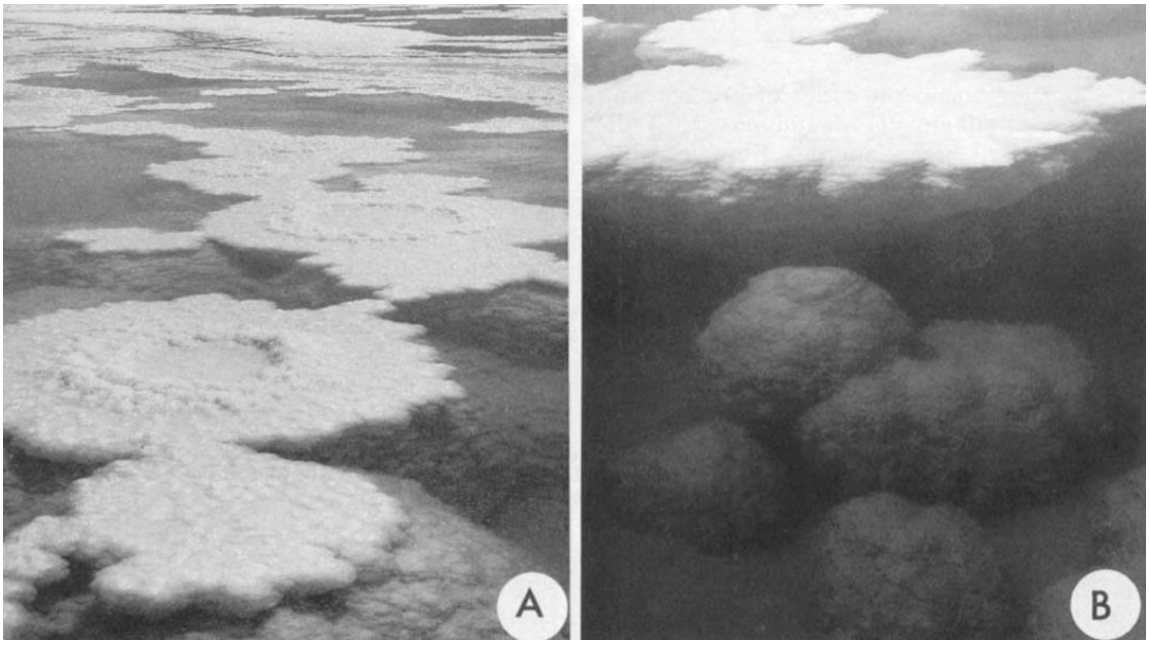

Figure 4.1. Halite mushrooms as observed at the Dead Sea, Israel, by Talbot et al. (1996). A) Tops of mushrooms propagating outward from air-water interface. B) Conical mushroom base observed from the subsurface. The diameter of the mushrooms is ~1 m. (Image credit: Talbot et al. 1996, *Sedimentology*)

After the initial formation of a chloride deposit, cavities can form on its surface due to rainfall, which can locally dissolve small volumes of salt. Cavities are especially important because they can behave as blackbody cavities, preventing accurate mineral identification due to geometric and spectral absorption effects. Finally, grains of chloride can be compressed to form a coherent, cemented unit due to overburden/pressure forces. Cemented and cavity-rich chlorides are secondary features, produced by the alteration of the primary features by interactions with the environment post-deposition.

4.2.6 Quantifying Emissivity

Each of the textures described above has a unique geometry, and will therefore have unique effects on infrared spectra. Because the fundamental modes of chloride minerals are in the far-infrared, far-infrared emissivity spectra are used in this study to measure the geometric effects of the various textures. Osterloo et al. (2012) conducted a study of the emissivity spectra of a number of geologic materials with varying degrees of roughness. Her study revealed that thermal infrared emissivity can be used as a proxy for surface roughness for certain geologic materials. The emissivity-reflection equation used by Osterloo (2012) can also be used to assess the efficacy of infrared emissivity on characterizing naturally occurring chlorides.

$$E_e = 1 - (1 - E)^{(\beta+1)}$$

where E_e is the effective emissivity, that is, the emissivity that is observed, E is the actual emissivity of the material surface, and β is the number of reflections that occurs before the reflected light interacts with the observer [*Osterloo et al.*, 2012].

4.2.7 Expected Variations in Spectral Properties

Christiansen feature. Wavelengths where minerals have high absorption coefficients are dominated by surface emission, with self-absorption resulting in emission only from the uppermost (1 – 10 μm) region. These locations of emissivity minima are known as reststrahlen bands and represent the fundamental absorptions of that mineral. At wavelengths slightly shorter than the fundamental, the index of refraction of the

mineral changes rapidly and is equal to that of the medium over a narrow wavelength range, resulting in very little scattering in this region. The absence of surface or volume scattering at this wavelength, together with a low absorption coefficient, results in the majority of infrared energy passing through the sample with little internal absorption or surface reflection. This emissivity maximum is known as the Christiansen feature and is diagnostic of a mineral species at a specific atmospheric pressure and temperature [*Salisbury*, 1993; *Salisbury and Wald*, 1992].

Particle Size. Variations in particle size have a direct effect on the depth of the fundamental absorption features of geologic materials [*Salisbury and Wald*, 1992]. Moersch and Christensen described four classes of optical behavior in minerals as a function of n, index of refraction, and k, absorption coefficient. Most silicate minerals are Class 1 over the mid-infrared, where k is large. Coarse particles are optically thick; as a result, energy that is absorbed and emitted by one molecule in Class 1 spectral regions will typically be absorbed by a nearby particle instead of passing through the sample. This enhanced absorption by the sample results in deeper features and greater spectral contrast at fundamental absorptions [*Salisbury and Wald*, 1992; *Moersch and Christensen*, 1995]. Additionally, larger particles have a lower number of pore spaces, reducing internal volume scattering relative to finer particles. Fine particles have a greater number of air-grain interfaces in a sample volume, resulting in a greater number of internal reflections. These reflections increase the emission component of energy in Class 1 regions, resulting in an overall increase in sample emissivity and decrease in spectral contrast. Fine particles also result in greater volume scattering due to the fact that the particles are optically thin. [*Aronson and Emslie*, 1967; *Vincent and Hunt*, 1968;

Hunt and Vincent, 1968; *Conel*, 1969; *Hunt and Logan*, 1972; *Clark and Roush*, 1984; *Salisbury and Wald*, 1992; *Salisbury et al.*, 1994; *Wald and Salisbury*, 1995; *Moersch and Christensen*, 1995; *Mustard and Hays*, 1997; *Lane and Christensen*, 1998; *Korb et al.*, 1999]

Class 2 regions have moderate absorption coefficients ($0.5 < k < 1$) and moderate index of refraction ($n \sim 2$). Weak absorptions that show decreasing emission with decreasing particle size are located in Class 2 regions. Class 3 regions are described by Moersch and Christensen (2005) as that spectral range where a mineral is weakly absorbing and $n > 1$; chloride minerals fall into this category in the mid-infrared ($n_{halite} = \sim 1.5$) and are characterized by low emission due to absorption by particles as energy is transmitted through the sample volume. For this reason, chloride (i.e., KCl) particles are typically used as a matrix in pressed pellets for transmission spectroscopy, because they are low-emission and have no absorptions in the mid-infrared. Class 4 regions are those regions where $k < 0.1$ and $n = 1$; these maximum-emission regions are where the Christiansen features are located [*Salisbury and Wald*, 1992; *Moersch and Christensen*, 1995].

4.3 Methods

4.3.1 Field Sample Collection

Chloride textures were observed in the field prior to constraining their spectral properties in a laboratory setting. While only one field site was used to constrain the sizes of the textures in question, these textures are known to occur at multiple playa

settings across the southwestern U+nited States and other playa/sabkha settings across the globe [*Crowley and Hook*, 1996; *Talbot et al.*, 1996; *Warren*, 2006b].

For this study, Bristol Dry Lake, California, was used as a Mars-analog site from which various halite textures were observed and sampled (Figure 4.2). Large (meter-scale) polygonal cracks over an area of over 10+ km^2 are thought to have formed from groundwater upwelling of calcium and sodium chloride-rich deep basinal brines [*Lowenstein and Risacher*, 2009]. Samples of well-cemented polygonally cracked halite (hereafter called "polygonal halite") from Bristol Dry Lake were used in this study to assess the efficacy by which chloride can be detected in a natural setting. Clays exist in layers on the underside of polygonally cracked structures, and were deposited as alluvial fan wash from the nearby Callumet, Bristol, and Bullion Mountains [*Rosen*, 1991]. Clay deposits on the polygonal halite samples were removed by physical abrasion, and one sample was crushed using a rock hammer to produce mm-scale chips of polygonal halite. The abraded polygonal halite has several dissolution pits on its surface, likely due to the effects of rainwater.

Figure 4.2. a) Surface view at Bristol Dry Lake, CA; polygonal cracks are approximately 1-2 meters across. b) Orbital image of Bristol Dry Lake, CA; large-scale polygonal structures are visible. (Orbital image credit: Google/DigitalGlobe.)

4.3.2 Synthetic Sample Preparation

To mitigate the effects of impurities, synthetic textures analogous to those observed in the field were produced. A labeled photo of the system used for producing these synthetic textures is shown in Figure 4.3. A 15-gallon acrylic aquarium was used to simulate a closed basin system; this aquarium was filled with 10-12 L of 300 g/L reagent-grade sodium chloride brine. Infrared lamps (75W) were used to simulate solar heating, and an aquarium fan system (Tunze Aquawind™) was used to simulate wind. Atmospheric pressure, temperature, and humidity were monitored daily. Because salt crusts coat submerged probes within a day, water temperature was tracked using two devices: an analog thermometer and a temperature probe connected to a Tunze SmartController 3000™. An aluminum foil sheet was used as a dust cover, and the water level was monitored to the nearest mm using a ruler on the tank exterior.

A series of experiments were conducted in which the brine was evaporatively concentrated at a range of evaporation rates while being actively heated. Water level, temperature and atmospheric conditions were recorded once daily. Different evaporation rates were achieved by varying the number of infrared lamps used (between 0-2) and adding/removing the fan system. Three polished glass coupons were placed at the bottom of the tank to allow collection of precipitates without disruption of their texture. Variations in texture and particle size were catalogued for each evaporation/precipitation experiment.

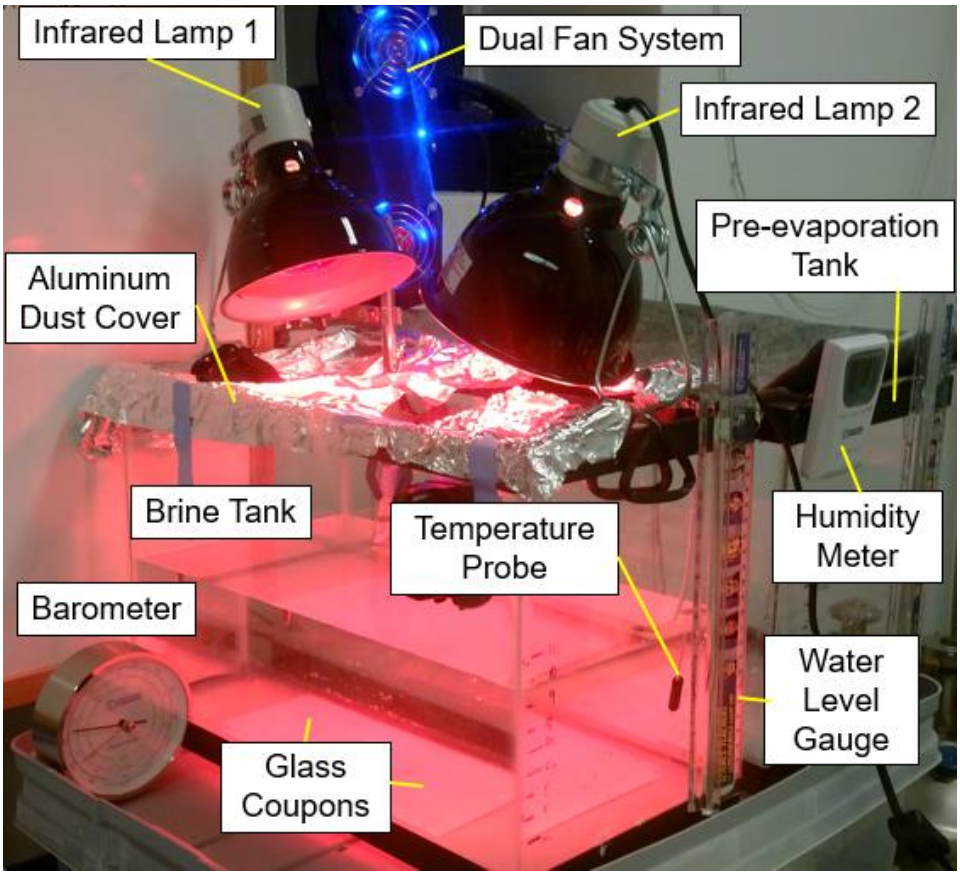

Figure 4.3. Photograph of the precipitation tank for producing synthetic chloride textures in the Mars Space Flight Facility geochemistry laboratory.

In addition to the artificially grown crystals, a hydraulic press was used to produce pressed pellets using reagent-grade anhydrous chloride powder (halite, sylvite, and $CaCl_2$). Pressed pellets are commonly used in transmission spectroscopy and have been used extensively to explore the various spectral properties of pure chloride salts. In this study, pressed pellets serve as a control to which the emission spectra of varying textures can be compared.

4.3.3 Infrared Emission Spectroscopy

Mid-Infrared Emission Spectra. Mid-infrared emission spectra (4000-400 cm^{-1} or 2.5-25 μm) with a spectral resolution of 2 cm^{-1} were collected at the Mars Space Flight Facility at Arizona State University using a Thermo-Fisher Nicolet Nexus 670 Fourier Transform Infrared (FTIR) Spectrometer configured for emission using a CsI beamsplitter. Additional mid-infrared spectra (2000-200 cm^{-1} or 5-50 μm) with a spectral resolution of 2 cm^{-1} were collected at the Vibrational Spectroscopy Laboratory at Stony Brook University using a Thermo-Fisher Nicolet 6700 FTIR spectrometer configured for emission and using a KBr beamsplitter. For both instruments, the sample analysis procedure described in Ruff et al. (1997) was used. Two blackbodies (at 70 and 100°C) were used to produce an instrument response function prior to sample analysis. Samples were placed in blackbody-painted copper sample cups and heated to 80°C prior to measurement. The sample cups were actively heated during measurement and the sample chamber cooled to minimize downwelling radiance and increase the signal-to-noise ratio. The sample chamber for both instruments is encased in a sealed acrylic box and purged with dry air to minimize water vapor and CO_2 absorptions in spectra. The sample

chamber was purged for a minimum of 15 minutes with dry air before data collection for each sample [*Ruff et al.*, 1997].

Far-Infrared Emission Spectra. Far-infrared emission spectra (600-50 cm^{-1} or 16.7-200 μm) with a spectral resolution of 2 cm^{-1} were collected at the Vibrational Spectroscopy Laboratory at Stony Brook University using a Thermo-Fisher Nicolet 6700 FTIR spectrometer configured for emission and using a solid-state beamsplitter. The sample analysis procedure was the same as described above for mid-infrared spectra and followed the procedure outlined in Ruff et al. (1997). To minimize the appearance of water vapor absorptions in the far-infrared, the sample chamber was purged for 30 minutes prior to data collection for each sample [*Ruff et al.*, 1997].

Calibration of Spectra. Because the peak emission of chloride minerals is in the far-infrared, Planck curves to calibrate the spectra must be fit to the emission peak in the far-infrared spectrum prior to calibrating the mid-infrared spectrum. The mid-infrared spectrum is then fit to an overlapping emissivity in the far-infrared; this wavelength range was limited to 400 - 600 cm^{-1}. The wavenumber at which the two spectra are joined is determined by finding the point in the overlap region with the lowest RMS error. The mid-infrared spectrum is then scaled such that the two spectra have the same emissivity at the low-RMS wavenumber.

4.3.4 Spectral Analysis

The fundamental absorptions, adsorbed water features, and contaminant minerals were identified using spectral data from previous studies. The libraries of Farmer (1974) and Chukanov (2004) were used to locate the approximate wavenumber of fundamental absorption features for anhydrous chlorides and sulfates [*Farmer*, 1974; *Chukanov*, 2014]. Baldridge (2008) identified a number of additional features using infrared reflectance spectroscopy; these features are included for previously unidentified absorptions [*Baldridge*, 2008]. Anhydrous chlorides are highly hygroscopic; therefore, the effect of adsorbed water on a nominally anhydrous mineral must be constrained [*Eastes*, 1989]. The library of Nyquist and Kagel (1971) was used to determine the absorption features due to water and/or hydroxyl. In each of the spectra shown below, the identification of fundamental and contaminant absorption features are according to the findings of these referenced sources.

The spectral contrast was determined using the Matlab script *findpeaks*, which locates the local maxima within a given dataset. Because emission absorptions are topographic lows (local minima), a value of 1 minus emissivity was used as an input to the Matlab function. *Findpeaks* measures the prominence of isolated maxima relative to the local continuum and provides peak maxima values (1 - emissivity), peak location (wavenumber), height (band depth), and base width. Peaks identified by this method were limited to those greater than 0.1 Δ-emissivity and confirmed by manual inspection. For comparison, the band depths of several absorption features were measured by Gaussian fit, third-order polynomial fit, and a simple difference calculation (continuum emissivity minus absorption minimum). All were within 0.03 emissivity of the corresponding

Matlab-derived value. Therefore, we consider the *findpeaks* function a valid metric by which to compare band depths and spectral contrast for different spectral features.

4.4 Results

4.4.1 Salt Precipitation Process

The rate of evaporation can play a major role in the morphology and particle size of crystalline materials. Sears and Chittenden (2005) modeled the evaporation rate of sodium chloride brines under the current atmospheric conditions on the martian surface; their modeled evaporation rates ranged from 0.04 to 0.9 mm/hr [*Sears and Chittenden*, 2005]. During the late Noachian/early Hesperian (3.5 – 4.0 Gya), when martian chloride deposits are thought to have formed, atmospheric conditions were likely very different: the atmosphere may have been thicker, and liquid water may have been more stable on the martian surface than it is today [*Catling*, 1999]. However, the estimates of Sears and Chittenden (2005) have been used in studies of ponded water on early Mars, a period during which the atmospheric conditions (P_{atm}, pCO_2, temperature, obliquity) are poorly understood [*Howard et al.*, 2009]. The evaporation rates of Sears and Chittenden (2005) were therefore used as a target for this study because they are the best estimate available for the behavior of brines on Mars.

In this study, four evaporation experiments were conducted to replicate, in a controlled environment, the precipitation rates at which chlorides may have formed on Mars and their textures relative to textures observed in the field. Measured brine evaporation rates ranged from 0.07 (no active heating or fan) to 0.5 mm/hr (two IR lamps

and fan system) - well within the range expected for sodium chloride brines on the martian surface.

Regardless of the evaporation rate, the sequence of precipitation was the same for each brine evaporation experiment. The sequence of precipitation is as follows. (1) Cubes of halite nucleated at the air-water interface; these cubes reached up to 2-mm on a side before falling to the base of the tank. Most commonly, small cubes at the air-water interface would accrete together, forming a thin crust at the water surface called a "raft." (Figure 4.4a) In some cases, these cubes grew disproportionately at the corners than on the cube faces, forming a staggered pyramid-type shape (Figure 4.4c, d). (2) The fallen cubes would continue to grow along either cube faces or edges until they interacted with other precipitated cubes. (Figure 4.4b) (3) Cube-cube interactions resulted in the formation of aggregate structures: disorganized but loosely cemented masses of halite. In some cases, cubes would continue to grow along all faces, forming hopper-like crystals, or along a single crystal face, forming a "spire"-type structure. (Figure 4.4e, f and Figure 4.5) (4) After the formation of aggregates, large cubes, and spires, the final veneer of brine became super-saturated; in this stage, micron-scale crystals precipitated directly on the surfaces of preexisting crystals, forming an efflorescent crust (Figure 4.4g). This sequence of evaporation and salt precipitation has been well-documented for active playa systems on Earth [*Gornitz and Schreiber*, 1981; *Warren*, 2006a].

Because the efflorescent crust is the natural final stage in the precipitation process, other textures (formed during 1-3 above) had to be collected prior to final evaporation of the brine. Residual brine was wicked away from these samples using a

laboratory wipe and baked in an oven after removal from the tank to prevent formation of a post-mortem efflorescent crust.

The varied atmospheric pressure and gravity on Mars could result in changes in this sequence of precipitation and deposition. For example, the lower gravity on Mars could allow larger crystals to form at the air-water interface before sinking to the bottom, resulting in more coarse-grained deposits than the ones produced in this study. If the original textures of primary chloride deposits are preserved on Mars, they may provide insights into the environmental differences between terrestrial versus martian climates.

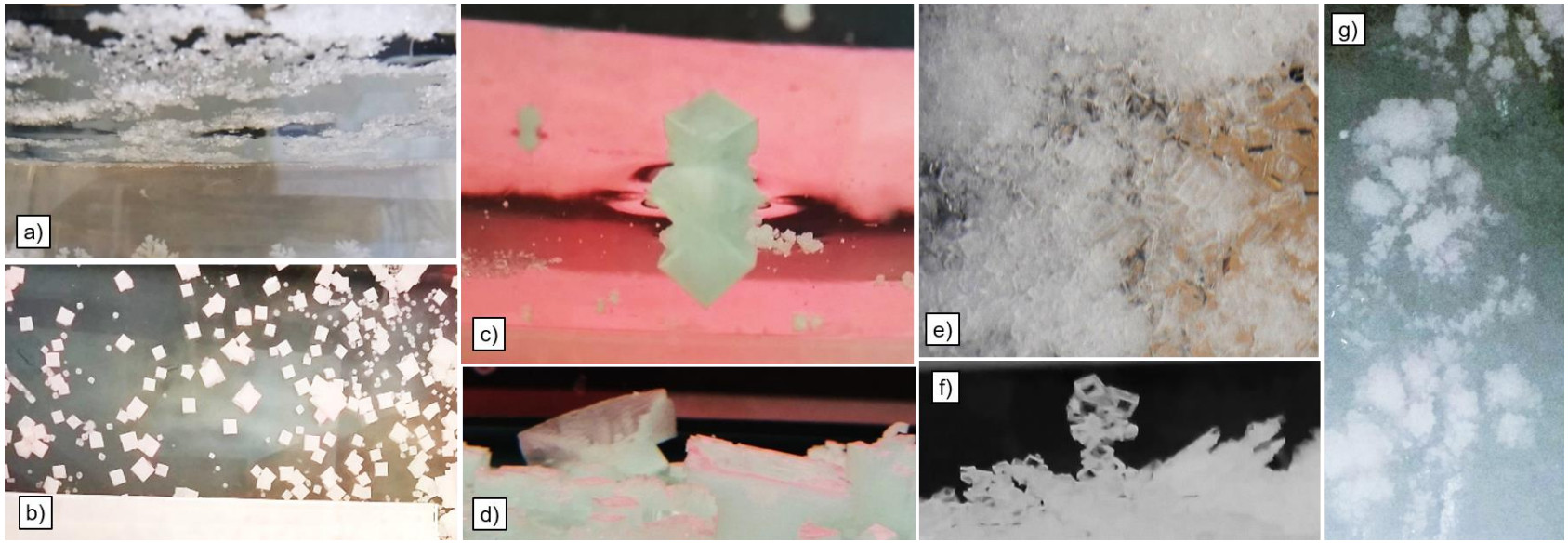

Figure 4.4. Photos of morphologies observed during crystal precipitation. a) Formation of rafts at air-water interface; b) growth of fallen cubes at base of evaporation tank; c) growth of large cube at air-water interface - cube is approximately 2-mm on a side; d) pyramid textures that sank to the bottom of the evaporation tank; e) formation of nascent crystal aggregates; f) unusual vertical superposition of cubes; and g) initial formation of efflorescent crust at the latest stage of brine evaporation.

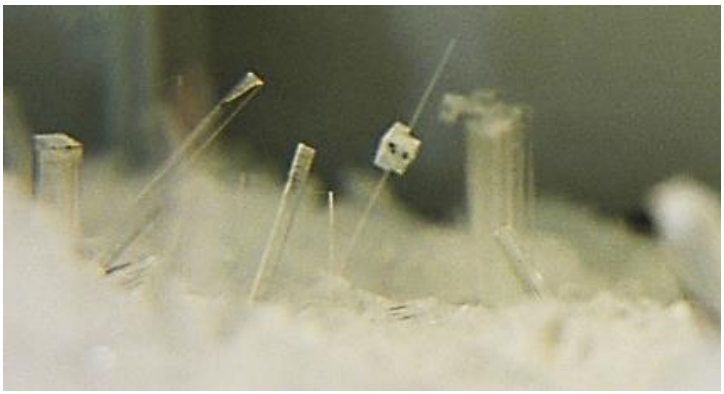

Figure 4.5. Unusual "spire"-type textures, where growth is primarily along a single crystal face.

4.4.2 Synthetic Samples and Spectra

The specific samples used for the collection of infrared emission spectra are shown in Figure 4.6. These samples were selected to represent both a range of textures produced in nature and a range of particle sizes that may be present on the martian surface. While primary textures may still be present on Mars, it is also likely that some portion of the chloride deposits may have been pulverized or shattered into smaller particles due to active erosional processes from wind or impacts. We therefore attempted to cover the full range of possible textures by including several samples of loose particles both above and below 180 μm in diameter and a sample of loose small cubes.

Figure 4.6. Synthetic samples used for spectral analysis. All samples are composed of halite. a) Efflorescent Crust, b) Aggregate, c) Small Cubes, d) Particles >180 μm, e) Pyramid, and f) Large Crystal.

The mid-infrared spectra of the halite (NaCl) pressed pellet (Figure 4.7) shows an absorption due to the bending mode of adsorbed water at 1627 cm^{-1} and an absorption due to sulfate at 1110 cm^{-1}. These absorption peaks appear as a result of the low background emissivity of the halite at these wavenumbers and are often referred to as "transmission-like" features. Far-infrared spectra (300-50 cm^{-1} or ~33-200 μm) of the pressed pellets are shown in Figure 4.8. Pressed pellets are labeled with the compound name (NaCl, KCl, or $CaCl_2$) and the sample number ("W#").

The fundamental absorption features of each chloride can be seen as broad, deep absorptions in Figure 4.8. The halite absorptions are at slightly different wavelengths than those measured in reflectance/transmission shown in Table 4.1 above. The broad absorption due to the Na-Cl transverse stretch is shifted to higher wavenumber (183 cm^{-1} in emission as opposed to 167 cm^{-1} in reflectance/transmission), whereas the Na-Cl longitudinal stretch is shifted to shorter wavenumber (260 cm^{-1} in emission as opposed to 264 cm^{-1} in reflectance/transmission). An additional absorption, that has also been observed in previous transmission studies (Hadni 1967), can be seen with a band center at 235 cm^{-1}; this feature is attributed to a "two-phonon" interaction, presumably where the fundamentals of the transverse and longitudinal modes constructively interfere [*Hadni*, 1967]. The Christiansen feature of halite was observed at 327 cm^{-1}.

The mid-infrared spectrum of the sylvite (KCl) pressed pellet shows a broad, low-emission background similar to halite. The 1627 cm^{-1} feature due to adsorbed water is visible, along with a sharp transmission-like feature attributed to nitrate at 1402 cm^{-1}; nitrate is a known contaminant in reagent-grade KCl powder and hence is expected here [*Nyquist and Kagel*, 1971; *Farmer*, 1974]. In the far-infrared, the K-Cl transverse stretch

is shifted to higher wavenumber (154 cm^{-1} in emission versus 146 cm^{-1} in reflectance/transmission), similar to halite, but the longitudinal stretch remains essentially the same (216 cm^{-1} in emission versus 214 cm^{-1} in reflectance/transmission). For both halite and sylvite, the transverse stretch is expressed as a deep, broad feature whereas the longitudinal stretch is a shallower, sharper feature. The Christiansen feature of sylvite is located at much lower wavenumber than that of halite: 279 cm^{-1}.

The mid-infrared spectrum of the $CaCl_2$ pellet is largely flat and featureless, with a higher average emissivity than either NaCl or KCl. Because $CaCl_2$ is highly hygroscopic, the effects on the $CaCl_2$ spectrum are largely attributable to the presence of adsorbed water. Small absorptions at 1631, 1024, and 646 cm^{-1} are due to the bending and rocking/wagging modes of water. A possible indication of Ca-O bonding occurs at 460 cm^{-1}. The 1840 cm^{-1} feature could be due to a combination of bending and libration of adsorbed HDO (water with a single deuterium atom) [*Walrafen and Stone*, 1972]. The small feature at 1120 cm^{-1} is attributable to trace quantities of sulfate. In the far-infrared, $CaCl_2$ is known to have several fundamental absorptions at 250, 230, and 139 cm^{-1} due to the various Ca-Cl stretching modes. In emission, however, there are only two fundamental absorptions and they are at 237 and 168 cm^{-1}. However, the feature at 237 cm^{-1} is extremely broad and could include the ~250 cm^{-1} feature, which is likely a low-spectral-contrast feature due to the asymmetric nature of the absorption. The location of the Christiansen feature for $CaCl_2$ is the same as that of NaCl (327 cm^{-1}); as a result, the identification of $CaCl_2$ in natural environments by infrared emission spectroscopy could be challenging due to the large overlap between NaCl and $CaCl_2$ absorption features and their typical colocation in the natural environment.

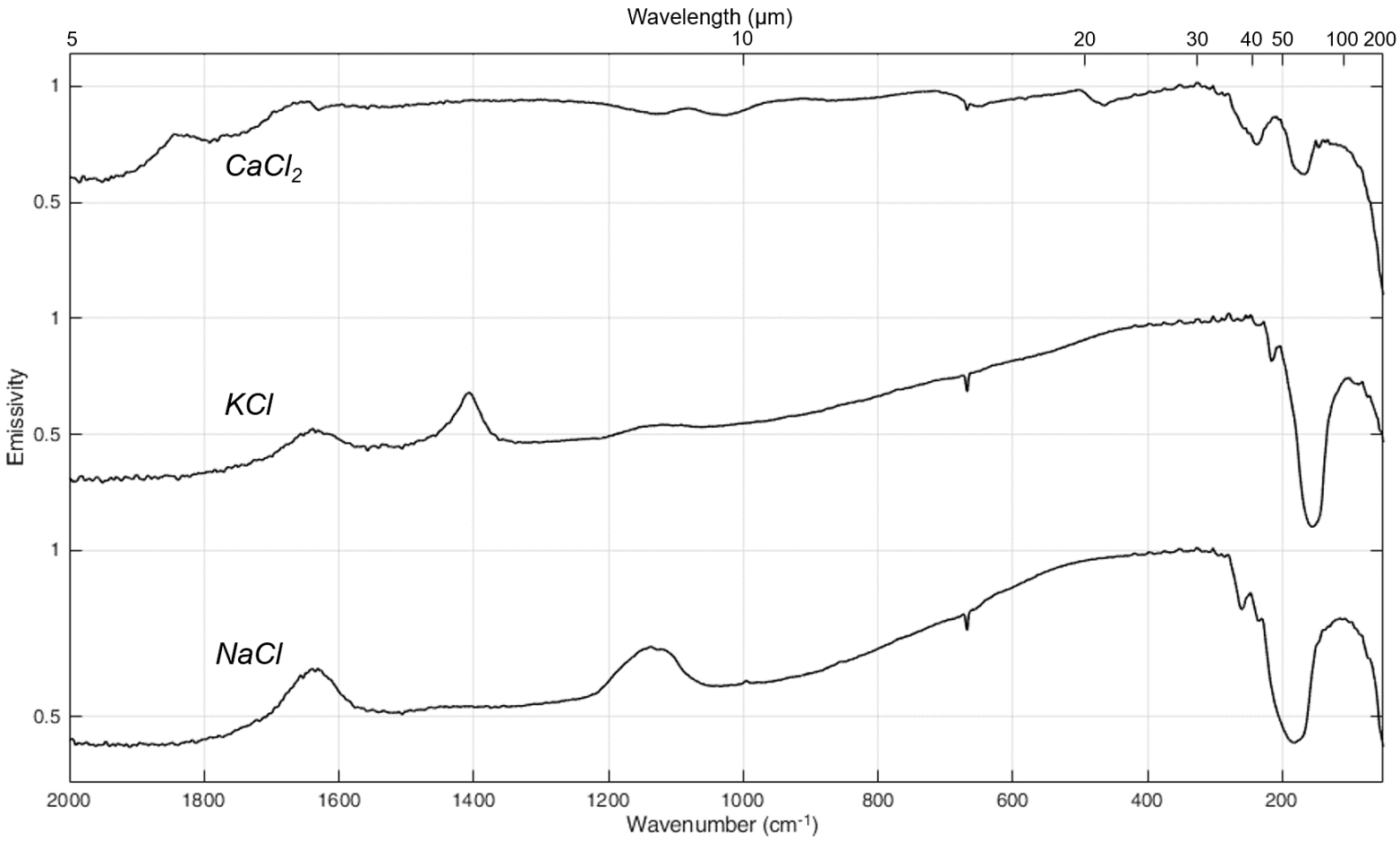

Figure 4.7. Mid-infrared through far-infrared emission spectra of pressed pellets. Top: $CaCl_2$, Middle: KCl (sylvite), Bottom: NaCl (halite).

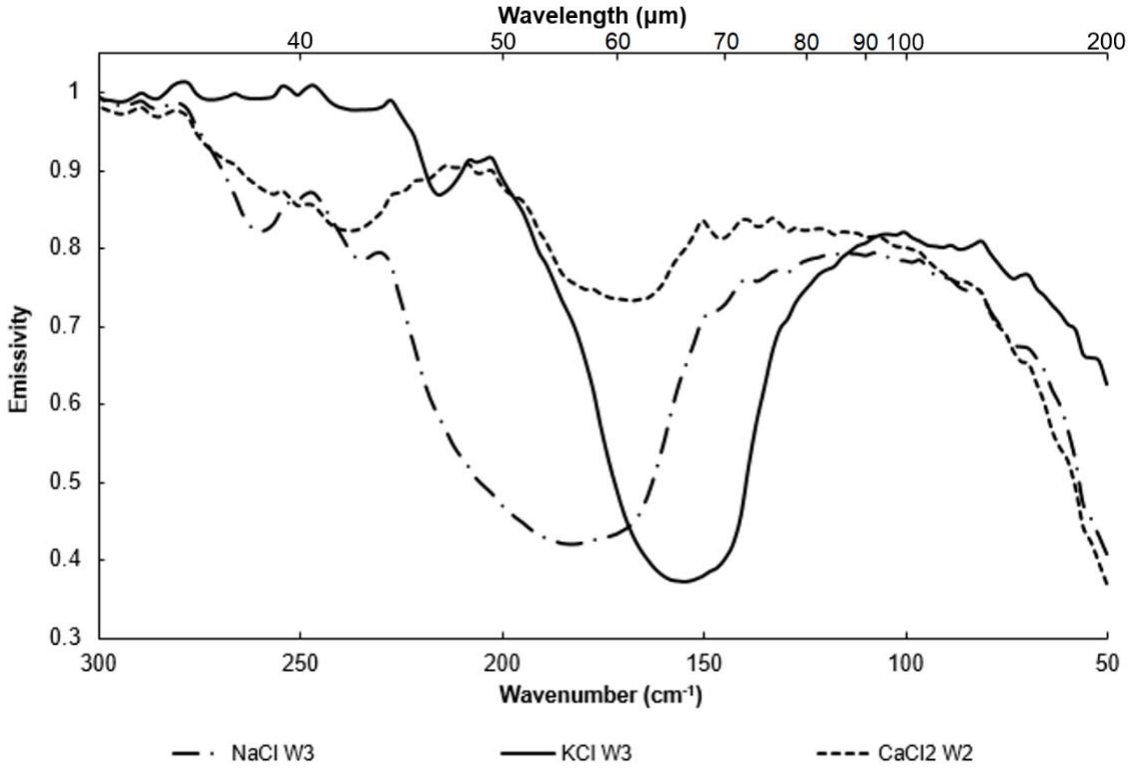

Figure 4.8. Far-infrared emissivity spectra of pressed pellets of several chloride species with sample names.

The mid-infrared spectra of the synthetic textures (Figure 4.9) show the adsorbed water absorption at 1627 cm^{-1}, while a subset of the samples (efflorescent crust, particles <180 μm, aggregate) show an absorption due to sulfate at 1110 cm^{-1}. The far-infrared emission spectra of the various chloride textures reveal systematic variations in both the depth and shape of their fundamental absorption features. These variations can largely be attributed to the particle size of the samples. The efflorescent crust has the smallest grains of all the synthetic samples, the sieved grains <180 μm are the second smallest, and the pressed pellet the third smallest. While the pressed pellet is used as reference, it is also composed of pure reagent-grade halite, and consists of grains that are largely in the ~180-200-μm size range. The sample with the next largest particle size is the >180 μm sample, which consists of asymmetric, fractured pieces of halite with an average size of 1.5 mm. The lab aggregate is the next largest sample, and consists of cemented cubes largely of the same size as the >180 μm particles. The small cubes are ~5 mm on a side, followed by the NaCl Pyramid: a single large cube that grew along its edges to produce the unique shape shown in Figure 4.6 above. Finally, the Large Crystal is as advertised: a single large, transparent crystal of halite with dimensions 12 x 24 x 3 mm.

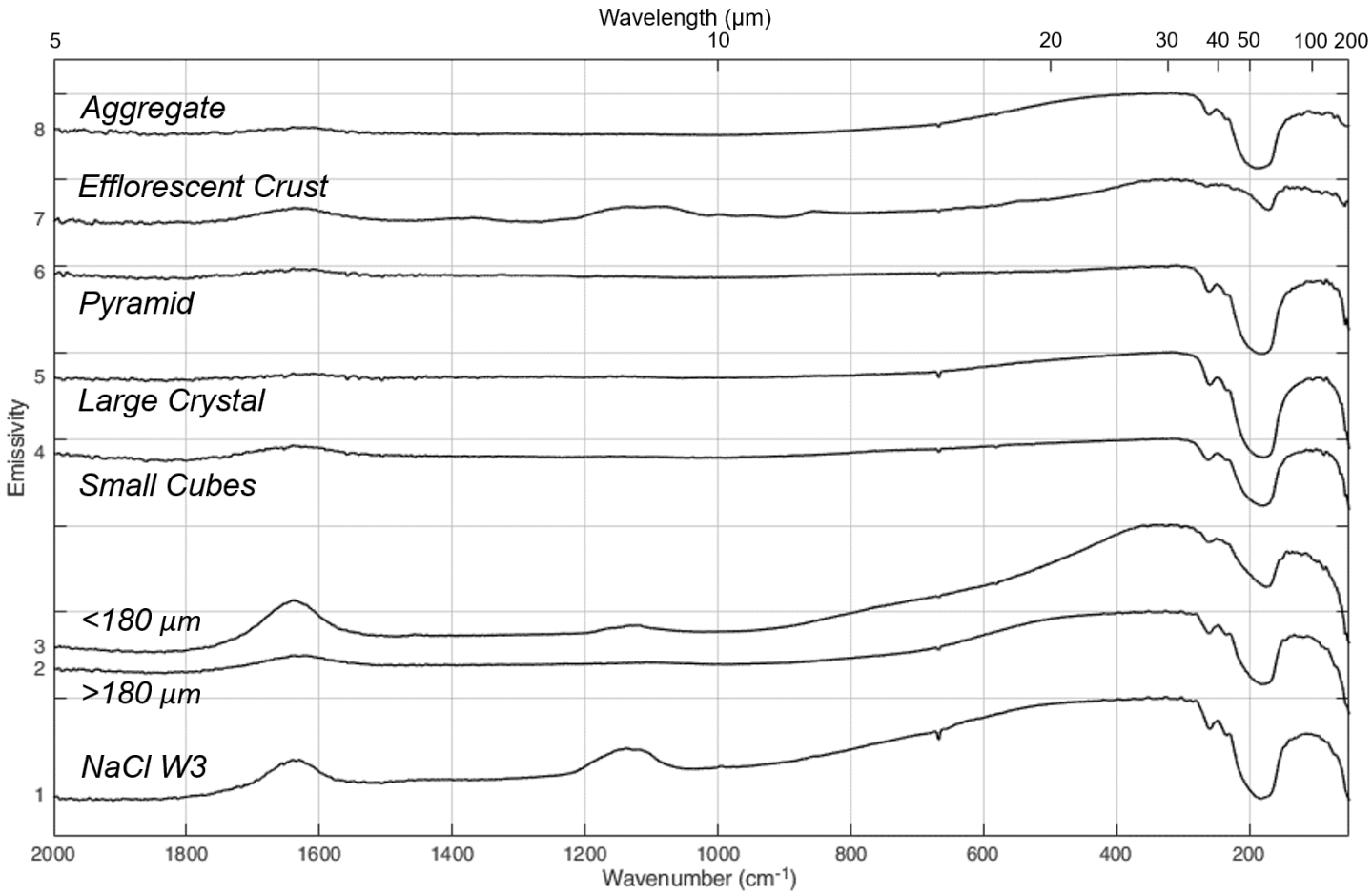

Figure 4.9. Mid-infrared and far-infrared spectra of synthetic chloride textures, offset for clarity. Emissivity spectra as labeled: 1) NaCl W3, 2) NaCl > 180um, 3) NaCl <180 um, 4) Small Cubes, 5) Large Crystal, 6) Pyramid, 7) Efflorescent Crust, 8) Lab Aggregate.

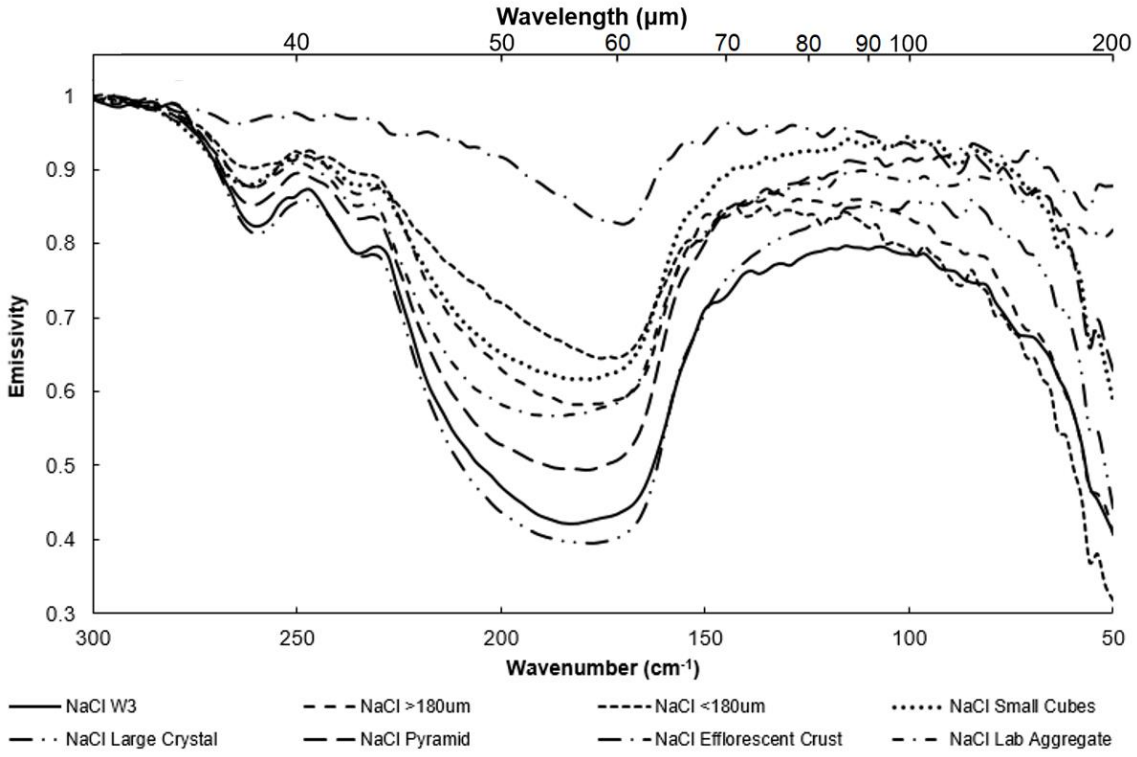

Figure 4.10. Far-infrared emission spectra of synthetic sodium chloride textures. “NaCl W3” refers to the halite pressed pellet.

Each spectrum in Figure 4.10 shows the fundamental absorption features of halite at ~180 cm^{-1} and ~260 cm^{-1}. Samples show variations in absorption asymmetry and depth with particle size. The two samples with the smallest particle size (efflorescent crust and <180 μm) show elevated absorption asymmetry relative to samples with larger particle sizes. At ~180 cm^{-1}, the higher wavenumber portion of the absorption is shallow with respect to the equivalent portion at low wavenumber for the efflorescent crust and <180 μm grains. Band asymmetries are often observed in silicates due to compositional variations (i.e., variations in Ca- versus Na-plagioclase in a single sample) [*Salisbury and Walter*, 1989; *Thomson and Salisbury*, 1993; *Lane et al.*, 2011]. Because the synthetic samples used in this study are all pure halite, we conclude that the asymmetry is due to scattering and is not the result of compositional variations.

Similar to silicates, the depths of chloride fundamental absorptions vary systematically with particle size, as shown in Figure 4.11, where samples are arranged in increasing particle size from left to right. An increase in the spectral contrast as a function of particle size shows that the effects of internal reflections, enhanced in samples with small grains, dominates at the fundamental transverse absorption feature. The pressed pellet ("NaCl W3") has a higher band depth than its particle size would suggest; however, this increased band depth is expected because the grains have been compressed as part of the pellet-making process. This compression artificially reduces/removes pore spaces, causing the whole of the sample to behave similar to a single large crystal. Indeed, the spectra of the pressed pellet and the large crystal overlap over most of the far-infrared; the major difference between the two is only at the height of the ~125 cm^{-1} shoulder, where the large crystal is higher by ~0.04 emissivity (Figure 4.10).

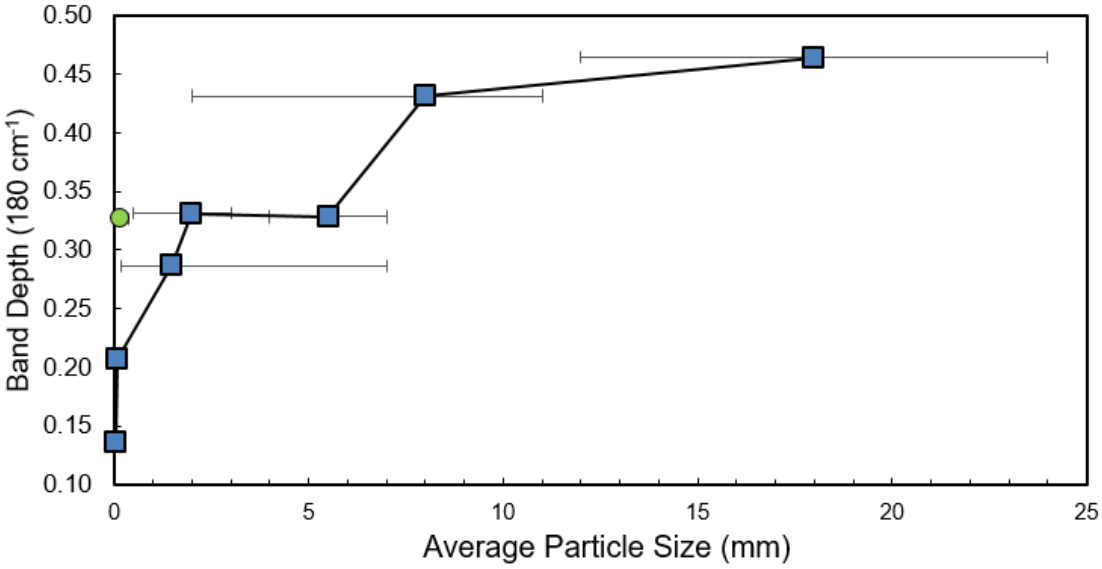

Figure 4.11. Band depth relative to continuum emissivity for synthetic sodium chloride textures for the fundamental ~180 cm^{-1} absorption feature, in order of increasing particle size from left to right. Green circle denotes band depth of NaCl pressed pellet projected on line fit. Horizontal lines indicate variations in particle size within each sample.

Another key property of the absorption features of all minerals is the location of the band center. The band center is known to shift for a material based on atmospheric conditions (temperature, pressure), minor compositional variations, and particle size; however, compositional variations have the most pronounced effect [*Salisbury*, 1993; *Salisbury and Wald*, 1992; *Mustard and Hays*, 1997; *Donaldson Hanna et al.*, 2016]. While the effects of particle size and texture are primarily expected to manifest in band depth/spectral contrast, their effect on band center has been observed for mixed-particle-size samples (i.e., lunar regolith) and must therefore be quantified. Figure 4.12 shows that the band center is at the highest wavenumber for intermediate particle sizes and samples with either cement-filled or compressed pores. Therefore, the effect of reduced pore spaces appears to shift the band center to higher wavenumber in a similar manner to

a reduction in atmospheric pressure. Decreasing atmospheric pressure reduces the gas in interstitial/pore spaces, inhibiting conduction through pores and limiting heat transfer to radiative-only [*Salisbury et al.*, 1994; *Donaldson Hanna et al.*, 2016]. The separate effects of particle size (where larger particles have higher spectral contrast) and the infilling of pore spaces (due to cementation or compression) have measurable effects on band center and band depth. The samples with the two highest band depths are the two single-crystal samples (the large crystal and pyramid). Figure 4.13 shows that band center position reaches a maximum wavenumber at intermediate band depths of ~0.3; samples that fell into this range include the halite pressed pellet, aggregate, and the small cubes. In their transverse fundamental absorption properties, we conclude that loose particles of 4-5 mm particle size (i.e., small cubes) behave similarly to smaller particles when the small particles are compressed/have reduced pore spaces (i.e., pressed pellet) or are well-cemented (i.e., aggregate).

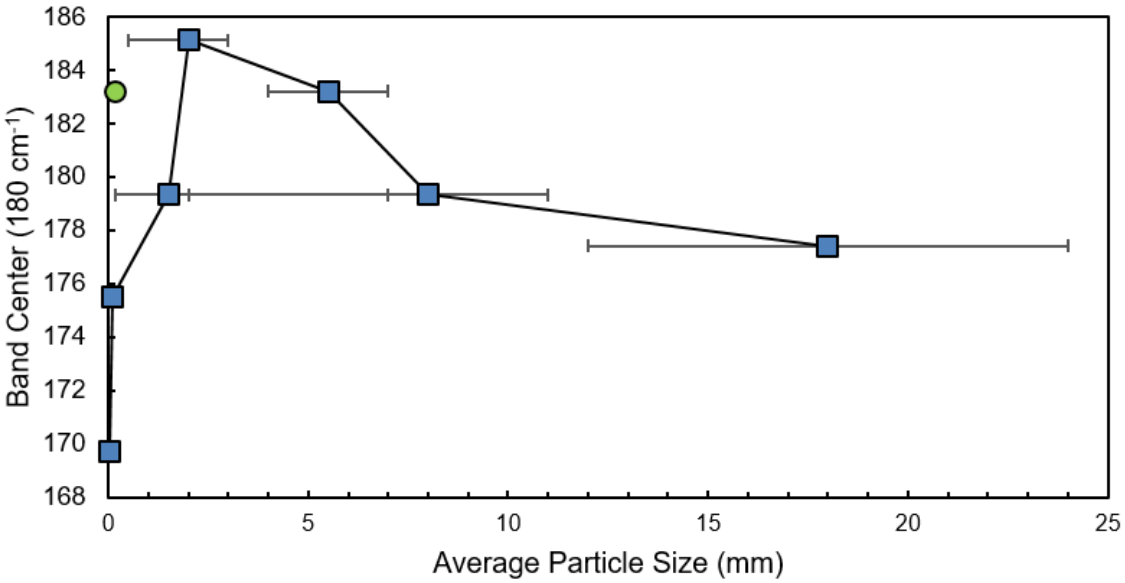

Figure 4.12. Locations of ~180 cm^{-1} band center versus average particle size of each synthetic sample, in order of increasing particle size from left to right. Green circle denotes band depth of NaCl pressed pellet. Horizontal bars show range of particle sizes observed in each sample.

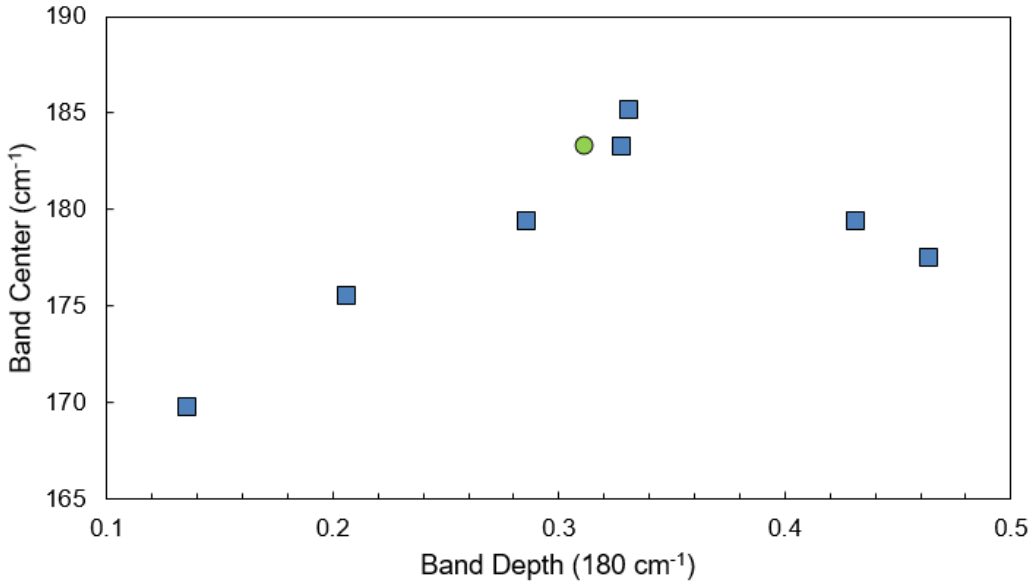

Figure 4.13. Band center of fundamental ~180 cm^{-1} absorption feature versus band depth for synthetic textures only. Green circle denotes band depth of NaCl pressed pellet; the two points close to the circle are the aggregate and small cubes samples.

The spectral contrast of the absorption feature associated with the Na-Cl longitudinal stretch at ~260 cm^{-1} was also explored. Because this is a lower-contrast feature than the transverse stretch, a lower range of band depths was expected as a function of particle size. In Figure 4.14, the band depth is shown to increase sharply with size through the >180-μm particle size, where it decreases as sharply before continuing with a less pronounced increase with particle size. A minimal band depth variation can be resolved for the three samples with the largest grains. The cause of the variation between the >180-μm particle size and the aggregate sample, which is largely composed of similar-sized grains that are cemented together, is difficult to constrain. The presence of a cement should increase band depth in the aggregate; therefore, it is most likely that numerous small (<180 μm) grains may be present in the aggregate sample which act to increase volume scattering in the sample and reduce spectral contrast. Regardless, the variation in band depth between the lowest-particle-size feature, the efflorescent crust (where this band could not be resolved) and the highest-particle-size is only ~0.04 emissivity; the spectral contrast at the 260 cm^{-1} absorption is a order of magnitude lower than that of the 180 cm^{-1} absorption.

Intermediate variations in band depth could be the result of transitions between scattering regimes; the wavelength of light at the 260 cm^{-1} absorption (~40 μm) is approximately 1/10 the size of many of the particles in the sample, which vary in size from 180 μm up to 2-3 mm. In this size regime, Mie scattering may occur, causing a marked increase in forward-scattered light from the interior of the sample; this effect would be detected as an increase in emission in the sample, resulting in lower spectral contrast at this wavelength range. This shorter-wavelength band is more sensitive to

small-scale textural variations and can therefore be used to compliment the larger variations in band depth versus particle size seen at longer wavelengths (lower wavenumber). The band center was virtually unchanged for all particle sizes for the 260 cm^{-1} feature, as shown in Figure 4.15.

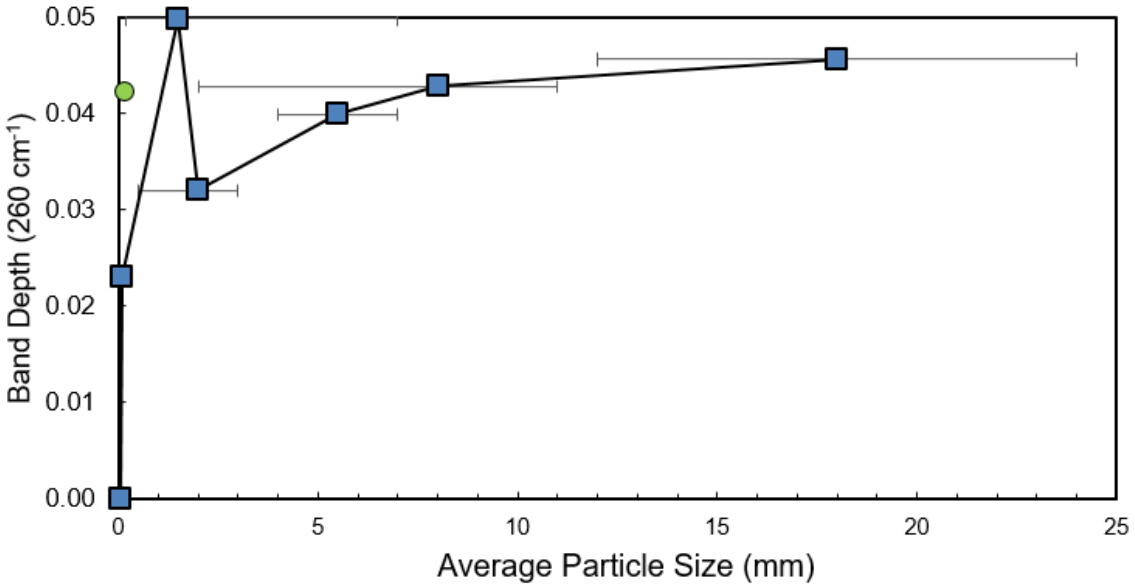

Figure 4.14. Band depth relative to continuum emissivity for synthetic sodium chloride textures for the fundamental ~260 cm^{-1} absorption feature, in order of increasing average particle size from left to right. Green circle denotes band depth of NaCl pressed pellet projected on line fit. Horizontal bars show range of particle sizes observed in each sample.

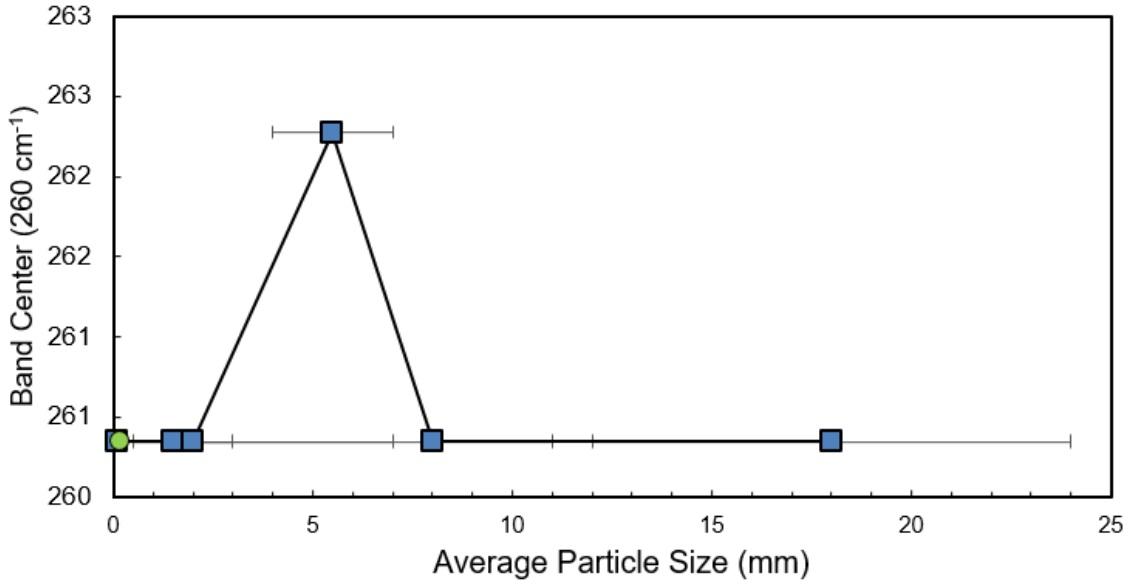

Figure 4.15. Locations of ~260 cm^{-1} band center for each sample, in order of increasing average particle size. Horizontal bars show range of particle sizes observed in each sample.

The location of the Christiansen feature is often used as an indicator of particle size in airless environments because it shifts systematically, and measurably, with particle size under vacuum conditions $<10^{-3}$ mbar [*Salisbury and Wald*, 1992; *Lane et al.*, 2011; *Donaldson Hanna et al.*, 2016]. Because each fundamental absorption has its own emissivity peak just short of the absorption, there can be multiple such features for a single mineral. In the case of chlorides, the fundamental absorptions are so closely spaced that the Christiansen feature of the transverse mode is subdued by the presence of the longitudinal mode and the combination ("two-phonon") band at ~235 cm^{-1} between them [*Hadni*, 1967]. For the purposes of this study, the "Christiansen feature" is referred to as the first Christiansen frequency, or the emissivity peak for the longitudinal mode. This is the only Christiansen feature that reaches emissivity = 1 through the entirety of

the mid- and far-infrared. Each of the samples in this study had broad Christiansen features, where emissivity = 1 across multiple wavenumbers; the wavenumber of the highest emission was used to define the precise location of the Christiansen feature. As shown in Figure 4.16, no resolvable or systematic variation in the location of the Christiansen feature was observed. The >180-μm particle size showed a distinct shift in the location of the Christiansen feature to lower wavenumber (longer wavelength), but it was the only sample to do so.

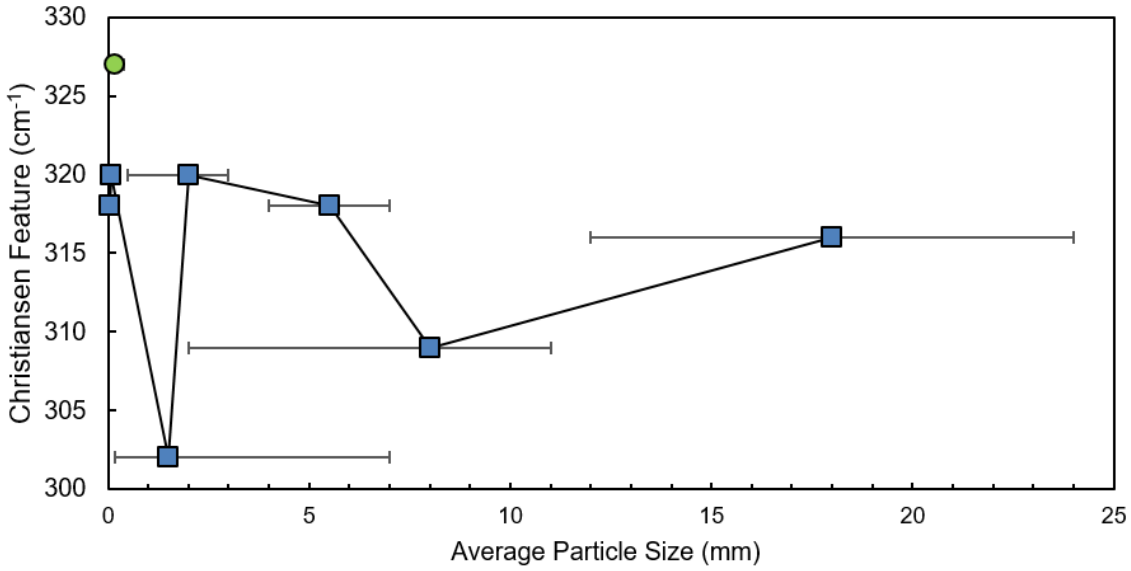

Figure 4.16. Christiansen feature (first emissivity peak) in cm^{-1} for each sample in order of increasing particle size. Horizontal bars show range of particle sizes observed in each sample.

Band ratios were used to assess the sensitivity of emissivity variations between the two fundamental modes to textural variation and particle size. The ratios of emission at the transverse fundamental (~180 cm^{-1}) to the longitudinal fundamental (~260 cm^{-1}) are shown for each sample in Figure 4.17 in order of increasing particle size from left to right. High band ratios indicate low/small differences in the emissivity at the two fundamentals, i.e. shallow absorptions for both features, while low band ratios indicate large differences between the two fundamentals. A general trend of decreasing band ratio with increasing particle size is evident. Additionally, samples consisting of loose or very small (< 180 μm) grains have consistently higher band ratios than coherent (single crystal, cemented, or compressed) samples. The large crystal has the greatest variation in

emissivity between the two fundamentals, and hence the lowest band ratio value, while the efflorescent crust has very similar emissivities between the two, and therefore the highest band ratio value.

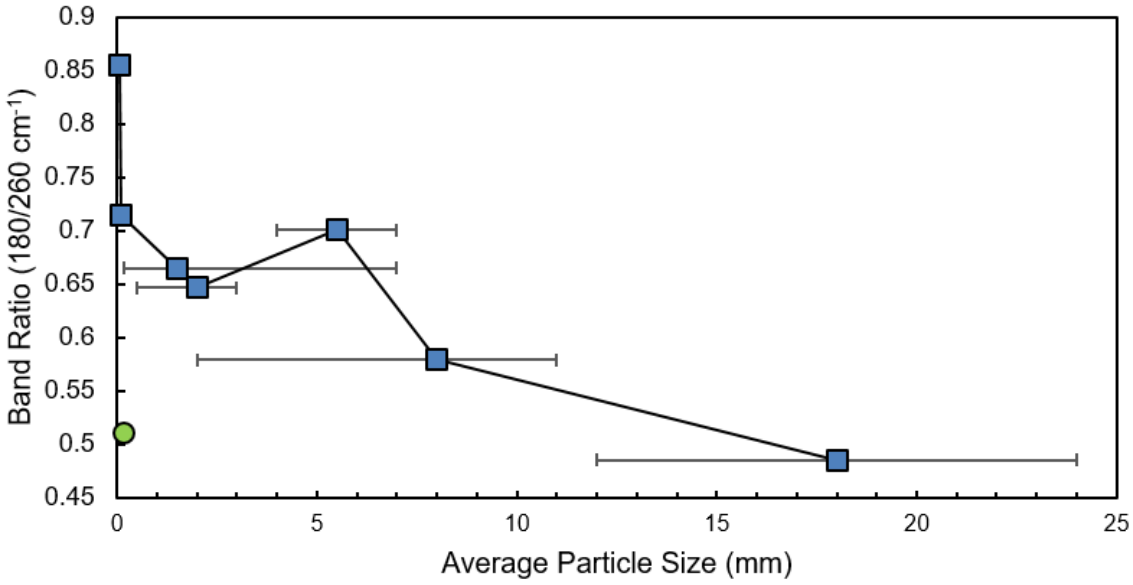

Figure 4.17. Band ratio, measured as emissivity at the transverse (180 cm^{-1}) fundamental divided by the emissivity at the longitudinal (260 cm^{-1}) fundamental, for each synthetic texture. Textures are ordered by increasing particle size from left to right. Green circle indicates the value for the NaCl pressed pellet projected between the two closest values. Horizontal bars show range of particle sizes observed in each sample.

4.4.3 Field Samples and Spectra

In order to determine the utility of the above measurements and observations for remote-sensing studies, a comparison must be made between laboratory samples and those observed in the field. Excluding the powders/pulverized samples, each of the textures produced in the laboratory was also observed in the field. Efflorescent crust (Figure 4.18a) was observed all across Bristol Dry Lake: between and on top of polygonally cracked halite, on mud-covered surfaces, coating desiccated trees and stray silicate rocks, etc. Because efflorescent crusts are extremely fragile and wash away quickly during rain showers, they are presumed to represent the most recent brine evaporation event.

Samples of polygonal halite (Figure 4.18b), which were the primary source of field sample spectra in this study, show a similar morphology to the aggregate samples in the lab. However, the polygonal halite lay on top of, and intermixed with, muds and clays that washed down from nearby alluvial fans. In contrast to the synthetic laboratory aggregates, naturally occurring polygonal halite is extremely hardy, to the point where most polygonally cracked structures at Bristol Dry Lake could support a person's weight with no surface deformation. These polygonally cracked structures are thought to be much older than the efflorescent crusts, and have likely experienced many years of wetting-desiccating cycles. This cyclic dissolution and re-precipitation has reinforced the cements in pore spaces and generally hardened the deposits. Their surfaces are smooth and highly reflective in the visible, suggesting a surface that is smooth on the sub-micron scale (Figure 4.2a).

Large single crystals (Figure 4.18c) were observed in the field, though they were uncommon and often coated in mud and clay. Storm events, rapid changes in evaporation rate, and contaminants (i.e., wind-blown dust) make it difficult for such crystals to form in nature. In spite of these hurdles, their identification in the field shows that single crystals are an important component of playa environments. Finally, hopper crystals (Figure 4.18d), show that the laboratory small cubes can also be identified in the field. The Bristol Dry Lake hoppers are numerous in damp, mud-rich portions of the playa where highly saline groundwater wets the surface from below. Dilute waters would prevent the formation of hoppers or dissolve hoppers that have already formed. The persistence and growth of hopper crystals indicates that a saturated brine is maintained in the groundwaters at Bristol Dry Lake. Unfortunately, because hoppers are typically found within/surrounded by wet muds, they represent only a fraction of the composition of the mud deposits. Therefore, these occurrences may be particularly challenging to locate or identify using remote sensing.

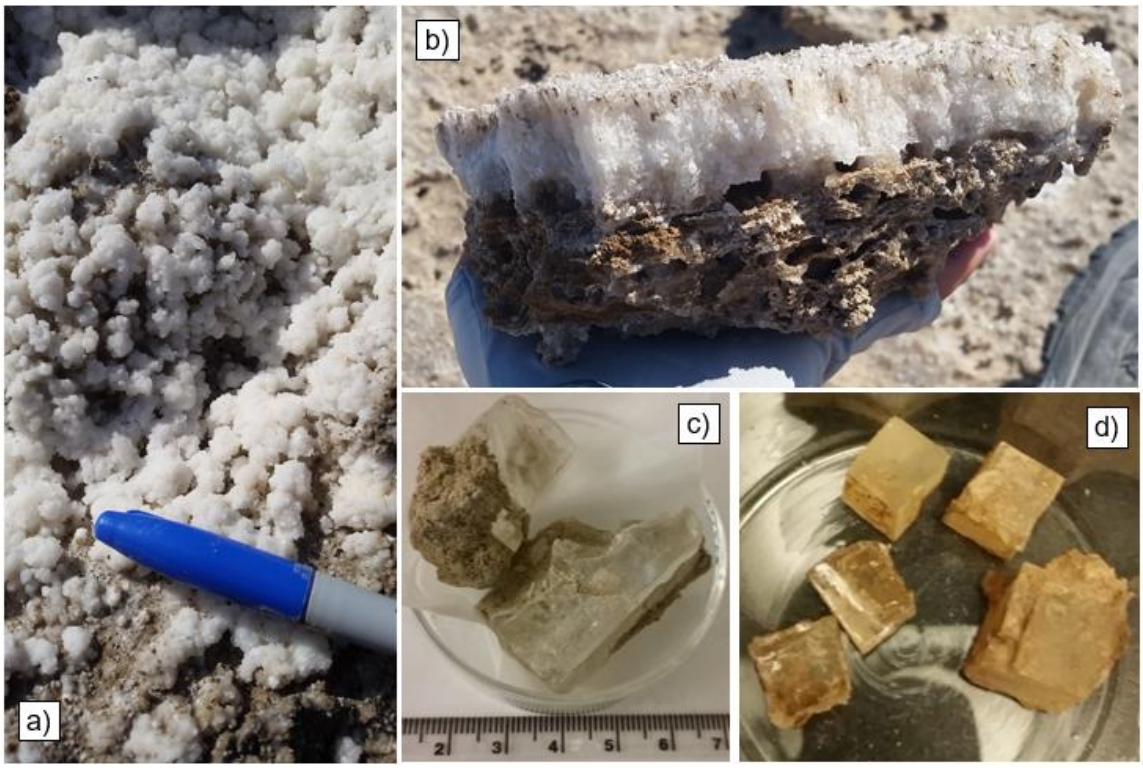

Figure 4.18. Field textures corresponding to synthetic samples. All textures observed at Bristol Dry Lake, CA. a) Efflorescent crust, b) Polygonal halite, c) large crystals, and d) small cubes (hoppers), average 1 cm on a side.

Three samples were used for the comparison of spectra between field and laboratory samples; these field samples are shown in Figure 4.19. Crushed polygonal halite (Figure 4.19a) was used to compare with the >180-μm particles and coherent polygonal halite. A large piece of polygonal halite, derived from the field sample shown in Figure 4.18b, was used to represent the surface of large halite polygon. This sample had a large amount of dried mud/clay on its underside as shown in Figure 4.18b; to prevent this clay from affecting the spectral analysis, it was removed using a Dremel™ tool and labeled as a "cleaned" sample in the spectra below. A photo of this cleaned sample is shown in Figure 4.19b. The final field sample was originally identified as

$CaCl_2$ due to its geographic location; this sample was labeled “Massive Salt” since its composition was unclear at the time of its collection (Figure 4.19c).

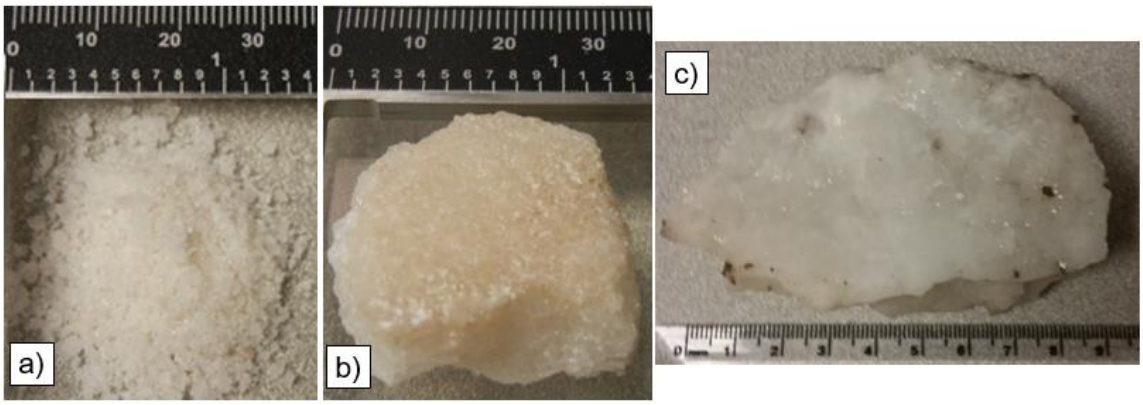

Figure 4.19. Field samples used for spectral analysis. a) Pulverized Polygonal Halite, b) Cleaned Polygonal Halite, and c) Massive Salt.

The mid-infrared spectra of the field samples (Figure 4.20) show a broad, reduced emissivity throughout the mid-infrared and the 1627 cm^{-1} feature indicative of adsorbed water. The sulfate absorption at ~1100 cm^{-1}, which is clearly visible in the pressed pellet reference, is virtually invisible in the field samples. Given the proximity of multiple sulfate species in the vicinity of Bristol Dry Lake [*Rosen et al.*, 1990], it is notable that they are not observable as trace contaminants in the polygonal halite samples. Additionally, there are no indications of clay or other silicates in the spectrum in spite of the discoloration that is evident in the samples and the fact that they were in direct contact with clay when collected in the field. Eastes (1989) observed evidence of montmorillonite (clay) mixed with halite in the mid-infrared for clay abundances as low

as 2% [*Eastes*, 1989]. Therefore, we conclude that the polygonal halite sample has <2% clay based on its lack of silicate features in the mid-infrared.

The far-infrared emission spectra of the field samples, with the pressed pellet ("NaCl W3") for reference, are shown in Figure 4.21. The broad absorption feature due to the transverse Na-Cl stretch is clearly visible in each sample, though shifted to lower wavenumber relative to synthetic samples (~175 cm^{-1} for field samples versus ~180 cm^{-1} for synthetic samples). The lower-contrast longitudinal feature in the field sample is immune to particle size or contamination and is located at 262 cm^{-1}, making it virtually indistinguishable from the synthetic samples. Additionally, the minor absorption at 235 cm^{-1} is resolvable for all of the field samples, again similar to those of the synthetic samples. The fundamental absorption of the "Massive Salt" sample distinctly identifies it as relatively pure halite; therefore, the usefulness of far-infrared analysis is shown by revealing the misidentification of this mineral species in the field.

The fundamental absorptions, while located at a similar wavenumber to synthetic samples (175 cm^{-1}), show asymmetries that are similar to the fine-grained synthetic samples (Figure 4.20, field samples, and Figure 4.9, efflorescent crust and <180 μm grains). This asymmetry in the field samples' spectra is unlikely to be due to scattering effects, since these samples are coherent and consist of grains much larger than 180 μm. However, the presence of sulfate or clay contaminants is not indicated in the mid-infrared; therefore, if the asymmetry is due to contamination, it is most likely to be from another chloride species. The presence of $CaCl_2$, however, may account for the asymmetry in the field samples. The fundamental absorption features of $CaCl_2$ largely overlap with those of halite and are significantly more shallow due to the fact that $CaCl_2$

is not isometric (Figure 4.7 and Figure 4.8). Therefore, the asymmetry in the halite absorption may be the expression of a Ca-Cl absorption that isn't strong enough to produce a resolvable absorption and instead produces a shallow shoulder. Additionally, because the deep-basinal brine at Bristol Dry Lake is calcium-chloride-rich [*Lowenstein and Risacher*, 2009], the likelihood of small quantities of calcium chloride in these samples is reasonable.

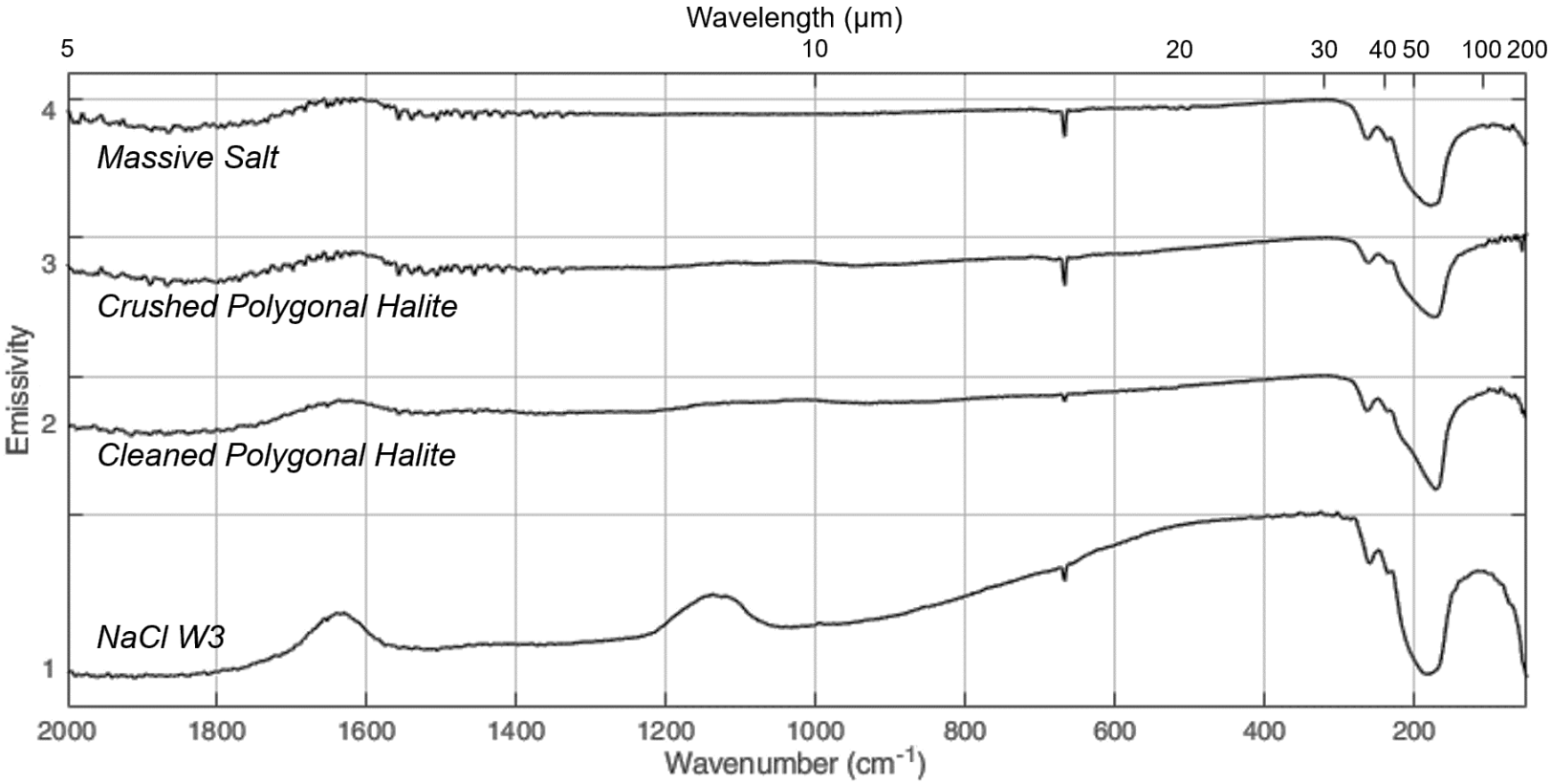

Figure 4.20. Mid-infrared and far-infrared spectra of field samples, with NaCl pressed pellet for reference. Emissivity values: 1) NaCl W3, 2) Polygonal Halite Cleaned, 3) Crushed Polygonal Halite, 4) Massive Salt. Spectra are offset for clarity, where numbered lines represent emissivity =1 for each spectrum.

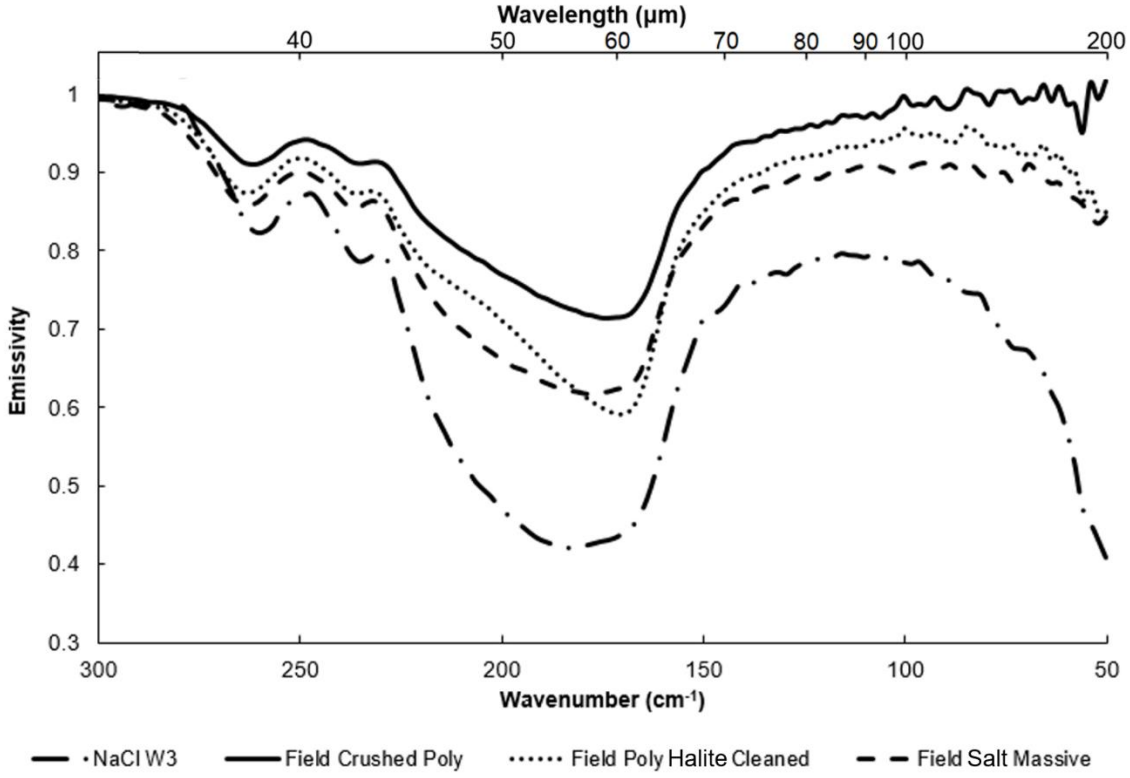

Figure 4.21. Far-infrared emissivity spectra of field samples, with NaCl pressed pellet ("NaCl W3") for reference.

The band depths and band centers for the field samples, with the pressed pellet for reference, are shown in Figure 4.22. No systematic variations in the band depth with particle size could be resolved, though the crushed polygonal halite sample did have a shallower band depth by ~0.1 emissivity. The Massive Salt in fact had a shallower band depth than either polygonal halite, perhaps due to the presence of minor antarcticite ($CaCl_2 \bullet 6H_2O$), which has no absorption at this wavenumber and is known to occur at Bristol Dry Lake, though this could not be confirmed [*Duning and Cooper*, 1969]. Additionally, no systematic variation in band center at the fundamental absorption could be ascertained.

The Christiansen features for each of the field samples fell within the range of what was measured in the synthetic samples, though the cleaned polygonal halite behaved most similarly to the pressed pellet, having a Christiansen feature at relatively high wavenumber (327 cm^{-1}). A summary of the Christiansen feature locations, band centers, and band depths for the two major absorption features for each sample are shown in Table 4.2. The band ratios for each field sample are shown with the synthetic samples in Figure 4.23; all of the field samples are intermediate in band ratio value between the efflorescent crust and the >180 μm particles. The variations in these values due to compositional, textural, and particle-size-related variations are discussed in the following section.

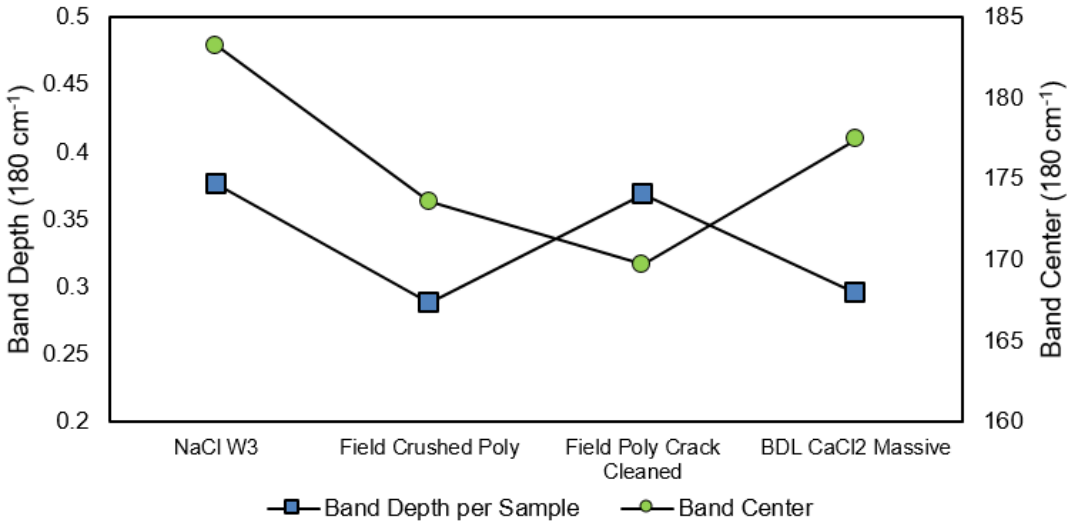

Figure 4.22. Band depth (left axis) and band center (right axis) for the ~180-cm^{-1} fundamental absorption feature for field samples, in order of increasing particle size. NaCl W3 pressed pellet included for reference.

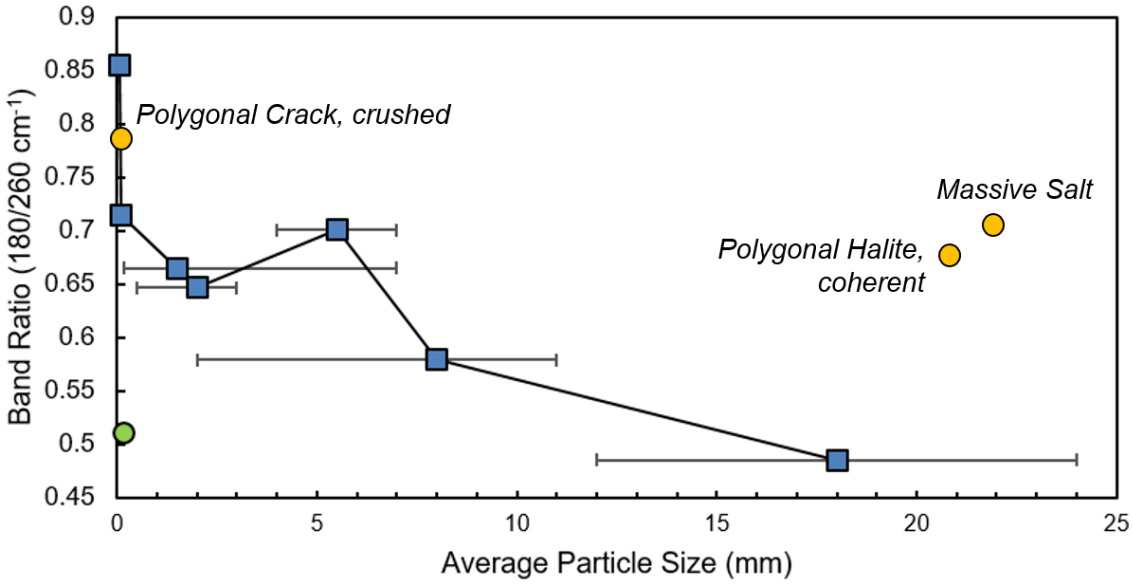

Figure 4.23. Band ratios between fundamental absorptions of all halite samples as a function of average particle size. Labeled field samples are marked by orange circles. Horizontal bars indicate variations in particle size for each texture.

The presence of atmospheric water vapor and carbon dioxide can pose particular challenges for mineral identification using far-infrared remote sensing [*Palchetti et al.*, 2009]. Numerous rotational and vibrational modes of these and other minor compounds (i.e., ozone, methane) can obscure the finer spectral features of minerals with absorptions in the far-infrared. We therefore conducted a first-order assessment of the resolvability of chloride absorptions in this water-dominated part of the electromagnetic spectrum by comparing radiance spectra for several samples. We observed that, in the absence of calibrated emissivity, radiance can be used qualitatively to assess the presence of chloride minerals. Figure 4.24 shows the radiance spectra of pressed pellets of halite (NaCl) and sylvite (KCl) and the interior of a sliced piece of basalt collected near El Malpaís, New Mexico. While dry air was used to purge the sample chamber, numerous water vapor and carbon dioxide absorptions persist in the radiance spectra; these absorptions are largely removed during the conversion from radiance to emissivity. In spite of the presence of water vapor and carbon dioxide, two major spectral properties allow the chlorides to be distinguished from basalt. First, the chloride minerals reach a much higher peak radiance than the basalt due to the location of their emission maxima (Christiansen features) in the far-infrared. Second, the fundamental absorptions of the chloride cause a substantial decrease in radiance at their respective fundamental wavenumbers. On Mars, the effect of a carbon dioxide-dominated atmosphere may deepen a subset of the atmospheric absorption features; however, these features are concentrated at higher wavenumber than the chloride fundamentals and should not prevent the first-order identification of chloride minerals on the martian surface.

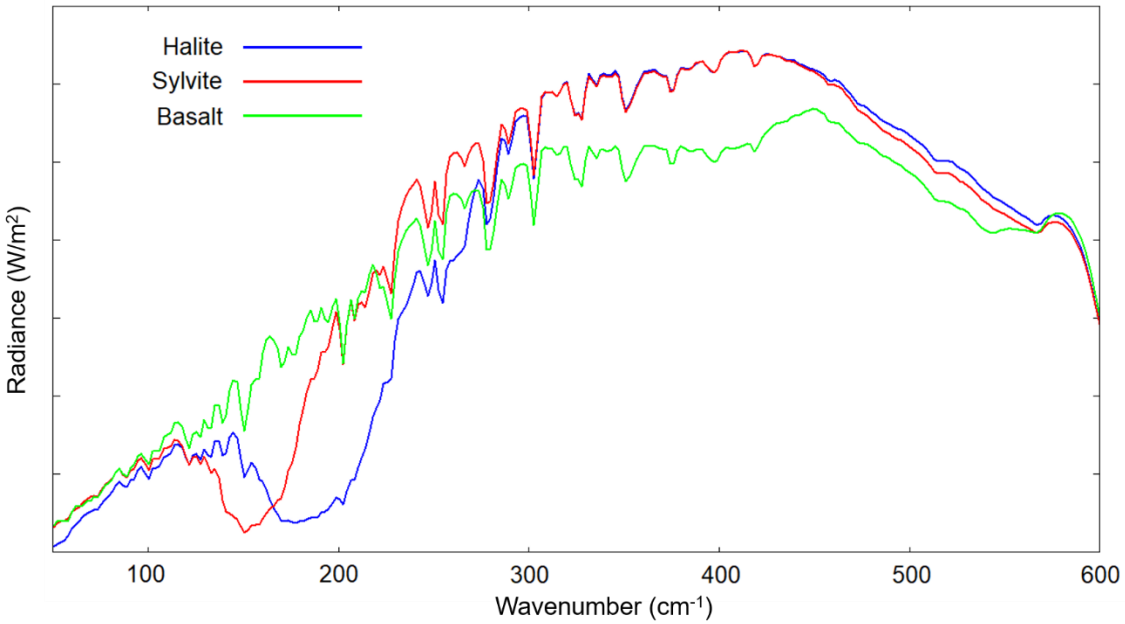

Figure 4.24. Radiance versus wavenumber (cm^{-1}) for pressed pellets of halite and sylvite compared to the interior of a sliced New Mexico basalt. Due to temperature variations between the samples, the sylvite spectrum has been scaled down by a factor of 0.75 and the basalt spectrum has been scaled up by a factor of four.

Table 4.2. Summary of Christiansen feature and band center locations for fundamental absorptions (in cm^{-1}) for all samples. Band depths are shown relative to approximate continuum emissivities for each absorption feature. For halite, Band 1 = ~180 cm^{-1} absorption (transverse Na-Cl stretch), and Band 2 = 260 cm^{-1} absorption (longitudinal Na-Cl stretch). For KCl, Band 1 = 154 cm^{-1} absorption (transverse K-Cl stretch), and Band 2 = 254 cm^{-1} absorption (longitudinal K-Cl stretch). For CaCl2, Band 1 = 168 cm^{-1} absorption (transverse Ca-Cl stretch), and Band 2 = combination of 230 and 250 cm^{-1} absorptions (longitudinal Ca-Cl stretch). *Band ratio = emissivity at Band 1 divided by emissivity at Band 2 for each sample.

	Sample Name	Christiansen Feature	Band 1 Center	Band 1 Depth	Band 2 Center	Band 2 Depth	Band Ratio*
Pellets	NaCl W3	327	183	0.31	260	0.05	0.51
	KCl W3	279	154	0.45	216	0.05	0.43
	CaCl2 W2	327	168	0.11	237	0.09	0.89
Lab Synthetic	NaCl Effl. Crust	318	170	0.14	--	--	0.86
	NaCl <180um	320	175	0.21	260	0.02	0.72
	NaCl >180um	302	179	0.29	260	0.05	0.67
	NaCl Lab Aggregate	320	185	0.33	260	0.03	0.65
	NaCl Small Cubes	318	183	0.33	262	0.04	0.70
	NaCl Pyramid	309	179	0.43	260	0.04	0.58
	NaCl Large Crystal	316	177	0.46	260	0.05	0.49
Field	Field Crushed Poly	316	174	0.29	262	0.03	0.68
	Field Poly Halite, Cleaned	327	170	0.37	262	0.04	0.78
	Massive Salt	318	177	0.30	262	0.04	0.72

In summary, we observed a predictable sequence of chloride morphologies for laboratory precipitation experiments at a range of evaporation rates (0.07 - 0.5 mm/hr). These evaporation rates fall into the range expected for current, and possibly ancient, Mars. The far-infrared spectra of pressed pellets of different chloride species showed distinct fundamental absorptions in the far infrared, though these absorptions largely overlap between halite and $CaCl_2$. The synthetic halite textures showed systematic variations in band depth at the 180 cm^{-1} transverse fundamental absorption, but this trend vanishes at the longitudinal 260 cm^{-1} due to the overlap of the transverse Christiansen feature with this absorption. There were no systematic variations in the location of the first (longitudinal) Christiansen feature with texture or particle size.

The textures produced in the lab were also observed in the field. Spectra of field samples of polygonally cracked halite and of an unknown salt were collected from Bristol Dry Lake, California; pulverized polygonal halite had a lower band depth than a coherent sample from the same source. The unknown ("Massive") salt proved to be halite; although it was a coherent (non-granular) sample, its transverse fundamental band depth was similar to that of the crushed/granular polygonal halite. Larger trends in band ratio between the two fundamentals were observed for both synthetic and field samples, and generally follow the same trend as band depth for the transverse fundamental absorption.

4.5 Discussion

4.5.1 Constraining Chloride Mineralogy

The lack of fundamental absorption features, and the generally high transparency of chlorides in the mid-infrared (~2000 - 400 cm^{-1}), prevent the mid-infrared from being useful for constraining the type of chloride. Hydrated chlorides, such as antarcticite ($CaCl_2 \cdot 6H_2O$) and bischofite ($MgCl_2 \cdot 6H_2O$), should be identifiable if they are present in high enough abundances due to the many vibrational modes of water that produce distinct hydration features in the visible, near-infrared, and mid-infrared. Each cation-oxygen bond has a specific bond energy that produces a unique absorption for each hydrated chloride [*Nyquist and Kagel*, 1971; *Farmer*, 1974; *Baldridge*, 2008]. Coupled with their largely featureless spectra in the mid-infrared, the hydrated chloride minerals should be detectable by current orbiting instruments.

Anhydrous chlorides have posed more of a challenge. Their featureless, low-emissivity spectra allow their presence to be inferred in the mid-infrared (5-25 μm), but not confirmed. Previous studies have estimated their abundances in the range of 10-25% at the chloride sites on Mars [*Baldridge*, 2008; *Osterloo et al.*, 2008, 2010; *Glotch et al.*, 2016]. This study has shown that halite can be definitively identified by its broad, deep absorptions in the far-infrared. Because sylvite is also an isometric, anhydrous chloride, it has the same mid-infrared detection hurdles as halite. The measured crustal Na_2O/K_2O ratio for Gusev Crater is 8.9 and martian meteorites have measured Na_2O/K_2O ratios of 12.5 [*McSween et al.*, 2009]. Therefore, if martian crustal ratios are reflected in evaporite deposits, sylvite abundance is likely much lower than that of halite due to the lower stoichiometric abundance of potassium relative to sodium on Mars. This study has

demonstrated that sylvite has distinct far-infrared emission features that allow it to be positively identified and distinguished from halite. If anhydrous calcium chloride exists on Mars, it can be approximately distinguished from halite due to the overlapping 250 and 230 cm^{-1} absorption features; however, it is unlikely that the large 168 cm^{-1} feature could be confidently distinguished from the ~180 cm^{-1} halite absorption due to the large width of both features. We have also shown that the location of the band centers and the band widths can be used to distinguish between halite and sylvite in the far-infrared. Because anhydrous calcium chloride has an overlapping transverse absorption with halite, other absorptions (i.e., the longitudinal stretch) will be needed to provide a confirmation of the exact mineral species in that case. However, it is unlikely that anhydrous calcium chloride exists on Mars because it is highly hygroscopic; water vapor is known to exist in Mars' atmosphere, therefore calcium chloride is most likely to be found as sinjarite ($CaCl_2 \bullet 2H_2O$) or antarcticite ($CaCl_2 \bullet 6H_2O$).

4.5.2 Constraining Chloride Texture and Particle Size

Systematic variations in particle size were observed for all of the synthetic spectra included in this study. The primary effect of particle size is to change the spectral contrast of the fundamental absorption features. This is a well-known property of common geologic (silicate) materials in the mid-infrared. [*Salisbury and Wald*, 1992; *Thomson and Salisbury*, 1993; *Salisbury et al.*, 1994; *Moersch and Christensen*, 1995; *Wald and Salisbury*, 1995; *Lane et al.*, 2011]. We have shown that these properties extend into the far-infrared for chloride minerals. Overall, we observe that chlorides have Class 3 (weakly absorbing and $n > 1$) behavior over virtually all of the mid-infrared

(2000 – 400 cm^{-1}). They transition to Class 4 ($k < 0.1$ and $n = 1$) at the first Christiansen feature, the exact location of which varies based on mineralogy [*Moersch and Christensen*, 1995]. In the far-infrared, chlorides transition to Class 1 (large k) spectral behavior, where they show an inverse relationship between emissivity and particle size at the fundamental absorption features.

The overlap of the transverse Christiansen frequency with the longitudinal and combination bands acts to increase the emissivity at those wavenumbers; the result is that the transverse mode is much more sensitive to changes in particle size and, hence, shows greater changes in emission with particle size than the longitudinal mode. We believe this overlap between Class 1 and Class 4 regions is why the band ratios decrease consistently with increasing particle size, as shown in Figure 4.23. Because there is some overlap between the Christiansen frequency of the transverse mode and the longitudinal and combination ("two-phonon") band, the two fundamentals behave dissimilarly with changes in particle size [*Hadni*, 1967]. In the absence of full characterization of the transverse absorption feature, the ratio between the transverse and longitudinal bands could be used as a proxy for particle size.

Cementation and compression of chloride particles have distinct effects on their far-infrared emission spectra [*Baldridge*, 2008]. Both act to reduce internal reflections, increasing spectral contrast and band depth for the fundamental absorption features relative to loose particles [*Salisbury and Wald*, 1992; *Lane et al.*, 2011]. The single large crystal of halite had the largest band depth of any sample in this study, showing that cementation and compression do not increase band depth to the fullest extent; this behavior is the same as that observed for silicate minerals. In contrast to the coarse

materials, the efflorescent crust showed the highest average emissivity of any sample in this study. This behavior is expected for fine-grained materials where pore spaces, and therefore internal reflections, are numerous; these reflections result in an enhanced sample emissivity in spectral regions where the emissivity would typically be low. The transverse fundamental absorption was visible in the efflorescent crust, but its band depth was low, and the longitudinal absorption was not resolvable. Therefore, we conclude that efflorescent crusts will be extremely difficult to detect using the techniques outlined in this study.

The trend of band ratio values in Figure 4.17 and Figure 4.23 indicates that the transverse fundamental absorption, which is at a longer wavelength (~55 μm) than the longitudinal fundamental (~38 μm), is disproportionately amplified relative to the longitudinal as the sample becomes more cemented and/or has larger grains. Based on band ratio alone, the field samples in Figure 4.23 would be interpreted as loose and/or fine-grained materials. Since the Cleaned Polygonal Halite and Massive Salt samples are large, coherent materials, they can in principle be discriminated from fine grains by assessing their diurnal temperature variations (thermal inertia). We conclude that a combination of properties, including mid-infrared peaks (if present), band depth for each fundamental, band ratio values, and thermal inertia, will be required to be distinguish each texture using far-infrared remote sensing.

4.5.3 Sensitivity to Contaminants

Sulfates, especially gypsum ($CaSO_4 \bullet 6H_2O$) and anhydrite ($CaSO_4$), are common in playa settings because they are the next most soluble species in natural waters after chlorides [*Hardie and Eugster*, 1970; *Catling*, 1999; *Lowenstein and Risacher*, 2009]. Typically, as natural waters evaporate and become more concentrated, sulfates precipitate out before chlorides, forming a ring around evaporating and constricting ponds that can be easily identified using remote sensing [*Hardie and Eugster*, 1970; *Baldridge et al.*, 2004]. Sulfate species have been observed in reagent-grade halite and show distinct features in their mid-infrared spectra. However, only textures with a large number of internal reflections (fine grains, weakly cemented aggregates, or compressed powders) show the sulfate feature. Coarser grains and single crystals in this study did not show indications of sulfate. On Mars, sulfate is a common mineral, and many hydrated and anhydrous species of sulfate minerals have been identified [*Clark et al.*, 2005; *Dalton et al.*, 2005; *Gendrin et al.*, 2005; *McLennan et al.*, 2005; *Lane*, 2007; *Roach et al.*, 2010; *Bibring et al.*, 2007; *Kaplan et al.*, 2016; *Rampe et al.*, 2016]. Therefore, we recommend that future ground and orbital investigations of chlorides on Mars be sensitive to the detection of sulfate minerals in the mid-infrared as chloride minerals are investigated in the far-infrared.

Other contaminants that were visibly observed in the field included muds and clay particles. While the exact clay species was not determined, it is notable that no indications of clays were seen in the mid- or far-infrared spectra of field samples. This lack of a clay signature was in spite of the fact that mud was physically abraded from the bottom surface of the polygonal halite sample, and almost certainly left behind some

residual clay. Eastes (1989) observed clay spectral features intermixed with halite for clay abundances as low as 2%; therefore, we conclude that lower than 2% clay was present in the field sample after cleaning.

As a result of the lack of sulfate or clay detection in the field samples, and the irregular expression of sulfate in the various chloride textures, we conclude that such contaminants are not a major hurdle in identifying chlorides using the techniques in this study. However, we expect that significant quantities of dust and basalt, or the presence of only thin deposits of chloride will pose unique challenges for detecting chlorides using far-infrared emission spectroscopy on Mars [*Berger et al.*, 2015; *Glotch et al.*, 2016].

4.5.4 Environmental Implications for Mars

The variations in evaporation rate in the production of synthetic samples showed several important characteristics in the production of chloride deposits. First, we observed that the range of evaporation rates from 0.07 – 0.5 mm/hr was not large enough to produce measureable changes in the evolution of chloride crystals during precipitation. Because this range of evaporation rates overlaps with that expected for the martian surface under present environmental conditions, the textures produced are considered reasonable for chlorides forming on the martian surface. Late-Noachian/early-Hesperian surface conditions were likely more favorable for the stability of water/brine on the surface due to the presence of water-bearing minerals and geomorphologic features dated to that time period. Thus, brines may have experienced lower evaporation rates due to environmental conditions more favorable for the presence of liquid water [*Sagan et al.*, 1973; *Poulet et al.*, 2005; *Baker*, 2006]. Lower evaporation rates could only have

resulted in larger crystals (at least upon initial deposition), showing that the textures represented in this study could be considered a "worst case" in terms of particle size and corresponding spectral contrast of the initial deposits.

Geomorphologic evidence shows that substantial amounts of liquid water – up to 10^8 m^3/s - flowed over the martian surface during the late-Noachian/early-Hesperian timeframe (3.5 - 4.0 Ga) [*Carr*, 1979; *Coleman*, 2003; *DiAchille and Hynek*, 2010; *Hynek et al.*, 2010; *Hoke et al.*, 2011]. This water may have provided the starting point from which a chloride-rich brine eventually formed. It is not known whether this brine originated from surface flows or manifested as groundwater upwelling. However, the elevated thermal inertia of chlorides on Mars shows that the chlorides present are likely well-cemented [*Osterloo et al.*, 2008, 2010]. Indeed, their mere presence on the martian surface – in spite of atmospheric phenomena and numerous meteorite impacts of various energies – shows that they are, to some extent, similar to the coherent polygonally cracked halite at Bristol Dry Lake. The terrestrial polygonal crack structures have undergone numerous wetting/desiccation cycles, with each cycle further cementing the structures of those features. It is therefore possible that martian chloride polygonal crack structures, which have been observed from orbit by the HiRISE camera at high spatial resolution, have undergone similar repeated wetting/desiccation cycles to account for their persistence on Mars [*El-Maarry et al.*, 2013, 2015].

If the martian chloride deposits do indeed represent multiple extended periods of wetting and drying on Mars, they preserve evidence of what may have been the most active hydrological period in Mars' history [*Poulet et al.*, 2005]. Now that we know we can correlate absorption location to composition and spectral contrast to particle size, we

can begin to explore the nature of these deposits more fully. The topographic lows where chlorides are now observed may show a range of particle sizes, where larger crystal aggregates formed in the center and thin crusts formed along the edges. Such a variation in texture would manifest as a decrease in spectral contrast from the center of the deposit to the edges. If such a trend were observed, it would provide indirect evidence for the sustained presence of liquid water on the surface of Mars. As chloride-bearing brines evaporated on early Mars, they became more concentrated and less hospitable for any microorganisms that may have existed at the time [*Tosca et al.*, 2008; *Davila et al.*, 2010; *Al Soudi et al.*, 2016]. It follows that the transition from coarse to fine textures/particle sizes in chloride deposits may encompass the time period in which life stopped or could no longer persist on Mars. Therefore, this study concludes that martian chloride deposits should be considered high-priority targets for future astrobiological studies. In particular, two chloride deposits in Terra Sirenum – one large deposit and another in the Eridania Basin - provide significant potential for future astrobiological investigations.

The Terra Sirenum region (~32.70° S, 205.84°E) hosts the largest chloride deposit on Mars (~25 km^2). Sinuous features, mostly likely carved by liquid water, provide geomorphologic evidence for a large supply of water to the basin where the large chloride deposit is located. Within these sinuous features, chlorides are found at topographic lows and in the form of inverted channels. The chloride-based inverted channels coalesce into a large chloride deposit at a topographic low within the basin. This large chloride deposit shows a fractured texture similar to that of terrestrial playas, though highly degraded and in many places scoured/scalloped. [*Osterloo et al.*, 2008, 2010] Phyllosilicates are co-located with chlorides in this region, lending further

evidence to the sustained presence of a body of water in this region. The stratigraphic relationships between the two materials indicate that the chlorides are somewhat younger than the phyllosilicates, though how much younger remains unknown. [*Glotch et al.*, 2010]

West of the large chloride deposit is the Eridania Basin, where the Eridania paleolake is thought to have existed during the late-Noachian and Hesperian Periods. Chlorides co-located with phyllosilicates are also observed in Eridania, and appear as polygonally fractured, light-toned features. Phyllosilicates in the Eridania Basin include both Fe/Mg- and Al- phyllosilicates in close proximity to chlorides, indicating a complex history of chemical evolution. The chlorides are concentrated in what is called the "Northern Basin" by Adeli et al. (2015), which feeds into Ma'adim Vallis, one of the largest martian outflow channels [*Adeli et al.*, 2015]. Recent studies have revealed the presence of a mineralogical suite indicative of an ancient seafloor hydrothermal system in Eridania Basin. The mineralogy includes saponite, Fe-rich mica, Fe- and Mg- serpentine, Mg-Fe-Ca-carbonate, and possible Fe-sulfide and dates to ~3.8 Gy. These minerals are located in a region adjacent to the chloride-bearing Northern Basin and are found in or near terrestrial oceanic hydrothermal systems. [*Michalski et al.*, 2017] Therefore, the northern portion Eridania provides a perfect testbed from which to assess the provenance of chlorides on Mars. Additionally, hydrothermal systems on Earth provide both chemical and thermodynamic conditions favorable for life. If the Eridania paleolake behaved similar to seafloor hydrothermal zones, it provided a habitable environment and is therefore a high-priority target for future astrobiological investigations of Mars.

4.5.5 Future Work

This study represents a limited introduction to the field of far-infrared emission spectroscopy for the identification and characterization of chloride minerals in the laboratory and field. Hydrated chloride species that should have many of the fundamental absorptions of their anhydrous counterparts were not included in this study. Specifically, spectra of sinjarite ($CaCl_2 \cdot 2H_2O$), antarcticite ($CaCl_2 \cdot 6H_2O$), and bischofite ($MgCl_2 \cdot 6H_2O$) should be obtained and compared to anhydrous calcium and magnesium chloride samples. Additionally, mixed-cation chlorides found in nature such as carnallite ($KMgCl_3 \cdot 6H_2O$) and tachyhydrite ($CaMg_2Cl_6 \cdot 12H_2O$) should be characterized and compared to monocationic species. Mixtures of chloride minerals should be evaluated to assess the potential for linear deconvolution of the chloride species; deconvolution of chloride spectra would allow their abundances to be determined quantitatively. Additional field samples of efflorescent crusts and other minor textures (i.e. large crystals and hoppers) should be characterized to further constrain the effects of contaminants and textural heterogeneity.

Finally, this study shows definitively that chloride minerals can be both identified and characterized using far-infrared emission spectroscopy. Chloride deposits on Mars cover square-kilometers of area, providing rich targets for future analysis. Instruments capable of measuring emission in the far-infrared (>45 μm or <225 cm^{-1}) therefore have the potential for high scientific impact and should be a priority for inclusion on future spacecraft.

4.6 Conclusions

The far-infrared provides a new and unexplored avenue for studying the chemistry and physical properties of chloride minerals on the martian surface. In this study, the mid- and far-infrared emission spectra of a suite of chloride compositions, synthetic textures, and field samples were compared. Spectral features were quantified as a function of composition and texture, including: the locations and depths of fundamental absorptions, the locations of Christiansen features, and the relative variations in band depth between the transverse and longitudinal absorptions. Sylvite was easily distinguished from halite and from $CaCl_2$ based on the locations of its fundamental absorption features. However, the low spectral contrast and overlap of multiple absorption features results in $CaCl_2$ largely overlapping with halite; because is extremely hygroscopic, it is expected to be found on Mars it its hydrated state, in which case, it can be readily distinguished from halite at shorter wavelengths.

Particle size was shown to have a significant effect on the depth of the transverse (~180 cm^{-1}) fundamental absorption feature and on the ratio between the transverse and longitudinal (260 cm^{-1}) fundamental absorption features. Therefore, in the far-infrared, chlorides behave in a similar way to silicates in the mid-infrared. Field samples from a Mars-analog terrestrial site were used to assess the behavior of spectral features in natural samples. Field samples showed similar variations in spectral contrast between loose grains and coherent samples of polygonal halite. Though the field samples were easily identifiable as halite, the band depths of their fundamental absorptions did not vary to the degree of synthetic textures, which may pose challenges for quantifying the textural variations of natural chloride deposits on Mars.

4.7 Acknowledgments

First, I thank Ashley Toland and Tara Fisher of the Mars Space Flight Facility for their endless assistance in obtaining and setting up the laboratory for the salt precipitation studies. I also extend a huge thanks to Drs. Tim Glotch and Deanne Rogers, along with the students of the CPx group at Stony Brook University; without their patience and positivity in training me in the collection of far-infrared spectra and their calibration, this work would not have been possible. I also thank the Mars Odyssey Project for funding this work.

CHAPTER 5

RECURRING SLOPE LINEAE AND CHLORIDES ON THE SURFACE OF MARS

The following is reproduced from Journal of Geophysical Research: Planets, *where it was published in September 2016. Co-author is Phil Christensen.*

5.1 Introduction

The presence of liquid water on the surface of Mars has substantial geologic and astrobiological implications. First, liquid water is thought to have played a key role in shaping the surface of Mars in the form of valley networks [*Craddock*, 2002; *Fassett and Head*, 2008; *Hynek et al.*, 2010], paleolakes [*Cabrol and Grin*, 1999], channels [*Coleman*, 2003], deltas [*DiAchille and Hynek*, 2010; *Hoke et al.*, 2014], and gullies [*Malin and Edgett*, 2000]. Second, sites where liquid water is or has been present are more likely to harbor extant or remnants of martian life compared to sites with no liquid water [*Farmer and Des Marais*, 1999; *Cady et al.*, 2003]. Earth analog studies have shown that microorganisms can persist even in very arid, saline environments and to substantial depths [*Rothschild*, 1990; *Rothschild and Mancinelli*, 2001; *Parro et al.*, 2011]. Potential sources and sinks of liquid water are therefore high-priority targets of study; the most likely candidates for active liquid water flow on the surface of Mars are Recurring Slope Lineae (RSL). RSL are seen on steep slopes in both equatorial and southern mid-latitudes of Mars, appearing as low-albedo streaks that grow down-slope over a single season (Figure 5.1) [*McEwen et al.*, 2011a].

Images from the High-Resolution Imaging Science Experiment (HiRISE) have shown that southern-hemisphere RSL appear, grow, and fade during the summer only (Ls = 270-360°). During this time, they reach lengths of tens to hundreds of meters and widths less than 10m. Equatorial RSL found in Valles Marineris are most prominent during Ls = 50-200° for northern-facing slopes and Ls = 200-290° for southern-facing

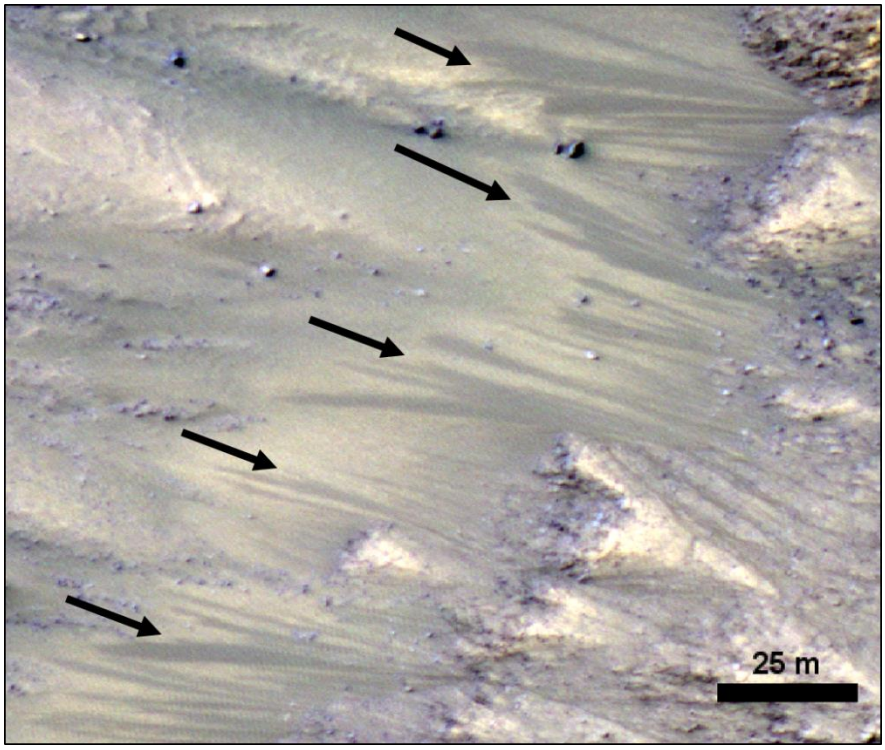

Figure 5.1. Recurring slope lineae seen at Palikir Crater in HiRISE false color imagery (largest RSL shown with black arrows). HiRISE image ID ESP_024034_1380.

slopes, and are hundreds of meters long. Previous studies have classified RSL according to their annual growth patterns. “Confirmed” RSL are those whose growth has been observed in the same locations over multiple years. “Partially confirmed” RSL are those whose growth has been observed in a single year, or have appeared statically in multiple years. “Candidate” RSL are static streaks that have not been observed to grow during a single season or recur over multiple seasons [*McEwen et al.*, 2011].

RSL could be produced by brine flow on the martian surface or shallow subsurface, as indicated by the recent detection of perchlorate near some RSL sites [*Ojha et al.*, 2015]. This study tests the hypothesis that RSL activity, over a sufficiently long period of time, could result in the precipitation of detectable lag deposits. Sustained flow of a chloride-enriched brine could produce chloride deposits of sufficient extent and thickness to be detectable by THEMIS. As a result, possible chloride deposits both up- and down-slope of RSL were investigated in this analysis. The purpose of this study is to assess the colocation of small-scale chloride deposits and confirmed RSL and the likelihood of chloride brine as an RSL formation mechanism. A positive correlation is detected, would provide strong evidence for chloride brine flow as the mechanism behind RSL formation.

5.2 Background

5.2.1 Evidence for previous water activity on the martian surface

Understanding the history of water on the martian surface is key to defining the role that water may play in RSL formation. The hypothesis that liquid water has persisted on the surface of Mars is supported by numerous observations. A variety of geomorphologic

features exist on the martian surface that may have been carved by liquid water. The large martian outflow channels and valley networks, including Mangala Valles, Maja Valles, Kasei Valles, and others, show evidence of catastrophic outflows that persisted for timescales of 10^5 - 10^7 years [*Fassett and Head*, 2008; *Hynek et al.*, 2010; *Hoke et al.*, 2011; *Keske et al.*, 2015]. The general consensus is that these features were created by large outflows of water and not by lava flows [*Baker*, 2001; *Wilson*, 2004; *Harrison and Grimm*, 2008]. While aqueous outflows likely occurred during the late-Noachian to early-Hesperian (3.6 - 3.8 Ga), they lend support to the prospect of large reservoirs of water in the martian sub-surface [*Carr*, 1979; *Baker*, 2001; *Hoke et al.*, 2011, 2014].

Many smaller channels on the martian surface could have been carved by water, though some are believed to have formed by thermal erosion from volcanic activity [*Carr*, 1974; *Williams et al.*, 2005]. On even smaller scales, martian gullies appear on a large number of slopes in both the northern and southern hemispheres. Many gullies are thought to have formed from debris flows and periodic CO_2-lubricated grain flows, but the likelihood of liquid water as a formation mechanism is still being investigated [*Christensen*, 2003; *Heldmann*, 2005; *Dickson et al.*, 2007; *Dickson and Head*, 2009; *Dundas et al.*, 2014; *Johnsson et al.*, 2014; *Rummel et al.*, 2014; *Conway et al.*, 2015; *Pilorget and Forget*, 2015; *Vincendon*, 2015].

The unique morphologies of deltas are almost certainly produced by the deposition of liquid water, as exemplified by the unique morphologies seen at Jezero Crater [*Ehlmann et al.*, 2009; *Goudge et al.*, 2015]. In addition, the evidence for ancient paleolakes is growing, indicating that standing bodies of liquid water may have persisted on the martian surface during the late-Noachian/early-Hesperian [*Cabrol and Grin*, 1999;

Goudge et al., 2012; *Hynek et al.*, 2015]. These paleolakes may have provided an environment hospitable to life, making them high-priority targets for future exploration [*Cabrol and Grin*, 1999].

Compositional and geochemical evidence that water persisted on the martian surface is abundant. The presence of aqueous weathering products demonstrates the large scale and depth of acidic weathering of basaltic materials, which was primarily driven by an abundance of liquid water and sulfur from volcanic activity [*Burt and Knauth*, 2003; *Bullock*, 2004; *Bandfield et al.*, 2011]. The presence of hydrated minerals, typified by the Mawrth Vallis and Nili Fossae regions (among others), shows that water persisted into the Amazonian, though bound in the crystal structures of various types of phyllosilicates [*Poulet et al.*, 2005; *Bibring et al.*, 2006; *Loizeau et al.*, 2007; *Ehlmann et al.*, 2009, 2011; *McKeown et al.*, 2009, 2013; *Murchie et al.*, 2009; *Mustard et al.*, 2009; *Michalski et al.*, 2010; *Carter et al.*, 2013]. In addition to the geomorphologic evidence, the existence of paleolakes is also indicated by the presence of evaporite deposits. Specifically, the presence of sulfates and chlorides at various locations on Mars (in addition to the phyllosilicates mentioned above) indicates a sustained period where liquid water persisted on the martian surface and subsequently evaporated away, leaving distinct mineralogical signatures that can be detected from orbit and by rovers [*Forsythe and Zimbelman*, 1995; *Clark et al.*, 2005; *Gendrin et al.*, 2005; *McLennan et al.*, 2005; *Tosca et al.*, 2005; *Osterloo et al.*, 2008, 2010; *Murchie et al.*, 2009; *Hynek et al.*, 2015].

In spite of the extensive evidence for the presence of liquid water on ancient Mars, the reservoir of water that remains in the mid-latitudes from that period has yet to be constrained. Water loss likely occurred via solar wind activity, impacts, transport to

the polar caps, and various other processes [*Jakosky and Phillips*, 2001; *Knauth*, 2002; *Byrne et al.*, 2009]. Understanding the abundance and distribution of the remaining water, specifically water in the subsurface, requires detailed field investigations of the martian subsurface which have not yet taken place. Mars Odyssey Neutron Spectrometer analyses show a range of water-equivalent hydrogen between 2 and 11% by mass within one meter of the surface, equivalent to a global water layer thickness of 14 cm [*Feldman et al.*, 2002, 2004]. Models of the martian hydrosphere/cryosphere invoke gas hydrates, hydrated salts, and /or thermally-insulating layers of rock and dust as mechanisms for trapping substantial quantities of water ice in the subsurface [*Malin and Edgett*, 2000; *Mellon and Phillips*, 2001; *Kargel et al.*, 2007; *Dickson and Head*, 2009].

5.2.2 Temperature constraints for RSL formation

Southern-hemisphere RSL form at subsolar angle (L_s) = 245 ± 11° and persist through L_s = 314 ± 12°, corresponding to the southern summer on Mars [*Stillman et al.*, 2014]. Equatorial RSL are active from L_s = 50°-196° for north-facing slopes and L_s=192°-288° for southern-facing slopes and correspond to times of year when the subsolar point crosses their latitudes [*McEwen et al.*, 2013]. Thermal infrared (TIR) data from the Thermal Emission Imaging System (THEMIS) have allowed the temperature conditions under which RSL form to be constrained at a spatial resolution of 100 m/px (meters per pixel), the highest of any TIR instrument to orbit Mars. Both southern/mid-latitude and equatorial RSL are active when THEMIS brightness temperatures are 250-300K [*McEwen et al.*, 2011a, 2013; *Ojha et al.*, 2014]. Some RSL are visible at temperatures well below the freezing point of water, such as Hale Crater, which has an

average annual temperature of 215K [*McEwen et al.*, 2013; *Ojha et al.*, 2014; *Stillman et al.*, 2016].

5.2.3 Water reservoirs for RSL

The source of water into which salts could dissolve is still a subject of debate. The most likely water reservoirs include a layer or layers of subsurface water-ice or shallow aquifers. Subsurface water ice could be thermally shielded from heating and sublimation by an overlying layer of 10-40 mm of dust as shown via modeling and laboratory experiments with Mars simulant [*Chevrier et al.*, 2007; *Grimm et al.*, 2014]. While a layer of dust would be necessary to prevent evaporation of a freshwater flow, little to no coverage by dust is required for intermittent surface brine flows. The quantity of freshwater needed to sustain a short-lived RSL-scale flow is estimated to be 2 - 10 m^3, assuming flow thicknesses of as little as 50 mm [*Stillman et al.*, 2014]. While the same flow thicknesses would be expected for a brine, water demands for brines are still imprecise due to the competing effects of evaporation (water loss) and salt deliquescence/low water activity (water gain and preservation). The observed average RSL growth rate of 1 m/sol could also be due to periodic slug flow - where liquid flows in discrete pockets with large gas volumes between them - which would decrease the amount of water required to produce RSL [*Grimm et al.*, 2014].

Another hypothesis for the formation/appearance of RSL is via wetting and capillary flow through a porous substrate. If the darkening observed at RSL is due to capillary draw of a small amount of solution from the subsurface to the surface, the volume of solution on the surface decreases substantially, while subsurface flow could

still take place with high volumes of solution [*Grimm et al.*, 2014]. Previous studies have shown that RSL activity can be explained by brine flow through a porous substrate similar to that observed at water tracks in the Dry Valleys, Antarctica [*Levy*, 2012; *Levy et al.*, 2014]. Such a scenario would likely form a discontinuous surface lag deposit because the soil does not need to be saturated to show visible darkening. It is unlikely that such a deposit could be detected using remote sensing from orbit because its size would be significantly lower than the pixel scale of THEMIS (100 m).

Multiple groups have investigated the possibility of deliquescence of water vapor from the martian atmosphere as a source of water for RSL [*McEwen et al.*, 2011a; *Leung and Rafkin*, 2015; *Rafkin et al.*, 2016]. The water vapor budget on Mars varies as a result of a number of factors, including latitude and time of year. Previous work has shown that in Valles Marineris, where RSL are often hundreds to several kilometers long, the water vapor column holds a maximum of 10-15 μm. The time of year when water vapor abundance is at its peak correlates poorly with periods of peak RSL activity [*Leung and Rafkin*, 2015]. Water ice fogs have been observed in Valles Marineris and are thought to be a possible source of water for RSL; however, atmospheric models show that these fogs would likely require a local water source to saturate the ambient atmosphere [*Rafkin et al.*, 2016]. Therefore, deliquescence of water from the atmosphere is considered an unlikely mechanism for RSL formation since the quantities of water vapor in the martian atmosphere are insufficient for that purpose.

5.2.4 Aqueous chemistry of RSL

The dissolution of salts in liquid water decreases the activity of the solution, allowing it to remain in a liquid state under conditions where fresh water would not be stable. Extensive laboratory analyses have been performed to characterize the behaviors of such brines under the low-pressure, low-temperature conditions of the martian surface [*Massé et al.*, 2014]. Even with the presence of high quantities of dissolved solids, the metastable nature of brines under martian conditions would cause only short-lived flows as a result of high evaporation rates. The evaporation rates and thermal profiles of brines with different dissolved salts were modeled by Chevrier and Rivera-Valentin [*Chevrier and Rivera-Valentin*, 2012]. Their results show that brines containing a sulfate such as $Fe_2(SO_4)_3$, a chloride such as $CaCl_2$, or a perchlorate could remain liquid at temperatures well below the freezing point of liquid water, and some cases as low as 205K.

Under the cold temperatures measured by THEMIS, a concentrated brine with the dissolved species listed above is consistent with the appearance and behavior of RSL as a direct result of the low eutectic temperatures of those species in solution. Thermodynamic modeling has shown that solutions with a freezing temperature of 223K under martian surface pressures best replicate the observed seasonal behaviors of RSL on the martian surface [*Chevrier and Rivera-Valentin*, 2012]. Thermodynamic modeling has further demonstrated that solutions of both calcium ($CaCl_2$) and magnesium ($MgCl_2$) chloride could exist seasonally on the martian surface and to depths of 20 cm in the subsurface based on known surface brightness temperatures and diurnal/annual thermal skin depths [*Chevrier and Rivera-Valentin*, 2012].

Ojha et al. (2015) detected the first change in surface hydration associated both temporally and spatially with RSL activity. In their study, the Compact Reconnaissance Imaging Spectrometer for Mars (CRISM) on the Mars Reconnaissance Orbiter (MRO) was used to assess the presence of hydrated perchlorate and chlorate minerals in the near-infrared (NIR) at various RSL sites across Mars. The presence of perchlorates on Mars has been confirmed *in-situ*, most notably at the Phoenix landing site where visible evidence of water ice was also found [*Chevrier et al.*, 2009]. In four locations – Palikir crater, Horowitz crater, Hale crater, and Coprates Chasma – hydrated mineral absorptions were seen from orbit at wavelengths of 1.4, 1.9, and/or 3.0 μm. The depth of the absorptions at these bands decreased and vanished as RSL faded and disappeared as shown in simultaneous MRO HiRISE images. Based on laboratory studies of hydrated perchlorates and chlorates, the best fit to the observed CRISM data included a mixture of magnesium and sodium perchlorate and magnesium chlorate [*Hanley et al.*, 2014, 2015; *Ojha et al.*, 2015]. While negative results were not included in their study, Ojha et al. report that observations of other RSL sites showed no temporal or spectral indications of perchlorate-driven brine flow.

Ferric sulfate has been detected in the NIR in a number of locations on Mars by CRISM, including the region where the Spirit rover was immobilized at the end of its mission [*Wang and Ling*, 2011]. Enhanced ferric iron detection has also occurred in certain southern-hemisphere RSL during their period of peak size, indicating a possible connection between the two [*Ojha et al.*, 2013]. This signature could be caused by seasonal exposure of a ferric iron-rich unit, precipitation of ferric oxides, or substrate wetting; in contrast to the hydrated perchlorate detection, ferric iron signatures are not

uniquely attributable to the presence of water. Laboratory experiments have demonstrated that ferric sulfate solutions would be stable on the surface of Mars long enough to account for the appearance and lifetimes of RSL [*Chevrier and Altheide*, 2008]. The presence of ferric sulfate on Mars and its possible connection to RSL has provided key evidence for brines as an RSL formation mechanism.

5.2.5 Detectability of RSL-scale chloride deposits

Remote sensing studies have investigated the distribution of chlorides across the surface of Mars. Hydrated chlorine and oxychlorine salts have distinct absorption features in the NIR which have been characterized by extensive laboratory analysis; these minerals have been found on the martian surface, but not at the chloride sites identified by Osterloo et al. (2008) and at only four RSL sites. [*Hanley et al.*, 2014, 2015; *Ojha et al.*, 2015]. A NIR best-fit linear mixture at an RSL site in Palikir crater includes a chloride, though the estimated percentage of chloride was 1.5% and the fit was not exact [*Ojha et al.*, 2015].

A chloride lag deposit on the martian surface could be anhydrous during periods of the martian year when RSL are not active. Because anhydrous chlorides lack distinct absorption features in near and thermal infrared spectra, they must be identified by their low (< 1) maximum emissivity and the resulting spectral slope when using a standard Planck function for determining emissivity (described more fully in the Methods section below) [*Eastes*, 1989; *Lane and Christensen*, 1998]. Osterloo et al. (2008) developed a chloride-detection method using THEMIS TIR decorrelation stretch (DCS) products [*Osterloo et al.*, 2008]. Their global map of chlorides on Mars shows strong parallels

between the latitudes of southern hemisphere RSL and large-scale chloride deposits (Figure 5.2).

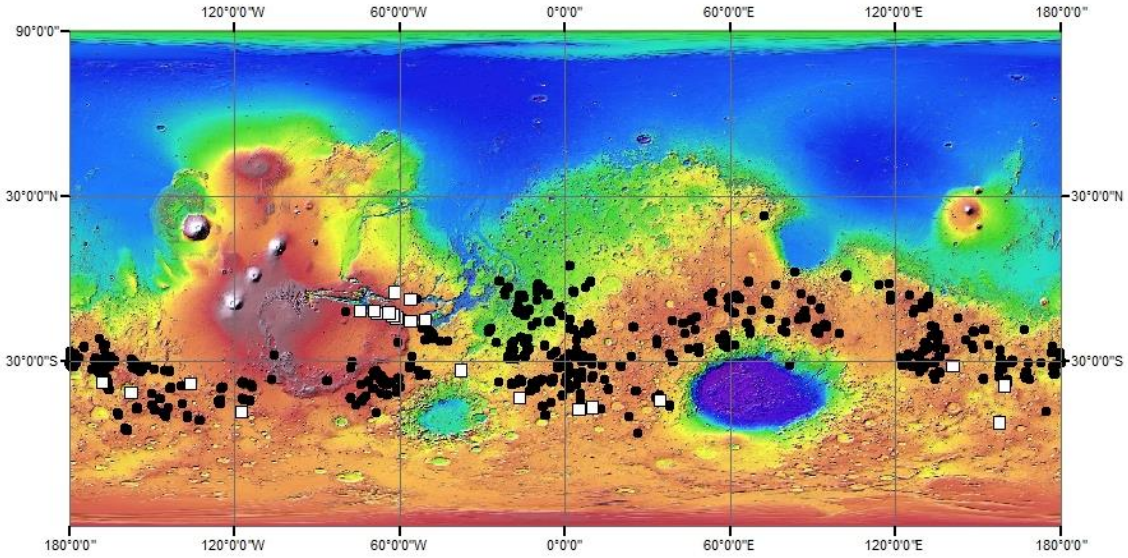

Figure 5.2. Distribution of chlorides and RSL on the surface of Mars. Black dots = chlorides from Osterloo et al. (2010), white squares = confirmed RSL sites included in this study from McEwen et al. (2011, 2013), basemap = global MOLA colorized elevation map of Mars. Map coverage: -90° to + 90° latitude, -180° to +180° longitude.

Osterloo et al. (2010) observed chloride-rich materials in topographic lows and regions of low albedo. More specifically, 63% of chloride deposits were observed in local lows at spatial scales of meters to tens of meters, 31% were observed in local basins, and 6% were observed in flat regions or elevated ridges. The majority of chloride deposits were localized to areas of 25 km^2 or less and appear eroded, indicating that chloride deposits are difficult to sustain under martian surface conditions. Most observed chloride deposits occur within Noachian and Hesperian regions, likely during the last sustained period where liquid water was stable on the surface and late enough such that no further surface water was present to wash them away. Chlorides are often colocated with geomorphologies consistent with channels and other sinuous water flow features. As the liquid water in the channel evaporated, a chloride (or other salt) precipitate would be left behind. This is consistent with the observation that almost all chlorides have been deposited as thin units [*Osterloo et al.*, 2010].

Osterloo et al. (2008) found that a maximum emissivity of 0.92 removed the slope in THEMIS spectra of martian chloride deposits. This 8% decrease in maximum emissivity could be caused by an optically-thin coating of halite over the entirety of the study area, an optically-thick coating covering approximately 90% of the area, or a varying proportion of intermixed chloride grains. To be detected by THEMIS, a chloride coating would need to cover enough area within a THEMIS pixel to cause a detectable decrease in maximum emissivity. Therefore, the densest regions of large RSL provide the highest potential for positive detection of chlorides in RSL. The detection limit of chloride coatings in the thermal infrared was explored by Berger et al. (2015) by studying a range of optically-thin (<150 μm) thicknesses. Thermal infrared reflectance minima

(emission maxima) did not change significantly between optically thick (1 mm) and the thinnest continuous chloride coating in their study (29 ± 2 μm) [*Berger et al.,* 2015]. Optically-thick coatings caused an increase in reflection minima (decrease in emission maxima) by 10% reflectance, where all optically-thin coatings increased reflection minima by ~5%.

Additional laboratory studies indicate that martian chloride spectra are best replicated by a mixture of chloride grains with the remainder best represented by surface type 1 (ST1) basalts [*Osterloo et al.*, 2008; *Jensen and Glotch*, 2011; *Glotch et al.*, 2016], The work of Glotch, et al. (2016) replicated the observed THEMIS spectral slope with mixtures of flood basalt and at 10-25% chloride abundances at 63-180-μm size fractions of halite for coarse particulate surfaces and <10- μm size fractions of halite for fine particulate surfaces.

In this study, we test the hypothesis that RSL are generated by chloride-rich brine flow by assessing whether the RSL deposited detectable anhydrous chloride lag deposits. These lag deposits could cover 10-25% of spatially large areas (multiple THEMIS pixels or 100s of meters in length/width), or be present in the form of a continuous coating. We approximate the mass of chloride required to produce a positive chloride detection, allowing the quantity of brine to be constrained to a first order at a given chloride concentration.

5.3 Materials and Methods

HiRISE is a visible imaging system onboard MRO with three bands (NIR, red, and blue-green) and over 20,000 individual CCD detectors. It produces high-resolution images of the martian surface with a pixel scale of 0.25 - 1.3 m/px, the highest of any instrument sent to Mars [*McEwen et al.*, 2007]. HiRISE has targeted steep (>20°) slopes since the discovery of the first RSL. In addition, the ability of HiRISE to discern small (<1 m) objects on the martian surface has allowed the geologic and morphologic context of RSL sites to be described. RSL sites are often colocated with narrow gullies and debris-rich slopes, with clasts appearing in a range of sizes down to the resolving limit of the HiRISE camera [*McEwen et al.*, 2011a].

Ojha et al. reported the most recent catalog of confirmed southern-hemisphere RSL in early 2014, which included a list of the associated HiRISE imagery and THEMIS products used for RSL temperature estimates [*Ojha et al.*, 2014]. Similarly, McEwen et al. released a catalog of equatorial RSL in 2013. Using the Java Mission Analysis and Remote Sensing (JMARS) software [*Christensen et al.*, 2009], regions where RSL have been confirmed were analyzed using selected HiRISE images from the Ojha et al. and McEwen et al. catalogs. For each region, all RSL on a given slope were mapped as a single unit, with multiple RSL units typically appearing within a single HiRISE image (Figure 5.3). HiRISE images were selected that correlate to the time-period when RSL are at their longest.

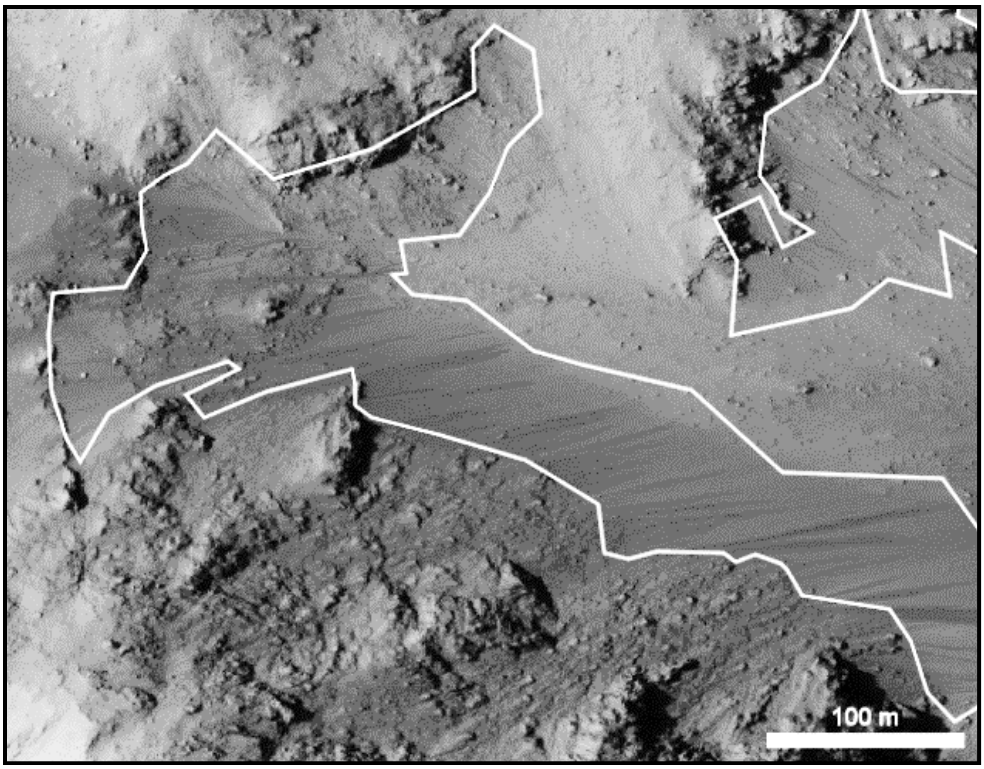

Figure 5.3. Area covered by RSL (outlined in white) mapped on HiRISE image of Horowitz Crater. HiRISE image ID ESP_022678_1475.

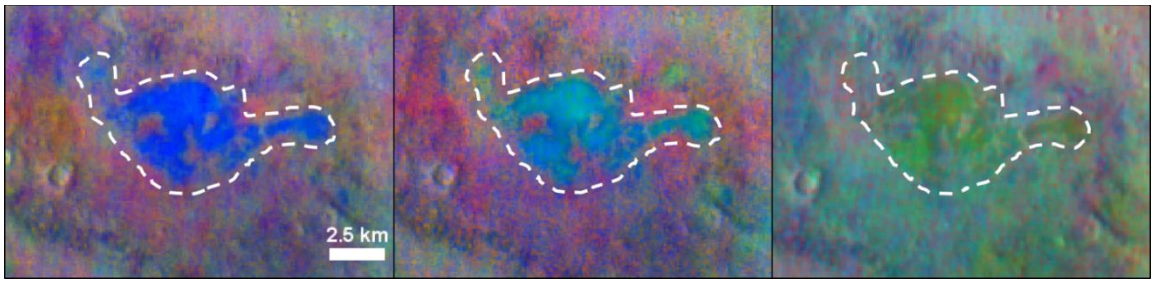

Figure 5.4. Example chloride deposit in Miyamoto Crater (dashed white area) appears blue in THEMIS DCS 875 (left), teal/green in 964 (middle), and yellow/orange in 642 (right). THEMIS image ID I17811024.

THEMIS is a dual visible and TIR pushbroom imager onboard the Mars Odyssey spacecraft which has been orbiting Mars for over a decade. THEMIS is the highest-spatial-resolution TIR instrument to orbit Mars, with a pixel scale of 100 m/px, allowing a wide range of temperatures, compositions, and grain sizes to be quantified. The long duration of its mission has allowed it to map the thermal properties of the martian surface temporally as well as spatially, observing single sites over multiple martian years and at multiple Ls values. The TIR imager has 320 cross-track detectors for each band, and 10 individual bands ranging in wavelength from ~6 to ~15 microns; nine bands (bands 1-9) are used for mineral identification.

A decorrelation stretch (DCS) of TIR data can be used to qualitatively enhance compositional variations by decoupling them from temperature effects [*Christensen et al.*, 2004; *Edwards et al.*, 2011]. Production of a DCS involves performing a principal component analysis of THEMIS calibrated radiance, with specific bands of interest incorporated into the analysis based on the material/property of interest [*Gillespie et al.*, 1986]. A DCS is required for chloride detection due to a) the absence of distinct absorption features in the detection range of THEMIS, and b) non-unit maximum emissivities, which result in a spectral slope using standard THEMIS processing techniques. Chloride absorption features are broad and found at longer wavelengths than those detectable by THEMIS due to the bulk vibration of atoms in the crystal structure. Detectors sensitive to these longer wavelengths (i.e. 45+ μm) would be required to observe chloride absorption features from Mars orbit [*Lane and Christensen*, 1998].

Three DCS products, incorporating THEMIS bands 8, 7, and 5, bands 9, 6, and 4, and bands 6, 4, and 2, are required for chloride detection. Chloride deposits appear blue

in 875, turquoise in 964, and yellow-orange in 642 (Figure 5.4) [*Osterloo et al.*, 2008]; this color combination in THEMIS DCS products was used for initial detection of candidate chloride deposits at RSL sites. However, because THEMIS DCS products are derived from calibrated radiance, they can be subject to topographic effects that may produce a spectral slope from other than compositional variations (i.e. anisothermal slopes [*Bandfield*, 2009]). An emissivity spectrum must therefore be used for final confirmation of the presence of chlorides.

THEMIS products used to derive emissivity were processed using the standard THEMIS IR processing procedure [*Bandfield*, 2004] in the Integrated Software for Imagers and Spectrometers (ISIS) provided by the United States Geological Survey (USGS) [*Keszthelyi et al.*, 2014]. The THEMIS standard IR processing procedure first removes time-dependent focal plane variations and temperature variations across the calibration flag [*Bandfield*, 2004]. THEMIS products are then map-projected and both time-dependent and time-independent row and line correlated noise are removed. Emissivity spectra were produced in the software package Davinci (davinci.asu.edu) by dividing the radiance spectrum by a Planck function that corresponds to the highest brightness temperature between bands 3-9 [*Christensen et al.*, 1998; *Bandfield*, 2000, 2004]. Emissivity spectra of chlorides are characterized by a featureless spectral slope in the wavelength range of detection for THEMIS. The spectral slope is produced as a result of an erroneous estimate of the maximum emissivity of the material, which for chlorides is less than 1. A representative chloride spectrum as described by Osterloo (2008) is shown for comparison with the spectra produced in this study.

The TIR emissivity spectrum of a mineral mixture is, in most cases, a linear combination of the spectra of its constituents. A linear deconvolution is therefore often used to assess the quantitative abundance of minerals using TIR remote sensing [*Thomson and Salisbury*, 1993; *Ramsey*, 1996; *Ramsey and Christensen*, 1998; *Feely and Christensen*, 1999; *Hamilton and Christensen*, 2000; *Christensen et al.*, 2004; *Huang et al.*, 2013]. However, chloride minerals behave non-linearly in the TIR as a result of spectral transmission/low maximum emissivities and lack of spectral features; therefore, linear deconvolution an unreliable method of assessing their areal abundance [*Eastes*, 1989; *Osterloo et al.*, 2008; *Berger et al.*, 2015]. The linear deconvolution technique was not used for this study because an accurate positive detection of chlorides cannot be made given the areal abundance estimate from linear deconvolution results.

Chloride sites with repeat THEMIS coverage show that chloride detections do not vary over multiple observations. RSL outlines were overlain on each DCS product and a direct comparison was made between them. For RSL sites with repeat coverage by THEMIS, each DCS product was surveyed for evidence of chlorides. Because the highest THEMIS spatial resolution is 100 m/px, most individual southern hemisphere RSL fall within a single THEMIS pixel. Given that RSL have likely been active for much longer timescales than they have been observed by orbiting instruments, it is possible that a detectable lag deposit has accumulated at the base of RSL flows. Therefore, the focus of this study was not to pinpoint specific RSL, but to search RSL slopes for both local- (hundreds of meters) and regional-scale (up to 1 km) evidence of colocated chlorides. For this reason, only confirmed RSL were included in the study, and

isolated RSL clusters that were smaller than 10 m in length and net width were not included.

5.4 Results

5.4.1 Remote sensing observations

Confirmed southern-hemisphere RSL were mapped at each location shown in Figure 5.2. In many cases, RSL were juxtaposed with gullies, eroded/weathering slopes, and cobble-to-boulder-sized clasts. Pixel-scale evidence of chlorides was observed at only one of the 11 southern-latitude RSL sites included in this study, showing no significant (>50%) correlation between RSL and chloride deposits. For all but two regions of study, there was no observable variation in THEMIS DCS signatures between slopes with RSL and the immediate surrounding area without RSL, indicating that the presence of RSL could not be correlated in any way to variations in thermal infrared spectra. In most cases, such as Triolet Crater, neither local- nor regional-scale evidence of chlorides was observed (Figure 5.5).

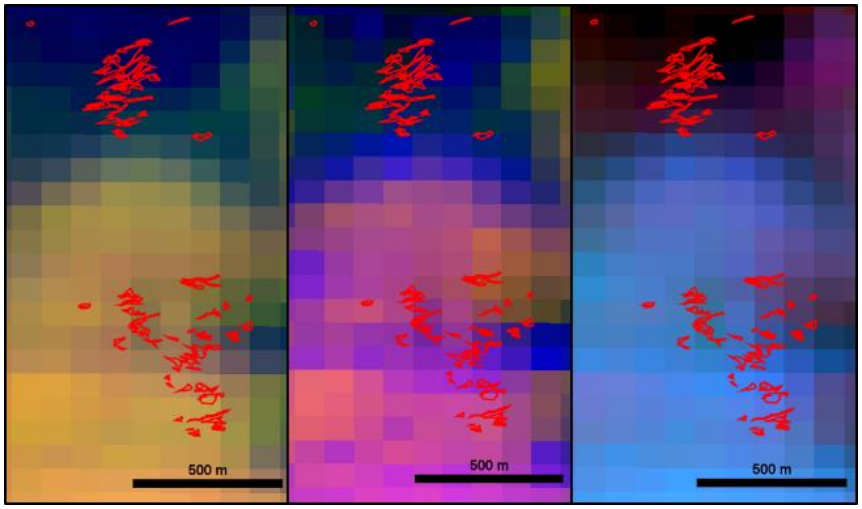

Figure 5.5. THEMIS DCS images and RSL in Triolet Crater. From left to right: DCS 875, 964, and 642 basemaps, with RSL outlines (red), THEMIS image ID I34201002.

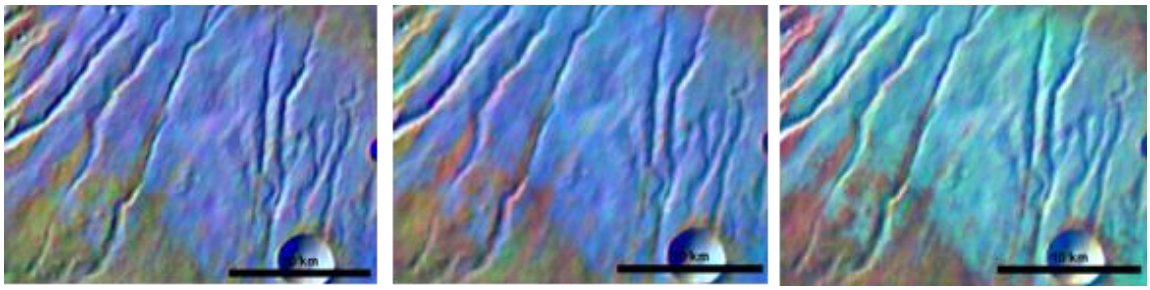

Figure 5.6. Example of steep slope with anisothermalities. Such slopes cannot be fit by a single blackbody curve because a single THEMIS pixel covers an area with multiple temperatures. This blackbody inaccuracy manifests itself as a spectral slope across all DCS products (left: 875, middle: 964, right: 642). This effect can be distinguished readily from chloride deposits by the color in THEMIS 642 DCS products. Chlorides appear blue in THEMIS DCS 875, cyan in DCS 964, and yellow/orange in 642, whereas anisothermal surfaces are blue across all bands. THEMIS image ID I02740006.

On a steep slope, a single blackbody curve is insufficient for approximating the thermal infrared continuum because a single THEMIS pixel can include a wide range of temperatures. This blackbody inaccuracy is manifested in a spectral slope (blue color) across all THEMIS DCS products (bands 875, 964, and 642) for some steep slopes. This anisothermality signature was first described by Bandfield (2009), and a type example can be seen in Figure 5.6. Even though both chlorides and steep slopes produce a spectral slope, anisothermal surfaces can be distinguished from chlorides because they maintain a blue color in DCS 642 whereas chlorides appear yellow-orange. The fact that many RSL occur on steep crater walls increases the likelihood of encountering anisothermal effects; in fact, several locales are dominated by the distinct steep-slope signature, as seen southeast of Huggins crater (Figure 5.7) [*Bandfield*, 2009].

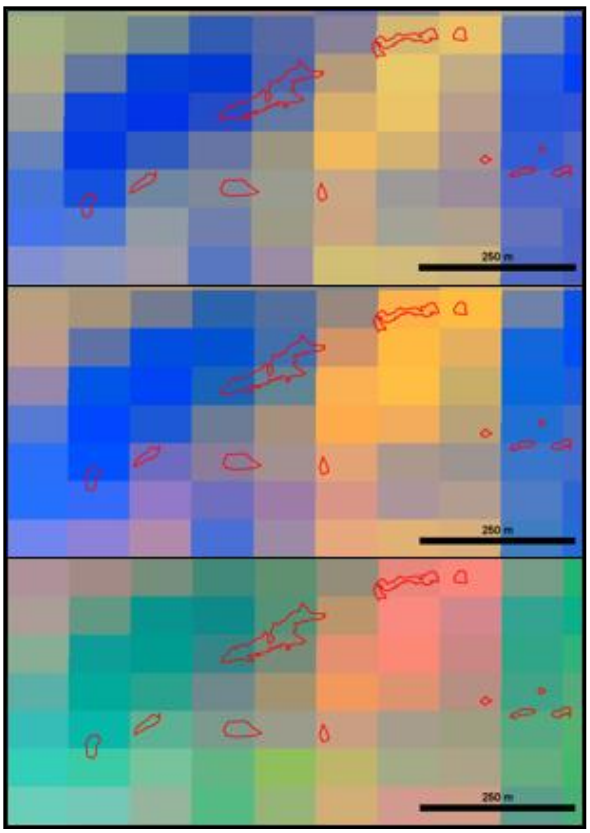

Figure 5.7. Southeast of Huggins Crater, showing spectral slopes indicative of anisothermal steep terrain. From top to bottom: DCS 875, 964, and 642 basemaps, with RSL outlines (red). THEMIS image ID I23609005.

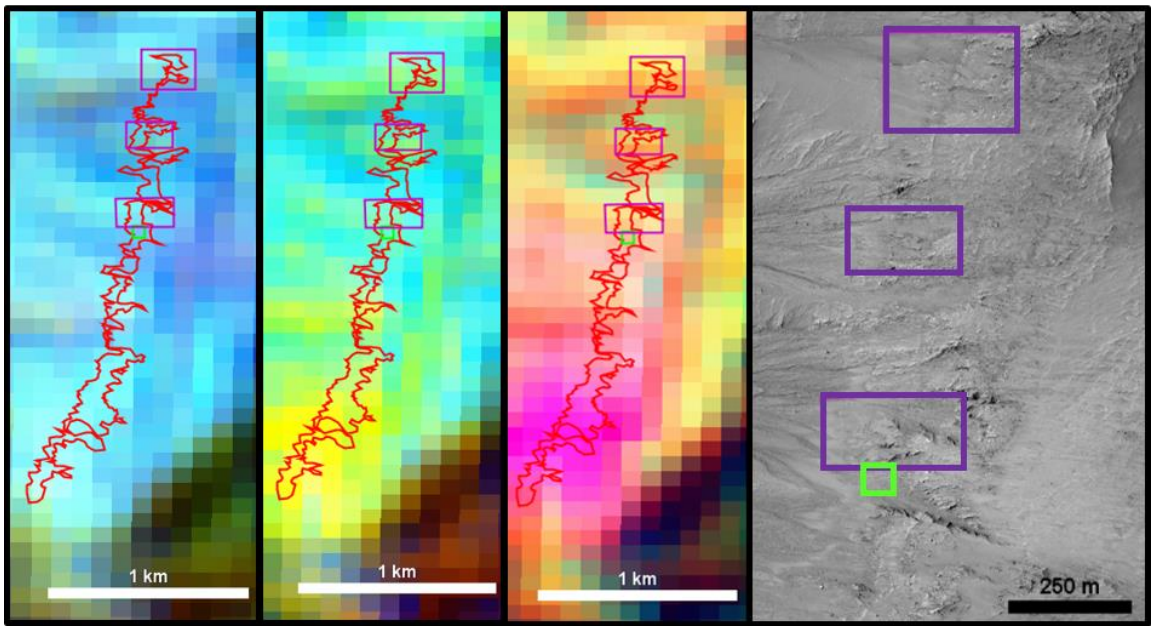

Figure 5.8. Outline (red) of RSL region of study in Palikir Crater. The areas with the strongest chloride signatures are shown in purple boxes; the location of hydrated perchlorates identified by Ojha, et al. (2015) is shown in a green box. Chlorides appear blue in THEMIS DCS 875 (far left), cyan in DCS 964 (left), and yellow/orange in 642 (center). Zoomed-in HiRISE image of region of interest is at right. (THEMIS image ID I34263004, HiRISE image ID ESP_024034_1380.)

Palikir Crater is known from previous work to have evidence of periodic ferric iron and hydrated perchlorates based on CRISM spectra [*Ojha et al.*, 2013, 2015]. In this study, Palikir was the most distinct locale in THEMIS DCS, showing local and regional-scale evidence of chlorides in areas where RSL were most densely located (Figure 5.8). Patches of possible chlorides between 200-400 m across were seen in proximity to locations of previous hydrated perchlorate detections.

Because THEMIS DCS products are generated using thermal radiance, they cannot be used for a final confirmation of the presence of chlorides because they are subject to topographic effects [*Edwards et al.*, 2011]. As a final verification of the presence of chlorides, an emissivity spectrum was produced to assess whether the spectral slope persisted once topographic effects were removed [*Bandfield*, 2004]. The emissivity spectrum for Palikir crater is shown in Figure 5.9 ("RSL"), with a chloride spectrum from Osterloo et al. (2008) for comparison. The spectral slope that was observed in the radiance image is not apparent in the emissivity spectrum. The spectrum does indicate a basaltic composition, which would be consistent with observations of basalt in the regional geology [*Bandfield et al.*, 2004 and others]. Spectra were also collected from a nearby region that did not show evidence of chlorides in THEMIS DCS products; the average spectrum of this surface ("Surface") is shown in Figure 5.9 and displays no significant variation from the RSL spectrum.

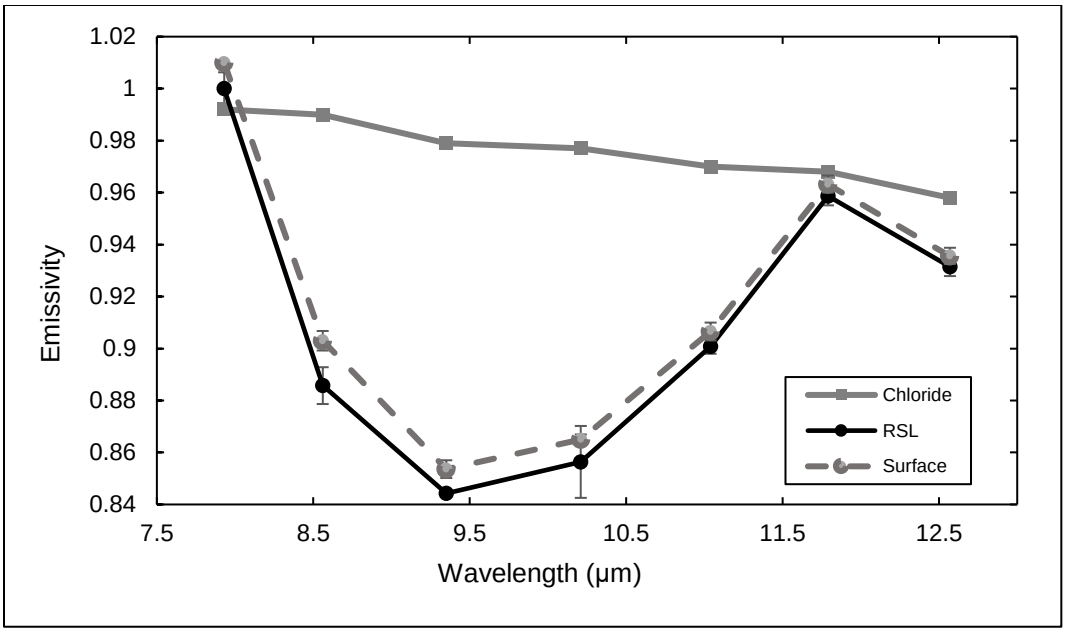

Figure 5.9. THEMIS emissivity spectrum for Palikir crater area indicative of chloride deposits ("RSL") compared to a reference chloride spectrum ("chloride") as described by Osterloo et al., 2008. There is no significant indications of chlorides because no spectral slope can be observed in the surface spectrum. A nearby surface with no indication of chlorides ("Surface," offset by 0.01 emissivity) is shown for comparison and retains the same spectral shape as the RSL.

While many confirmed chloride deposits are in the southern mid-latitudes, many have been detected in the vicinity of Valles Marineris, where the equatorial RSL population is located (Figure 5.10) [*McEwen et al.*, 2013]. Because RSL in the Valles Marineris region are much larger than southern-hemisphere RSL and encompass multiple THEMIS pixels, an investigation of RSL in the Valles Marineris region allowed the presence of chlorides to be more confidently constrained.

Observations of Eos Chasma, at the easternmost edge of Valles Marineris, show no evidence of chloride deposits in the vicinity of RSL. Other equatorial sites in proximity to Coprates, Capri, Hydrae, Ius, Juventae, and Melas Chasmas were examined using THEMIS DCS products to assess the presence or absence of chloride signatures. A map showing the locations of equatorial RSL included in this study is shown in Figure 5.11.

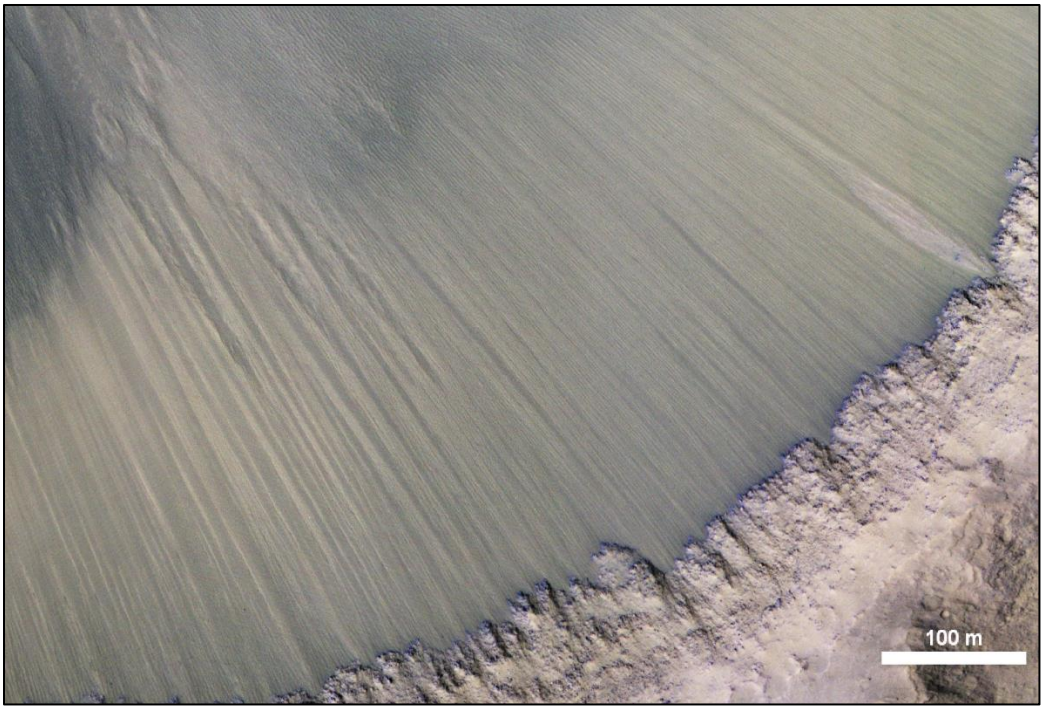

Figure 5.10. Large RSL site in southeast Melas Chasma, Valles Marineris. Equatorial RSL are consistently longer than those found in the southern hemisphere. HiRISE image ESP_031059_1685.

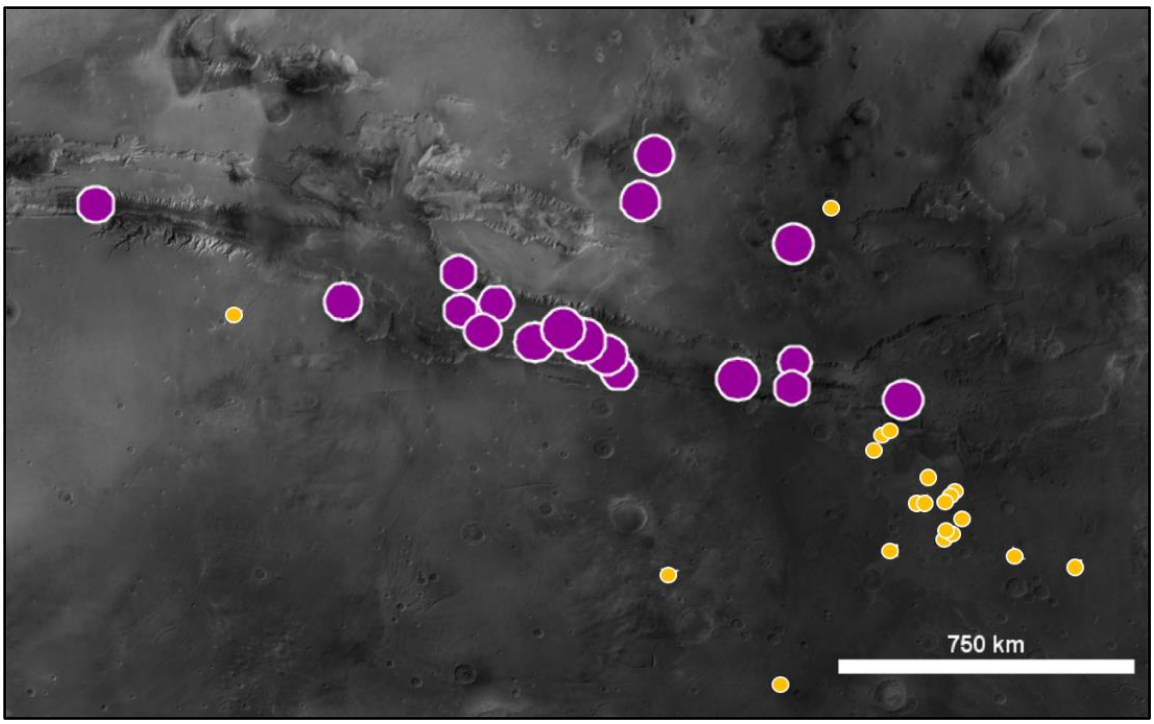

Figure 5.11. Locations of equatorial RSL sites (purple circles) and published chloride deposits (orange dots) in the Valles Marineris region on a greyscale MOLA elevation basemap (latitude: ~5°N – 30°S, longitude: 264°E – 324°E) [*Zuber et al.*, 1992; *Osterloo et al.*, 2010; *McEwen et al.*, 2013].

Only one equatorial RSL site showed possible evidence of chloride signatures in THEMIS DCS products. Located between Melas and Coprates Chasmas (12.86°S, 293.41°E), a south-facing slope on the southern side of Valles Marineris contained a localized (1.0-1.5 km^2 area) diffuse signature consistent with the presence of chlorides. HiRISE and THEMIS DCS images of this slope are shown in Figure 5.12. To confirm the presence of chlorides, an emissivity spectrum was produced for those pixels that showed a possible chloride signature. The emissivity spectrum for the RSL-bearing slope ("RSL") is shown in Figure 5.13 with a known chloride spectrum as described by Osterloo (2008) for comparison. The absence of a spectral slope is consistent with a lack of chlorides at this RSL site. A spectrum was also produced for a nearby slope that showed no evidence of chlorides; this spectrum ("Surface" in Figure 5.13) is virtually identical to the emissivity spectrum of the RSL-bearing slope. Because of the weakness of the evidence at this site, and because this was the only equatorial site that showed a colocation of chlorides and RSL, a summary of the observations is that no indications of chlorides were detected in any of the equatorial RSL sites.

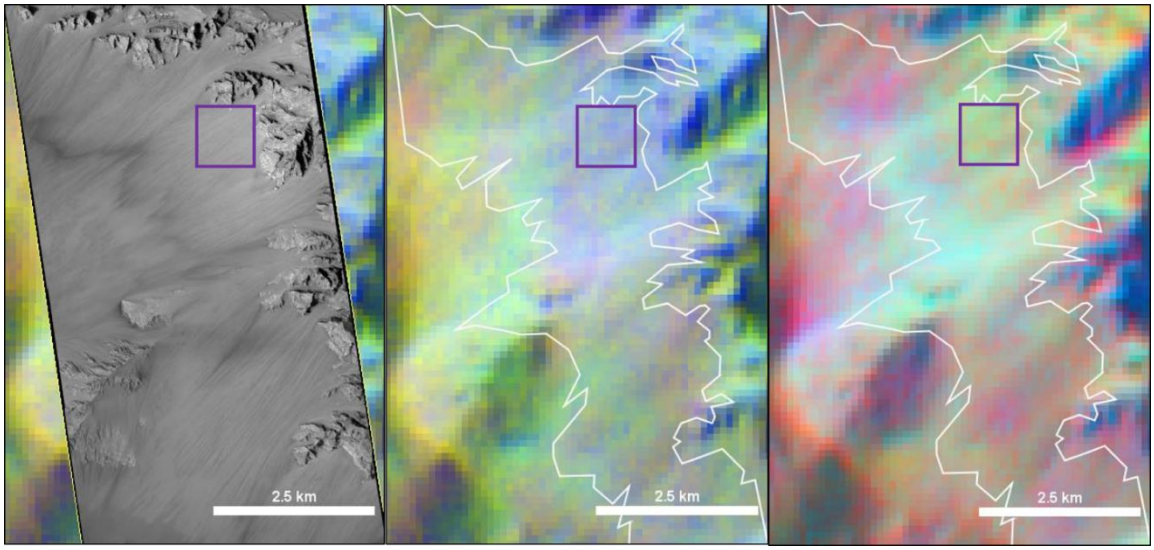

Figure 5.12. Indication of chloride deposits in Valles Marineris (chloride signature at 12.86°S, 293.41°E, purple box). HiRISE image ESP_30070_1670 (left), THEMIS DCS 875 (I06357001, middle), DCS 642 (right). Chlorides appear blue in THEMIS DCS 875, cyan in DCS 964, and yellow/orange in 642. Location of dense RSL outlined in white.

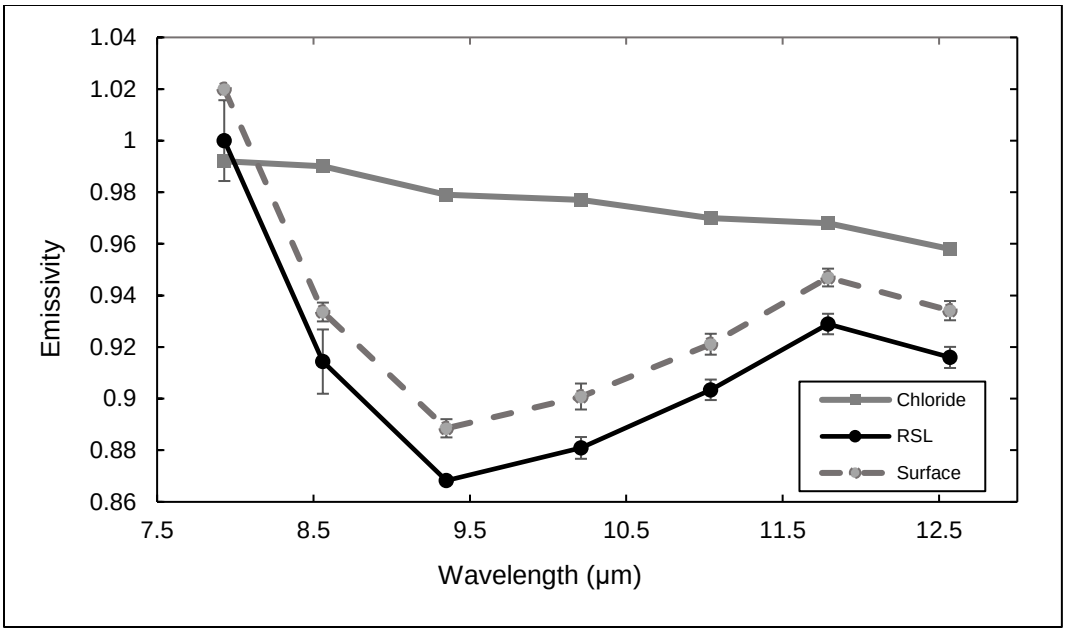

Figure 5.13. THEMIS emissivity spectrum of RSL indicative of chloride deposits ("RSL") compared to a reference chloride spectrum as described in Osterloo et al., 2008. A nearby region with no indications of chloride in THEMIS DCS is shown ("Surface", offset by 0.01 emissivity). Note the lack of spectral slope. The broad absorption at ~9.5 μm is typical of basaltic background material.

5.4.2 Assessing the abundance of chlorides

The lack of a positive chloride detection by THEMIS provides an opportunity for establishing an upper limit for the amount of chloride that could be in RSL lag deposits. In this section, we calculate the threshold of detection for a chloride lag deposit based on previous laboratory studies and use that value to assess the volume of brine that would be required to produce such a deposit. The abundance of chloride described in this section serves as an end-member maximum abundance of chloride that could be present in some or all RSL sites.

A simple assessment of the threshold for detection of chlorides in RSL by THEMIS was performed using Equation 1.

$$\rho \times (1 - P) \times F \times A \times B = M \quad (1)$$

The total mass (M) of chloride required for detection of chloride at the scale of THEMIS (100 m/px) was determined using: the density of the chloride mineral (ρ), the average porosity of the material (P), the areal fraction of chloride (F), the area of a THEMIS pixel (A), and the optical depth of TIR into chloride minerals (B). The estimated porosity of this surface is 45%, based on previous studies of terrestrial playa such as Lake Bonneville [*Turk et al.*, 1973]. The areal fraction of chloride required to produce spectral slopes in the TIR is estimated to have a range of 10-25% [*Glotch et al.*, 2016]. The optical depth of TIR in chloride minerals is approximately ~150 μm [*Berger et al.*, 2015]. The density of crystallized calcium chloride is 2.2 g/mL (2.2 x 10^3 kg/m^3). Using these quantities in Equation 1, we calculated the threshold mass of chloride per THEMIS pixel to be ~200 – 450 kg for areal abundances of 10-25%, respectively, over a THEMIS pixel area of 1 x 10^4 m^2. This equates to a threshold area density of ~30 ± 15 g/m^2 of calcium chloride.

The volume of brine produced by RSL can be estimated, provided the chloride in solution is constrained using the above range of values as a maximum threshold for the mass of their residual lag deposits. The seasonal behavior of RSL provides a key boundary condition because the observations of RSL activity can best be explained by a solution with a freezing point of 223K. A eutectic solution of $CaC1_2$ (T_E = 223.2K where T_E is the freezing point of the eutectic solution) meets this constraint [*Chevrier and Rivera-Valentin*, 2012]. The eutectic concentration of $CaC1_2$ brine is ~30 wt. % [*Brass*, 1980; *Sears and Moore*, 2005], resulting in a range of brine abundances of ~80 ± 35

mL/m^2. Ojha et al. (2015) observed a 1.5% chloride component in hydrated perchlorate near-infrared reflectance spectra at Palikir crater, indicating the possibility of a mixed brine at that RSL site. In a mixed brine that consists of some proportion of both chloride and perchlorate, the eutectic point and dissolved masses of individual species could vary significantly from the above values [*Hanley et al.*, 2012; *Stillman et al.*, 2016]. While other dissolved compounds or mixed brines could satisfy the freezing point constraint, they are not included in this analysis.

The above quantity of brine need not be produced in a single season. A significant lag deposit could be accumulated over large timescales, provided RSL activity is consistent throughout that time period and no episodes of significant erosion occur. If the source of water for RSL is subsurface ice, this ice would likely have been emplaced during the most recent climate cycle, where Mars' obliquity was higher than it is today. Estimates for the average timescale of Mars' climate cycle range from 100 – 600 kyr [*Mustard et al.*, 2001; *Head et al.*, 2003; *Chamberlain and Boynton*, 2007; *Schorghofer*, 2007; *Dickson et al.*, 2015]. Assuming RSL have been active since the most recent of these values (100 kyr), a maximum rate of brine production per year was determined to be $\sim 8 \pm 3 \times 10^{-4}$ mL/m^2-yr; surface brine production rates higher than this would have resulted in a positive detection of chloride in this study. If RSL processes have been occurring for more than one climate cycle, which seems likely, then the average volume of brine required each year would be even lower.

To obtain a greater understanding of the mass of salt available for brine production, the paleolake chloride deposit at Miyamoto crater (Figure 5.4) is used as a comparison. A 30-km^2 chloride deposit sits in the center of Miyamoto crater and has a

maximum thickness of 4 m; the volume of the deposit was found to be 0.12 km^3. Assuming a porosity of 45% and the density of halite (2.16 g/mL), the mass of the deposit was calculated to be 140 x 10^9 kg [*Hynek et al.*, 2015]. If a comparable mass of calcium chloride existed in the subsurface at RSL sites, it could produce a minimum of ~4 x 10^7 lag deposits of the size of the large recurring slope linea shown in Figure 5.14 that all remain undetectable by THEMIS.

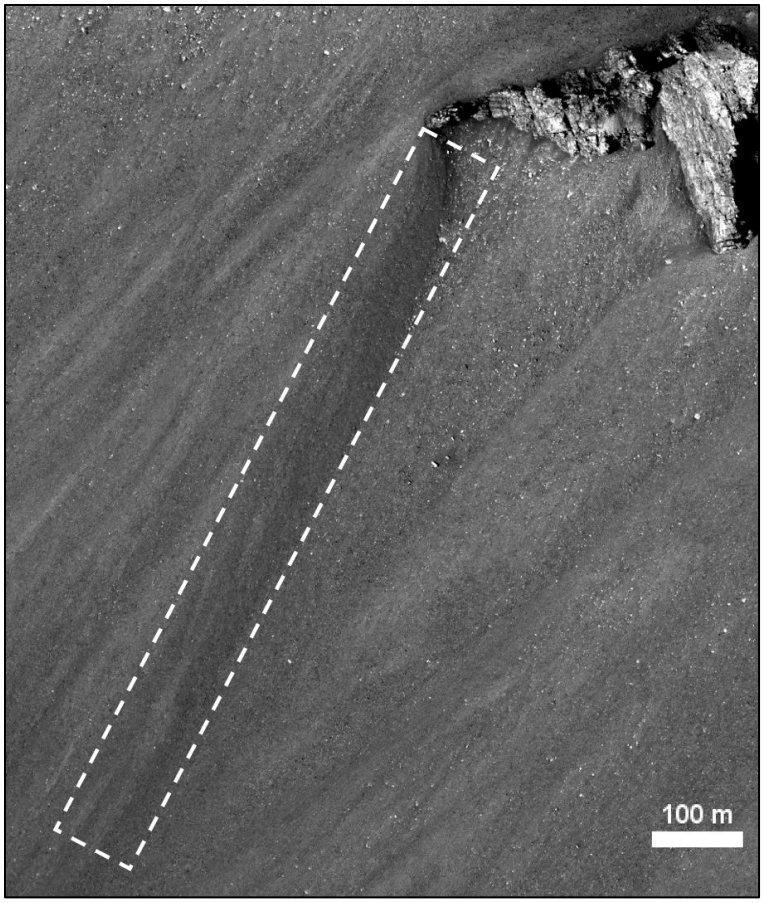

Figure 5.14. Representative RSL in Valles Marineris and dimensions shown in white dotted outline; boxed area is ~83 x 10^3 m^2. HiRISE image ID ESP_030070_1670, contrast enhanced for clarity. THEMIS pixel scale is 100 m.

5.5 Discussion

The lack of chloride signatures could be the result of one of two scenarios. In the first case, RSL may not contain chlorides, either because they a) are not aqueous flow features or b) are not chloride-based brines. In the second case, RSL may be the products of chloride brines but do not generate large enough lag deposits to be detected by THEMIS. If RSL are not aqueous flow features, the astrobiological implications are substantial due to the absence of substantial liquid water, i.e. if RSL are water-lubricated granular flows as some have hypothesized [*McEwen et al.*, 2011a; *Ojha et al.*, 2013]. If RSL are not chloride-based brines, other dissolved species such as perchlorates and ferric sulfate could account for the seasonal behavior of RSL. Recent evidence of perchlorates at four RSL sites supports the hypothesis that at least some RSL are produced by liquid water flow. However, other RSL sites show no evidence of liquid water or perchlorates, leaving open the question of a unique RSL formation mechanism.

In the second case, the concentration of chlorides could be non-zero, but below the detection limits of THEMIS. If this is indeed the case, any chlorides at or near RSL are masked by the TIR emissions of the surrounding terrain. Variations in the concentration of chlorides in solution and the presence/interference of other dissolved constituents could certainly complicate the detection of chlorides, either in their anhydrous or hydrated state. If RSL are dominated by subsurface flow, with only a small portion of the flow drawn to the surface by capillary action, then a surface lag deposit would likely not be large enough to be detectable by current remote sensing instruments. Additionally, the presence of clasts of various sizes would make it difficult to produce a coherent lag deposit.

To constrain the upper limit for the mass of chloride that could be present at RSL sites, a simple model for chloride detection was created. Using this model, we determined that a chloride lag deposit would need to have an area density of ~30 ± 15 g/m^2 to exceed the threshold of detection in the thermal infrared. This area density translates to ~80 ± 35 mL/m^2 of brine at the eutectic concentration of calcium chloride. If RSL water is sourced from ice emplaced during the most recent martian climate cycle (100 kyr), then an average brine production rate of $8 \pm 3 \times 10^{-4}$ mL/m^2-yr would be required to produce a detectable lag deposit.

Chloride deposits on the martian surface cover between 0.33 - 1300 km^2, with most on the order of ~25 km^2 (i.e. the chloride deposit in Miyamoto Crater), indicating that they are a) highly susceptible to erosion, and/or b) largely buried in the subsurface [*Osterloo et al.*, 2010]. The thickness (~4 m) of the deposit at Miyamoto crater indicates that chloride deposits, while possibly laterally extensive, do not extend to great depths [*Hynek et al.*, 2015]. Consumption of a laterally extensive subsurface deposit would lead to significant mass wasting, which thus far has not been observed at RSL sites [*Kite*, 2013]. The mass of the Miyamoto Crater chloride deposit could cover ~4×10^7 RSL of the scale of those in Valles Marineris and remain undetected by THEMIS. The amount of chloride needed to support all RSL on Mars could be present and accessible in the subsurface for dissolution into a brine. Therefore, this study concludes that the presence of chloride is not a limiting factor in the production of RSL.

Because RSL are found at many latitudes and geologic environments on Mars, it is possible that a range of RSL formation mechanisms exists. Further high-resolution (spatial and spectral) analyses of these sites in the NIR and TIR will help to ascertain

whether the formation mechanism is singular on a global scale or consists of a range of processes. Measurements at longer wavelengths (45+ μm) would allow diagnostic absorption features of chloride species to be observed. In light of the results of this study, alternative hypotheses for RSL formation that do not involve significant brine flow should be further explored. For example, capillary wicking of brines to the surface could account for the visible darkening of the surface without the presence of large quantities of brine [*Grimm et al.*, 2014]. In addition, granular flow due to lubrication of grains by a thin film of water [*McEwen et al.*, 2011] is considered more plausible due to the relatively low demand of resources needed to initiate it.

5.6 Conclusions

A survey of RSL on Mars was conducted to assess the likelihood of RSL formation via brine flow. Specifically, the accumulation of a lag deposit resulting from the evaporation of a chloride brine was investigated using THEMIS decorrelation stretch products and emissivity spectra. Of the 30 RSL sites included in this investigation, one southern-hemisphere site and one equatorial site showed evidence of small-scale chloride deposits in proximity to RSL. Comparison of the RSL spectra to those of the surrounding region revealed that the initial indications of chlorides were likely due to topographic effects and not the presence of a chloride lag deposit. Possible reasons for the negative detection included a complete lack of chlorides or the presence of a chloride lag deposit of insufficient size/thickness to be detectable by THEMIS. The following conclusions can be drawn from this non-detection.

1. A minimum threshold of detection in the thermal infrared was established to be 30 ± 15 g/m^2 for a calcium chloride lag deposit, which translates into a mass of ~180 – 450 kg of chloride per THEMIS pixel. Detection of a lag deposit using remote sensing requires much higher spatial resolution and longer wavelength infrared spectral measurements than provided by currently orbiting assets.
2. A volume of 80 ± 35 mL/m^2 of eutectic-concentration calcium chloride brine would be required to produce the mass distribution in 1. If RSL have been active since the last martian climate cycle (100 kyr), brines could have been produced at a maximum of $8 \pm 3 \times 10^{-4}$ mL/m^2-yr without generating a detectable lag deposit. A longer history of RSL production would require even less brine.
3. While large areas of buried chlorides (25+ km^2) are possible, they are not necessary to produce the volumes of brine listed in 2. If RSL consumed large quantities of salt, they would likely produce resolvable mass wasting, which has not been observed at RSL sites. Therefore, we conclude that salt abundance is not the limiting factor for RSL formation.
4. If RSL are brine-driven features, it is likely that the majority of RSL flow occurs in the subsurface with only small exposure to the surface. This limited surface wetting could be due to capillary wicking of a chloride-rich brine from a subsurface reservoir upward to the surface.

5.7 Acknowledgments

This manuscript was greatly enhanced with the helpful feedback of reviewers Briony Horgan and Mathieu Vincendon. The authors would like to acknowledge funding support from the THEMIS/Mars Odyssey Project Office for this work. The authors would also like to acknowledge the support of the Mars Space Flight Facility and JMARS staff for their assistance with HiRISE and THEMIS products. All images/data products can be found via NASA's Planetary Data System (https://pds.nasa.gov/).

CHAPTER 6

CONCLUSIONS

Multiple analytical and measurement techniques are required to fully characterize and interpret potential water-bearing environments on the Moon and Mars. Remote sensing at a range of wavelengths, coupled with laboratory analyses and terrestrial field analog studies, will be needed to select future sites for ground operations by human and robotic missions. The work described in the above investigations shows that this multi-technique approach can be used to construct a context for future exploration efforts prior to the first "boots on the ground." While this work has provided new insights into water-bearing environments on the Moon and Mars, it has also revealed the limitations of what remote sensing can tell us about such environments.

Chapter 2: Using Complementary Remote Sensing Techniques to Assess the Abundance of Water Ice at the Lunar North Pole. In this chapter, multiple instruments on the Lunar Reconnaissance Orbiter spacecraft were used to explore the distribution and abundance of potential ice-bearing regions in permanently shadowed regions (PSRs) at the lunar north pole. PSRs may harbor water ice deposits because they receive little to no sunlight through the lunar year and, as a result, reach some of the coldest temperatures in the inner Solar System. Four potential ice-bearing craters at the lunar north pole were examined, along with two polar craters not considered candidates for water ice and two equatorial craters as control regions. The Mini-RF radar instrument was used to reconnoiter regions of double-bounce backscatter using the *m-chi* decomposition, where double-bounce backscatter is indicative of either coherent, pure water ice deposits or

blocks at or multiples of the radar wavelength (~13 cm) in size. To determine whether regions of double-bounce backscatter were due to water ice or blocks, long-exposure images from the LRO Camera Narrow Angle Camera (NAC) were used to search for visible evidence of blocks.

Regions of double-bounce backscatter were mapped and each crater searched for blocks at using LROC NAC images. Regions with double-bounce backscatter and a lack of blocks were interpreted to have a high likelihood of containing water ice, while double-bounce backscatter regions with visible blocks were considered to have a low likelihood for ice. Of all the craters in this study, Rozhdestvenskiy N is considered the most likely candidate for containing water ice. Rozhdestvenskiy N had a pure double-bounce backscatter signature (no other types of backscatter indicated) with no visible blocks in its interior. Two other polar craters, Lovelace and Lovelace E, showed indications of single-bounce scattering, while Whipple Crater showed a combination of double-bounce, single-bounce, and volume scattering; all of these indicate a lack of coherent water ice deposits.

While long-exposure NACs are able to "see" inside PSRs, their above-nominal exposure times result in an increase in pixel scale and a decrease in spatial resolution: only blocks greater than 20-m diameter were able to be resolved within PSRs. Block size-frequency distributions were used to estimate the numbers of blocks below the resolving limit of the NAC by fitting a power law to the observed blocks and extrapolating down to smaller block sizes. For both potential ice-bearing craters and those without ice, block abundances in crater interiors were consistently higher than exteriors, showing that mass wasting of crater slopes can produce erroneous radar

signatures indicative of ice. Additionally, the slope of the block size-frequency power law (known as the B value) showed no systematic variations between potential ice-bearing craters and those known to not have ice.

This study indicates that there are few, if any, meter-thick or greater ice deposits at the lunar north pole. This result does not preclude the presence of any water-ice, however. Ice could be diffused through or within thin layers covered by regolith, neither of which would be detectable by Mini-RF or LROC. Other remote sensing techniques (i.e., near-infrared reflectance and high-resolution neutron spectroscopy) or surface sampling/sample return can and should be used to assess the presence and abundance of water ice and other volatiles at the lunar north pole. Additionally, larger PSRs at the lunar south pole should be explored using the techniques in this study and other techniques to assess the likelihood of water ice globally.

Chapter 3: Chloride-Rich Brines – Analogs for Water on Ancient Mars. Chloride-rich brines are thought to be the last form of widespread liquid water on the surface of ancient Mars. This unique chemical composition is the result of a sequence of mineral precipitation, where chloride minerals are the most soluble and hence the last to come out of solution. On Earth, chloride brines can form in a number of natural systems, including: continental hydrothermal activity, oceanic hydrothermal activity, concentration in desert endorheic basins, concentration and reactions in cold endorheic basins, and water-rock reactions in deep basinal brines. In this investigation, terrestrial chloride-rich brines were studied to assess general patterns in chemical properties (major ions, trace metals, precipitation sequences) among chloride-rich brines produced through multiple processes. Systematic variations in composition and precipitation sequence can

be used in future studies of chloride deposits – and perhaps water inclusions – on the martian surface.

Both continental and oceanic hydrothermal brines have a marked deficiency in Mg relative to other brines. This deficiency is most likely due to water-rock reactions (i.e., serpentinization) that preferentially remove Mg from hydrothermal fluids. Endorheic basins can be challenging to characterize because many are already saturated with respect to halite and, in some cases, sylvite or antarcticite. However, all concentrated endorheic basins show a marked increase in Ca that is inversely proportional to Na, while Mg and K show less distinct trends due to their sensitivity to water-rock interactions. Therefore, the final precipitation sequence is considered the key metric for assessing the provenance of a chloride-rich brine. This study showed that most natural chloride-rich brines precipitate halite first, followed by sylvite. However, the sequence of the final chloride species to precipitate (limited here to antarcticite, bischofite, and carnallite) show differences that can be grouped by brine type. Hydrothermal fluids and deep basinal brines are distinct from endorheic basins in terms of their precipitation sequences; therefore, these processes could potentially be identified if a dried inclusion or intact layered deposit were located and characterized on Mars.

One particular location – Don Juan Pond, Antarctica – showed a composition and precipitation sequence unique among the brines included in this study. Don Juan Pond showed a marked deficiency in K relative to other brines of a similar ionic strength. Additionally, Don Juan Pond precipitates antarcticite prior to sylvite, which no other brine was shown to do. Because Don Juan Pond is considered an analog to both current and ancient Mars due to the presence of nearby water tracks and its cold, dry

environment, it could prove to be a critical analog locality for studying the composition and behavior of brines on modern and ancient Mars.

Chapter 4: The Effects of Composition and Texture on the Infrared Emission Spectra of Chloride Minerals. The detailed characterization of chloride deposits on Mars must begin with remote sensing. While chlorides have been identified on Mars by THEMIS, their composition and texture remain unknown. New space-worthy instruments capable of collecting emission spectra in the far-infrared have provided an opportunity for refining our knowledge of martian chlorides. Previous studies of chlorides in reflectance and transmission have identified the locations of fundamental absorption modes of chloride minerals; however, emission studies provide a more practical means of interpreting chlorides in nature. Additionally, spectral emissivity is determined by the internal vibrations of a mineral and is therefore a more accurate indicator of composition than reflectance. This study represents the first characterization of chloride minerals and their natural textures in emission and in the far-infrared, where their fundamental absorptions can be observed and described.

Pressed pellets of halite, sylvite, and $CaCl_2$ were produced from reagent-grade powders of each compound. Synthetic textures made from halite were produced in the laboratory by evaporating a halite brine under infrared lamps at a range of evaporation rates expected for current – and possibly ancient – Mars. Field samples of polygonal crack halite and an unidentified salt were collected from Bristol Dry Lake, a terrestrial playa in the Mojave Desert, California. Emission spectra of the pressed pellets, synthetic textures, and field samples were characterized from 2000 cm^{-1} to 50 cm^{-1} (mid-infrared to far-infrared).

Sylvite has distinct fundamental absorption features in the far-infrared that do not overlap with those of halite or $CaCl_2$. However, $CaCl_2$ has several absorption features in the far-infrared that overlap with those of halite. The $CaCl_2$ absorptions are much shallower than those of halite (when comparing pressed pellets) and are very broad, indicating the possible overlap of several absorptions at similar wavenumbers. The synthetic halite textures showed distinct variations with grain size, where finer-grained samples had shallower absorption features (lower spectral contrast) than samples with multiple large or single crystals. Samples that have been compressed, have interstitial cements, or are composed of loose grains larger than ~2-mm in size all have similar band depths at the transverse fundamental (~180 cm^{-1}). Band ratios between the two fundamental absorptions vary with grain size, likely because one band (the transverse fundamental) is more sensitive to grain size variations than the other (the longitudinal fundamental). Field samples showed a similar trend, with finer grain sizes having lower spectral contrast than coarser samples.

This study shows that far-infrared emission spectroscopy can be used to distinguish composition and, to a limited extent, the texture of chlorides in nature. Halite can be distinguished from $CaCl_2$ at shorter wavelengths, where adsorbed or structural water in calcium-chloride-based minerals (i.e., sinjarite or antarcticite) would differentiate it from anhydrous halite. Large variations in grain size could be determined based on the spectral contrast of the transverse fundamental absorption feature. However, more moderate variations in grain size, compaction, and/or the presence of cements are more difficult to resolve using far-infrared spectroscopy alone. Future work

should explore the thermal inertias of these textures in the laboratory and the field to complement the information provided by far-infrared emission spectroscopy.

Chapter 5: Recurring Slope Lineae and Chlorides on the Surface of Mars. Recurring slope lineae (RSL) are dark streaks that propagate down-slope on warm, steep slopes on Mars. Numerous studies have attributed these features to water flows; however, the hypothesis that RSL are the result of water outflow has numerous hurdles because fresh water is not stable on the martian surface due to low pressures and temperatures. For liquid water to be stable long enough to produce RSL, salt must be dissolved in the water to depress its freezing point, providing thermodynamic stability at low pressure. Only certain salts can depress the freezing point low enough to allow water to remain liquid under Mars surface conditions: perchlorate, ferric sulfate, and calcium chloride. Perchlorate and ferric sulfate have been studied in the visible/near-infrared, with extremely limited evidence of their role in the production of RSL on Mars. Of these three compounds, calcium chloride has been least studied, and then only in laboratory or theoretical models. The purpose of this study was to search for empirical evidence of chloride in proximity to RSL in order to assess calcium chloride as the dissolved salt in the production of RSL brine.

The co-location of RSL and chloride was undertaken by first mapping the locations of known RSL in the martian mid-latitudes and in Valles Marineris using high-resolution images from the HiRISE camera. Then, THEMIS decorrelation stretch products were used to qualitatively assess the presence of chloride minerals by measuring the spectral slope imparted to thermal infrared spectra in the presence of significant quantities of chloride mineral. In addition to searching for empirical evidence of

chlorides at RSL sites, the threshold of detection of chloride was assessed for THEMIS spectra, which consist of ten bands in the thermal infrared.

Of the 30 RSL sites surveyed for chlorides, only two showed possible evidence of a chloride lag deposit left behind after the possible evaporation of a brine. One site, in Palikir Crater, was in close proximity to a recent putative detection of hydrated perchlorate minerals. A second site, in Valles Marineris, was at a site with RSL an order of magnitude larger than those seen at Palikir Crater. In both cases, THEMIS spectra showed no detectable variation compared to the spectra of surrounding materials, which indicates that: 1) small RSL may have chlorides, but they are not large enough to affect thermal infrared spectra, and 2) the effect of slopes on thermal infrared spectra may falsely indicate chlorides when, in fact, there are none. The second case was tested by examining another THEMIS decorrelation stretch product that showed no persistence of spectral slope across all bands.

A simple model of chloride detection in the thermal infrared shows that a minimum of ~30 g/m^2 calcium chloride is needed to produce a detectable spectral variation; this equates to ~300 kg of calcium chloride per THEMIS pixel. This means that ~80 mL/m^2 of concentrated brine would be required for detection. Over the last estimated climate cycle on Mars (100 ky), a maximum of ~8 x 10^{-4} mL/m^2-yr could flow across the martian surface without its lag deposit being detected by THEMIS. This low volume of brine could easily be met with annual observed RSL activities, assuming the entirety of the flow is on the surface. We therefore conclude that, if RSL are actually brine-driven features, they are produced by subsurface brine flow with only a small portion of brine wicked to the surface. Additionally, the amounts of salt required to

produce detectable masses of chloride by THEMIS would likely result in resolvable mass wasting in nearby regions where salt was being removed. Subsurface salt deposits of this size likely exist on Mars because they have been observed at meters-thick scales on the surface, where they have been significantly eroded.

Future Work: This study has incorporated numerous techniques for the study of water-bearing environments on the Moon and Mars. Because many of these studies were the first of their kind, they leave open the door for more detailed investigations. Investigations of PSRs at the lunar poles should include a greater number of data sets, including Diviner brightness temperatures, and LOLA reflectance measurements. Studies of chloride-rich brines should be completed with updated analyses of brine compositions across a larger number of terrestrial localities. Far-infrared spectra of well-characterized grain sizes and hydrated chloride minerals should be completed to allow thorough characterization of these minerals in emission. New RSL have been discovered and should be assessed for the presence of chlorides: especially new RSL that have been found in cold environments in the northern hemisphere of Mars.

Many of the techniques used in this study are limited by spectral or spatial resolution, or by the absence of instruments in orbit around the Moon and/or Mars that are sensitive to the necessary wavelengths of study. This work provides justification for the development and implementation of a new generation of spacecraft at the Moon and Mars that will allow the distribution, abundance, and provenance of water-bearing environments to be characterized. These measurements will pave the way for future human and robotic exploration of the inner Solar System and will enable a deeper understanding of Solar System evolution.

REFERENCES

Adeli, S., E. Hauber, L. Le Deit, and R. Jaumann (2015), Geologic evolution of the eastern Eridania basin: Implications for aqueous processes in the southern highlands of Mars, *J. Geophys. Res.: Planets, 120(1774-1799)*, doi:10.1002/2015JE004898.

Albarede, F., C. Ballhaus, J. Blichert-Toft, C.-T. Lee, B. Marty, F. Moynier, Q.-Z. Yin (2013), Asteroidal impacts and the origin of terrestrial and lunar volatiles, *Icarus, 222(44-52*), doi: 10.1016/j.icarus.2012.10.026.

Alexander, C. M. O., R. Bowden, M. L. Fogel, K. T. Howard, C. D. K. Herd, and L. R. Nittler (2012), The provenances of asteroids, and their contributions to the volatile inventories of the terrestrial planets, *Science*, *337*, 721–723, doi:10.1126/science.1223474.

Altheide, T., V. Chevrier, C. Nicholson, and J. Denson (2009), Experimental investigation of the stability and evaporation of sulfate and chloride brines on Mars, *Earth Planet. Sci. Lett.*, *282*(1–4), 69–78, doi:10.1016/j.epsl.2009.03.002.

Anand, M., I. A. Crawford, M. Balat-Pichelin, S. Abanades, W. Van Westrenen, G. Péraudeau, R. Jaumann, and W. Seboldt (2012), A brief review of chemical and mineralogical resources on the Moon and likely initial in situ resource utilization (ISRU) applications, *Planet. Space Sci.*, *74*, 42–48, doi:10.1016/j.pss.2012.08.012.

Arnold, J. R. (1979), Ice in the lunar polar regions, *J. Geophys. Res.*, *84*(B10), 5659–5668, doi:10.1029/JB084iB10p05659.

Aronson, J., and A. Emslie (1967), Studies of the middle-and far-infrared spectra of mineral surfaces for application in remote compositional mapping of the moon and planets, *J. Geophys.*, *72* (2).

Baker, V. R. (2006), Geomorphological evidence for water on Mars, *Elements*, *2*, 141–145.

Baker, V. R. (2001), Water and the martian landscape, *Nature*, *412*(6843), 228–236, doi:10.1038/35084172.

Baldridge, A. M. (2008), Thermal Infrared Spectral Studies of Sulfates and Chlorides; Applications to Salts on the Martian Surface, PhD dissertation, 207 pp., Arizona State University, Tempe.

Baldridge, A. M., J. D. Farmer, and J. E. Moersch (2004), Mars remote-sensing analog studies in the Badwater Basin, Death Valley, California, *J. Geophys. Res. E Planets*,

109(12), 1–18, doi:10.1029/2004JE002315.

Bandfield, J., A. D. Rogers, and C. S. Edwards (2011), The role of aqueous alteration in the formation of martian soils, *Icarus*, *211*(1), 157–171, doi:10.1016/j.icarus.2010.08.028.

Bandfield, J. L. (2000), A global view of martian surface compositions from MGS-TES, *Science*, *287*, 1626–1630, doi:10.1126/science.287.5458.1626.

Bandfield, J. L. (2004), Atmospheric correction and surface spectral unit mapping using Thermal Emission Imaging System data, *J. Geophys. Res.*, *109*(E10), E10008, doi:10.1029/2004JE002289.

Bandfield, J. L. (2009), Effects of surface roughness and graybody emissivity on martian thermal infrared spectra, *Icarus*, *202*(2), 414–428, doi:10.1016/j.icarus.2009.03.031.

Bandfield, J. L., V. E. Hamilton, P. R. Christensen, and H. Y. McSween (2004), Identification of quartzofeldspathic materials on Mars, *J. Geophys. Res. E Planets*, *109*(1), 1–14, doi:10.1029/2004JE002290.

Bandfield, J. L., R. R. Ghent, A. R. Vasavada, D. A. Paige, S. J. Lawrence, and M. S. Robinson (2011), Lunar surface rock abundance and regolith fines temperatures derived from LRO Diviner Radiometer data, *J. Geophys. Res.*, *116*, 1-18, doi:10.1029/2011JE003866.

Banin, A. (1996), The missing crystalline minerals in Mars soil, *Adv. Sp. Res.*, *18*(12), 233–240, doi:10.1016/0273-1177(96)00112-3.

Bąbel, M., and B. C. Schreiber (2013), Geochemistry of evaporites and evolution of seawater, *Treatise on Geochemistry*, Elsevier, 483-560.

Barnes, J. J., D. A. Kring, R. Tartèse, I. A. Franchi, M. Anand, and S. S. Russell (2016), An asteroidal origin for water in the Moon, *Nat. Commun.*, *7*(11684), 1-10, doi:10.1038/ncomms11684.

Barnes, J. D., and M. Cisneros (2012), Mineralogical control on the chlorine isotope composition of altered oceanic crust, *Chem. Geology*, 326-327(51-60), doi: 10.1016/j.chemgeo.2012.07.022.

Battler, M. M., G. R. Osinski, and N. R. Banerjee (2013), Mineralogy of saline perennial

cold springs on Axel Heiberg Island, Nunavut, Canada and implications for spring deposits on Mars, *Icarus*, *224*(2), 364–381, doi:10.1016/j.icarus.2012.08.031.

Baumberger, T., G. L. Früh-Green, I. H. Thorseth, M. D. Lilley, C. Hamelin, S. M. Bernasconi, I. E. Okland, and R. B. Pedersen (2016), Fluid composition of the sediment-influenced Loki's Castle vent field at the ultra-slow spreading Arctic Mid-Ocean Ridge, *Geochim. Cosmochim. Acta*, *187*, 156–178, doi:10.1016/j.gca.2016.05.017.

Beaufort, D., C. Rigault, S. Billon, V. Billault, A. Inoue, S. Inoue, and P. Patrier (2015), Chlorite and chloritization processes through mixed-layer mineral series in low-temperature geological systems – a review, *Clay Miner.*, *50*(4), 497–523, doi:10.1180/claymin.2015.050.4.06.

Benison, K. C., and D. A. Laclair (2003), Modern and ancient extremely acid saline deposits: terrestrial analogs for martian environments?, *Astrobiology*, *3*(3).

Berger, J. A., P. L. King, A. Green, M. A. Craig, M. N. Spilde, S. P. Wright, T. S. Kunkel, and R. J. Lee (2015), Effect of halite coatings on thermal infrared spectra, *J. Geophys. Res. Solid Earth*, 1–17, doi:10.1002/2014JB011712.

Bibring, J.-P., R. E. Arvidson, A. Gendrin, B. Gondet, Y. Langevin, S. Le Mouelic, N. Mangold, R. V. Morris, J. F. Mustard, F. Poulet, C. Quantin and C. Sotin (2007), Coupled ferric oxides and sulfates on the martian surface, *Science*, *317*(5842), 1206–1210.

Bibring, J.-P., Y. Langevin, J. F. Mustard, F. Poulet, R. E. Arvidson, A. Gendrin, B. Gondet, N. Mangold, P. Pinet, F. Forget and The OMEGA Team (2006), Global mineralogical and aqueous mars history derived from OMEGA/Mars Express data., *Science*, *312*(5772), 400–404, doi:10.1126/science.1122659.

Bingqiu, Z., and Y. Hui (1995), The use of geochemical indicator elements in the exploration for hot water sources within geothermal fields, *J. of Geochem. Expl.*, *55*, 125–136.

Birch, S. (1866), On the glacial condition of the Moon's surface, *Geol. Mag.*, 3(20), 91-93, doi:10.1017/S0016756800165379.

Blake, D. F., R. V. Morris, G. Kocurek, S. M. Morrison, R. T. Downs, D. Bish, D. W. Ming, K. S. Edgett, D. Rubin, W. Goetz, M. B. Madsen, R. Sullivan, R. Gellert, I. Campbell, A. H. Treiman, S. M. McLennan, A. S. Yen, J. Grotzinger, D. T. Vaniman, S. J. Chipera, C. N. Achilles, E. B. Rampe, D. Sumner, P.-Y. Meslin, S. Maurice, O. Forni, O. Gasnault, M. Fisk, M. Schmidt, P. Mahaffy, L. A. Leshin, D. Glavin, A. Steele, C. Freissinet, R. Navarro-González, R. A. Yingst, L. C. Kah, N. Bridges, K. W. Lewis, T. F. Bristow, J. D. Farmer, J. A. Crisp, E. M. Stolper, D. J.

Des Marais, P. Sarrazin, MSL Science Team (2013), Curiosity at Gale Crater, Mars: Characterization and analysis of the Rocknest sand shadow, *Science*, *341*(6153), 1239505, doi:10.1126/science.1239505.

Bogard, D. D., and W. C. Hirsch (1975), Noble gas studies on grain size separates of Apollo 15 and 16 drill cores, *Proc. Lunar Sci. Conf. 6th*, 2057–2083, doi:10.1017/CBO9781107415324.004.

Boschetti, T., G. Cortecci, M. Barbieri, and M. Mussi (2007), New and past geochemical data on fresh to brine waters of the Salar de Atacama and Andean Altiplano, northern Chile, *Geofluids*(7), 33–50, doi:10.1111/j.1468-8123.2006.00159.x.

Brass, G. W. (1980), Stability of brines on Mars, *Icarus*, *42*(1), 20–28, doi:10.1016/0019-1035(80)90237-7.

Bucher, K., and I. Stober (2011), Fluids in the upper continental crust, *Front. Geofluids*, *3*(1), 241–253, doi:10.1002/9781444394900.ch17.

Bullock, M. A. (2004), Aqueous alteration of Mars-analog rocks under an acidic atmosphere, *Geophys. Res. Lett.*, *31*(14), L14701, doi:10.1029/2004GL019980.

Burt, D. M., and L. P. Knauth (2003), Electrically conducting, Ca-rich brines, rather than water, expected in the martian subsurface, *J. Geophys. Res.*, *108*, 1–6, doi:10.1029/2002JE001862.

Burt, D. M., P. Adams, L. Kirkland, and K. Herr (2003), First airborne thermal infrared hyperspectral imaging of a dry lake: site geology and TES/THEMIS interpretations of Mars., Abstract 1860 presented at Lunar and Plan. Sci. Conf. XXXIV.

Bussey, D. B. J. (2003), Permanent shadow in simple craters near the lunar poles, *Geophys. Res. Lett.*, *30*(6), 1278, doi:10.1029/2002GL016180.

Bussey, D. B. J., P. D. Spudis, and M. S. Robinson (1999), Illumination conditions at the lunar South Pole, *Geophys. Res. Lett.*, *26*(9), 1187–1190, doi:10.1029/1999GL900213.

Bussey, D. B. J., J. A. McGovern, P. D. Spudis, C. D. Neish, H. Noda, Y. Ishihara, and S.-A. Sorensen (2010), Illumination conditions of the south pole of the Moon derived using Kaguya topography, *Icarus*, *208*, 558–564, doi:10.1016/j.icarus.2010.03.028.

Butterfield, D. A. (2009), A Si-Cl geothermobarometer for the reaction zone of high-temperature, basaltic-hosted mid-ocean ridge hydrothermal systems, *Geochem., Geophys, Geosys.*, *10(5)*, 1–9, doi:10.1029/2009GC002407.

Byrne, S., C. M. Dundas, M. R. Kennedy, M. T. Mellon, A. S. McEwen, S. C. Cull, I. J. Daubar, D. E. Shean, K. D. Seelos, S. L. Murchie, B. A. Cantor, R. E. Arvidson, K. S. Edgett, A. Reufer, N. Thomas, T. N. Harrison, L. V. Posiolova, F. P. Seelos (2009), Distribution of mid-latitude ground ice on Mars from new impact craters., *Science*, *325*(5948), 1674–6, doi:10.1126/science.1175307.

Cabrol, N., and E. Grin (1999), Distribution, classification, and ages of martian impact crater lakes, *Icarus*, *142*(1), 160–172, doi:10.1006/icar.1999.6191.

Cabrol, N. A., and E. A. Grin (2010), *Lakes on Mars*, 1st ed., Elsevier Science, 1-410.

Cady, S. L., J. D. Farmer, J. P. Grotzinger, J. W. Schopf, and A. Steele (2003), Morphological biosignatures and the search for life on Mars., *Astrobiology*, *3*(2), 351–368, doi:10.1089/153110703769016442.

Caron, M., S. E. Grasby, and M. C. Ryan (2008), Spring water trace element geochemistry : A tool for resource assessment and reconnaissance mineral exploration, *Applied Geochemistry*, *23*, 3561–3578, doi:10.1016/j.apgeochem.2008.07.020.

Carr, M. H. (1974), The role of lava erosion in the formation of lunar rilles and Martian channels, *Icarus*, *22*(1), 1–23, doi:10.1016/0019-1035(74)90162-6.

Carr, M. H. (1979), Formation of Martian flood features by release of water from confined aquifers, *J. Geophys. Res.*, *84*, 2995–3007, doi:10.1029/JB084iB06p02995.

Carr, M. H., and J. W. Head (2010), Geologic history of Mars, *Earth Planet. Sci. Lett.*, *294*(3–4), 185–203, doi:10.1016/j.epsl.2009.06.042.

Carrier, B. L., and S. P. Kounaves (2015), The origins of perchlorate in the Martian soil, *Geophys. Res. Letters*, 1–7, doi:10.1002/2015GL064290.

Carroll, B. Y. D. (1959), Ion exchange in clays and other minerals, *Bulletin of Geo. Soc. of America*, *70*(June), 70–100.

Carter, J., F. Poulet, A. Ody, J. Bibring, and S. Murchie (2011), Global distribution, composition and setting of hydrous minerals on Mars: A reappraisal, *42nd Lunar Planet. Sci. Conf., Abstract #2593*, 1–2.

Carter, J., F. Poulet, J. P. Bibring, N. Mangold, and S. Murchie (2013), Hydrous minerals on Mars as seen by the CRISM and OMEGA imaging spectrometers: Updated global view, *J. Geophys. Res. E Planets*, *118*(4), 831–858, doi:10.1029/2012JE004145.

Catling, D. C. (1999), A chemical model for evaporites on early Mars: Possible

sedimentary tracers of the early climate and implications for exploration, *J. Geophys. Res.*, *104*, 16453, doi:10.1029/1998JE001020.

Catling, D. C., M. W. Claire, K. J. Zahnle, R. C. Quinn, B. C. Clark, M. H. Hecht, and S. Kounaves (2010), Atmospheric origins of perchlorate on mars and in the Atacama, *J. Geophys. Res. E Planets*, *115*(1), 1–15, doi:10.1029/2009JE003425.

Chabot, N. L., C. M. Ernst, B. W. Denevi, H. Nair, A. N. Deutsch, D. T. Blewett, S. L. Murchie, G. A. Neumann, E. Mazarico, D. A. Paige, J. K. Harmon, J. W. Head, and S. C. Solomon (2014), Images of surface volatiles in Mercury's polar craters acquired by the MESSENGER spacecraft, *Geology*, *42*(12), 1051–1054, doi:10.1130/G35916.1.

Chamberlain, M. A., and W. V. Boynton (2007), Response of Martian ground ice to orbit-induced climate change, *J. Geophys. Res. E Planets*, *112*(6), 1–20, doi:10.1029/2006JE002801.

Cheek, L. C., C. M. Pieters, J. W. Boardman, R. N. Clark, J. P. Combe, J. W. Head, P. J. Isaacson, T. B. McCord, D. Moriarty, J. W. Nettles, N. E. Petro, J. M. Sunshine, and L. A. Taylor (2011), Goldschmidt crater and the Moon's north polar region: Results from the Moon Mineralogy Mapper (M3), *J. Geophys. Res.*, *116*, doi:10.1029/2010JE003702.

Chevrier, V., D. W. G. Sears, J. D. Chittenden, L. A. Roe, R. Ulrich, K. Bryson, L. Billingsley, and J. Hanley (2007), Sublimation rate of ice under simulated Mars conditions and the effect of layers of mock regolith JSC Mars-1, *Geophys. Res. Lett.*, *34*(L02203), 3–7, doi:10.1029/2006GL028401.

Chevrier, V. F., and T. S. Altheide (2008), Low temperature aqueous ferric sulfate solutions on the surface of Mars, *Geophys. Res. Lett.*, *35*(22), doi:10.1029/2008GL035489.

Chevrier, V. F., and E. G. Rivera-Valentin (2012), Formation of recurring slope lineae by liquid brines on present-day Mars, *Geophys. Res. Lett.*, *39*, doi:10.1029/2012GL054119.

Chevrier, V. F., J. Hanley, and T. S. Altheide (2009), Stability of perchlorate hydrates and their liquid solutions at the Phoenix landing site, Mars, *Geophys. Res. Lett.*, *36*(10), L10202, doi:10.1029/2009GL037497.

Christensen, P. R. (2003), Formation of recent martian gullies through melting of extensive water-rich snow deposits, *Nature*, *422*, 45–48, doi:10.1038/nature01436.

Christensen, P. R., D. L. Anderson, S. C. Chase, R. T. Clancy, R. N. Clark, B. J. Conrath,

H. H. Kieffer, R. O. Kuzmin, M. C. Malin, J. C. Pearl, T. L. Roush and M. D. Smit (1998), Results from the Mars Global Surveyor Thermal Emission Spectrometer, *Science*, *279*(5357), 1692–8.

Christensen, P. R., J. L. Bandfield, V. E. Hamilton, D. A. Howard, M. D. Lane, J. L. Piatek, S. W. Ruff, and W. L. Stefanov (2000), A thermal emission spectral library of rock-forming minerals, *J. Geophys. Res.*, *105*(E4), 9735, doi:10.1029/1998JE000624.

Christensen, P. R., J. L. Bandfield, M. D. Smith, V. E. Hamilton, and R. N. Clark (2000), Identification of a basaltic component on the Martian surface from Thermal Emission Spectrometer data, *J. Geophys. Res.*, *105*(E4), 9609, doi:10.1029/1999JE001127.

Christensen, P. R., B. M. Jakosky, H. H. Kieffer, M. C. Malin, H. Y. McSween, K. Nealson, G. H. Mehall, S. H. Silverman, S. Ferry, M. Caplinger, and M. Ravine (2004), The Thermal Emission Imaging System (THEMIS) for the Mars 2001 Odyssey Mission, *Space Sci. Rev.*, *110*, 85–130, doi:10.1023/B:SPAC.0000021008.16305.94.

Christensen, P. R., E. Engle, S. Anwar, S. Dickenshied, D. Noss, N. Gorelick, and M. Weiss-Malik (2009), JMARS – A Planetary GIS, in *American Geophysical Union, Fall Meeting 2009*, p. IN22A–06.

Christov, C. and M. Moller (2015), A chemical equilibrium of solution behavior and solubility in the H-Na-K-Ca-OH-Cl- HSO4-SO4-H2O system to high concentration and temperature, *Geochem. et Cos. Acta*, 68(18), 3717-3739, doi:10.1016/j.gca.2004.03.006.

Chukanov, N. V (2014), *Infrared spectra of mineral species. Extended library*. Vol 1., pp. 1733., Springer Geochemistry/Mineralogy, The Netherlands, doi:10.1007/978-94-007-7128-4.

Cintala, M. J., and K. M. M. McBride (1994), Block distributions on the lunar surface: A comparison between measurements obtained from surface and orbital photography, *NASA Tech. Memo.*, *104804*.

Clark, B. C., A. K. Baird, H. J. Rose, Jr., P. Toulmin III, K. Keil, A. J. Castro, W. C. Kelliher, C. D. Rowe, and P. H. Evans (1976), Inorganic analyses of martian surface samples at the Viking landing sites, *Science, 194(4271), 1283-8,* doi: 10.1126/science.194.4271.1283.

Clark, B. C., R.V. Morris, S.M. McLennan, R. Gellert, B. Jolliff, A.H. Knoll, S.W. Squyres, T.K. Lowenstein, D.W. Ming, N.J. Tosca, A. Yen, P.R. Christensen, S. Gorevan, J. Bruckner, W. Calvin, G. Dreibus, W. Farrand, G. Klingelhoefer, H.

Waenke, J. Zipfel, J.F. Bell III, J. Grotzinger, H.Y. McSween, R. Rieder (2005), Chemistry and mineralogy of outcrops at Meridiani Planum, *Earth Planet. Sci. Lett.*, *240*(1), 73–94, doi:10.1016/j.epsl.2005.09.040.

Clark, R. N., and T. L. Roush (1984), Reflectance spectroscopy - Quantitative analysis techniques for remote sensing applications, *Jour. Geophys. Res.*, *89*, 6329–6340, doi:10.1029/JB089iB07p06329.

Clark, B. C., and D. C. Van Hart (1981), The salts of Mars, *Icarus*, *45*(2), 370–378, doi:10.1016/0019-1035(81)90041-5.

Cocks, F. H., P. A. Klenk, S. A. Watkins, W. N. Simmons, J. C. Cocks, E. E. Cocks, and J. C. Sussingham (2002), Lunar ice: adsorbed water on subsurface polar dust, *Icarus, 160*, 386–397, doi:10.1006/icar.2002.6972.

Colaprete, A., P. Schultz, J. Heldmann, D. Wooden, M. Shirley, K. Ennico, B. Hermalyn, W. Marshall, A. Ricco, R. C. Elphic, D. Goldstein, D. Summy, G. D. Bart, E. Asphaug, D. Korycansky, D. Landis, L. Sollitt (2010), Detection of water in the LCROSS ejecta plume, *Science, 330*(6003), 463–468, doi:10.1126/science.1186986.

Committee on the Scientific Context for Exploration of the Moon, N. R. C. (2007), *The Scientific Context for the Exploration of the Moon*.

Coleman, N. M. (2003), Aqueous flows carved the outflow channels on Mars, *J. Geophys. Res.*, *108*(E9), 6225–6225, doi:10.1029/2003JE002137.

Conel, J. E. (1969), Infrared emissivities of silicates: Experimental results and a cloudy atmosphere model of spectral emission from condensed particulate mediums, *J. Geophys. Res.*, *74*(6), 1614–1634, doi:10.1029/JB074i006p01614.

Conway, S. J., M. R. Balme, M. A. Kreslavsky, J. B. Murray, and M. C. Towner (2015), The comparison of topographic long profiles of gullies on Earth to gullies on Mars: A signal of water on Mars, *Icarus, 253*, 189–204, doi:10.1016/j.icarus.2015.03.009.

Cortecci, G., T. Boschetti, M. Mussi, C. H. Lameli, C. Mucchino, and M. Barbieri (2005), New chemical and original isotopic data on waters from El Tatio geothermal field, northern Chile, *Geochem. J.*, *39*(6), 547–571, doi:10.2343/geochemj.39.547.

Craddock, R. A. (2002), The case for rainfall on a warm, wet early Mars, *J. Geophys. Res.*, *107*(E11), 5111, doi:10.1029/2001JE001505.

Crawford, I. A., M. An, C. S. Cockell, H. Falcke, D. A. Green, R. Jaumann, M. A. Wieczorek, and M. Anand (2012), Back to the Moon: The scientific rationale for resuming lunar surface exploration, *Planet. Space Sci.*, *74*, 3–14.

Crider, D. H., and R. R. Vondrak (2002), Hydrogen migration to the lunar poles by solar wind bombardment of the moon, *Adv. Sp. Res.*, *30*(8), 1869–1874, doi:10.1016/S0273-1177(02)00493-3.

Crider, D. H., and R. R. Vondrak (2003), Space weathering effects on lunar cold trap deposits, *J. Geophys. Res.*, *108*(E7), doi:10.1029/2002JE002030.

Crowley, J. K., and S. J. Hook (1996), Mapping Playa Evaporite Minerals and Associated Sediments in Death Valley, California, with multispectral thermal infrared images, *J. Geophys. Res.*, *101(B1)*, 643–660.

Cusicanqui, H., W. A. J. Mahon, and A. J. Ellis (1975), The geochemistry of the El Tatio geothermal field, northern Chile, *Proc. Second United Nations Symp. Dev. Use Geotherm. Resour.*, *1*, 703–711, doi:10.1080/09640560701402075.

Dalton, J. B. B., O. Prieto-Ballesteros, J. S. S. Kargel, C. S. S. Jamieson, J. Jolivet, and R. Quinn (2005), Spectral comparison of heavily hydrated salts with disrupted terrains on Europa, *Icarus*, *177*(2), 472–490, doi:10.1016/j.icarus.2005.02.023.

Von Damm, K. L., S. E. Oostling, R. Kozlowski, L. G. Buttermore, D. C. Colodner, H. N. Edmonds, J. M. Edmond, and J. M. Grebmeier (1995), Evolution of East Pacific Rise hydrothermal vent fluids following a volcanic eruption, *Nature*, *375*(6526), 47–50, doi:10.1038/375047a0.

Dasgupta, P. K., P. K. Martinelango, W. A. Jackson, T. A. Anderson, K. Tian, R. W. Tock, and S. Rajagopalan (2005), The origin of naturally occurring perchlorate: The role of atmospheric processes, *Environ. Sci. Technol.*, *39*(6), 1569–1575, doi:10.1021/es048612x.

Davila, A. F., L. G. Duport, R. Melchiorri, J. Janchen, S. Valea, A. de los Rios, A. G. Fairen, D. Mohlmann, C. P. McKay, C. Ascaso, and J. Wierzchos (2010), Hygroscopic salts and the potential for life on Mars., *Astrobiology*, *10*(6), 617–628, doi:10.1089/ast.2009.0421.

Deocampo, D. M., and B. F. Jones (2013), Geochemistry of Saline Lakes, *Treatise on Geochemistry*, 2nd ed., Elsevier Ltd., pp. 437-469.

DiAchille, G., and B. M. Hynek (2010), Deltas and valley networks on Mars: implications for a global hydrosphere, in *Lakes on Mars*, pp. 223–248, Elsevier B.V.

DiFrancesco, N. J., H. Nekvasil, D. H. Lindsley, and A. D. Rogers (2016), Modifying Martian Surface Chemistry: Chlorides as Sublimates from Volcanic Degassing on Mars, *Icarus*, 9–10, doi:10.1016/j.icarus.2007.12.027.

Dickson, J. L., and J. W. Head (2009), The formation and evolution of youthful gullies on

Mars: Gullies as the late-stage phase of Mars' most recent ice age, *Icarus*, *204*(1), 63–86, doi:10.1016/j.icarus.2009.06.018.

Dickson, J. L., J. W. Head, and M. Kreslavsky (2007), Martian gullies in the southern mid-latitudes of Mars: Evidence for climate-controlled formation of young fluvial features based upon local and global topography, *Icarus*, *188*(2), 315–323, doi:10.1016/j.icarus.2006.11.020.

Dickson, J. L., J. W. Head, T. A. Goudge, and L. Barbieri (2015), Recent climate cycles on Mars: Stratigraphic relationships between multiple generations of gullies and the latitude dependent mantle, *Icarus, 252*, 83–94, doi:10.1016/j.icarus.2014.12.035.

Ding, K., W. E. Seyfried, Z. Zhang, M. K. Tivey, K. L. Von Damm, and A. M. Bradley (2005), The in situ pH of hydrothermal fluids at mid-ocean ridges, *Earth and Plan. Sci. Lett.*, *237*, 167–174, doi:10.1016/j.epsl.2005.04.041.

Dolginko, L. (2014), The Influence of Magmatic Activity on Brine Evolution in Closed Basins: Searles Lake, California, and Bristol Dry Lake, California., M. S. thesis, pp. 1-82, Binghamton Univ., Binghamton, New York.

Donaldson Hanna, K. L., B. T. Greenhagen, W. M. Patterson III, C. M. Pieters, J. F. Mustard, N. E. Bowles, D. A. Paige, T. D. Glotch, and C. Thompson (2016), Effects of varying environmental conditions on emissivity spectra of bulk lunar soils: Application to Diviner thermal infrared observations of the Moon, *Icarus*, *283*, doi:10.1016/j.icarus.2016.05.034.

Drebushchak, V. A., A. G. Ogienko, and A. S. Yunoshev (2017), Metastable eutectic melting in the NaCl-H2O system, *Thermochim. Acta*, *647*, 94–100, doi:10.1016/j.tca.2016.12.004.

Dreibus, G., and H. Wanke (1985), Mars, a volatile-rich planet, *Meteoritics*, *20*(2), 367–381, doi:10.1017/CBO9781107415324.004.

Dundas, C. M., S. Diniega, and A. S. McEwen (2014), Long-term monitoring of martian gully formation and evolution with MRO/HiRISE, *Icarus*, *251*, 244-263, doi:10.1016/j.icarus.2014.05.013.

Duning, G. E., and J. F. Cooper (1969), A second occurrence of antarcticite, from Bristol Dry Lake, California, *Am. Mineral.*, *54*, 1018–1025.

Eastes, J. W. (1989), Spectral properties of halite-rich mineral mixtures: Implications for middle infrared remote sensing of highly saline environments, *Remote Sens. Environ.*, *27*(3), 289–303, doi:10.1016/0034-4257(89)90089-8.

Edwards, C. S., K. J. Nowicki, P. R. Christensen, J. Hill, N. Gorelick, and K. Murray (2011), Mosaicking of global planetary image datasets: 1. Techniques and data

processing for Thermal Emission Imaging System (THEMIS) multi-spectral data, *J. Geophys. Res. E Planets*, *116*, 1–21, doi:10.1029/2010JE003755.

Ehlmann, B. L., J. F. Mustard, S. L. Murchie, F. Poulet, J. L. Bishop, A. J. Brown, W. M. Calvin, R. N. Clark, D. J. Des Marais, R. E. Milliken, L. H. Roach, T. L. Roush, G. A. Swayze, J. J. Wray (2008), Orbital identification of carbonate-bearing rocks on Mars., *Science*, *322*(5909), 1828–1832, doi:10.1126/science.1164759.

Ehlmann, B. L., G. Berger, N. Mangold, J. R. Michalski, D. C. Catling, S. W. Ruff, E. Chassefiere, P. B. Niles, V. Chevrier, and F. Poulet (2013), Geochemical consequences of widespread clay mineral formation in Mars' ancient crust, *Space Sci. Rev.*, *174*(1–4), 329–364, doi:10.1007/s11214-012-9930-0.

Ehlmann, B. L., J. F. Mustard, G. A. Swayze, R. N. Clark, J. L. Bishop, F. Poulet, D. J. Des Marais, L. H. Roach, R. E. Milliken, J. J. Wray, O. Barnouin-Jha, and S. L. Murchie (2009), Identification of hydrated silicate minerals on Mars using MRO-CRISM: Geologic context near Nili Fossae and implications for aqueous alteration, *J. Geophys. Res.*, *114*, E00D08, doi:10.1029/2009JE003339.

Ehlmann, B. L., J. F. Mustard, S. L. Murchie, J.-P. Bibring, A. Meunier, A. A. Fraeman, and Y. Langevin (2011), Subsurface water and clay mineral formation during the early history of Mars, *Nature*, *479*(7371), 53–60.

Eke, V. R., S. A. Bartram, D. A. Lane, D. Smith, and L. F. A. Teodoro (2014), Lunar polar craters - Icy, rough or just sloping?, *Icarus*, *241*, 66–78, doi:10.1016/j.icarus.2014.06.021.

El-Maarry, M. R., W. A. Watters, Z. Yoldi, A. Pommerol, D. Fischer, U. Eggenberger, and N. Thomas (2015), Field investigation of dried lakes in western United States as an analogue to desiccation fractures on Mars, *J. Geophys. Res. Planets*, *120*, 2241–2257, doi:10.1002/2014JE004730.

El-Maarry, M. R., A. Pommerol, and N. Thomas (2013), Analysis of polygonal cracking patterns in chloride-bearing terrains on Mars: Indicators of ancient playa settings, *J. Geophys. Res. E Planets*, *118*(11), 2263–2278, doi:10.1002/2013JE004463.

El-Maarry, M. R., W. A. Watters, Z. Yoldi, A. Pommerol, D. Fischer, U. Eggenberger, and N. Thomas (2016), Dried Lakes in Western United States as Analogue to Desiccation Fractures on Mars, *Lunar Planet. Sci. Conf.*, *2078*, doi:10.1002/2015JE004895.

Elders, W. A. (1976), Quaternary volcanism in the Salton Sea geothermal field, Imperial Valley, California, *Geol. Soc. of Am. Bulletin*, 87, 347–360.

Fa, W., and Y. Cai (2013), Circular polarization ratio characteristics of impact craters

from Mini-RF observations and implications for ice detection at the polar regions of the Moon, *J. Geophys. Res.*, *118*, 1582–1608, doi:10.1002/jgre.20110.

Fa, W., M. Wieczorek, and E. Heggy (2011), Modeling polarimetric radar scattering from the lunar surface: Study on the effect of physical properties of the regolith layer, *J. Geophys. Res.*, *116*, doi:10.1029/2010JE003649.

Fan, Q., and H. Wei (2017), Abnormal Rb / Sr ratio in lacustrine sediments of Qaidam Basin, NE QinghaieTibetan Plateau: A significant role of aeolian dust input, *Quat. Int.*, (May), doi:10.1016/j.quaint.2016.12.050.

Farmer, J. D., and D. J. Des Marais (1999), Exploring for a record of ancient Martian life., *J. Geophys. Res.*, *104*(E11), 26977–26995, doi:10.1029/1998JE000540.

Farmer, V. C. (1974), *The Infrared Spectra of Minerals*, edited by V. C. Farmer, Mineralogical Society of Great Britain and Ireland, Londan.

Fassett, C. I., and J. W. Head (2008), The timing of martian valley network activity: Constraints from buffered crater counting, *Icarus*, *195*(1), 61–89, doi:10.1016/j.icarus.2007.12.009.

Fassett, C. I., and J. W. Head (2008), Valley network-fed, open-basin lakes on Mars : Distribution and implications for Noachian surface and subsurface hydrology, *Icarus*, *198*, 37–56, doi:10.1029/2004JE002287.

Feely, K. C., and P. R. Christensen (1999), Quantitative compositional analysis using thermal emission spectroscopy: Application to igneous and metamorphic rocks, *J. Geophys. Res.*, *104*(E10), 24,195-24,210.

Feldman, W. C., W. V. Boynton, R. L. Tokar, T. H. Prettyman, O. Gasnault, S. W.Squyres, R. C. Elphic, D. J. Lawrence, S. L. Lawson, S. Maurice, G. W. McKinney, K. R.Moore and R. C. Reedy (2002), Global distribution of neutrons from Mars: Results from Mars Odyssey, *Science*, *297*(5578), 75–78, doi:10.1126/science.1073541.

Feldman, W. C., T. H. Prettyman, S. Maurice, J. J. Plaut, D. L. Bish, D. T. Vaniman, M. T. Mellon, A. E. Metzger, S. W. Squyres, S. Karunatillake, W. V. Boynton, R. C. Elphic, H. O. Funsten, D. J. Lawrence, and R. L. Tokar (2004), Global distribution of near-surface hydrogen on Mars, *J. Geophys. Res. E Planets*, *109*(9), 1–13, doi:10.1029/2003JE002160.

Feldman, W. C., S. Maurice, A. B. Binder, B. L. Barraclough, R. C. Elphic, and D. J. Lawrence (1998), Fluxes of fast and epithermal neutrons from Lunar Prospector: Evidence for water ice at the lunar poles, *Science*, *281*, 1496–1500, doi:10.1126/science.281.5382.1496.

Feldman, W. C., D. J. Lawrence, R. C. Elphic, B. L. Barraclough, S. Maurice, I. Genetay, and A. B. Binder (2000), Polar hydrogen deposits on the Moon, *J. Geophys. Res.*, *105*(E2), 4175–4195, doi:10.1029/1999JE001129.

Feldman, W. C., S. Maurice, D. J. Lawrence, R. C. Little, S. L. Lawson, O. Gasnault, R. C. Wiens, B. L. Barraclough, R. C. Elphic, T. H. Prettyman, J. T. Steinberg, and A. B. Binder (2001), Evidence for water ice near the lunar poles, *J. Geophys. Res.*, *106*(E10), pp. 23,231-23,251, doi:10.1029/2000JE001444.

Ferraro, J. R. (1995), *Low-Frequency Vibrations of Inorganic and Coordination Compounds*, Springer US, Boston, MA.

Ferraro, J. R., and A. Walker (1966), Comparison of the infrared spectra of the hydrates and anhydrous salts in the systems UO2(NO3)2 and Th(NO3)4, *J. Chem. Phys.*, *45*(2), 550–553, doi:10.1063/1.1727603.

Filiberto, J., A. H. Treiman, P. A. Giesting, C. A. Goodrich, and J. Gross (2014), High-temperature chlorine-rich fluid in the martian crust: A precursor to habitability, *Earth Planet. Sci. Lett.*, *401*, 110–115, doi:10.1016/j.epsl.2014.06.003.

Fischer, E., G. M. Martínez, and N. O. Rennó (2016), Formation and persistence of brine on Mars: Experimental simulations throughout the diurnal cycle at the Phoenix landing site, *Astrobiology*, *16*(12), 937–948, doi:10.1089/ast.2016.1525.

Forsythe, R. D., and J. R. Zimbelman (1995), A case for ancient evaporite basins on Mars, *J. Geophys. Res.*, *100*(E3), 5553–5563, doi:10.1029/95JE00325.

Fritz, Æ. B. (2009), Origin of salts and brine evolution of Bolivian and Chilean salars Franc, *Aq. Geochem.*, *15(123–157)*, doi:10.1007/s10498-008-9056-x.

Ganor, J., and A. Katz (1989), The geochemical evolution of halite structures in hypersaline lakes: The Dead Sea, Israel, *Limnol. Oceanogr.*, *34*(7), 1214–1223, doi:10.4319/lo.1989.34.7.1214.

Gendrin, A., N.Mangold, J.-P. Bibring, Y. Langevin, B. Gondet, F. Poulet, G. Bonello, C. Quantin, J. Mustard, R. Arvidson, and S. LeMouelic (2005), Sulfates in Martian Layered Terrains: The OMEGA/Mars Express View, *Science*, *307*(5715), 1587–1591, doi:10.1126/science.1109087.

Giggenbach, W. F. (1978), The isotopic composition of waters from the El Tatio geothermal field, Northern Chile, *Geochim. Cosmochim. Acta*, *42*(7), 979–988, doi:10.1016/0016-7037(78)90287-9.

Gillespie, A. R., A. B. Kahle, and R. E. Walker (1986), Color enhancement of highly correlated images. I - Decorrelation and HSI contrast stretches, *Remote Sens.*

Environ., *20*, 209–235, doi:10.1016/0034-4257(86)90044-1.

Gladstone, G. R., S. A. Stern, K. D. Retherford, R. K. Black, D. C. Slater, M. W. Davis, M. H. Versteeg, K. B. Persson, J. W. Parker, D. E. Kaufmann, A. F. Egan, T. K. Greathouse, P. D. Feldman, D. Hurley, W. R. Pryor, A. R. Hendrix (2010), LAMP: The lyman alpha mapping project on NASA's lunar reconnaissance orbiter mission, *Space Sci. Rev.*, *150*, 161–181, doi:10.1007/s11214-009-9578-6.

Gladstone, G. R., K. D. Retherford, A. F. Egan, D. E. Kaufmann, P. F. Miles, J. W. Parker, D. Horvath, P. M. Rojas, M. H. Versteeg, M. W. Davis, T. K. Greathouse, D. C. Slater, J. Mukherjee, A. J. Steffl, P. D. Feldman, D. M. Hurley, W. R. Pryor, A. R. Hendrix, E. Mazarico, and S. A. Stern (2012), Far-ultraviolet reflectance properties of the Moon's permanently shadowed regions, *J. Geophys. Res.*, *117*, doi:10.1029/2011JE003913.

Gläser, P., F. Scholten, D. De Rosa, R. Marco Figuera, J. Oberst, E. Mazarico, G. A. Neumann, and M. S. Robinson (2014), Illumination conditions at the lunar south pole using high resolution digital terrain models from lola, *Icarus*, *243*, 78–90, doi:10.1016/j.icarus.2014.08.013.

Glotch, T. D., J. L. Bandfield, L. L. Tornabene, H. B. Jensen, and F. P. Seelos (2010), Distribution and formation of chlorides and phyllosilicates in Terra Sirenum, Mars, *Geophys.* Res. Lett., 37(L16202), doi: 10.1029/2010GL044557.

Glotch, T. D., J. L. Bandfield, M. J. Wolff, J. A. Arnold, and C. Che (2016), Constraints on the composition and particle size of chloride salt-bearing deposits on Mars, *J. Geophys. Res. Planets*, *121*, 454–471, doi:10.1002/2015JE004989.Received.

Gornitz, V. M., and B. C. Schreiber (1981), Displacive halite hoppers from the Dead Sea; some implications for ancient evaporite deposits, *J. Sediment. Res.*, *51*(3), 787–794, doi:10.1306/212F7DAB-2B24-11D7-8648000102C1865D.

Gooding, L., S. J. Wentworth, and M. E. Zolensky (1991), Aqueous alteration of the Nakhla meteorite, *Meteoritics*, *26*, 135–143, doi:10.1111/j.1945-5100.1991.tb01029.x.

Gorodnichev, E. E., S. L. Dudarev, and D. B. Rogozkin (1990), Coherent wave backscattering by random medium. Exact solution of the albedo problem, *Phys. Lett. A*, *144*(1), 48–54, doi:10.1016/0375-9601(90)90047-R.

Goudge, T., J. Head, J. Mustard, and C. Fassett (2012), An analysis of open-basin lake deposits on Mars: Evidence for the nature of associated lacustrine deposits and post-lacustrine modification processes, *Icarus*, *219*(1), 211–229, doi:10.1016/j.icarus.2012.02.027.

Goudge, T., J. Mustard, J. Head, C. Fassett, and S. Wiseman (2015), Assessing the mineralogy of the watershed and fan deposits of the Jezero crater paleolake system, Mars, *J. Geophys. Res. E Planets*, *120(775-808)*, doi:10.1002/2014JE004782.

Gough, R. V, J. Wong, J. L. Dickson, J. S. Levy, J. W. Head, D. R. Marchant, and M. A. Tolbert (2017), Brine formation via deliquescence by salts found near Don Juan Pond , Antarctica : Laboratory experiments and field observational results, *Earth Planet. Sci. Lett.*, *476*, 189–198, doi:10.1016/j.epsl.2017.08.003.

Grimm, R. E., K. P. Harrison, and D. E. Stillman (2014), Water budgets of martian recurring slope lineae, *Icarus*, *233*, 316–327, doi:10.1016/j.icarus.2013.11.013.

Gross, J., J. Filiberto, and A. S. Bell (2013), Water in the martian interior: Evidence for terrestrial MORB mantle-like volatile contents from hydroxyl-rich apatite in olivine-phyric shergottite NWA 6234, *Earth Planet. Sci. Lett.*, *369–370*, 120–128, doi:10.1016/j.epsl.2013.03.016.

Guo, P., C. Liu, P. Wang, K. Wang, H. Yuan, and B. Li (2017), Geochemical behavior of rare elements in Paleogene saline lake sediments of the Qaidam Basin, NE Tibetan Plateau, *Carbonates and Evaporites*, doi:10.1007/s13146-017-0394-x.

Hadni, A. (1967), *Essentials of Modern Physics Applied to the Study of the Infrared*. Elsevier, pp. 744.

Hamilton, V. E., and P. R. Christensen (2000), Determining the modal mineralogy of mafic and ultramafic igneous rocks using thermal emission spectroscopy, *J. Geophys. Res.*, *105*(E4), 9717, doi:10.1029/1999JE001113.

Hanley, J., V. F. Chevrier, D. J. Berget, and R. D. Adams (2012), Chlorate salts and solutions on Mars, *Geophys. Res. Lett.*, *39*(8), doi:10.1029/2012GL051239.

Hanley, J., J. B. Dalton, V. F. Chevrier, C. S. Jamieson, and R. S. Barrows (2014), Reflectance spectra of hydrated chlorine salts: The effect of temperature with implications for Europa, *J. Geophys. Res. E - Planets*, *119(2370–2377)*, doi:10.1002/2013JE004565.

Hanley, J., V. F. Chevrier, R. S. Barrows, C. Swaffer, and T. S. Altheide (2015), Near- and mid-infrared reflectance spectra of hydrated oxychlorine salts with implications for Mars, *J. Geophys. Res. Planets*, *120*(8), 1415–1426, doi:10.1002/2013JE004575.

Handford, C. R. (1982), Sedimentology and evaporite genesis in a Holocene continental sabkha playa basin, Bristol Dry Lake, California, *Sedimentology*, *29*, 239–254.

Hapke, B. (1973), Darkening of silicate rock powders by solar wind sputtering, *Moon*, *7*, 342–355, doi:10.1007/BF00564639.

Hapke, B. (1990), Coherent backscatter and the radar characteristics of outer planet satellites, *Icarus*, *88*, 407–417, doi:10.1016/0019-1035(90)90091-M.

Hardie, L. A., and H. P. Eugster (1970), The evolution of closed-basin brines, *Miner. Soc. Amer. Spec. Pap.*, *3*, 273–290.

Hardie, L. A., J. P. Smoot, and H. P. Eugster (1978), Saline lakes and their deposits: a sedimentological approach, in *Special Publication of the International Association of Sedimentologists*, vol. 2, pp. 7–41.

Hardie, L. A., and R. Sea (1983), Origin of CaCl2 brines by basalt-seawater interaction: Insights provided by some simple mass balance calculations, *Contrib. Min. Petrol.*, *82(205-213)*, doi:10.1007/BF01166615.

Harrison, K. P., and R. E. Grimm (2008), Multiple flooding events in Martian outflow channels, *J. Geophys. Res.*, *113*(E02002), doi:10.1029/2007JE002951.

Harrison, K. P., and M. G. Chapman (2008), Evidence for ponding and catastrophic floods in central Valles Marineris, Mars, *Icarus*, *198*(2), 351–364, doi:10.1016/j.icarus.2008.08.003.

Hartmann, W. K. (1969), Terrestrial, lunar and interplanetary rock fragmentation., *Icarus*, *10*, 201–213, doi:10.1016/0019-1035(69)90022-0.

Haskin, L. A. et al. (2005), Water alteration of rocks and soils on Mars at the Spirit rover site in Gusev crater, *Nature*, *436*(7047), 66–69, doi:10.1038/nature03640.

Hayne, P. O., P. I. Andrew, and D. A. Paige (2012), New approaches to lunar ice detection and mapping, *Keck Institute for Space Studies*, pp. 1–77.

Hayne, P. O., A. Hendrix, E. Sefton-Nash, M. A. Siegler, P. G. Lucey, K. D. Retherford, J.-P. Williams, B. T. Greenhagen, and D. A. Paige (2015), Evidence for exposed water ice in the Moon's south polar regions from Lunar Reconnaissance Orbiter ultraviolet albedo and temperature measurements, *Icarus*, *255*, 58–69, doi:10.1016/j.icarus.2015.03.032.

Head, J. W., J. F. Mustard, M. a Kreslavsky, R. E. Milliken, and D. R. Marchant (2003), Recent ice ages on Mars., *Nature*, *426*(6968), 797–802, doi:10.1038/nature02114.

Hecht, M. H., S. P. Kounaves, R. C. Quinn, S. J. West, S. M. M. Young, D. W. Ming, D. C. Catling, B. C. Clark, W. V. Boynton, J. Hoffman, L. P. DeFlores, K. Gospodinova, J. Kapit, and P. H. Smith (2009), Detection of perchlorate and the soluble chemistry of martian soil at the Phoenix lander site., *Science*, *325*(5936), 64–67, doi:10.1126/science.1172466.

Heldmann, J. L. (2005), Formation of Martian gullies by the action of liquid water flowing under current Martian environmental conditions, *J. Geophys. Res.*, *110*(E5), E05004, doi:10.1029/2004JE002261.

Hellman, M. J., and M. S. Ramsey (2004), Analysis of hot springs and associated deposits in Yellowstone National Park using ASTER and AVIRIS remote sensing, *J. Volcanol. Geotherm. Res.*, *135*(1–2), 195–219, doi:10.1016/j.jvolgeores.2003.12.012.

Hemingway, D. J., I. Garrick-Bethell, and M. A. Kreslavsky (2015), Latitudinal Variation in Spectral Properties of the Lunar Maria and Implications for Space Weathering, *Icarus*, *261*, 66–79, doi:10.1016/j.icarus.2015.08.004.

Hoke, M. R. T., B. M. Hynek, and G. E. Tucker (2011), Formation timescales of large Martian valley networks, *Earth Planet. Sci. Lett.*, *312*(1–2), 1–12, doi:10.1016/j.epsl.2011.09.053.

Hoke, M. R. T., B. M. Hynek, G. Di Achille, and E. W. H. Hutton (2014), The effects of sediment supply and concentrations on the formation timescale of martian deltas, *Icarus*, *228*, 1–12, doi:10.1016/j.icarus.2013.09.017.

Howard, A. D., J. M. Moore, and R. P. Irwin (2005), An intense terminal epoch of widespread fluvial activity on early Mars: 1. Valley network incision and associated deposits, *J. Geophys. Res.*, *110*(E12), E12S14, doi:10.1029/2005JE002459.

Howard, A. D., Y. Matsubara, C. J. Barnhart, J. M. Moore, T. A. Maxwell, M. Higbie, P. Sciences, S. Cruz, and M. Field (2009), Hydrology of early mars, in *Second Workshop on Mars Valley*, vol. 4123, pp. 35–38.

Huang, J., C. S. Edwards, S. W. Ruff, P. R. Christensen, and L. Xiao (2013), A new method for the semiquantitative determination of major rock-forming minerals with thermal infrared multispectral data: Application to THEMIS infrared data, *J. Geophys. Res. E Planets*, *118*(10), 2146–2152, doi:10.1002/jgre.20160.

Humm, D. C., M. Tschimmel, S. M. Brylow, P. Mahanti, T. N. Tran, S. E. Braden, S. Wiseman, J. Danton, E. M. Eliason, and M. S. Robinson (2016), Flight calibration of the LROC Narrow Angle Camera, *Space Sci. Rev.*, *150*, doi:10.1007/s11214-015-0201-8.

Hunt, G. R., and L. M. Logan (1972), Variation of single particle mid-infrared emission spectrum with particle size, *Appl. Opt.*, *11*(1), 142–147, doi:10.1364/AO.11.000142.

Hunt, G. R., and R. K. Vincent (1968), The behavior of spectral features in the infrared emission from particulate surfaces of various grain sizes, *J. Geophys. Res.*, *73*(18), 6039–6046, doi:10.1029/JB073i018p06039.

Hurley, D. M., D. J. Lawrence, D. B. J. Bussey, R. R. Vondrak, R. C. Elphic, and G. R. Gladstone (2012), Two-dimensional distribution of volatiles in the lunar regolith from space weathering simulations, *Geophys. Res. Lett.*, *39*, doi:10.1029/2012GL051105.

Hussien, B. M., and A. S. Faiyad (2016), Modeling the Hydrogeochemical Processes and Source of Ions in the Groundwater of Aquifers within Kasra-Nukhaib Region, *Internat. Journ. Geosci.*, *7(1156–1181)*, doi:10.4236/ijg.2016.710087.

Hynek, B. M., M. Beach, and M. R. T. Hoke (2010), Updated global map of Martian valley networks and implications for climate and hydrologic processes, *J. Geophys. Res.*, *115*(E9), E09008, doi:10.1029/2009JE003548.

Hynek, B. M., M. K. Osterloo, and K. S. Kierein-Young (2015), Late-stage formation of Martian chloride salts through ponding and evaporation, *Geology*, G36895.1, doi:10.1130/G36895.1.

Ingersoll, A. P., T. Svitek, and B. C. Murray (1992), Stability of polar frosts in spherical bowl-shaped craters on the Moon, Mercury, and Mars, *Icarus*, *100*, 40–47, doi:10.1016/0019-1035(92)90016-Z.

Ingle, S., and N. R. Banerjee (2008), Boron and chlorine contents of upper oceanic crust: Basement samples from IODP Hole 1256D, *Geochem., Geophys., Geosys.*, *9(12)*, doi:10.1029/2008GC002182.

Iskandar, I., C. Purnandi, A. P. Arifin, S. Notosiswoyo, K. Kashiwaya, Y. Tada, and K. Koike (2016), Hydrochemical Characterization for Identifying Hydrothermal Systems in the Bandung Volcanic Basin, *Proceedings of 41st Workshop on Geotherm. Res. Eng.*, SGP-TR-209, 1–6.

Jakosky, B. M., and R. J. Phillips (2001), Mars' volatile and climate history, *Nature*, *412*(6843), 237–244, doi:10.1038/35084184.

Jawin, E. R., W. S. Kiefer, C. I. Fassett, D. B. J. Bussey, and J. T. S. Cahill (2014), The relationship between radar scattering and surface roughness of lunar volcanic features, *J. Geophys. Res. - Planets*, *119*, 2331–2348, doi:10.1002/2014JE004668.Received.

Jensen, H. B., and T. D. Glotch (2011), Investigation of the near-infrared spectral character of putative Martian chloride deposits, *J. Geophys. Res.*, *116*, doi:10.1029/2011JE003887.

Ji, D., and Z. Ping (2000), Characteristics and genesis of the Yangbajing geothermal field, *Proc. World Geotherm. Congr. 2000, 1083-1088.*

Johns, W. D., and W. H. Huang (1967), Distribution of chlorine in terrestrial rocks, *Geochim. Cosmochim. Acta*, *31*(1), 35–49, doi:http://dx.doi.org/10.1016/0016-7037(67)90096-8.

Johnsson, A., D. Reiss, E. Hauber, H. Hiesinger, and M. Zanetti (2014), Evidence for very recent melt-water and debris flow activity in gullies in a young mid-latitude crater on Mars, *Icarus*, *235*, 37–54, doi:10.1016/j.icarus.2014.03.005.

Jones, B. F., D. L. Naftz, R. J. Spencer, and C. G. Oviatt (2009), Geochemical Evolution of Great Salt Lake , Utah , USA, *Aquat. Geochem.*, *95–121*, doi:10.1007/s10498-008-9047-y.

Kaplan, H. H., R. E. Milliken, D. Fernández-remolar, R. Amils, K. Robertson, and A. H. Knoll (2016), Orbital evidence for clay and acidic sulfate assemblages on Mars based on mineralogical analogs from Rio Tinto, Spain, *Icarus*, *275*(45–64), doi:10.1016/j.icarus.2016.03.019.

Kargel, J. S., R. Furfaro, O. Prieto-Ballesteros, J. A. P. Rodriguez, D. R. Montgomery, A. R. Gillespie, G. M. Marion, and S. E. Wood (2007), Martian hydrogeology sustained by thermally insulating gas and salt hydrates, *Geology*, *35*(11), 975, doi:10.1130/G23783A.1.

Kawamoto, T., M. Yoshikawa, Y. Kumagai, M. Hannah, T. Mirabueno, and M. Okuno (2013), Mantle wedge infiltrated with saline fluids from dehydration and decarbonation of subducting slab, *Proceedings of the National Academy of Sciences*, *110*(24), 24–29, doi:10.1073/pnas.1302040110.

Keller, W. D. (1961), Hydrothermal kaolinization (endellitization) of volcanic glassy rock, *Clays and Clay Miner.*, *10*(1), 333–343, doi:10.1346/CCMN.1961.0100129.

Kelley, D. S., J. A. Baross, and J. R. Delaney (2002), Volcanoes, fluids, and life at mid-ocean ridge spreading centers, *Annu. Rev. Earth Planet. Sci.*, *30*(1), 385–491, doi:10.1146/annurev.earth.30.091201.141331.

Keske, A. L., C. W. Hamilton, A. S. McEwen, and I. J. Daubar (2015), Episodes of fluvial and volcanic activity in Mangala Valles, Mars, *Icarus*, *245*, 333–347, doi:10.1016/j.icarus.2014.09.040.

Keszthelyi, L. P., T. Becker, T. Titus, S. Sides, L. Gaddis, T. Hare, R. Kirk, K. Edmundson, and J. Anderson (2014), Utilizing the Integrated Software for Imagers and Spectrometers (ISIS) to Support Future Missions, 45th *Lunar and Planetary Science Conference*, Abstract # 1686.

Kharaka, Y. K., and J. S. Hanor (2013), *Deep Fluids in Sedimentary Basins*, Treatise on

Geochemistry, 2nd ed., Elsevier Ltd., pp. 471-515, doi:10.1016/B978-0-08-095975-7.00516-7.

Kienenberger, R. L., and R. Greeley (2012), Field analog studies of the distribution of windblown sediments at Amboy Crater, California, with application to Mars, *Planet. Space Sci., 68*(1), 25–33, doi:10.1016/j.pss.2011.03.003.

Kirsimae, K., S. Suuroja, J. Kirs, A. Karki, M. Polikarpus, V. Puura, and K. Suuroja (2002), Hornblende alteration and fluid inclusions in Kardla impact crater, Estonia: Evidence for impact-induced hydrothermal activity, *Meteorit. Planet. Sci., 37*(3), 449–457, doi:10.1017/CBO9781107415324.004.

Kite, E. S. (2013), Mass balance constraints on the sustainability of Mars's recurrent slope lineae (RSL): should RSL be an astrobiology priority?, *The Present Day Habitability of Mars Workshop*.

Knauth, L. (2002), Eutectic brines on Mars: Origin and possible relation to young seepage features, *Icarus, 158*(1), 267–271, doi:10.1006/icar.2002.6866.

Knauth, L. P. (1998), Salinity history of the Earth's early ocean, *Nature, 395*(6702), 554–555, doi:10.1038/26879.

Kneissl, T., S. van Gasselt, and G. Neukum (2011), Map-projection-independent crater size-frequency determination in GIS environments—New software tool for ArcGIS, *Planet. Space Sci., 59*, 1243–1254, doi:10.1016/j.pss.2010.03.015.

Koeber, S. D., M. S. Robinson, and E. J. Speyerer (2014), LROC observations of permanently shadowed regions on the Moon, *45th Lunar and Planetary Science Conference*, Abstract #2811.

Korb, R., W. Salisbury, and D. M. D. Aria (1999), Thermal-infrared remote sensing and Kirchhoff's law 2. Field measurements. *J. Geophys. Res., 104(B7), pp. 15,339-15,350*, doi:10.1029/97JB03537.

Lane, M. D. (2007), Mid-infrared emission spectroscopy of sulfate and sulfate-bearing minerals, *Am. Mineral., 92*(1), 1–18, doi:10.2138/am.2007.2170.

Lane, M. D., and P. R. Christensen (1998), Thermal infrared emission spectroscopy of salt minerals predicted for Mars, *Icarus, 135*, 528–536.

Lane, M. D., T. D. Glotch, M. D. Dyar, C. M. Pieters, R. Klima, T. Hiroi, J. L. Bishop, and J. Sunshine (2011), Midinfrared spectroscopy of synthetic olivines: Thermal emission, specular and diffuse reflectance, and attenuated total reflectance studies of forsterite to fayalite, *J. Geophys. Res. E Planets, 116*(8), 1–20, doi:10.1029/2010JE003588.

Lawrence, S. J., J. D. Stopar, B. R. Hawke, B. T. Greenhagen, J. T. S. Cahill, J. L. Bandfield, B. L. Joliff, B. W. Denevi, M. S. Robinson, T. D. Glotch, D. B. J. Bussey, P. D Spudis, T. A. Giguere, and W. B. Garry (2013), LRO observations of morphology and surface roughness of volcanic cones and lobate lava flows in the Marius Hills, *J. Geophys. Res. - Planets*, *118*, 615–634, doi:10.1002/jgre.20060.

Le Bas, M. J., R. W. Le Maitre, A. Streckeisen, and B. Zanettin (1986), A chemical classification of volcanic rocks based on the total alkali silica diagram, *J. Petrol.*, *27*(3), 745–750, doi:10.1093/petrology/27.3.745.

Lemelin, M., D. M. Blair, C. E. Roberts, K. D. Runyon, D. Nowka, and D. A. Kring (2014), High-priority lunar landing sites for in situ and sample return studies of polar volatiles, *Planet. Space Sci., 101(149-161),* doi:10.1016/j.pss.2014.07.002.

Leshin, L. A., P. R. Mahaffy, C. R. Webster, M. Cabane, P. Coll, P. G. Conrad, P. D. Archer Jr., S. K. Atreya, A. E. Brunner, A. Buch, J. L. Eigenbrode, G. J. Flesch, H. B. Franz, C. Freissinet, D. P. Glavin, A. C. McAdam, K. E. Miller, D. W. Ming, R. V. Morris, R. Navarro-González, P. B. Niles, T. Owen, R. O. Pepin, S. Squyres, A. Steele, J. C. Stern, R. E. Summons, D. Y. Sumner, B. Sutter, C. Szopa, S. Teinturier, M. G. Trainer, J. J. Wray, J. P. Grotzinger, and MSL Science Team (2013), Volatile, isotope, and organic analysis of martian fines with the Mars Curiosity rover., *Science*, *341*(6153), 1238937, doi:10.1126/science.1238937.

Leung, C. W. S., and S. C. R. Rafkin (2015), Mesoscale atmospheric modeling of water vapor in Valles Marineris, *46th Lunar and Planetary Science Conference*, Abstract #2959.

Levy, J. S., A. G. Fountain, M. N. Gooseff, K. A. Welch, and W. B. Lyons (2011), Water tracks and permafrost in Taylor Valley, Antarctica: Extensive and shallow groundwater connectivity in a cold desert ecosystem, *Geol. Soc. Am. Bull.*, *123*(11–12), 2295–2311, doi:10.1130/B30436.1.

Levy, J. (2012), Hydrological characteristics of recurrent slope lineae on Mars: Evidence for liquid flow through regolith and comparisons with Antarctic terrestrial analogs, *Icarus*, *219*(1), 1–4, doi:10.1016/j.icarus.2012.02.016.

Levy, J., A. Nolin, A. Fountain, and J. Head (2014), Hyperspectral measurements of wet, dry and saline soils from the McMurdo Dry Valleys: soil moisture properties from remote sensing, *Antarct. Sci.*, *26*(05), 565–572, doi:10.1017/S0954102013000977.

Li, J., T. K. Lowenstein, and I. R. Blackburn (1997), Responses of evaporite mineralogy to inflow water sources and climate during the past 100 k.y. in Death Valley, California, *GSA Bull.*, 109(10), 1361–1371.

Light, B., R. E. Brandt, and S. G. Warren (2009), Hydrohalite in cold sea ice : Laboratory observations of single crystals, surface accumulations, and migration rates under a temperature gradient, with application to “Snowball Earth”, *J. Geophys. Res.*, *114*, 1–17, doi:10.1029/2008JC005211.

Loizeau, D., N. Mangold, F. Poulet, J.-P. Bibring, A. Gendrin, V. Ansan, C. Gomez, B. Gondet, Y. Langevin, P. Masson, and G. Neukum (2007), Phyllosilicates in the Mawrth Vallis region of Mars, *J. Geophys. Res.*, *112*(E8), E08S08, doi:10.1029/2006JE002877.

Lowenstein, T. K., and L. A. Hardie (1985), Criteria for the recognition of salt-pan evaporites, *Sedimentology*, *32*(5), 627–644, doi:10.1111/j.1365-3091.1985.tb00478.x.

Lowenstein, T. K., and F. Risacher (2009), Closed basin brine evolution and the influence of Ca–Cl inflow waters: Death Valley and Bristol Dry Lake California, Qaidam Basin, China, and Salar de Atacama, Chile, *Aquat. Geochem.*, *15*, 71–94, doi:10.1007/s10498-008-9046-z.

Lowenstern, J. B., D. Bergfeld, W. C. Evans, and S. Hurwitz (2012), Generation and evolution of hydrothermal fluids at Yellowstone: Insights from the Heart Lake Geyser Basin, *Geochem., Geophys. Geoys.*, *13*(1), 1–20, doi:10.1029/2011GC003835.

Lower, S. K. (1999), Carbonate equilibria in natural waters, Chem 1 Reference Text., *Simon Fraser Univ.*

Lu, Z., and L. Xu (2010), Freezing desalination process, *Therm. Desalin. Process., Vol. II*, *Encyclopedia of Desalination and Water Resources*, Eolss Publisher Co Ltd, United Kingdom.

Lucchitta, B. K. (1978), *Geologic Map of the North Side of the Moon*, USGS.

Lucey, P., R. L. Korotev, J. J. Gillis, L. A. Taylor, D. Lawrence, B. A. Campbell, R. Elphic, B. Feldman, L. L. Hood, D. Hunten, M. Mendillo, S. Noble, J. J. Papike, R. C. Reedy, S. Lawson, T. Prettyman, O. Gasnault, S. Maurice (2006), Understanding the lunar surface and space-Moon interactions, *Rev. Mineral. Geochemistry*, *60*, 83–219, doi:10.2138/rmg.2006.60.2.

Lucey, P. G., G. A. Neumann, M. A. Riner, E. Mazarico, D. E. Smith, M. T. Zuber, D. A. Paige, D. B. Bussey, J. T. Cahill, A. McGovern, P. Isaacson, L. M. Corley, M. H. Torrence, H. J. Melosh, J. W. Head, and E. Song (2014), The global albedo of the Moon at 1064 nm from LOLA, *J. Geophys. Res. Planets*, *119*, 1665–1679, doi:10.1002/2013JE004592.

Machette, M., N., C. N. Martinez, A. J. Crone, K. M. Haller, and G. D'Addezio (1999), *Geologic and seismic hazards investigations of the Cow Creek Area, Death Valley National Park, California,* USGS Open-File Report, #99-155.

Magna, T., M. Šimčíková, and F. Moynier (2014), Lithium systematics in howardite–eucrite–diogenite meteorites: Implications for crust–mantle evolution of planetary embryos, *Geochim. Cosmochim. Acta*, *125*, 131–145, doi:10.1016/j.gca.2013.10.015.

Mahanti, P., D.C. Humm, M.S. Robinson, A.K. Boyd, R. Stelling, H. Sato, B.W. Denevi, S.E. Braden, E. Bowman-Cisneros, S.M. Brylow, and M. Tschimmel (2016), Inflight calibration of the Lunar Reconnaissance Orbiter Camera Wide Angle Camera, *Space Sci. Rev., 150*, doi:10.1007/s11214-015-0197-0.

Malin, M. C., and K. S. Edgett (2000), Evidence for recent groundwater seepage and surface runoff on Mars, *Adv. Sci., 288*(5475), 2330–2335.

Margot, J. L., D. B. Campbell, R. F. Jurgens, and M. A. Slade (1999), Topography of the lunar poles from radar interferometry: a survey of cold trap locations, *Science*, *284*(5420), 1658–1660, doi:10.1126/science.284.5420.1658.

Marty, B. and R. Yokochi (2006), Water in the early Earth, *Reviews in Mineralogy and Geochemistry, 62(421-450)*.

Massé, M., P. Beck, B. Schmitt, A. Pommerol, A. McEwen, V. Chevrier, O. Brissaud, and A. Séjourné (2014), Spectroscopy and detectability of liquid brines on Mars, *Planet. Space Sci., 92*, 136–149, doi:10.1016/j.pss.2014.01.018.

Mazarico, E., G. A. Neumann, D. E. Smith, M. T. Zuber, and M. H. Torrence (2011), Illumination conditions of the lunar polar regions using LOLA topography, *Icarus*, *211*, 1066–1081, doi:10.1016/j.icarus.2010.10.030.

McClanahan, T. P., L. G. Evans, R. D. Starr, and I. G. Mitrofanov (2009), Fast ray tracing of lunar digital elevation models, *40th Lunar and Planetary Science Conference*, Abstract #2092.

McEwen, A. S., E. M. Eliason, J. W. Bergstrom, N. T. Bridges, C. J. Hansen, W. A. Delamere, J. A. Grant, V. C. Gulick, K. E. Herkenhoff, L. Keszthelyi, R. L. Kirk, M. T. Mellon, S. W. Squyres, N. Thomas, and C. M. Weitz (2007), Mars Reconnaissance Orbiter's High Resolution Imaging Science Experiment (HiRISE), *J. Geophys. Res. E Planets*, *112*, 1–40, doi:10.1029/2005JE002605.

McEwen, A. S., L. Ojha, C. M. Dundas, S. S. Mattson, S. Byrne, J. J. Wray, S. C. Cull, S. L. Murchie, N. Thomas, and V. C. Gulick (2011), Seasonal flows on warm martian slopes, *Science*, *333*, 740–743, doi:10.1126/science.1204816.

McEwen, A. S., C. M. Dundas, S. S. Mattson, A. D. Toigo, L. Ojha, J. J. Wray, M. Chojnacki, S. Byrne, S. L. Murchie, and N. Thomas (2013), Recurring slope lineae in equatorial regions of Mars, *Nat. Geosci.*, *7*(1), 53–58, doi:10.1038/ngeo2014.

McGovern, J. A., D. B. Bussey, B. T. Greenhagen, D. a. Paige, J. T. S. Cahill, and P. D. Spudis (2013), Mapping and characterization of non-polar permanent shadows on the lunar surface, *Icarus*, *223*(1), 566–581, doi:10.1016/j.icarus.2012.10.018.

McKeown, N., J. Bishop, and E. Silver (2013), Variability of rock texture and morphology correlated with the clay-bearing units at Mawrth Vallis, Mars, *J. Geophys. Res. Planets*, *118*(6), 1245–1256.

McKeown, N. K., J. L. Bishop, E. Z. Noe Dobrea, B. L. Ehlmann, M. Parente, J. F. Mustard, S. L. Murchie, G. A. Swayze, J.-P. Bibring, and E. A. Silver (2009), Characterization of phyllosilicates observed in the central Mawrth Vallis region, Mars, their potential formational processes, and implications for past climate, *J. Geophys. Res.*, *114*, E00D10, doi:10.1029/2008JE003301.

McLennan, S. M., J.F. Bell III, W.M. Calvin, P.R. Christensen, B.C. Clark, P.A. de Souza, J. Farmer, W.H. Farrand, D.A. Fike, R. Gellert, A. Ghosh, T.D. Glotch, J.P. Grotzinger, B. Hahn, K.E. Herkenhoff, J.A. Hurowitz, J.R. Johnson, S.S. Johnson, B. Jolliff, G. Klingelhofer, A.H. Knoll, Z. Learner, M.C. Malin, H.Y. McSween Jr., J. Pocock, S.W. Ruff, L.A. Soderblom, S.W. Squyres, N.J. Tosca, W.A. Watters, M.B. Wyatt, and A. Yen (2005), Provenance and diagenesis of the evaporite-bearing Burns formation, Meridiani Planum, Mars, *Earth Planet. Sci. Lett.*, *240*, 95–121, doi:10.1016/j.epsl.2005.09.041.

McSween, H. Y., G. J. Taylor, and M. B. Wyatt (2009), Elemental composition of the martian crust, *Science*, *324*(5928), 736–739, doi:10.1126/science.1165871.

Mellon, T., and J. Phillips (2001), Recent gullies on Mars and the source of liquid water, *J. Geophys. Res. Planets*, *106*(E10), 23165–23179.

Metz, S., and J. H. Trefry (2000), Chemical and mineralogical influences on concentrations of trace metals in hydrothermal fluids, *Geochim. Cosmochim. Acta*, *64*(13), 2267–2279, doi:10.1016/S0016-7037(00)00354-9.

Michael, G. G. (2013), Planetary surface dating from crater size-frequency distribution measurements: Multiple resurfacing episodes and differential isochron fitting, *Icarus*, *226*, 885–890, doi:10.1016/j.icarus.2013.07.004.

Michalski, J., F. Poulet, J.-P. Bibring, and N. Mangold (2010), Analysis of phyllosilicate deposits in the Nili Fossae region of Mars: Comparison of TES and OMEGA data, *Icarus*, *206*(1), 269–289, doi:10.1016/j.icarus.2009.09.006.

Michalski, J. R., and R. L. Fergason (2009), Composition and thermal inertia of the Mawrth Vallis region of Mars from TES and THEMIS data, *Icarus*, *199*(1), 25–48, doi:10.1016/j.icarus.2008.08.016.

Michalski, J. R., E. Z. N. Dobrea, P. B. Niles, and J. Cuadros (2017), Ancient hydrothermal seafloor deposits in Eridania basin on Mars, *Nat. Commun.*, *8*, 15978, doi:10.1038/ncomms15978.

Ming, D. W., and R. V Morris (2017), Chemical, mineralogical, and physical properties of Martian dust and soil, *Dust Atmos. Mars 2017*, LPI Contrib. No. 1966, Abstract #6027.

Ming, D. W., P. D. Archer Jr., D. P. Glavin, J. L. Eigenbrode, H. B. Franz, B. Sutter, A. E. Brunner, J. C. Stern, C. Freissinet, A. C. McAdam, P. R. Mahaffy, M. Cabane, P. Coll, J. L. Campbell, S. K. Atreya, P. B. Niles, J. F. Bell III, D. L. Bish, W. B. Brinckerhoff, A. Buch, P. G. Conrad, D. J. Des Marais, B. L. Ehlmann, A. G. Fairén, K. Farley, G. J. Flesch, P. Francois, R. Gellert, J. A. Grant, J. P. Grotzinger, S. Gupta, K. E. Herkenhoff, J. A. Hurowitz, L. A. Leshin, K. W. Lewis, S. M. McLennan, K. E. Miller, J. Moersch, R. V. Morris, R. Navarro-González, A. A. Pavlov, G. M. Perrett, I. Pradler, S. W. Squyres, R. E. Summons, A. Steele, E. M. Stolper, D. Y. Sumner, C. Szopa, S. Teinturier, M. G. Trainer, A. H. Treiman, D. T. Vaniman, A. R. Vasavada, C. R. Webster, J. J. Wray, R. A. Yingst, and the MSL Science Team (2014), Volatile and organic compositions of sedimentary rocks in Yellowknife Bay, Gale crater, Mars, *Science (80-.).*, *343*(6169), 1245267, doi:10.1126/science.1245267.

Mishchenko, M. I. (1992), The angular width of the coherent back-scatter opposition effect: An application to icy outer planet satellites, *Astrophys. Space Sci.*, *194*, 327–333.

Mitchell, J. L., and P. R. Christensen (2016), Recurring slope lineae and chlorides on the surface of Mars, *J. Geophys. Res. Planets*, *121*, 1–18, doi:10.1002/2014JE004627.Received.

Mitrofanov, I. G., A. B. Sanin, W. V. Boynton, G. Chin, J. B. Garvin, D. Golovin,L. G. Evans, K. Harshman, A. S. Kozyrev, M. L. Litvak, A. Malakhov, E. Mazarico, T.McClanahan, G. Milikh, M. Mokrousov, G. Nandikotkur, G. A. Neumann, I. Nuzhdin, R.Sagdeev, V. Shevchenko, V. Shvetsov, D. E. Smith, R. Starr, V. I. Tretyakov, J. Trombka,D. Usikov, A. Varenikov, A. Vostrukhin and M. T. Zuber (2010a), Hydrogen Mapping of the Lunar South Pole Using the LRO Neutron Detector Experiment LEND, *Science*, *330*(6003), 483–486.

Mitrofanov, I. G., A. Bartels, Y.I. Bobrovnitsky,W. Boynton, G. Chin, H. Enos, L. Evans, S. Floyd, J. Garvin, D.V. Golovin, A.S. Grebennikov, K. Harshman, L.L. Kazakov, J. Keller, A.A. Konovalov, A.S. Kozyrev, A.R. Krylov, M.L. Litvak, A.V.

Malakhov, T. McClanahan, G.M. Milikh, M.I. Mokrousov, S. Ponomareva, R.Z. Sagdeev, A.B. Sanin, V.V. Shevchenko, V.N. Shvetsov, R. Starr, G.N. Timoshenko, T.M. Tomilina, V.I. Tretyakov, J. Trombka, V.S. Troshin, V.N. Uvarov, A.B. Varennikov, and A.A. Vostrukhin (2010b), Lunar exploration neutron detector for the NASA lunar reconnaissance orbiter, *Space Sci. Rev.*, *150*, 183–207, doi:10.1007/s11214-009-9608-4.

Moersch, J. E., and P. R. Christensen (1995), Thermal emission from particulate surfaces: A comparison of scattering models with measured spectra, *J. Geophys. Res.*, *100*(E4), 7465-7477.

Mohan, S., S. Saran, and A. Das (2013), Scattering mechanism-based algorithm for improved mapping of water-ice deposits in the lunar polar regions, *Curr. Sci.*, *105*(11), 1579–1587.

Möller, P., V. Lüders, and M. De Lucia (2017), Formation of Rotliegend Ca-Cl brines in the North German Basin compared to analogues in the geological record, *Chem. Geol.*, *459(32-42)*, doi:10.1016/j.chemgeo.2017.04.001.

Morbidelli, A., J. Chambers, J. I. Lunine, J. M. Petit, F. Robert, G. B. Valsecchi, and K. E. Cyr (2000), Source regions and timescales for the delivery of water to the Earth, *Meteoritics and Planetary Science, 35(1309-13*20), doi:10.1111/j.1945-5100.2000.tb01518.x.

Morris, R. V., G. Klingelhofer, C. Schroder, D. S. Rodionov, A. Yen, D. W. Ming, P. A. de Souza Jr., I. Fleischer, T. Wdowiak, R. Gellert, B. Bernhardt, E. N. Evlanov, B. Zubkov, J. Foh, U. Bonnes, E. Kankeleit, P. Gutlich, F. Renz, S. W. Squyres, and R. E. Arvidson (2006), Mössbauer mineralogy of rock, soil, and dust at Gusev crater, Mars: Spirit's journey through weakly altered olivine basalt on the plains and pervasively altered basalt in the Columbia Hills, *J. Geophys. Res. E Planets*, *111*(2), doi:10.1029/2005JE002584.

Müntener, O. (2010), Serpentine and serpentinization: A link between planet formation and life, *Geology*, *38*(10), 959–960, doi:10.1130/focus102010.1.

Murchie, S. L., J. F. Mustard, B. L. Ehlmann, R. E. Milliken, J. L. Bishop, N. K. McKeown, E. Z. N. Dobrea, F. P. Seelos, D. L. Buczkowski, S. M. Wiseman, R. E. Arvidson, J. J. Wray, G. Swayze, R. N. Clark, D. J. Des Marais, A. S. McEwen, and J.-P. Bibring (2009), A synthesis of Martian aqueous mineralogy after 1 Mars year of observations from the Mars Reconnaissance Orbiter, *J. Geophys. Res.*, *114*, E00D06, doi:10.1029/2009JE003342.

Mustard, J. F., and J. E. Hays (1997), Effects of hyperfine particles on reflectance spectra from 0.3 to 25 μm, *Icarus*, *125*(1), 145–163, doi:10.1006/icar.1996.5583.

Mustard, J. F., C. D. Cooper, and M. K. Rifkin (2001), Evidence for recent climate change on Mars from the identification of youthful near-surface ground ice, *Nature, 412(411–414)*.

Mustard, J. F., S. L. Murchie, S. M. Pelkey, B. L. Ehlmann, R. E. Milliken, J. A. Grant, J.-P. Bibring, F. Poulet, J. Bishop, E. Noe Dobrea, L. Roach, F. Seelos, R. E. Arvidson, S. Wiseman, R. Green, C. Hash, D. Humm,E. Malaret, J. A. McGovern, K. Seelos, T. Clancy, R. Clark, D. Des Marais, N. Izenberg, A. Knudson, Y. Langevin, T. Martin, P. McGuire, R. Morris, M. Robinson, T. Roush, M. Smith, G. Swayze, H. Taylor, T. Titus and M. Wolff (2008), Hydrated silicate minerals on Mars observed by the Mars Reconnaissance Orbiter CRISM instrument., *Nature, 454*(7202), 305–9, doi:10.1038/nature07097.

Mustard, J. F., F. Poulet, B. L. Ehlmann, R. Milliken, and A. A. Fraeman (2009), Sequestration of volatiles in the martian crust through hydrated minerals: A significant planetary reservoir of water, *43rd Annual Lunar and Planetary Science Conference*, Abstract #1539.

Mustard, J. F., B. L. Ehlmann, and F. Poulet (2011), Sequestration of volatiles in the martian crust through hydrated minerals, *AGU Fall Meeting 2011*, Abstract #P33H-05.

Neumann, G. A., J. F. Cavanaugh, X. Sun, E. M. Mazarico, D. E. Smith, M. T. Zuber, D. Mao, D. A. Paige, S. C. Solomon, C. M. Ernst, and Olivier S. Barnouin. (2013), Bright and dark polar deposits on Mercury: evidence for surface volatiles, *Science, 339*, 296–300, doi:10.1126/science.1229764.

Niederberger, T. D., N. N. Perreault, S. Tille, B. S. Lollar, G. Lacrampe-couloume, D. Andersen, C. W. Greer, W. Pollard, and L. G. Whyte (2010), Microbial characterization of a subzero, hypersaline methane seep in the Canadian High Arctic, *The ISME Journal, 4(1326–1339)*, doi:10.1038/ismej.2010.57.

Nield, J. M., C. Mckenna, P. O. Brien, R. G. Bryant, and G. F. S. Wiggs (2016), Evaporative sodium salt crust development and its wind tunnel derived transport dynamics under variable climatic conditions, *Aeolian Res.*, *23*, 51–62, doi:10.1016/j.aeolia.2016.09.003.

Niemi, T. M., Z. Ben-Avraham, and J. R. Gat (1997), The Dead Sea: The lake and its setting, *Oxford Monographs on Geology and Geophysics*, Oxford Univ. Press.

Nissenbaum, A. (1977), Minor and trace elements in Dead Sea water, *Chem. Geol.*, *19(99-111)*, doi:10.1016/0009-2541(77)90008-0.

Noda, H., H. Araki, S. Goossens, Y. Ishihara, K. Matsumoto, S. Tazawa, N. Kawano, and S. Sasaki (2008), Illumination conditions at the lunar polar regions by KAGUYA

(SELENE) laser altimeter, *Geophys. Res. Lett.*, *35*, doi:10.1029/2008GL035692.

Nozette, S., C. L. Lichtenberg, P. Spudis, R. Bonner, W. Ort, E. Malaret, M. Robinson, and E. M. Shoemaker (1996), The Clementine bistatic radar experiment, *Science*, *274*, 1495–1498, doi:10.1126/science.274.5292.1495.

Nozette, S. et al. (2010), The Lunar Reconnaissance Orbiter Miniature Radio Frequency (Mini-RF) technology demonstration, *Space Sci. Rev.*, *150*, 285–302, doi:10.1007/s11214-009-9607-5.

Nyquist, R. A., and R. O. Kagel (1971), *Infrared Spectra of Inorganic Compounds*, Academic Press, pp. 1-495.

Ogawa, Y., H. Koibuchi, K. Suto, and C. Inoue (2014), Effects of the chemical compositions of Salars de Uyuni and Atacama brines on lithium concentration during evaporation, *Resource Geol.*, *64*(2), 91–101, doi:10.1111/rge.12030.

Ojha, L., J. J. Wray, S. L. Murchie, A. S. McEwen, M. J. Wolff, and S. Karunatillake (2013), Spectral constraints on the formation mechanism of recurring slope lineae, *Geophys. Res. Lett.*, *40*(21), 5621–5626, doi:10.1002/2013GL057893.

Ojha, L., A. McEwen, C. Dundas, S. Byrne, S. Mattson, J. Wray, M. Masse, and E. Schaefer (2014), HiRISE observations of Recurring Slope Lineae (RSL) during southern summer on Mars, *Icarus*, *231*, 365–376, doi:10.1016/j.icarus.2013.12.021.

Ojha, L., M. B. Wilhelm, S. L. Murchie, A. S. Mcewen, J. J. Wray, J. Hanley, M. Massé, and M. Chojnacki (2015), Spectral evidence for hydrated salts in recurring slope lineae on Mars, *Nat. Geosci.*, *8*, 829–832, doi:10.1038/NGEO2546.

Osterloo, M., V. Hamilton, and J. Bandfield (2008), Chloride-bearing materials in the southern highlands of Mars, *Science*, *319*, 1651–1654, doi:10.1126/science.1150690.

Osterloo, M. M., and B. M. Hynek (2015), Martian chloride deposits: The last gasps of widespread surface water, 46th *Lunar and Planetary Science Conference*, Abstract #1054.

Osterloo, M. M., F. S. Anderson, V. E. Hamilton, and B. M. Hynek (2010), Geologic context of proposed chloride-bearing materials on Mars, *J. Geophys. Res.*, *115*(E10012), doi:10.1029/2010JE003613.

Osterloo, M. M., V. E. Hamilton, and F. S. Anderson (2012), A laboratory study of the effects of roughness on the thermal infrared spectra of rock surfaces, *Icarus*, *220*(2), 404–426, doi:10.1016/j.icarus.2012.04.020.

Ostro, S. J. (1993), Planetary radar astronomy, *Rev. Mod. Phys.*, *65*(4), 1235–1279, doi:10.1103/RevModPhys.65.1235.

Paige, D. A., M. A. Siegler, J. A. Zhang, P. O. Hayne, E. J. Foote, K. A. Bennett, A. R. Vasavada, B. T. Greenhagen, J. T. Schofield, D. J. McCleese, M. C. Foote, E. Dejong, B. G. Bills, W. Hartford, B. C. Murray, C. C. Allen, K. Snook, L. A. Soderblom, S. Calcutt, F. W. Taylor, N. E. Bowles, J. L. Bandfield, R. Elphic, R. Ghent, T. D. Glotch, M. B. Wyatt, and P. G. Lucey (2010a), Diviner Lunar Radiometer observations of cold traps in the Moon's south polar region., *Science*, *330*, 479–482, doi:10.1126/science.1187726.

Paige, D. A., M.C. Foote, B.T. Greenhagen, J.T. Schofield, S. Calcutt, A.R. Vasavada, D.J. Preston, F.W. Taylor, C.C. Allen, K. J. Snook, B.M. Jakosky, B.C. Murray, L.A. Soderblom, B. Jau, S. Loring, J. Bulharowski, N.E. Bowles, I.R. Thomas, M.T. Sullivan, C. Avis, E.M. De Jong, W. Hartford, and D.J. McCleese (2010b), The Lunar Reconnaissance Orbiter Diviner Lunar Radiometer Experiment, *Space Sci. Rev.*, *150*, 125–160, doi:10.1007/s11214-009-9529-2.

Paige, D., S. Wood, and A. R. Vasavada (1992), The thermal stability of water ice at the poles of Mercury, *Science, 258(5082), 643-646*, doi:10.1126/science.258.5082.643.

Palchetti, L., G. Bianchini, B. Carli, and C. Serio (2009), Ground-based and balloon-borne characterization of the far infrared atmospheric emission spectrum, *AIP Conference Proceedings*, *1100(147)*, doi:10.1063/1.3116935.

Parkhurst, B. D. L., and C. J. Appelo (1999), User's Guide To PHREEQC (version 2) — a Computer Program for Speciation, and Inverse Geochemical Calculations, *Exch. Organ. Behav. Teach. J.*, *D*(Version 2), 326, doi:Rep. 99-4259.

Parkhurst, D. L., and C. A. J. Appelo (2013), Description of Input and Examples for PHREEQC Version 3 - A Computer Program for Speciation, Batch-Reaction, One-Dimensional Transport, and Inverse Geochemical Calculations, *U. S. Geological Survey Techniques and Methods*, Book 6, Chapter A43, 497 p. 6–43A, doi:10.1016/0029-6554(94)90020-5.

Parro, V., G. de Diego-Castilla, M. Moreno-Paz, Y. Blanco, P. Cruz-Gil, J. A. Rodrıguez-Manfredi, D. Fernandez-Remolar, F. Gomez, M. J. Gomez, L. A. Rivas, C. Demergasso, A. Echeverrıa, V. N. Urtuvia, M. Ruiz-Bermejo, M. Garcıa-Villadangos, M. Postigo, M. Sanchez-Roman, G. Chong-Dıaz, and J. Gomez-Elvira (2011), A microbial oasis in the hypersaline Atacama subsurface discovered by a life detector chip: Implications for the search for life on Mars, *Astrobiology*, *11*(10), 969–996, doi:10.1089/ast.2011.0654.

Peters, K. (1992), Coherent-backscatter effect: A vector formulation accounting for polarization and absorption effects and small or large scatterers, *Phys. Rev. B*, *46*(2),

801–812, doi:10.1103/PhysRevB.46.801.

Phillips, F. M. (2003), Cosmogenic 36Cl ages of Quaternary basalt flows in the Mojave Desert, California, USA, *Geomorphology*, *53*(3–4), 199–208, doi:10.1016/S0169-555X(02)00328-8.

Pieters, C. M., L. A. Taylor, S. K. Noble, L. P. Keller, B. W. Hapke, R. V Morris, C. C. Allen, D. S. McKay, and S. J. Wentworth (2000), Space weathering on airless bodies: Resolving a mystery with lunar samples, *Meteorit. Planet. Sci.*, *35*, 1101–1107, doi:10.1111/j.1945-5100.2000.tb01496.x.

Pieters, C. M., J. N. Goswami, R. N. Clark, M. Annadurai, J. Boardman, B. Buratti, J.-P. Combe, M. D. Dyar, R. Green, J. W. Head, C. Hibbitts, M. Hicks, P. Isaacson, R. Klima, G. Kramer, S. Kumar, E. Livo, S. Lundeen, E. Malaret, T. McCord, J. Mustard, J. Nettles, N. Petro, C. Runyon, M. Staid, J. Sunshine, L. A. Taylor, S. Tompkins and P. Varanasi (2009a), Character and spatial distribution of OH/H2O on the surface of the Moon seen by M3 on Chandrayaan-1, *Science*, *326*(5952), 568–572, doi:10.1126/science.1178658.

Pieters, C. M., J. Boardman, B. Buratti, A. Chatterjee, R. Clark, T. Glavich, R. Green, J. Head III, P. Isaacson, E. Malaret, T. McCord, J. Mustard, N. Petro, C. Runyon, M. Staid, J. Sunshine, L. Taylor, S. Tompkins, P. Varanasi and M. White (2009b), The Moon mineralogy mapper (M3) on Chandrayaan-1, *Curr. Sci.*, *96*(4), 500–505.

Pike, R. (1974), Depth/Diameter Relations of Fresh Lunar Craters: Revision from Spacecraft Data, *Geophys. Res. Lett.*, *1*(7), 291–294, doi:10.1029/GL001i007p00291.

Pilorget, C., and F. Forget (2015), Formation of gullies on Mars by debris flows triggered by CO2 sublimation, *Nat. Geosci.*, *9*(1), 65–69, doi:10.1038/ngeo2619.

Piquette, M., M. Horányi, and S. A. Stern (2017), Laboratory experiments to investigate sublimation rates of water ice in nighttime lunar regolith, *Icarus*, *293*, 180–184, doi:10.1016/j.icarus.2017.04.017.

Poulet, F., J.-P. Bibring, J. F. Mustard, A. Gendrin, N. Mangold, Y. Langevin, R. E. Arvidson, B. Gondet, C. Gomez & the Omega Team (2005), Phyllosilicates on Mars and implications for early martian climate, *Nature*, *438*(7068), 623–627, doi:10.1038/nature04274.

Quinn, R. C., H. F. H. Martucci, S. R. Miller, C. E. Bryson, F. J. Grunthaner, and P. J. Grunthaner (2013), Perchlorate radiolysis on Mars and the origin of martian soil reactivity, *Astrobiology*, *13*(6), 515–20, doi:10.1089/ast.2013.0999.

Rafkin, S. C. R., D. E. Stillman, and A. S. McEwen (2016), Fogs and clouds are a

potential indicator of local water source in Valles Marineris, *47th Lunar and Planetary Science Conference*, Abstract #2878.

Rampe, E. B., R. V. Morris, P. Douglas Archer, D. G. Agresti, and D. W. Ming (2016), Recognizing sulfate and phosphate complexes chemisorbed onto nanophase weathering products on Mars using in-situ and remote observations, *Am. Mineral., 101*(3), 678–689, doi:10.2138/am-2016-5408CCBYNCND.

Ramsey, M. S. (1996), Quantitative analysis of geological surfaces: a deconvolution algorithm for midinfrared remote sensing data, PhD dissertation, 276 pp., Arizona State University.

Ramsey, M. S., and P. R. Christensen (1998), Mineral abundance determination: Quantitative deconvolution of thermal emission spectra, *J. Geophys. Res., 103*(B1), 577–596, doi:10.1029/97JB02784.

Raney, R. K., P. D. Spudis, B. Bussey, J. Crusan, J. R.Jensen, W. Marinelli, P. McKerracher, C. Neish, Marzban Palsetia, Ron Schulze, H. B. Sequeira, and H. Winters (2011), The lunar Mini-RF radars: Hybrid polarimetric architecture and initial results, *Proc. IEEE, 99*(5), 808–823, doi:10.1109/JPROC.2010.2084970.

Raney, R. K., J. T. S. Cahill, G. W. Patterson, and D. B. J. Bussey (2012), The m-chi decomposition of hybrid dual-polarimetric radar data with application to lunar craters, *J. Geophys. Res., 117*, doi:10.1029/2011JE003986.

Rao, B., T. A. Anderson, A. Redder, and W. A. Jackson (2010), Perchlorate formation by ozone oxidation of aqueous chlorine/oxy-chlorine species: Role of ClxOy radicals, *Environ. Sci. Technol.*, 44(2961–2967), doi:10.1021/es903065f.

Retting, S. L., B. F. Jones, and F. Risacher (1980), Geochemical evolution of brines in the Salar of Uyuni, Bolivia, *Chem. Geol., 30*, 57–79.

Risacher, F., and B. Fritz (1991), Geochemistry of Bolivian salars, Lipez, southern Altiplano: Origin of solutes and brine evolution, *Geochim. Cosmochim. Acta*, *55*(3), 687–705, doi:10.1016/0016-7037(91)90334-2.

Risacher, F., H. Alonso, and C. Salazar (2003), The origin of brines and salts in Chilean salars: A hydrochemical review, *Earth-Science Rev., 63*(3–4), 249–293, doi:10.1016/S0012-8252(03)00037-0.

Roach, L. H., J. F. Mustard, M. D. Lane, J. L. Bishop, and S. L. Murchie (2010), Diagenetic haematite and sulfate assemblages in Valles Marineris, *Icarus*, *207*(2), 659–674, doi:10.1016/j.icarus.2009.11.029.

Robert, F., D. Gautier, and B. Dubrulle (1999), The solar system D/H ratio: Observations

and theories, *Space Sci. Rev., 92(201-224)*, doi:10.1023/A:1005291127595.

Robinson, M. S., S.M. Brylow, M. Tschimmel, D. Humm, S.J. Lawrence, P.C. Thomas, B.W. Denevi, E. Bowman-Cisneros, J. Zerr, M.A. Ravine, M.A. Caplinger, F.T. Ghaemi, J.A. Schaffner, M.C. Malin, P. Mahanti, A. Bartels, J. Anderson, T.N. Tran, E.M. Eliason, A.S. McEwen, E. Turtle, B.L. Jolliff, and H. Hiesinger (2010), Lunar Reconnaissance Orbiter Camera (LROC) Instrument Overview, *Space Sci. Rev.*, *150*, 81–124, doi:10.1007/s11214-010-9634-2.

Rosen, M. R. (1991), Sedimentologic and geochemical constraints on the evolution of Bristol Dry Lake Basin, California, U.S.A., *Palaeogeogr. Palaeoclimatol. Palaeoecol.*, *84*, 229–257.

Rosen, M. R. (1994), The importance of groundwater in playas: A review of playa classifications and the sedimentology and hydrology of playas, *Geol. Soc. Am. Spec. Pap.*, *289*(January 1994), 1–18, doi:10.1130/SPE289-p1.

Rosen, M. R., J. K. Warren, G. Sciences, N. Centre, P. Geology, and G. P. O. Box (1990), The origin and significance of groundwater-seepage gypsum from Bristol Dry Lake, California, USA, *Sedimentology*, *37*(6), 983–996, doi:10.1111/j.1365-3091.1990.tb01840.x.

Rothschild, L. J. (1990), Earth analogs for martian life. Microbes in evaporites, a new model system for life on Mars, *Icarus*, *88*, 246–260, doi:10.1016/0019-1035(90)90188-F.

Rothschild, L. J., and R. L. Mancinelli (2001), Life in extreme environments, *Nature*, *409*, 1092–1101.

Rubin, A. E., M. E. Zolensky, and R. Bodnar (2002), The halite-bearing Zag and Monahans (1998) meteorite breccias: Shock metamorphism, thermal metamorphism and aqueous alteration on the H-chondrite parent body, *Meteoritics and Planetary Science*, 37(125-141), doi:10.1111/j.1945-5100.2002.tb00799.x.

Rudnick, R. L., P. B. Tomascak, H. B. Njo, and L. R. Gardner (2004), Extreme lithium isotopic fractionation during continental weathering revealed in saprolites from South Carolina, *Chem. Geol.*, *212*(1–2), 45–57, doi:10.1016/j.chemgeo.2004.08.008.

Ruff, S. W., P. R. Christensen, P. W. Barbera, and D. L. Anderson (1997), Quantitative thermal emission spectroscopy of minerals: A laboratory technique for measurement and calibration, *J. Geophys. Res.*, *102*(B7), 14,899-14,913, doi:Doi 10.1029/97jb00593.

Rummel, J. D., D. W. Beaty, M. A. Jones, C. Bakermans, N. G. Barlow, P. J. Boston, V.

F. Chevrier, B. C. Clark, J.-P. P. de Vera, R. V. Gough, J. E. Hallsworth, J. W. Head, V. J. Hipkin, T. L. Kieft, A. S. McEwen, M. T. Mellon, J. A. Mikucki, W. L. Nicholson, C. R. Omelon, R. Peterson, E. E. Roden, B. S. Lollar, K. L. Tanaka, D. Viola, and J. J. Wray (2014), A New Analysis of Mars "Special Regions": Findings of the Second MEPAG Special Regions Science Analysis Group (SR-SAG2), *Astrobiology*, *14*(11), 887–968, doi:10.1089/ast.2014.1227.

Saal, A. E., E. H. Hauri, M. L. Cascio, J. A. Van Orman, M. C. Rutherford, and R. F. Cooper (2008), Volatile content of lunar volcanic glasses and the presence of water in the Moon's interior, *Nature*, *454*(7201), 192–195, doi:10.1038/nature07047.

Sagan, C., O. B. Toon, and P. J. Gierasch (1973), Climatic change on Mars., *Science*, *181*(4104), 1045–9, doi:10.1126/science.181.4104.1045.

Salisbury, J. W. (1993), Mid-infrared spectroscopy: laboratory data, *Remote geochemical analysis*, University of Cambridge, pp. 594, New York.

Salisbury, J. W., and A. Wald (1992), The role of volume scattering in reducing spectral contrast of reststrahlen bands in spectra of powdered minerals, *Icarus*, *96*(1), 121–128, doi:10.1016/0019-1035(92)90009-V.

Salisbury, J. W., and L. S. Walter (1989), Thermal infrared spectroscopic remote sensing of igneous rock types on particulate planetary surfaces, *J. Geophys. Res.*, *94(B7)*, 9192–9202, doi:10.1029/JB094iB07p09192.

Salisbury, J. W., A. Wald, and D. M. D'Aria (1994), Thermal-infrared remote sensing and Kirchhoff's law 1: Laboratory measurements, *J. Geophys. Res.*, *99*(B6), 11897–11911, doi:10.1029/93JB03600.

Salvail, J., and F. Fanale (1994), Near-surface ice on Mercury and the Moon: A topographic thermal model, *Icarus*, *111*, 441–455, doi:10.1006/icar.1994.1155.

Sanin, A. B., I. G. Mitrofanov, M. L. Litvak, A. Malakhov, W. V. Boynton, G. Chin, G. Droege, L. G. Evans, J. Garvin, D. V. Golovin, K. Harshman, T. P. McClanahan, M. I. Mokrousov, E. Mazarico, G. Milikh, G. Neumann, R. Sagdeev, D. E. Smith, R. D. Starr, and M. T. Zuber (2012), Testing lunar permanently shadowed regions for water ice: LEND results from LRO, *J. Geophys. Res.*, *117*, doi:10.1029/2011JE003971.

Sautter, V., A. Jambon, and O. Boudouma (2006), Cl-amphibole in the nakhlite MIL 03346: Evidence for sediment contamination in a Martian meteorite, *Earth Planet. Sci. Lett.*, *252*(1–2), 45–55, doi:10.1016/j.epsl.2006.09.024.

Schorghofer, N. (2007), Dynamics of ice ages on Mars, *Nature*, *449*(7159), 192–4, doi:10.1038/nature06082.

Schorghofer, N., and O. Aharonson (2014), the Lunar Thermal Ice Pump, *Astrophys. J.*, *788*(2), 169, doi:10.1088/0004-637X/788/2/169.

Schubert, B. A., T. K. Lowenstein, and M. N. Timofeeff (2009), Microscopic identification of prokaryotes in modern and ancient halite, Saline Valley and Death Valley, California, *Astrobiology*, *9*(5), 467–482, doi:10.1089/ast.2008.0282.

Sears, D. W. G., and J. Chittenden (2005), On laboratory simulation and the evaporation rate of water on Mars, *Geophys. Res. Lett.*, *32*(16), 1–4, doi:10.1029/2005GL023443.

Siegler, M. A., B. G. Bills, and D. A. Paige (2011), Effects of orbital evolution on lunar ice stability, *J. Geophys. Res.*, *116*, doi:10.1029/2010JE003652.

Siegler, M. A., R. S. Miller, J. T. Keane, M. Laneuville, D. A. Paige, I. Matsuyama, D. J. Lawrence, A. Crotts, and M. J. Poston (2016), Lunar true polar wander inferred from polar hydrogen, *Nature*, *531*(7595), 480–4, doi:10.1038/nature17166.

Sinke, G. C., E. H. Mossner, and J. L. Curnutt (1985), Enthalpies of solution and solubilities calcium chloride and its lower hydrates, *J. Chem. Thermo.*, *17(893–899*), doi:10.1016/0021-9614(85)90083-7.

Smith, R. J., B. H. N. Horgan, P. Mann, E. A. Cloutis, and P. R. Christensen (2017), Acid weathering of basalt and basaltic glass: 2. Effects of microscopic alteration textures on spectral properties, *J. Geophys. Res. Planets*, *122*(1), 203–227, doi:10.1002/2016JE005112.

Smith, D. E., M. T. Zuber, G. B. Jackson, J. F. Cavanaugh, G. A. Neumann, H. Riris, X. Sun, R. S. Zellar, C. Coltharp, J. Connelly, R. B. Katz, I. Kleyner, P. Liiva, A. Matuszeski, E. M. Mazarico, J. F. McGarry, A.-M. Novo-Gradac, M. N. Ott, C. Peters, L. A. Ramos-Izquierdo, L. Ramsey, D. D. Rowlands, S. Schmidt, V. Stanley Scott III, G. B. Shaw, J. C. Smith, J.-P. Swinski, M. H. Torrence, G. Unger, A. W. Yu, and T. W. Zagwodzki (2010), The lunar orbiter laser altimeter investigation on the lunar reconnaissance orbiter mission, *Space Sci. Rev.*, *150*, 209–241, doi:10.1007/s11214-009-9512-y.

Soderblom, L. A. (1970), A model for small-impact erosion applied to the lunar surface, *J. Geophys. Res.*, *75*(14), 2655–2661, doi:10.1029/JB075i014p02655.

Al Soudi, A. F., O. Farhat, F. Chen, B. C. Clark, and M. a. Schneegurt (2016), Bacterial growth tolerance to concentrations of chlorate and perchlorate salts relevant to Mars, *Int. J. Astrobiol.*, (Ericksen 1981), 1–7, doi:10.1017/S1473550416000434.

Speyerer, E. J., and M. S. Robinson (2013), Persistently illuminated regions at the lunar poles: Ideal sites for future exploration, *Icarus*, *222*, 122–136,

doi:10.1016/j.icarus.2012.10.010.

Speyerer, E. J., R. V. Wagner, M. S. Robinson, A. Licht, P. C. Thomas, K. Becker, J. Anderson, S. M. Brylow, D. C. Humm, and M. Tschimmel (2016), Pre-flight and on-orbit geometric calibration of the Lunar Reconnaissance Orbiter Camera, *Space Sci. Rev.*, 357–392, doi:10.1007/s11214-014-0073-3.

Spudis, P., S. Nozette, B. Bussey, K. Raney, H. Winters, C. L. Lichtenberg, W. Marinelli, J. C. Crusan, and M. M. Gates (2009), Mini-SAR: An imaging radar experiment for the Chandrayaan-1 mission to the Moon, *Curr. Sci.*, *96*(4), 533–539.

Spudis, P. et al. (2010), Initial results for the north pole of the Moon from Mini-SAR, Chandrayaan-1 mission, *Geophys. Res. Lett.*, *37*.

Spudis, P. D., and A. R. Lavoie (2011), Using the resources of the Moon to create a permanent, cislunar space faring system, *AIAA Space 2011 Conference and Exposition*, #2011-7185.

Spudis, P. D., D. B. J. Bussey, S. M. Baloga, J. T. S. Cahill, L. S. Glaze, G. W. Patterson, R. K. Raney, T. W. Thompson, B. J. Thomson, and E. A. Ustinov (2013), Evidence for water ice on the Moon: Results for anomalous polar craters from the LRO Mini-RF imaging radar, *J. Geophys. Res. - Planets*, *118*, 2016–2029, doi:10.1002/jgre.20156.

Squyres, S. W., and A. H. Knoll (2005), Sedimentary rocks at Meridiani Planum: Origin, diagenesis, and implications for life on Mars, *Earth Planet. Sci. Lett.*, *240*(1), 1–10, doi:10.1016/j.epsl.2005.09.038.

Stiller, M., Y. Yechieli, and I. Gavrieli (2007), The rate of dissolution of halite in diluted Dead Sea brines, *Geological Survey of Israel Report*, Report #GSI/01/2007.

Stiller, M., Y. Yechieli, and I. Gavrieli (2016), Rates of halite dissolution in natural brines: Dead Sea solutions as a case study, *Chem. Geol.*, *447*, doi:10.1016/j.chemgeo.2016.10.023.

Stillman, D. E., T. I. Michaels, R. E. Grimm, and K. P. Harrison (2014), New observations of martian southern mid-latitude recurring slope lineae (RSL) imply formation by freshwater subsurface flows, *Icarus*, *233*, 328–341, doi:10.1016/j.icarus.2014.01.017.

Stillman, D. E., T. I. Michaels, R. E. Grimm, and J. Hanley (2016), Observations and modeling of northern mid-latitude recurring slope lineae (RSL) suggest recharge by a present-day martian briny aquifer, *Icarus*, *265*, 125–138, doi:10.1016/j.icarus.2015.10.007.

Stober, I., J. Zhong, L. Zhang, and K. Bucher (2016), Deep hydrothermal fluid – rock interaction : the thermal springs of Da Qaidam, China, *Geofluids*, *16(4)*, *711-728*, doi:10.1111/gfl.12190.

Stopar, J. D. (2016), Ponds, flows, and ejecta of impact cratering and volcanism: A remote sensing perspective of a dynamic Moon, PhD dissertation, Arizona State Univ., 304 pp.

Stopar, J. D., B. R. Hawke, M. S. Robinson, B. W. Denevi, T. A. Giguere, and S. D. Koeber (2014), Occurrence and mechanisms of impact melt emplacement at small lunar craters, *Icarus*, *243*, 337–357, doi:10.1016/j.icarus.2014.08.011.

Svetsov, V. V., and V. V. Shuvalov (2015), Water delivery to the Moon by asteroidal and cometary impacts, *Planet. Space Sci.*, *117*, 444–452, doi:10.1016/j.pss.2015.09.011.

Taj, R. J., and M. A. Aref (2015), Structural and textural characteristics of surface halite crusts of a supratidal, ephemeral halite pan, South Jeddah, Red Sea Coast, Saudi Arabia, *Facies, 61(2)*, doi:10.1007/s10347-014-0426-0.

Takamatsu, N., N. Kat, G. Matsumot, and T. Torn (2017), The origin of salts in water bodies of the McMurdo Dry Valleys, *Antarctic Science*, *10*(4), 439–448.

Talbot, C. J., W. Stanley, R. Soub, and N. Al-Sadoun (1996), Epitaxial salt reefs and mushrooms in the southern Dead Sea, *Sedimentology, 43(6), 1025-1047*, doi: 10.1111/j.1365-3091.1996.tb01517.x.

Teiber, H., M. A. W., Marks, T. Wenzel, W. Siebel, R. Altherr, and G. Markl (2014), The distribution of halogens (F, Cl, Br) in granitoid rocks, *Chem. Geol.*, *374–375*, *92–109*, doi:10.1016/j.chemgeo.2014.03.006.

Teodoro, L. F. A., V. R. Eke, and R. C. Elphic (2010), Spatial distribution of lunar polar hydroden deposits after KAGUYA (SELENE), *Geophys. Res. Lett.*, *37(12)*, doi: 10.1029/2010GL042889.

Thompson, T. W., H. Masursky, R. W. Shorthill, G. L. Tyler, and S. H. Zisk (1974), A comparison of infrared, radar, and geologic mapping of lunar craters, *Moon*, *10*, 87–117, doi:10.1007/BF00562019.

Thomson, J. L., and J. W. Salisbury (1993), The mid-infrared reflectance of mineral mixtures (7-14 μm), *Remote Sens. Environ.*, *45*(1), 1–13, doi:10.1016/0034-4257(93)90077-B.

Thomson, B. J., D. B. J. Bussey, C. D. Neish, J. T. S. Cahill, E. Heggy, R. L. Kirk, G. W. Patterson, R. K. Raney, P. D. Spudis, T. W. Thompson, and E. A. Ustinov (2012a), An upper limit for ice in Shackleton crater as revealed by LRO Mini-RF

orbital radar, *Geophys. Res. Lett.*, *39*, doi:10.1029/2012GL052119.

Thomson, B. J., D. B. J. Bussey, J. T. S. Cahill, C. D. Neish, R. Kirk, G. W. Patterson, R. K. Raney, and P. D. Spudis (2012b), Excess Numbers of Enhanced CPR Craters in the Lunar Polar Regions, *43rd Lunar and Planetary Science Conference*, Abstract #2104.

Toner, J. D. and R. S. Sletten (2013), The formation of Ca-Cl-rich groundwaters in the Dry Valleys of Antarctica: Field measurements and modeling of reactive transport, *Geochem. et Cosmo. Acta*, 110(84-105), doi:10.1016/j.gca.2013.02.013.

Toner, J. D., D. C. Catling, R. S. Sletten, D. J. Pond, and D. J. Pond (2017), The geochemistry of Don Juan Pond : Evidence for a deep groundwater flow system in Wright Valley, Antarctica, *Earth Planet. Sci. Lett.*, *474*, 190–197, doi:10.1016/j.epsl.2017.06.039.

Torii, T., S. Murata, N. Yamagata, T. Toni, S. Murata, and N. Yamagata (2017), Geochemistry of the Dry Valley lakes, *Journal of the Royal Society of New Zealand, 11:4, 387-399*, doi:10.1080/03036758.1981.10423329.

Tosca, N. J., and S. M. McLennan (2006), Chemical divides and evaporite assemblages on Mars, *Earth Planet. Sci. Lett.*, *241*(1–2), 21–31, doi:10.1016/j.epsl.2005.10.021.

Tosca, N. J., S. M. McLennan, D. H. Lindsley, and M. A. A. Schoonen (2004), Acid-sulfate weathering of synthetic Martian basalt: The acid fog model revisited, *J. Geophys. Res. E Planets*, *109*, doi:10.1029/2003JE002218.

Tosca, N. J., A. H. Knoll, and S. M. McLennan (2008), Water activity and the challenge for life on early Mars, *Science*, *320*(2008), 1204–1207, doi:10.1126/science.1155432.

Tosca, N. J., S. M. McLennan, B. C. Clark, J. P. Grotzinger, J. A. Hurowitz, A. H. Knoll, C. Schröder, and S. W. Squyres (2005), Geochemical modeling of evaporation processes on Mars: Insight from the sedimentary record at Meridiani Planum, *Earth Planet. Sci. Lett.*, *240*, 122–148, doi:10.1016/j.epsl.2005.09.042.

Turk, L. J., S. N. Davis, and C. P. Bingham (1973), Hydrogeology of lacustrine sediments Bonneville Salt Flats, Utah: Economic Geology and the Bulletin of the Society of Economic Geologists, *Econ. Geol.*, *68*, 65–78.

Uz-Zaman, S. (2013), Chemical Assessment of Icelandic Geothermal Fluids for Direct Applications, *United Nations Geotherm. Train. Program., Reports 2013, No. 38*.

J. G. Webster (1994), Trace-metal behaviour in oxic and anoxic Ca-C1 brines of the Wright Valley drainage, Antarctica, *Chem. Geol.*, *112*, 255–274, doi:10.1016/0009-

2541(94)90028-0.

Vasavada, A. R., D. Paige, and S. E. Wood (1999), Near-surface temperatures on Mercury and the Moon and the stability of polar ice deposits, *Icarus*, *141*, 179–193, doi:10.1006/icar.1999.6175.

Vincendon, M. (2015), Identification of Mars gully activity types associated with ice composition, *J. Geophys. Res. Planets*, *120*(11), 1859–1879, doi:10.1002/2014JD022994.Received.

Vincent, R. K., and G. R. Hunt (1968), Infrared Reflectance from Mat Surfaces, *Applied Optics*, *7*(1), 53–59.

Vondrak, R., J. Keller, G. Chin, and J. Garvin (2010), Lunar reconnaissance orbiter (LRO): Observations for lunar exploration and science, *Space Sci. Rev.*, *150*, 7–22, doi:10.1007/s11214-010-9631-5.

Wald, A. E., and J. W. Salisbury (1995), Thermal infrared directional emissivity of powdered quartz, *J. Geophys. Res.*, *100*(B12), 24,665–24,675, doi:10.1029/95JB02400.

Walrafen, G. E., and J. Stone (1972), Intensification of spontaneous Raman spectra by use of liquid core optical fibers, *Appl. Spectrosc.*, *26*(6), 585–589, doi:10.1366/000370272774351688.

Wang, A., and Z. C. Ling (2011), Ferric sulfates on Mars: A combined mission data analysis of salty soils at Gusev crater and laboratory experimental investigations, *J. Geophys. Res.*, *116*, E00F17, doi:10.1029/2010JE003665.

Warren, J. K. (2006), *Evaporites:Sediments, Resources and Hydrocarbons*, Springer, 1042 pp., New York.

Watson, K., B. C. Murray, and H. Brown (1961a), On the possible presence of ice on the Moon, *Technology*, *66*(5), 1598–1600.

Watson, K., B. C. Murray, and H. Brown (1961b), The behavior of volatiles on the lunar surface, *J. Geophys. Res.*, *66*(9), 3033–3045, doi:10.1029/JZ066i009p03033.

Weis, P., T. Driesner, D. Coumou, and S. Geiger (2014), Hydrothermal, multiphase convection of H2O-NaCl fluids from ambient to magmatic temperatures: a new numerical scheme and benchmarks for code comparison, *Geofluids*, *14(347–371)*, doi:10.1111/gfl.12080.

Wetherill, G. W. (1976), Where do the meteorites come from? A re-evaluation of the Earth-crossing apollo objects as sources of chondritic meteorites, *Geochim.*

Cosmochim. Acta, *40*, 1297–1317, doi:10.1016/0016-7037(76)90120-4.

White, A. F., and H. L. Buss (2013), Natural Weathering Rates of Silicate Minerals, *Treatise on Geochemistry*, 2nd ed., pp., 329-359, Elsevier Ltd.

Wilcox, B. B., M. S. Robinson, P. C. Thomas, and B. R. Hawke (2005), Constraints on the depth and variability of the lunar regolith, *Meteorit. Planet. Sci.*, *40*(5), 695–710, doi:10.1111/j.1945-5100.2005.tb00974.x.

Williams, D. A., R. Greeley, E. Hauber, K. Gwinner, and G. Neukum (2005), Erosion by flowing Martian lava: New insights for Hecates Tholus from Mars express and MER data, *J. Geophys. Res. E Planets*, *110*, 1–13, doi:10.1029/2004JE002377.

Wilson, L. (2004), Mars outflow channels: A reappraisal of the estimation of water flow velocities from water depths, regional slopes, and channel floor properties, *J. Geophys. Res.*, *109*(E9), E09003, doi:10.1029/2004JE002281.

Witherow, R. A. and W. B. Lyons (2011), The fate of minor alkali elements in the chemical evolution of salt lakes, *Saline Systems, 7*(1), doi:10.1186/1746-1448-7-2.

Yang, L., F. J. Ciesla, C. M. O. D. Alexander (2010), The D/H ratio of water in the solar nebula during its formation and evolution, *Icarus, 226(256-267)*, doi:10.1016/j.icarus.2013.05.027.

Zhang, J. A., and D. A. Paige (2009), Cold-trapped organic compounds at the poles of the moon and Mercury: Implications for origins, *Geophys. Res. Lett.*, *36*, doi:10.1029/2009GL038614.

Zhijie, L., and G. U. O. Guoying (1986), Geology of the Tengchong Geothermal Field and Surrounding Area, West Yunnan, China, *Geothermics*, *15*(3), 339-345, doi:10.1016/0375-6505(86)90110-0.

Zimmerman, M. I., W. M. Farrell, T. J. Stubbs, J. S. Halekas, and T. L. Jackson (2011), Solar wind access to lunar polar craters: Feedback between surface charging and plasma expansion, *Geophys. Res. Lett.*, *38*, doi:10.1029/2011GL048880.

Zolensky, M. E. (2007), Asteroidal Water Within Fluid Inclusion – Bearing Halite in an H5 Chondrite, Monahans (1998), *Science*, 1377–1380, doi:10.1126/science.285.5432.1377.

Zolotov, M. Y., and M. V. Mironenko (2016), Chemical models for martian weathering profiles: Insights into formation of layered phyllosilicate and sulfate deposits, *Icarus*, *275*, 203–220, doi:10.1016/j.icarus.2016.04.011.

Zuber, M. T., D. E. Smith, S. C. Solomon, D. O. Muhleman, J. W. Head, J. B. Garvin, J. B. Abshire, and J. L. Bufton (1992), The Mars Observer laser altimeter

investigation, *J. Geophys. Res.*, *97*(E5), 7781–7797, doi:10.1029/92JE00341.

APPENDIX A

IMAGE IDS FOR LRO DATA PRODUCTS USED

Table S1. Image IDs for LROC NAC and Mini-RF products used in this study.

	Nominal NACs	Pixel Scale (m)	Long-Exp. NACs	Pixel Scale (m)	Stokes Parameter Maps (s1-s4)
Rozhdestvenskiy N	M107943788R	1.708762218	M1148294146L	9.302545902	lsz_04698_2s1_oku_82n203_v1
	M1097414120L	2.28511747	M1175170925L	9.299648691	lsz_04700_2s1_oku_82n202_v1
	M1097406880L	2.283331815	M1117638788L	19.02793487	lsz_04496_2s1_oku_82n202_v1
	M1097392589L	2.285705599			lsz_04476_2s1_oku_84n211_v1
Lovelace	M105190616L	2.861680923	M1117333294R	19.05390407	lsz_04446_2s1_oku_82n251_v1
	M105212081R	2.857805722	M1117333294L	19.06031504	
	M105212081L	2.863641919			
Lovelace E	M105126213L	2.871902461	M1119620473L	8.846548902	lsz_04434_2s1_oku_82n265_v1
	M105126213R	2.865994511	M1119620473R	8.842451308	lsz_04436_2s1_oku_82n263_v1
	M105147680L	2.875853511			
	M105147680R	2.870002848			
Main L	M192847909L	2.253863203	M1121147163L	8.880541305	lsz_04868_2s1_oku_83n026_v1
	M192847909R	2.251022189	M1121147163R	8.875686545	lsz_04870_2s1_oku_83n024_v1
	M192840805L	2.259740275	M1116431138L	19.08790916	lsz_04872_2s1_oku_83n022_v1
	M192840805R	2.256851066	M1116431138R	19.08151149	
Whipple	M1095127503R	2.276947531	M1118732802L	11.73512959	lsz_06752_2s1_oku_89n104v1
	M101353952L	3.678406436	M1118732802R	11.73857581	lsz_06701_2s1_oku_89n123v1
	M101353952R	3.672879133	M1121360339L	10.33472978	
	M101318146L	3.689372117	M1121360339R	10.34437064	
Plaskett U	M105835784R	3.7063077	M1115529033L	19.03468937	lsz_04742_2s1_oku_82n160_v1
	M105835784L	3.711932072	M1115529033R	19.01746182	
Byrgius C	M1145212304L	0.819114126			lsz_02687_2s1_eku_20s295_v1
	M1145212304R	0.81794328			lsz_06680_2s1_eku_14s296_v1
Gardner	M185662630R	1.020774218			lsz_01371_2s1_eku_16n034_v1
	M185662630L	1.02269873			lsz_01371_2s1_eku_19n034_v1
	M180944879L	1.290906281			

APPENDIX B

PREVIOUS PUBLICATION/STATEMENT OF CO-AUTHORS

Chapter 2 was reproduced from *Planetary and Space Science*, where it was published in July 2017. Co-authors are S. J. Lawrence, M. S. Robinson, E. J. Speyerer, and B. W. Denevi.

Chapters 3 and 4 are manuscripts in work that will be submitted to TBD journals, with the coauthors P. Christensen (Chapters 3 and 4) and H. Hartnett (Chapter 3 only).

Chapter 5 was reproduced from *Journal of Geophysical Research: Planets*, where it was published in September 2016. Co-author is P. Christensen.